3-22-2012

Design, Modeling, and Measurement of a Metamaterial Electromagnetic Field Concentrator

Noel A. Humber

DESIGN, MODELING, AND
MEASUREMENT OF A METAMATERIAL
ELECTROMAGNETIC FIELD CONCENTRATOR

THESIS

Noel A. Humber, Captain, USAF

AFIT/GE/ENG/12-22

DEPARTMENT OF THE AIR FORCE
AIR UNIVERSITY

AIR FORCE INSTITUTE OF TECHNOLOGY

Wright-Patterson Air Force Base, Ohio

AFIT/GE/ENG/12-22

DESIGN, MODELING, AND MEASUREMENT OF A METAMATERIAL ELECTROMAGNETIC FIELD CONCENTRATOR

THESIS

Presented to the Faculty

Department of Electrical and Computer Engineering

Graduate School of Engineering and Management

Air Force Institute of Technology

Air University

Air Education and Training Command

In Partial Fulfillment of the Requirements for the

Degree of Master of Science in Electrical Engineering

Noel A. Humber, B.S.M.E.

Captain, USAF

March 2012

APPROVED FOR PUBLIC RELEASE; DISTRIBUTION UNLIMITED

AFIT/GE/ENG/12-22

DESIGN, MODELING, AND MEASUREMENT OF A METAMATERIAL ELECTROMAGNETIC FIELD CONCENTRATOR

Noel A. Humber, B.S.M.E.

Captain, USAF

Approved:

Peter J. Collins, PhD (Chairman)	Date
Ronald A. Coutu, Jr., PhD (Member)	Date
Milo Hyde, Maj, USAF (Member)	Date

AFIT/GE/ENG/12-22

Abstract

Popularized by such proposed applications as electromagnetic cloaks or perfect lenses, the field of metamaterials has become a source of great fascination for the public and a subject of great scrutiny for researchers. Defined in the most general manner, metamaterials are materials designed to display unusual and sometimes controversial electromagnetic properties, such as negative refraction. Metamaterials are made from inclusions sized and spaced such that for large enough incident wavelengths, the inclusions form what appears to be a homogeneous material.

An increasingly popular tool for developing applications for metamaterials is transformation optics that is a method of producing a desired electromagnetic behavior by altering the constitutive parameters of the target material. Most research involved with using transformation optics to produce devices such as electromagnetic field concentrators has been limited to simulation because rapidly producing metamaterials is not an easy task. Transformation optics produces anisotropic, spatially variant tensors of constitutive parameters that can be exactly manufactured. In fact, designing a device for a particular set of constitutive parameters is an involved task.

AFIT has produced a means to rapidly design a metamaterial device to a specified tensor of constitutive parameters. This thesis has three areas of focus: validation of the rapid design method, optimization of the rapid design method, and electromagnetic characterization of the device produces using the optimized design method. The first task was to create an electromagnetic field concentrator by using embedded transformation

optics that compress incident plane waves into a small area. COMSOL® was used to model the ideal, anisotropic and spatially variant device designed for resonance at 10 GHz.

The second task was to use both the AFIT rapid design process and a newly developed process to homogenize the anisotropic, spatially-variant relative constitutive parameter material created by transformation optics. The second task also involved optimizing the match between the desired relative constitutive parameters and those achievable by the rapid design method. This optmization was realized by several methods with emphasis on altering the ratio of the shapes forming the concentric geometry device to minimize the mismatch between ideal and achievable relative constitutive parameters from potentially well over 10000% error to 75% error. The optimized homogenous design was tested in CST Microwave Studio®. S-parameters and time-average fields were measured to characterize the expected performance of the field concentrator.

The third and final task was completed by creating a stack of printed circuit boards with the metamaterial cell traces and testing both S-parameters and field concentration of the device with a focus beam measurement system. The experimental data are too preliminary to report with much confidence and further testing appers necessary before drawing definitive conclusions.

Finally, recommendations for improving the device presented in this thesis or developing an alternative are presented. A cylindrical design based on the concept of concentric geomtries is recommended for manufacturing and future testing in AFIT's BANTAM measurement system.

Acknowledgments

I owe a debt of gratitude to my family and friends for frequent acts of encouragement, large and small, as I endeavored to complete my graduate studies. I cannot express my profound appreciate for the support structure I have been lucky to turn to as I have made my transition from my undergraduate studies in mechanical engineering to my graduate research in electrical engineering.

There are many people that were instrumental to me in the completion of this thesis. I must first recognize the daily support provided by my loving wife. She provided constant encouragement and tried to ensure I maintained a healthy balance between schoolwork and life. Her love and support meant the world to me. I must also thank our seven four-footed children who each provided unconditional love and attention. I also want to thank all my friends at AFIT. They provided friendship, comic relief, and proof that even the best of us can struggle with the simplest of problems. Thanks also to my advisor who provided encouragement, direction, and was always willing to answer my many questions.

Finally, I would be remiss if I did not recognize my parents who have always wanted me to succeed and encouraged my inquisitive nature. I especially appreciate that they provided me advice when it was asked for and were constantly ready to listen quietly to me when I needed to vent. They are the two smartest people I know. They are my role models and I love them both very much. Thanks again.

Noel A. Humber

Table of Contents

List of Figures

List of Tables

List of Abbreviations

DESIGN, MODELING, AND MEASUREMENT OF A METAMATERIAL ELECTROMAGNETIC FIELD CONCENTRATOR

I. Introduction

1.1 Problem Description

The fantastic promises of modern electrical engineering require increasingly intricate system designs. Ever-growing system complexity can be juxtaposed with the fundamental laws of electricity and magnetism that serve as the foundation for any electromagnetic device. The contemporary focus on applied electromagnetics is the natural evolution of what has been termed the classical era [69].

In 1733, Charles-Francois du Fay discovered the existence of positive and negative charges and showed that unlike charges attract while like charges repel. In 1820, Hans Christian Oersted showed that a wire carrying a current produced a magnetic field. In 1831, Englishman Michael Faraday discovered that an electromotive force or voltage can result from a changing magnetic flux, while four years later Carl Friedrich Gauss developed a mathematical relationship tying an electric charge to the electric flux through a surface enclosing said charge. Several decades later, in 1873, one of the most important achievements in the field of electromagnetics occurred when Scottish scientist James Maxwell synthesized a set of four vector equations by uniting the theories of his contemporaries [69]. The set of four equations is now known as Maxwell's equations.

Maxwell's equations are distinguished as the first unified set of electromagnetic equations. These equations and several constitutive relations are the basis upon which all modern electrical and magnetic systems are designed. In particular, Maxwell's equations can be used to describe a material's dielectric constant or permittivity as well as its magnetic permeability. These bulk material properties or constitutive parameters determine material impedance and the index of refraction and therefore dictate the manner in which electromagnetic waves propagate through a medium.

Until the 1960s, scientists utilized Maxwell's equations to characterize the electromagnetic properties of materials using the implicit assumption that permittivity and permeability could never be simultaneously negative since no such natural condition has ever been observed. In 1968, Russian scientist Victor Veselago suggested that materials with simultaneously negative values of permittivity and permeability could exist [70]. Technological limitations prevented Veselago from confirming the existence of these double negative (DNG) materials, but he promised that they would exhibit material properties inimitable by nature [70].

The promised extraordinary behaviors included negative refraction and reversed Doppler effect [70]. These and other unusual properties were attributed to a DNG material's ability to induce negative group velocity on an incident electromagnetic wave. The negative group velocity associated with DNG materials means that energy flux opposes the propagation direction of a wave and the phase velocity of a wave in the DNG material. Such wave behavior can be described only by a vector quantity representing energy flux that forms a left-handed set with the electric and magnetic field vectors. Therefore, DNG materials are called left-handed metamaterials (LHM).

The prefix *meta* used to describe DNG materials is a Greek term meaning "after" and is used to emphasize the infancy of a new and developing class of materials [58].

Metamaterials are often associated with either a negative value of permittivity, a negative value of permeability, or a DNG material. However, one definition correctly restates metamaterials more broadly as: "composite materials with useful and unusual electromagnetic properties offered by the specific response of constituents and their arrangement" [60]. Therefore, metamaterials do not necessarily have negative constitutive parameters; they exhibit unusual behavior in the presence of electromagnetic waves.

Metamaterials and their unusual behavior truly represent a new area of research. Indeed, in the last two decades much research has been focused on this new branch of science. Scientists would like to take advantage of the basic laws of electromagnetics to generate exotic effects such as electromagnetic cloaks that heretofore were confined to the fantasy creations of television and movies.

1.2 Potential Metamaterial Applications

Innumerable applications have been conceived to take advantage of the unusual properties generated by the subwavelength (less than $\lambda/10$) structures that compose a metamaterial surface. Research has explored potential military and civilian applications. Air forces around the world, including the USAF, would like to incorporate metamaterials in aircraft and subsystem designs to gain leverage over potential adversaries and create synergistic battlefield effects. Particular applications interesting military organizations include radar cross-section reduction, imaging, communication, and radar. Proposed civilian applications of metamaterials have ranged from antennas and filters to employment with flexible technology for smart sensors or health monitoring systems [22].

The most exotic proposed applications of metamaterials utilize DNG materials that leverage a negative index of refraction to bend electromagnetic waves in ways not observed in nature. Transformation optics (TO) is the mathematical tool used to describe that bending or refraction and defined by the principle of adaptive coordinate system transformations. The goal of transforming coordinate systems is to describe realizable bending of electromagnetic waves. A number of fantastical material effects might be realized if an electromagnetic wave can travel in a straight line in its own coordinate system, traversing its path in the least amount of time while appearing to bend in the coordinate system of the observer [71]. Therefore, if the proper choice of permittivity and permeability can induce a relative coordinate transformation, metamaterials can be tuned to create effective bulk parameters capable of bending incident electromagnetic waves. Two of the most exotic and therefore most publicized proposed applications of wave bending with metamaterials include the electromagnetic cloak and the perfect lens.

Perhaps the most trumpeted application of metamaterials is the electromagnetic cloak. The concept of the electromagnetic cloak, proposed in 2006, is supported by the mathematical arguments of TO [26, 49]. A perfect cloak involves directing electromagnetic waves about a central region by developing an anisotropic cloak material. The permittivity and permeability gradient developed must be continuous over the extended path about the cloaked target to avoid reflections [30]. A matched impedance at the boundary between the cloak and free space prevents backscattering from the target and ensures perfect target invisibility.

Of course, there are limitations to the implementation of an actual cloak. Smooth and continuous variation of the constitutive parameters is not possible, for example, due to the finite size of unit cells that constitute the DNG metamaterial. Additionally, anybody hoping to implement a useable cloak must consider reciprocity; if an observer cannot see a cloaked target, the cloaked target cannot see the observer. Therefore, potential applications of a cloak may be limited to buildings, fortifications, and immobile objects yet the appeal of creating a cloak is no less exciting.

The other well-known application of metamaterials is the perfect lens. The mathematical postulation of such a device was published in 2000 [45]. As Pendry explained, the perfect lens can perfectly focus light and therefore does not suffer from diffraction-limited focusing of conventional optics. It can also provide full image reconstruction. These effects are possible by using a DNG material in the near field of a target (on the order of wavelengths of separation). Its placement in the near field and its negative index of refraction allow a perfect lens to capture, amplify, and refract evanescent waves that conventional lenses ignore [45]. The perfect lens uses not only the evanescent waves which, if not captured would exponentially decay as they are emitted from a target, but also the propagating waves to resolve a perfect image of the target.

Unfortunately there are limitations to achieving a perfect lens, much as there are for achieving a perfect electromagnetic cloak. Any material used to construct a perfect lens will have a finite value of absorptivity (mathematically expressed as the imaginary component of permittivity and physically expressed as energy absorbtion). Energy absorption will prevent perfect image construction. Nonetheless, the goal of extremely small resolution capability is scientifically worthy. The implications of accomplishing this goal are grand enough to ensure research on the subject continues despite the strident theoretical objections by a small subset of the academic community.

The goals of most metamaterial research are not nearly as lofty as the creation of an electromagnetic cloak or perfect lens but they are potentially more attainable and more useful. For example, the achievement of a homogenous, discretized approximation to the anisotropic materials required by TO can be a long and tedious process. A goal of this thesis is to apply a rapid metamaterial design process to a TO approach for building an optimized, tunable electromagnetic concentrator.

Proving the feasibility of rapidly producing an optimized metamaterial field concentrator could make metamaterial designs feasible for a large number of applications. One practical application is metamaterial-based sensor for signal detection. This device is similar to the perfect lens in that the goal is to create a tunable subwavelength surface that captures and concentrates electromagnetic fields.

Modern aircraft design emphasis on minimizing component size, weight and power requirements means that a metamaterial sensor would be particularly advantageous. Current sensors generally draw significant amounts of power to power sometimes large and relatively complex electromechanical designs. A metamaterial signal detection sensor could potentially draw very little power. A set of tunable subwavelength metamaterial surfaces could be combined with active electro-optical modulators to several simple sensors. These sensors could be joined to form a distributed array for signal sensing, particularly in lower bands of the frequency spectrum.

1.3 Research Goals

This research effort is directed towards the sequential achievement of two interconnected goals, the first of which is the development and characterization of an electromagnetic field concentrator using TO techniques and an Air Force Institute of Technology (AFIT) rapid design methodology. The characterization of its field behavior is completed via various computational models. The second goal is the construction and testing of a concentrator. Experimental results will be compared to previous theoretical predictions.

1.3.1 Model Development of a Metamaterial Field-Concentrating Device.

The initial goal of this research effort is to enhance electromagnetic field strength in the presence of metamaterial structures. These structures can be formed from individual unit cells or from fractals that display origin symmetry and self-similarity [17]. However, metamaterials have primarily been produced from arrangements of individual unit cells. In particular, field concentration can also be obtained within the gaps of split-ring resonators (SRR) or from unit cells arranged to produce a super cell that creates a macroscopic area of electromagnetic field strength far greater in spatial extent than any individual gap size used in its construction.

This thesis will use a TO approach to create a super cell to create local permittivity and permeability values that effect field concentration. The required constitutive parameters will be approximated with unit cells whose geometry is set by AFIT's rapid design process. Geometrical features of concern include the unit cell width and height, width of the trace, trace material, gap size, and spacing of intra-cell components.

Characterization of the field concentration is first conducted via predictive methods. Predictions of field strength enhancement utilize computational electromagnetic models discussed in Chapter III. These models use time- and frequency-domain techniques dependent on Maxwell's equations to generate necessary theoretical predictions. Construction of a field concentrator used to verify the model simulations is also discussed in Chapter III.

1.3.2 Device Construction and Characterization of Electromagnetic Response.

The second thesis objective involves two steps. First, the device developed using TO and the rapid design process must be constructed. Second, the physical construction must be measured. Basic S-parameter measurements are generated with AFIT's focus beam measurement system. Measurements of the field concentration produced by the device are conducted with the focus beam measurement system and a Hertzian dipole probe attached to a table providing 2-D translation capability.

The calibration and setup of all test equipment and instrumentation is discussed in Chapter IV. Measurements generated with AFIT's focus beam system are analyzed to characterize both resonance frequencies and field strength enhancement. Measured results are compared with the predicated performance obtained from simulations. General methods of enhancing both the manufacturing process and the field concentrating design are noted.

1.4 Organization of Thesis

This thesis is organized into five chapters. Chapter II provides theoretical background information related to the concepts investigated through this research effort as well a review of analogous past, recent, and on-going research efforts. Chapter III first describes the modeling of the field concentrator using TO and the rapid design process. This chapter specifically discusses the creation, implementation, and results of computational models built to produce some theory-based predictions. Chapter III next discusses the creation of a physical model with which experimental data will be collected. This chapeter provides a surface-level discussion of the manufacturing process. Chapter IV explains the manufacturing of the concentrator, the experimental equipment and instrumentation, the test procedures, and the results produced from the laboratory measurements utilizing the focus beam system. Chapter V includes conclusions drawn from the research effort and suggests avenues for follow-on research efforts that can build upon the results drawn in this thesis.

II. Theory

2.1 Chapter Overview

The field of metamaterials is still in its formative years with respect to more classical branches of electrical engineering yet there already exists a substantial body of research that this background investigation was able to draw upon. Chapter I introduced the objectives that directed the research effort for this thesis. This chapter substantiates the validity of the chosen research objectives by providing a selective analysis of classical and contemporary research efforts related to those objectives.

The research objectives of this thesis relate to the design, construction, and quantitative evaluation of an electromagnetic field concentrator or, simply, a field concentrator. This chapter provides necessary depth of knowledge in the field of electromagnetism to appreciate the design and simulation of a concentrator. Discussion topics include effective media, constitutive parameter extraction, and TO. This theory discussion is backed by a review of both the finite element method (FEM) and the finite integration technique (FIT) used to conduct the simulations.

Beyond the theoretical underpinnings of this thesis, contemporary research efforts to exploit these and other concepts are introduced. Efforts utilizing TO for field concentration are particularly emphasized.

2.2 Metamaterial Characterization

The burgeoning science of metamaterials may trace its roots to initial studies conducted in the last half of the nineteenth century when Bose started microwave experiments with twisted structures [15] but colloquial conceptions of what it means to be a metamaterial have been shaped by the advances of the past two decades. Myopic public perceptions seem to link metamaterial research exclusively to the pursuit of electromagnetic cloaks, if not also the pursuit of a limited number of other fantastical applications. Admittedly, much research has focused on understanding and improving wave bending for the purposes of cloak formation. However, there is a multitude of research involving other applications.

The race to develop electromagnetic cloaks and other metamaterial applications has had the fortuitous result of greatly expanding body of knowledge about the design, physics, and testing of metamaterials. In particular, studies of metamaterials have led to alternate and sometimes antithetical theories describing the physics of metamaterials.

A prime example of disagreement is the explanation of the source for the physical phenomena observed from metamaterials subjected to electromagnetic illumination. Explanations of the origins of such phenomena generally divide scientists into two camps: those that ascribe the source of the phenomena to a theory of effective media and those that believe surface wave models are the best explanation.

The differing explanations for the origins of observed metamaterial physical phenomena are rooted in an inherent disagreement about whether or not the constitutive parameters can be negative or not. Temporarily accepting the fact that constitutive parameters may be negative over limited frequency bands, this section first examines the concept of a negative index of refraction. This section then introduces the concept of surface waves and contrasts it with an effective media approach.

2.2.1 Negative Index of Refraction.

In his treatise, “The First Book Opticks,” Sir Isaac Newton described a property of light rays called refrangibility to explain how incident rays have the propensity to be “turned out of their way” [39]. The property he described was refraction. The familiar, non-mathematical definition of refraction describes how waves incident upon a medium at an inhomogeneous material boundary are bent by that medium. This bending is described by Snell’s law as [16]

$$n_1 \sin(\theta_1) = n_2 \sin(\theta_2) \tag{1}$$

where n is the index of refraction, θ is the angle of incidence or transmission, and the subscripts 1 and 2 denote the incident and transmission material respectively. The index of refraction n is s material-dependent term and can be described as

$$n = \frac{c}{v} = \frac{c}{f\lambda} \tag{2}$$

where c is the speed of light in a vacuum, v is the phase velocity, f is the frequency of the wave, and λ is the wavelength of the wave in the material of interest.

A common mathematical abstraction, approximately valid outside of applications involving high amplitude electric fields such as lasers [16], is that the wave’s frequency is not modulated by the incident or transmission medium. This assumption simplifies comparisons of indices between media and clarifies various observations wave propagation in a medium including whether they speed up or slow down, whether they spread out or not, etc. For centuries, research has focused on understanding the index of refraction while simultaneously employing the implicit assumption that the term must be a positive property.

All discussions about the sign of the index of refraction are rooted in Maxwell's equations. The differential forms of the rotational equations and constitutive relations for time-harmonic fields in a source-free environment are [4]

$$\nabla \times \boldsymbol{E} = -\boldsymbol{M}_i - j\omega \boldsymbol{B}, \tag{3a}$$

$$\nabla \times \boldsymbol{H} = \boldsymbol{J}_i + \boldsymbol{J}_c + j\omega \boldsymbol{D}, \tag{3b}$$

$$\boldsymbol{D} = \varepsilon \boldsymbol{E}, \tag{3c}$$

$$\boldsymbol{B} = \mu \boldsymbol{H}, \tag{3d}$$

where $\boldsymbol{E}$ and $\boldsymbol{H}$ are the electric and magnetic fields respectively, $\boldsymbol{D}$ and $\boldsymbol{B}$ are the electric and magnetic flux respectively, $\boldsymbol{M}_i$ is the impressed our source magnetic current density, $\boldsymbol{J}_i$ is the impressed our source electric current density, $\boldsymbol{J}_c$ is the conduction electric current density, ε and μ are the electric permittivity and magnetic permeability of the medium respectively, and j is the imaginary term representing $\sqrt{-1}$.

Plane waves are often exploited in research and use a reduced form of Equations (3). Simplifying these rotational equations given the assumption of a monochromatic plane wave with angular frequency ω and wave vector $\boldsymbol{k}$ leads to [70]

$$|\boldsymbol{kE}| = \frac{\omega}{c} \mu \boldsymbol{H}, \tag{4a}$$

$$|\boldsymbol{kH}| = \frac{\omega}{c} \varepsilon \boldsymbol{E}, \tag{4b}$$

Time-varying electromagnetic fields have measureable energy and power that provide the means to track the travel and interference (both constructive and destructive) of traveling waves in simulations. Power density can be described by the Poynting vector, which, in time-averaged form, is [4]

$$\boldsymbol{S} = \frac{1}{2}\Re\left[\boldsymbol{E}\times\boldsymbol{H}^{*}\right] \tag{5}$$

where $\Re$ denotes the real part of the cross-product and $*$ denotes the complex conjugate.

The vector set $\boldsymbol{k}$, $\boldsymbol{E}$, and $\boldsymbol{H}$ that form the foundation for the Poynting vector and previously defined equations define the electromagnetic nature of a material. This set can either be described as right- or left-handed depending on the sign of the material's permittivity and permeability. When these constitutive parameters are both greater than zero the material is considered right-handed and when both parameters are less than zero the material is considered left-handed [70]. The traditional set of Maxwell's equations is right-handed. Note that $\boldsymbol{S}$, the time-averaged Poynting vector, implicitly depends on the constitutive parameters yet only forms a right-hand set with the vector quantities $\boldsymbol{E}$ and $\boldsymbol{H}$ [70].

Until the 1960s only right-handed sets were presumed to exist. In 1968, Veselago challenged the academic community by contending that left-handed sets were at least mathematically conceivable [70]. He asserted that a consequence of the assignment of right- or left-handedness is readily apparent when evaluating the direction cosines attached to the components of $\boldsymbol{k}$, $\boldsymbol{E}$, and $\boldsymbol{H}$ for a wave traveling in a medium. These direction cosines α, β, and γ respectively and may be compiled in a matrix as [70]

$$G = \begin{pmatrix} \alpha_1 & \alpha_2 & \alpha_3 \\ \beta_1 & \beta_2 & \beta_3 \\ \gamma_1 & \gamma_2 & \gamma_3 \end{pmatrix} \tag{6}$$

where the subscripts 1, 2, and 3 represent the different coordinate axes. The determinant of G is denoted as p; $p = 1$ for right-handed media and $p = -1$ for LHM.

Now consider a wave traveling from one medium into another. Given two media of finite conductivity and assuming no sources or charges then the tangential fields and normal flux values in each medium at the material interface should be equivalent and can be written as [4, 70]

$$\hat{n}\times\left(\boldsymbol{E}_2-\boldsymbol{E}_1\right) = 0, \tag{7a}$$

$$\hat{n}\times\left(\boldsymbol{H}_2-\boldsymbol{H}_1\right) = 0, \tag{7b}$$

$$\hat{n}\times\left(\varepsilon_2\boldsymbol{E}_2-\varepsilon_1\boldsymbol{E}_1\right) = 0, \tag{7c}$$

$$\hat{n}\times\left(\mu_2\boldsymbol{H}_2-\mu_1\boldsymbol{H}_1\right) = 0, \tag{7d}$$

where $\hat{n}$ is the unit normal vector of the incident medium at the interface and the subscripts 1 and 2 indicate the incident and transmission mediums respectively.

Now, using θ_1 and θ_2 to represent the incident and transmission angles respectively, refraction can be described per Snell's law. The ratio of the indices of refraction can be written as [70]

$$\frac{n_2}{n_1} = \frac{\sin(\theta_1)}{\sin(\theta_2)} = \sqrt{\frac{\varepsilon_2\mu_2}{\varepsilon_1\mu_1}}. \tag{8}$$

Veslago underlined the assumption in Equations (7) that also appears in Equation (8) that both media are using the same vector set, be it left- or right-handed. The result of this assumption is positive refraction, displayed in Figure 1. When the rightnesses differ, Equation (8) must account for each material's directional cosine matrix determinant and can be written as [70]

$$\frac{n_2}{n_1} = \frac{p_2}{p_1}\left|\sqrt{\frac{\varepsilon_2\mu_2}{\varepsilon_1\mu_1}}\right| \tag{9}$$

An obvious conclusion from Equation (9) is that when one material is right-handed and the other material is left-handed, negative refraction such as that depicted in Figure 1 will occur.

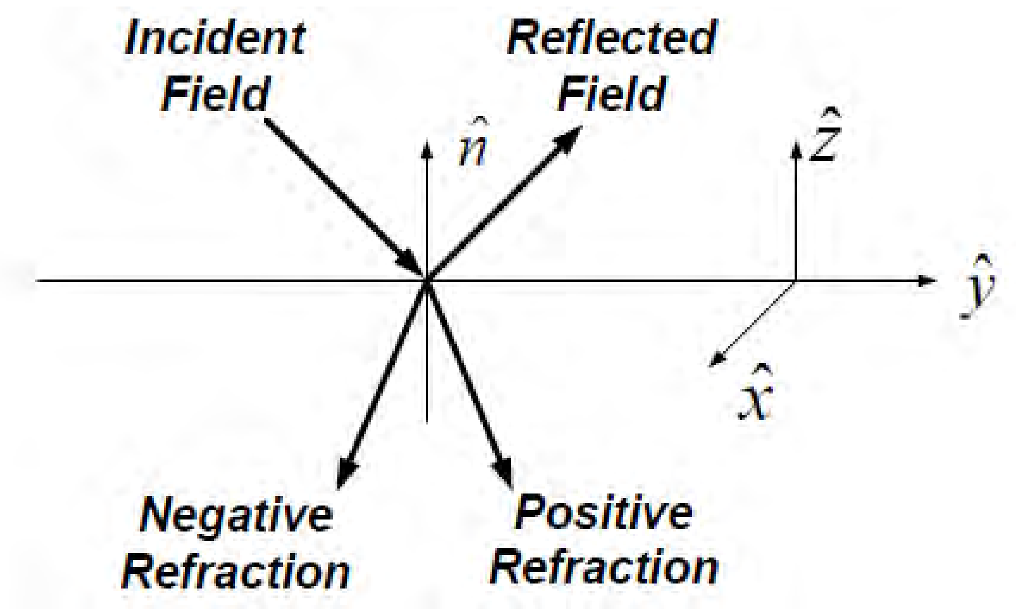

Figure 1. Graphical depiction of negative and positive refraction in [30]. A field incident upon a material interface will experience reflection and refraction. The handedness of the material impinged upon, left-handed or right-handed, will determine the refraction direction. LHM cause negative refraction.

2.2.2 Realization of Negative Refraction.

Veselago postulated that LHM could exist but at the time of the publication of his article, no natural or manmade material existed to confirm his hypothesis. Were such a material to exist, physics as it has been known for centuries would be turned on its head.

Convex lenses made of LHM and illuminated by light rays in a vacuum would diverge the rays and left-handed concave lenses would converge rays, as is shown in Figure 2.

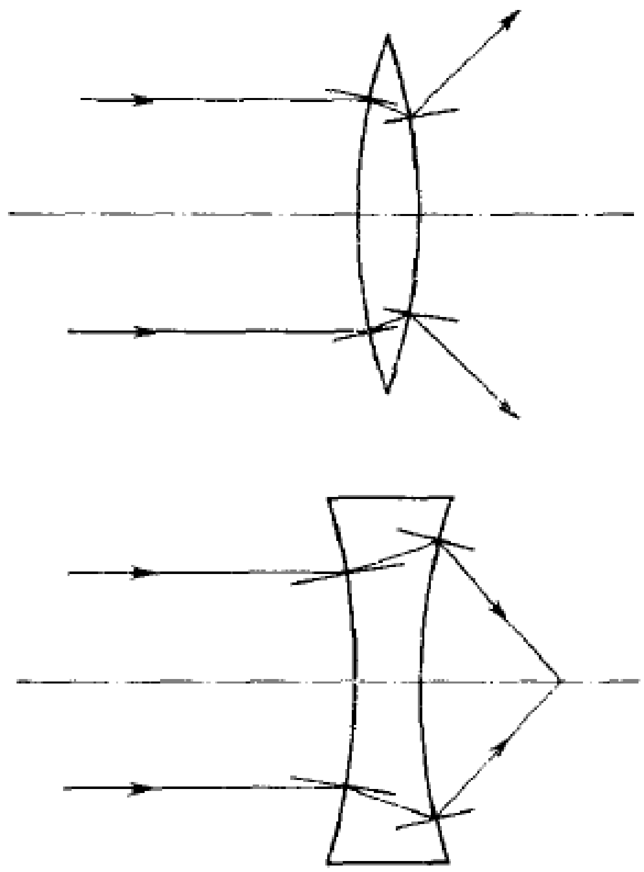

Figure 2. Lenses made of LHM published in [70]. Due to negative refraction, lenses exhibit opposite behavior in the presence of incident fields. Instead of converging the fields, a convex lens will cause divergence. A concave lens will focus the incident fields.

Further, as was shown previously, the Poynting vector always forms a right-handed vector set with $\boldsymbol{E}$ and $\boldsymbol{H}$ so in a left-handed material the wave travels opposite the power/energy flow. Waves of this nature, pictured in Figure 3, are said to be backward traveling [36]. While still up to debate, LHM are therefore considered to have negative group and phase velocity conditions that lead to a reversal of both the Doppler effect and the Vavilov-Cerenkov effect, as mentioned in Chapter I [70].

Scientists seized upon the potential benefits of LHM and after decades of research, Shelby et al. created just such a material in 2001 that displayed negative refraction [57]. This achievement was realized with artificial materials utilizing subwavelength structures or inclusions that created an appearingly homogenous material to the incident radiaton's relatively large wavelength. To this date in time, all materials exhibiting negative indices of refraction have been made of these artificial, frequency-dependent materials.

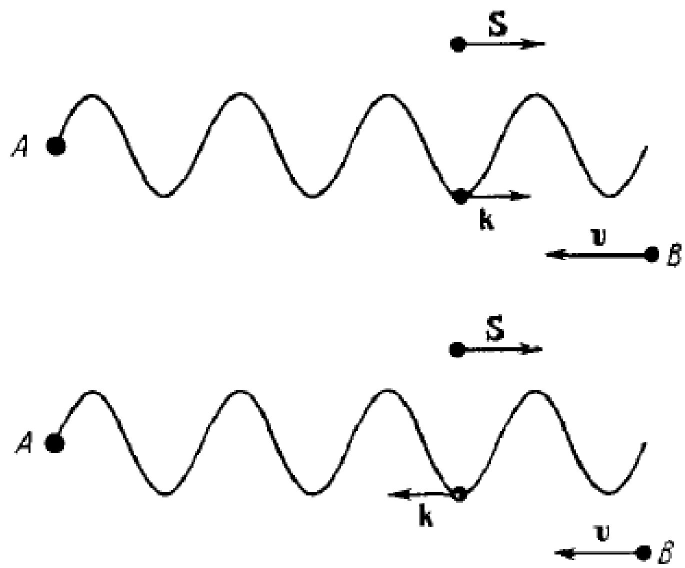

Figure 3. Power flow in a material in [70]. The top wave shows a field traveling in a right-handed material. The Poynting vector *S* is in the same direction as the wave. In LHM, *S* opposes the wave's direction of travel; that is, energy flux flows opposite the direction of wave travel; group and phase velocity will be negative.

2.2.2.1 Negative Permittivity Materials.

Negative refraction is inherent in LHM, which are in turn the product of simultaneously negative effective constitutive parameters. No natural materials are left-handed so various mechanisms must be applied to artificially and simultaneously drive effective constitutive parameters negative. Pendry et al. showed that the frequency-dependent nature of electric permittivity could be used to generate negative effective values of permittivity [48]. They based their findings on an analysis of the plasmon.

A plasmon is “a collective oscillation of electron density” [48]. Chemistry teaches that metals are a sea of valence electrons hence all metals exhibit a plasma frequency. Plasma frequency or ω_p is the frequency at which the plasmons oscillate. It can be written in a form describing its harmonic motion [48]

$$\omega_p^{\,2} = \frac{n_{ed} e^2}{\varepsilon_o m_{eff}} \tag{10}$$

where n_{ed} is the electron density, e is the charge of an electron, ε_o is the permittivity of free space, and m_{eff} is the effective mass of the electron.

The work conducted by Pendry et al. was designed to further old research on the dielectric properties of wire lattices. Some half a century previous in a publication introducing a new antenna made of parallel conductive metal plates, the idea of using wires to create a create an effective index of refraction was first posed [23]. Several years later in 1953 Brown investigated using what he called a rodded dielectric made from rectangular lattice of *y*-directed wires to create an artificial dielectric with a refractive index less than unity [7].

The new research conducted by Pendry et al. and pictured in Figure 4, employed a cubic wire lattice structure composed of infinite, very thin wires to investigate effective permittivity. By taking into account wire inductance, the plasma frequency can be rewritten as [48]

$$\omega_p{}^2 = \frac{n_{ed}e^2}{\varepsilon_o m_{eff}} = \frac{2\pi c^2}{a^2 \ln\left(\dfrac{a}{r_{tw}}\right)} \tag{11}$$

where a is inter-wire spacing and r_{tw} is the radius of the wires. Based on this function, the frequency-dependent dielectric function can be written as [48]

$$\varepsilon(\omega) = 1 - \frac{\omega_p^2}{\omega\left(\omega + j\gamma_p\right)} \tag{12}$$

where γ_p represents plasmon energy dissipation. The product $\omega\gamma_p$ is negligible for metals in which γ_p is normally small with respect to ω_p. Pendry et al. therefore proposed and subsequently confirmed that for frequencies less than the plasma frequency permittivity will be negative [46, 48]. In reality, there is a limited frequency band below the plasma frequency in which permittivity will be negative.

2.2.2.2 Negative Permeability Materials.

Negative permeability has also been achieved through engineered materials. Pendry et al. were able to develop a negative, effective permeability by pioneering the use of split-ring-shaped microstructures [47]. Their attempts to manipulate permeability involved three types designs that evolved from a simplification from previous research with a square lattice of cylinders [48]. This lattice, shown in Figure 4, displayed limited magnetic response to an electromagnetic field parallel to the cylinder. Pendry et al. tried to correct by adding capacitive elements like gaps. The cylinders were redesigned into the split ring and “Swiss Roll” configurations, both of which are shown in Figure 4.

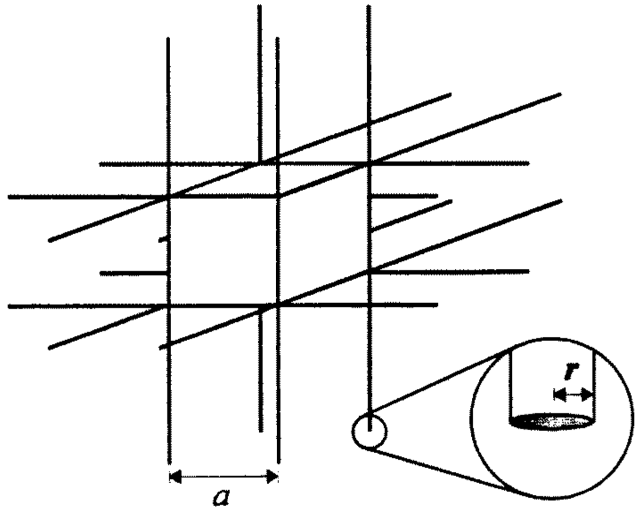

(a)

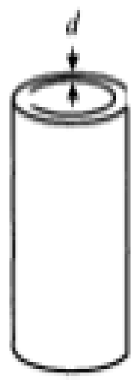

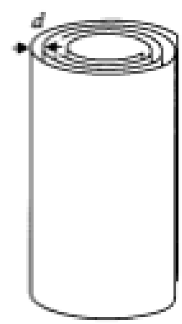

(b) (c)

Figure 4. Wire and cylinder designs used to achieve negative constitutive parameters in [47]. (a) The wire lattice used by Pendry et al. to generate a negative permittivity. Wires have radius r. Pendry et al. also used two different designs to achieve negative permeability. (b) Split cylinder design used to introduce capacitance during studies designed to generate negative permeability. (c) "Swiss Roll" cylinder also used to generative negative permeability. Designs (b) and (c) utilized an intracylinder spacing of d.

The geometry of these cylindrical designs made creating a compact structural array difficult and allowed the arrays to act like an effective metal for polarizations with the electric field not parallel to the length of the cylinders. In order to address the geometrical concerns of the array and the anisotropic nature of the cylindrical lattices, Pendry et al. created the SRR from their split cylinder design.

The creation of the split-ring resonator was elegant yet simple. A single split ring can be modeled as an inductance-resistance-capacitance (LRC) circuit. A SRR can partially be modeled as two LRC circuits. However, Smith [66] explains that in the presence of a time-varying magnetic field, a full model of the SRR requires consideration of the gap between the concentric rings. He explains that this gap provides a capacitance that allows current to flow, as shown in Figure 5. Given the incidence of a time-varying field then Faraday's law dictates that the induced electric currents will produce magnetic flux "that may either oppose or enhance the incident field" [66].

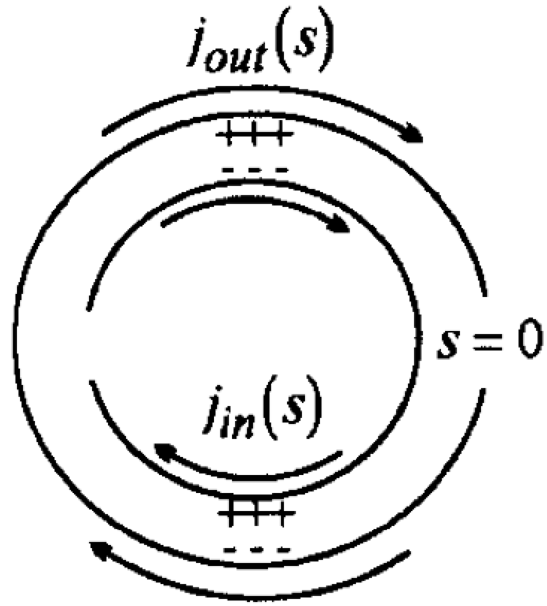

Figure 5. Top down view of the split cylinders used by Pendry et al. in [47]. A magnetic field parallel to the cylinder will induce currents to flow as pictured. Therefore, the stronger the magnetic field, the larger the current.

The gap between the rings also serves to simultaneously lower the resonant frequency of the SRR while concentrating the electric field. Smith explains that the splits in the ring-shaped traces also serve to concentrate the electric field and lower the resonant frequency of the SRR [66].

Using the SRR as a 2-D approximation of the cylinder, Pendry et al. created a structure with cubic symmetry. Stacking these cubes into periodic arrays with spacing of a created a compact lattice that mimics the continuous cylinder but minimizes electrical activity in the direction of the metal cylinders by eliminating the continuous electric path of those cylinders.

Pendry et al. used the newly introduced split ring resonator to tune the effective values of bulk permeability that they argued should exist [47]. The premise of their mathematical proof was that a material formed from subwavelength inclusions should create a homogeneous structure for which a discussion of average fields would be logical. They showed that the effective permeability of the split rings can be mathematically represented in terms of the original square lattice of cylinders and from the geometry of the split rings. Pendry et al. applied the following assumptions to first provide an accurate calculation of the inter-element capacitance of the SRR in Figure 6 [46]

$$r \gg w, \tag{13a}$$

$$r \gg d, \tag{13b}$$

$$l < r, \tag{13c}$$

$$\ln\left(\frac{w}{d}\right) \gg \pi, \tag{13d}$$

where r is the radius of the inner SRR, w is the width of the split-ring traces, d is the channel gap width of the SRR, and l is the spacing between the sheets of rings. Incorporating the capacitance in any calculation of the effective permeability was important because the inter-ring capacitance can cause resonance lowering. This drop in the resonance can potentially compromise the homogeneity of a metamaterial structure such as the one built by Pendry et al. so small periodic structure spacing should be enforced. They showed that the effective permeability was [47]

$$\mu_{eff} = 1 - \frac{\frac{\pi r^2}{a^2}}{1 + j\frac{2l\sigma_1}{\omega r \mu_o} - \frac{3lc^2}{\pi\omega^2 \ln\frac{2w}{d} r^3}} \tag{14}$$

where σ_1 is the resistivity of the split rings and μ_o is the permeability of the environment or free space.

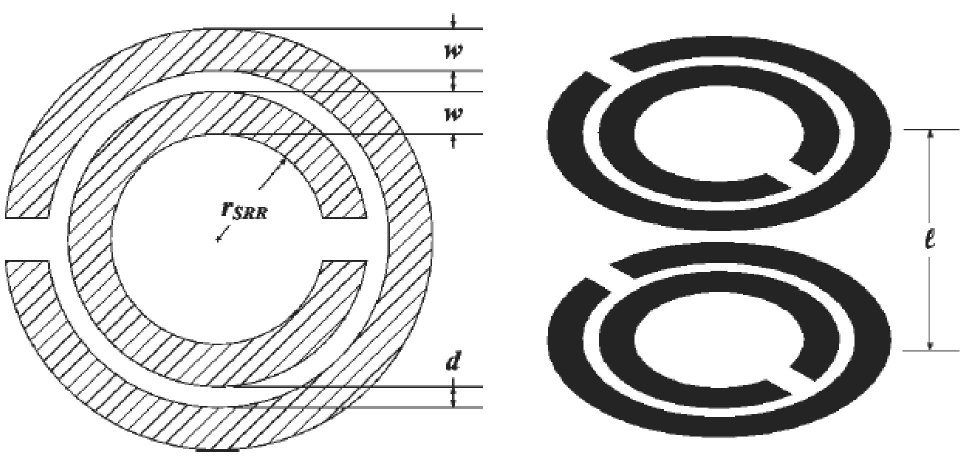

Figure 6. SRR based on a 2-D slice of the split cylinders proposed in [47]. Stacks of rings are made to approximate a cylinder while avoiding the continouous electrical path of a cylinder. In Equations (13) through (16), w is used in place of c for the trace width.

2.2.2.3 Double Negative Metamaterials.

More than three decades after Veselago introduced the idea of LHM, the existence metamaterial displaying simultaneously negative constitutive parameters was experimentally confirmed [66]. Smith et al. developed the first DNG metamaterial using a composite medium of periodically placed SRRs and thin wires [66]. The experiment was based on the analysis of effective permittivity and effective permeability for two polarizations designed to excite magnetic and dielectric responses. First, assuming magnetic coupling given an array of SRRs, an effective permeability in the form of Equation (14) was written in the following resonant form [66]

$$\mu_{eff} = 1 - \frac{F\omega^2}{\omega^2 - \omega_o^2 + j\omega\Gamma} \tag{15}$$

where F represents the ratio of the area covered by the split ring's interior to the area of the unit cell, ω_o is the natural frequency, and Γ is the dissipation factor. The later two terms ω_o and Γ can be defined with respect to Equation (14) as

$$\omega_o = \sqrt{\frac{3lc^2}{\pi\omega^2 \ln\frac{2w}{d} r^3}} \tag{16a}$$

$$\Gamma = \frac{2l\sigma_1}{\omega^2 r\mu_o} \tag{16b}$$

The resonance in permeability can then expressed through the dispersion relation [66]

$$\omega = \frac{ck}{\sqrt{\varepsilon(\omega)\mu(\omega)}} \tag{17}$$

where k is the wave number or the magnitude of the wave vector $\boldsymbol{k}$ and is defined as

$$k = \frac{2\pi}{\lambda} \tag{18}$$

Smith et al. plotted the dispersion curves for illumination of just the SRRs by both polarizations and then repeated the plots for the SRRs in the presence of thin wires spaced uniformly between the rings. The plot of the dispersion for parallel magnetic field polarization incident on the SRR displays a gap, as shown below in Figure 7.

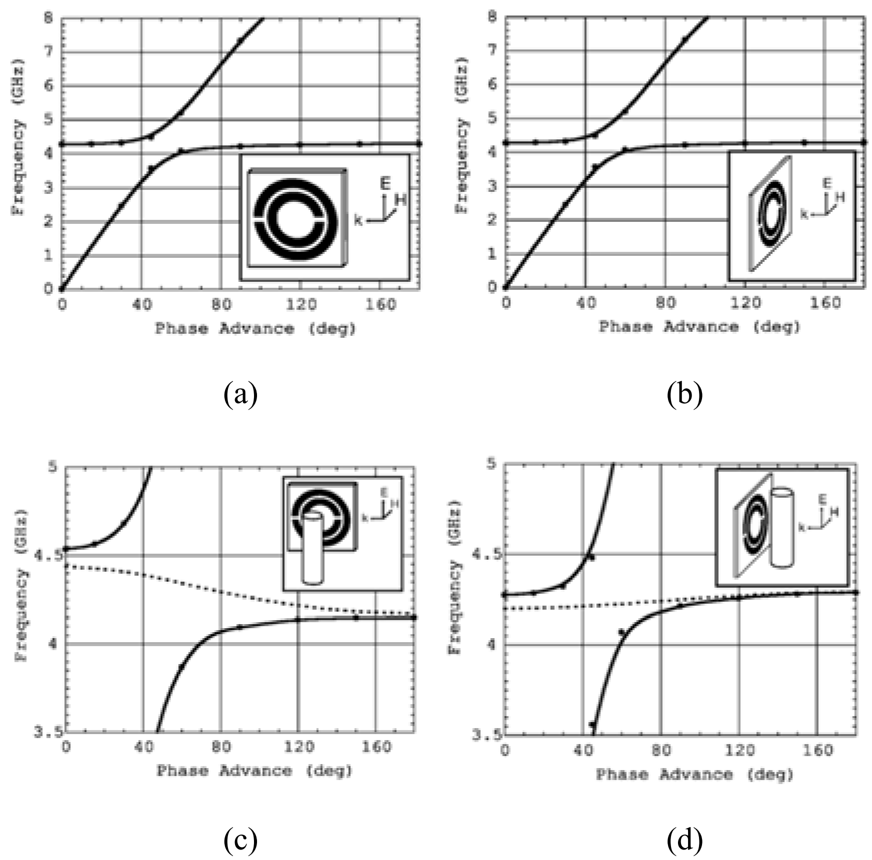

Figure 7. Dispersion curves for SRRs and SRR-wire combinations in various orientations from [66]. (a) Plot of dispersion for H parallel to the SRR axis. (b) Plot of dispersion for H perpendicular to the SRR axis. (c) Close-up view of (a) with a wire added. The dotted line represents the SRR dispersion. (d) Close-up view of (b) with a wire added. The dotted line represents the SRR dispersion only. These plots show lower and upper passbands separated by a gap caused by either a negative permittivity or permeability.

Smith et al. claimed that by assuming both a resonant effective permeability and a positive and relatively constant effective permittivity the gap observed in Figure 7 above indicated a negative effective permeability. They could not determine whether the observed gap was due to a magnetic or electric response. That is, they could not determine whether the gap was the outcome of magnetic resonance with an associated constant effective permittivity or due to electric resonance with an associated constant effective permeability. Their findings led to attempts to control the permittivity and hence the background dispersion with a lattice of wires. The goal of these later investigations was the differentiation of the electric and magnetic responses so that the superposition of their responses could be better articulated.

The conclusions about the results of the superposition of wire and ring microstructures, pictured in Figure 7, are best summarized from the plot of transmitted power recreated in Figure 8 below. The passband generated using a negative effective permittivity from the wire lattice exists in the original dispersion gap of the SRRs. Therefore Smith et al. found the combination of two kinds of microstructures, each providing a different negative constitutive parameter, created LHM that allowed wave propagation. The presence of the gaps between the LHM dispersion curves in Figure 7 serve as reminder of the limited nature of the wave propagation allowed [33].

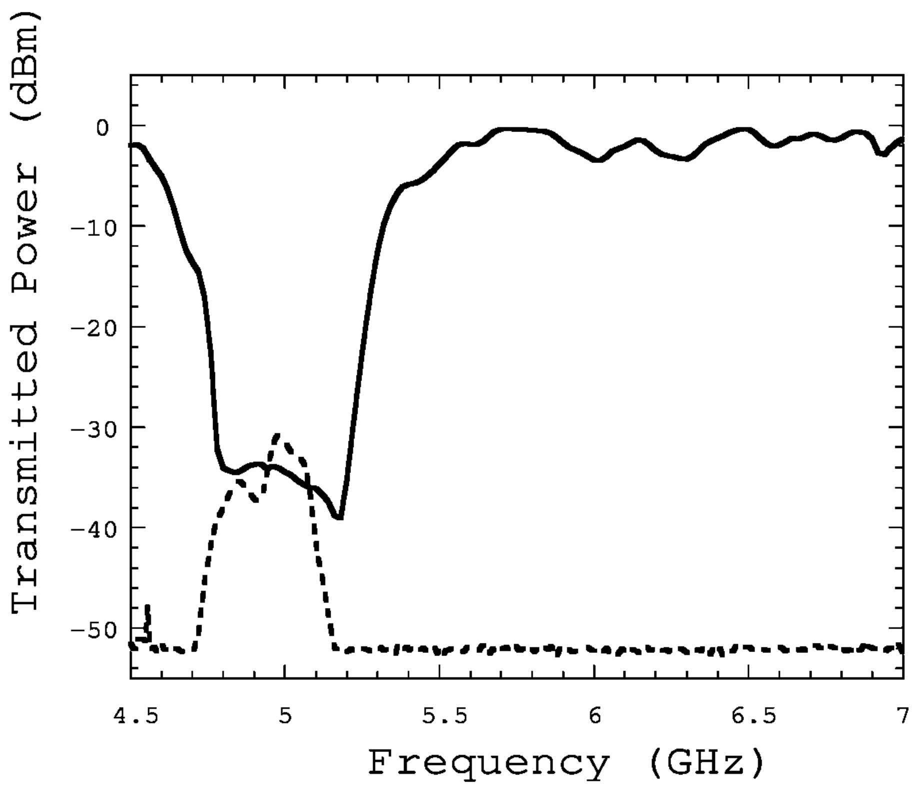

Figure 8. Experimental transmission data for a DNG metamaterial formed from SRRs and a wire lattice in [66]. The results are obtained for the case of H parallel to the SRR axes. The solid line is the plot for illumination of the SRR array. The combination of the SRR array and the wires is plotted with a dotted line. Adding the wires creates a pass band where a dispersion gap for the SRRs existed.

2.2.3 Surface Wave Phenomena.

The concept of negative refraction has been extensively researched in the last two decades and most scientists appear to subscribe to the associated concept of materials with simultaneously negative constitutive parameters. However, there exists a minority that subscribes to a concept antithetical to LHM: surface waves. The most outspoken proponent of the surface wave hypothesis is Benadikt Munk, who went so far as to author a book expounding what he considered gross misunderstandings about metamaterials rife within the research community [36]. In his book, Munk conducted a thorough critique of the some of the more extraordinary claims associated with the application of metamatierials. Of particular interest to this thesis, Munk aimed to highlight and correct not only what he argued was an erroneous belief in negative constitutive parameters but also the assertion that certain physical phenomena are the exclusive result of LHM and their applications. These phenomena include [36]

1. a negative index of refraction characterizes the material,
2. increasing separation between a wave front and the source associated with signal phase advancement,
3. increasing separation between a wave front and the source associated with an increase in evanescent wave amplitude, and
4. the electric and magnetic fields can form a left-handed set with the phase propagation direction.

Munk and other scientific counterculturalists ascribe the generally accepted characteristics of LHM listed above to surface wave behavior. Surface waves can be visualized as plane waves. These planes of constant phase propagate along and parallel to a material interface defined by a discontinuity in the index of refraction, as pictured in Figure 9 [4]. Munk has worked extensively with surface waves on periodic structures in a stratified medium as well as conducted theoretical investigations of surfaces waves on finite frequency selective surfaces (FSS) [36, 37]. His definition of surface waves for periodic structures in a stratified medium is succinctly given as “grating lobes trapped inside the dielectric media” [37]. These FSS grating lobes are the mechanism he uses to explain the various observed LHM phenomena.

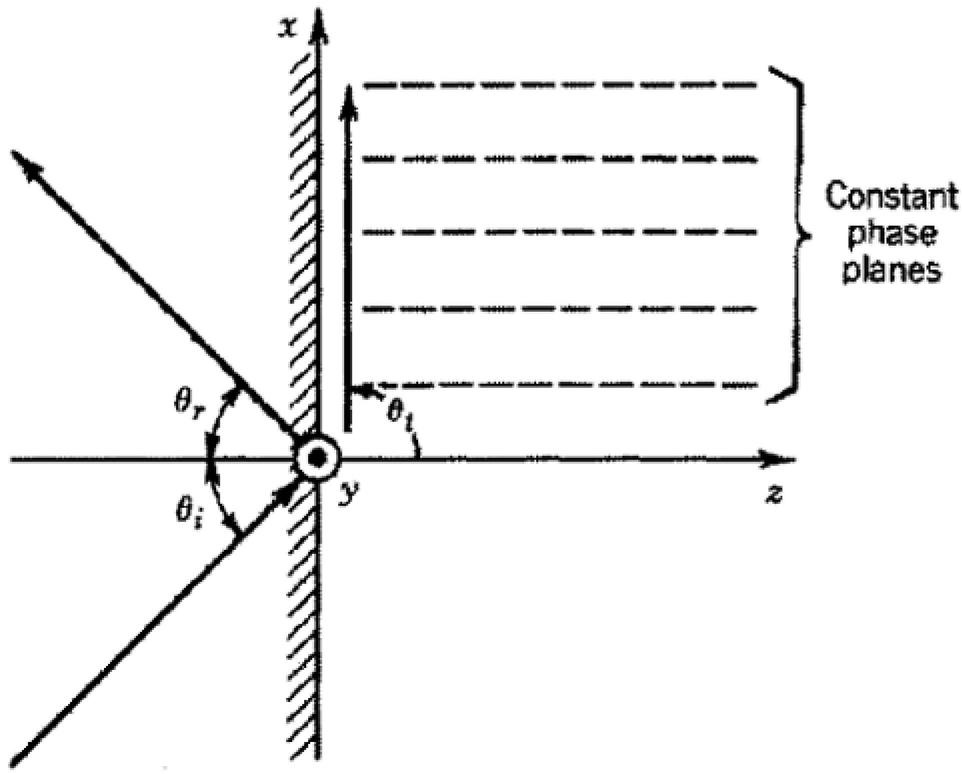

Figure 9. Transmission response at a material interface for a wave incident at the critical angle in [4]. This is the condition $\theta_i = \theta_c$. The planes of constant phase generated by a transmission angle θ_t of 90° define a generated surface wave.

Munk's argument that grating lobes explain all physical phenomena associated with LHM is grounded in long-accepted theories of transmission lines. Consider first a continuous, infinite metamaterial array. The definition of continuity is borrowed from transmission line theory and its definition of input impedance. Given the load impedance Z_L and the characteristic line impedance (not the measured line impedance), Z_o then the input impedance Z_i is [25]

$$Z_i = Z_o \frac{Z_L \cos(kl_{line}) + jZ_o \sin(kl_{line})}{Z_o \cos(kl_{line}) + jZ_L \sin(kl_{line})} = Z_o \frac{Z_L + jZ_o \tan(kl_{line})}{Z_o + jZ_L \tan(kl_{line})} \tag{19}$$

where l_{line} is the distance from the load at which impedance is measured. Then for a half wavelength spacing, $l_{line} = \lambda/2$, the product $kl_{line} = m\pi$, and $Z_i = Z_L$ for all integers m. This equality means that at the specified conditions, the transmission line is irrelevant in the analysis. Consequently, Z_i will always equals the Z_L no matter the value of Z_L and the elements forming the transmission line can therefore be considered continuous and forming a wire.

The results of Equation (19) above show that the smallest nonzero element spacing of the transmission line occurs for $m = 1$. Munk used this fact to define an infinite array of elements with inter-element spacing of D_z and a phase advance of $kD_z\left(s_z - s_{az}\right)$ where s_z represents the magnitude of the $\hat{z}$-component of the re-radiated wave's specular direction vector and s_{az} represents magnitude of the z-component of an arbitrarily directed re-radiated wave [36]. Munk showed that the $\lambda/2$ condition for the inter-element spacing is met for $m = 1$ and $s_z = \pm 1$ [36]. The positive value of s_z represents upward-directed grazing incidence and the negative value of s_z represents downward-directed grazing incidence. Thus, given Equation (19) above and the conditions on the continuous transmission line then re-radiation is possible in the principal or specular and forward directions only (given an infinite array). Other re-radiation directions are introduced when the continuity condition doesn't apply and $D_z > \lambda/2$, as shown in Figure 10.

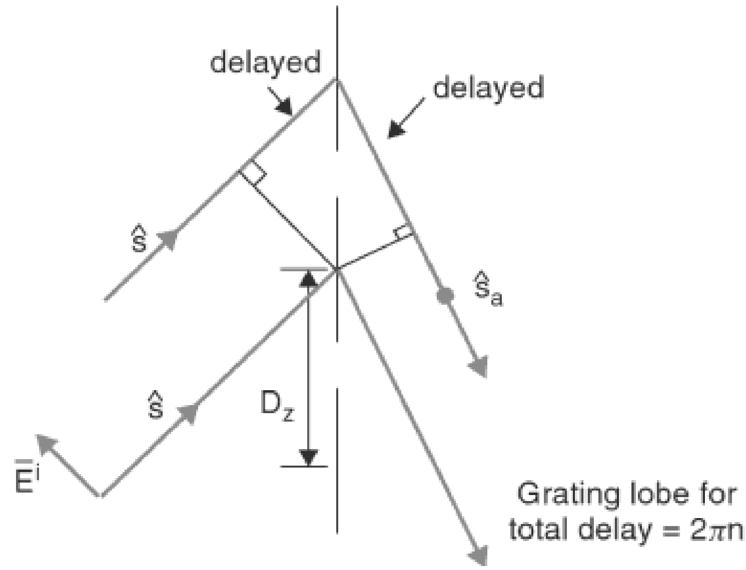

Figure 10. Grating lobe formation due to wave on individual elements with separation D_z in [36]. Grating lobes will only form for a separation of more than $\lambda/2$ and no refraction will occur for continuous, infinite media.

Using the previously defined variables, the total spectrum of directions of the inhomogeneous re-radiated plane wave, $\hat{r}$, can be written as [36]

$$\hat{r}_{\pm} = \hat{x}r_x + \hat{y}r_y + \hat{z}r_z = \hat{x}\left(s_x + k\frac{\lambda}{D_x}\right) + \hat{y}r_y + \hat{z}\left(s_z + n\frac{\lambda}{D_z}\right) \tag{20}$$

for $y \geq 0$ with

$$r_y = \sqrt{1 - \left(s_x + k\frac{\lambda}{D_x}\right)^2 - \left(s_z + n\frac{\lambda}{D_z}\right)^2} \tag{21}$$

where D_x is the inter-element spacing in the x direction.

Munk pointed out that the other re-radiation directions are simply grating lobe directions [36]. Per Figure 10, a backward-traveling wave exists for the lowest grating lobe, when the wave's phase velocity opposes the incident phase velocity. Therefore the backward-traveling waves that typify metamaterials only exist for $D_z > \lambda/2$, a spacing far greater than the $\lambda/10$ spacing required used to consider metamaterials homogeneous. Below this $\lambda/2$ threshold, grating lobes are suppressed. It can be deduced that no negative refraction can exist because below the threshold, reradiation is only allowed in the specular or forward directions.

The conclusion applies only to infinite arrays that are impossible to manufacture and test. Only finite arrays can be manufactured and, per Munk, these arrays will respond differently than infinite arrays to incident waves due to different supported currents [36]. First, the residual surface current of a finite array accounts for end currents off the edges of the array that help support a variety of surface waves impossible on an array of infinite extent. Second, a finite array will produce both a main beam and a variety of suppressed sidelobes in response to incident waves.

The surface current associated with a finite array is large and can be stronger than the current associated with the main beam. A surface current will radiate and contribute to the farfield pattern but due to poor radiation efficiency, Munk showed that the surface current response is typically 14 – 20 dB lower than the main lobe [36]. End currents will also re-radiate however due to radiation inefficiency and their low strength, they minimally contribute to the response of the surface currents. The pattern from the residual current radiation is very similar to the pattern observed from a metamaterial as seen in Figure 11. If refraction were dominant in a metamaterial, the noted similarity in Figure 11 would not exist. In fact, neither would the 14 – 20 dB lower response nor the sidelobes in so Munk finished his analysis of finite arrays by reaffirming his belief that metamaterials don't negatively refract [36].

Munk concluded his extensive discussion of surface waves and grating lobes by dissecting the foundation of metamaterial research: Vesealago's paper on LHM. Munk pointed out that while Veselago's derivation of a negative index of refraction was mathematically proper, it disregarded applications that could result in negative time or a violation of causality [36]. Munk's conclusion was drawn from the fact that materials with $n > 0$ experience a phase delay and materials with $n < 0$ experience a phase advance, as shown in Figure 12.

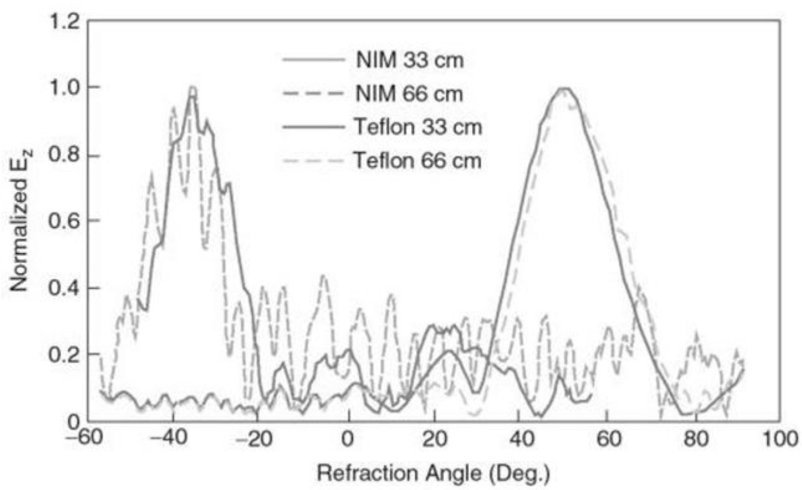

Figure 11. Comparison of surface current radiation between Teflon and a negative index material in [36]. Munk used this plot to show that the farfield radiation pattern supposedly due to negative refraction looks very similar to the pattern formed by grating lobes generated with Teflon.

His first complaint with Veselago's argument was that the phase delay and counterclockwise rotation violate Foster's Reactance Theorem (note, however, that no such violation exists at least for lossless material [14]). Even if such a phase delay can exist, Munk argued, certain applications such as the frequency-independent perfect lens argument by Pendry [45] would violate causality. Pick two rays entering a DNG lens. Munk argued that if two rays entering a DNG lens, one will experience a phase delay with respect to the other. Once in the material, that same phase-delayed ray would require a phase advance so that both rays would cross the focal point not only in phase, per Pendry's arguments [45], but at the same time. Admittedly, waves can arrive in phase at the same location at different times but only as a mathematical abstraction and for a single frequency only [36]. However, the benefits of the perfect lens would be most enjoyed for a large band of frequencies experiencing temporal and spatial focus.

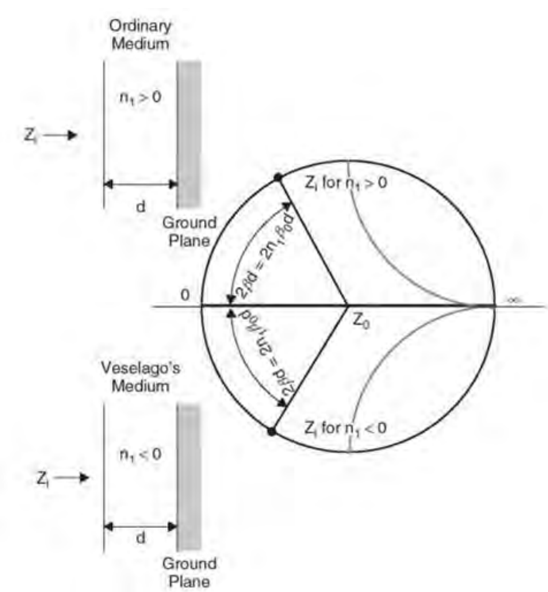

Figure 12. Depiction of Smith chart and the resulting rotation for different input impedances in [36]. Munk claimed that the input impedance for a DNG lens requires a phase advance or counterclockwise rotation about the Smith chart associated with a violation of causality.

In summary, Munk brought up a set of compelling counterclaims to the existence of LHM. There many avenues for rich debate over the existence of LHM or the causes of the phenomena attributed to such material however the scope of this thesis is merely focused on exploiting some of the observed characteristics attributed to LHM. Be these characteristics due to grating lobes or negative constitutive parameters, the existence and usefulness of such characteristics is undeniable.

2.3 Transformation Optics

Science fiction has paralleled the diligent efforts of scientists who have conducted research that has explicitly or implicitly advanced our understanding of TO. Popular cultural references to TO over the last three decades can be found in both electronic and print media, from Star Trek and the Romulan's cloakable Stormhawk class warship to Harry Potter's cloak of invisibility. According to a review of the subject by Kundtz, science fact and fiction merged when the use of TO was first published in 2003 in an application for negative index superlenses [24]. Since that introduction, the use of TO has quickly become a prominent tool in the search for cloaks, optical black holes, negative refraction lenses, field rotators, waveguides, and more [24, 31, 56].

The fabrications of science fiction may make the proposed applications of TO equally implausible yet not only is TO achievable, it occurs naturally and is commonplace in scientific applications. Firstly, TO appears naturally in the form of a mirage. Temperature inversions near the earth's surface create a non-uniform medium that bends light and produces a displaced reconstruction of distant objects or the sky. Secondly, this mathematical sleight of hand is commonly implemented in computational methods to create perfectly matched layers (PML, called open boundary conditions in certain computation programs) [5, 68].

2.3.1 Invariant and Conformal Maps.

Leonhardt and Philbin pointed out in [26] that any discussion of TO involves the specialized application of general relativity. General relativity involves the curvature of space-time; TO is employed to create geometries that bend light in an arbitrary and desired manner. TO may appear to be focused exclusively on ray optics with the express purpose of developing devices such as gradient index lenses that utilize inhomogeneous or non-uniform constructions to effect anisotropic constitutive parameters and unusual light bending. However this conclusion is false; TO is not ray optics. TO is the subject of wave optics. Kundtz points out that the first problem with ray optics is that it does not distinguish between electric and magnetic fields yet these differences must particularly be accounted for in subwavelength devices [24]. He further points out that the ray approximation also falls short because it neglects the wave nature of light and consequently fails to account for the diffraction that occurs when the microstructures forming a metamaterial are not negligibly small with respect to the incident wavelength.

Despite the deficiencies of applying ray optics to electric and magnetic fields in the microwave regime, the concept of ray optics translates well to wave optics and provides a simple means with which to understand electromagnetic wave interactions with materials. Ray optics is grounded in Fermat's principle, which most people associate with the concept of light traveling the shortest optical path possible between two points (a straight line). However, as in any natural phenomenon there are exceptions; Fermat's principle should be written to state that light will travel an extremal optical path length between two points, such as in Figure 13 [26]. Light traverses a straight line or the shortest path length for uniform media but follows a curved path for nonuniform media whose index of refraction is spatially variant.

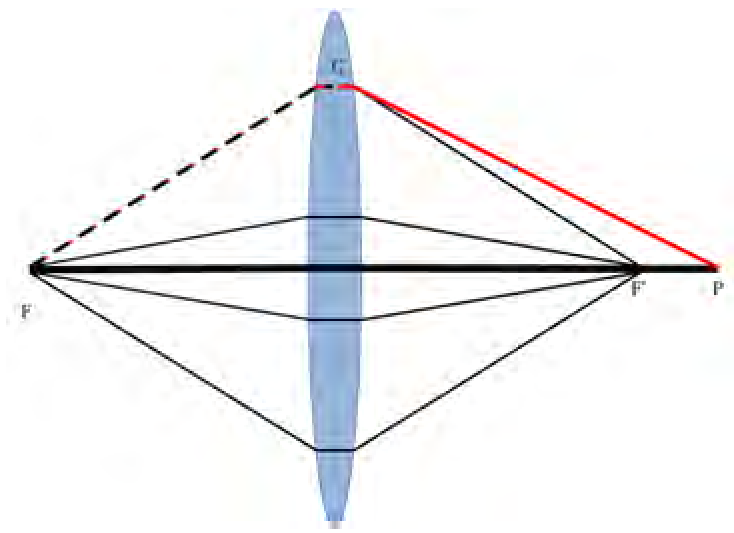

Figure 13. Example of light following an extremal path to a point P in [26]. A light traveling between the two focal points F and F' will travel the same optical path length through the lens regardless of the location of the path chosen, depicted by the thin black lines. Light from F will reach P by taking the longest optical path, the thick black line through the center of the lens. Compared to the virtual path $\overline{FCP}$ denoted by the red line, $\overline{FP}$ is longer by an amount equal to the difference between the sum of the short sides and the long side of the triangle $F'CP$.

The engineered geometries that bend light per the designer's desires lead to contorted coordinate systems. It is important to remember when viewing the contorted coordinates such as those in Figure 14 that one can "not bend the spoon. That's impossible...it is not the spoon that bends, it is only yourself" [59]. In other words, any apparent coordinate curvature is an illusion based on the mathematical manipulations of

TO. In fact, Fermat's principle holds for transformed space [26]. Following Fermat's mathematical argument as laid out in [26], transformations in Cartesian space and confined to the x-y plane produce an optical path length OPL is written as [26]

$$OPL = \int n\sqrt{dx^2 + dy^2} = \int n'\sqrt{dx'^2 + dy'^2} \tag{22}$$

where the prime notation defines transformed space. The transformed differential terms can be rewritten as [26]

$$dx' = \frac{\partial x'}{\partial x}dx + \frac{\partial x'}{\partial y}dy, \tag{23a}$$

$$dy' = \frac{\partial y'}{\partial x}dx + \frac{\partial y'}{\partial y}dy. \tag{23b}$$

By using Cauchy-Riemann differential equations displayed here as for two variables u and v as

$$\frac{\partial u}{\partial x} = \frac{\partial v}{\partial y}, \tag{24a}$$

$$\frac{\partial u}{\partial y} = -\frac{\partial v}{\partial x}, \tag{24b}$$

the radicand of the transformed space from Equation (22) above can be related to the radicand in the original space by a constant. Leonhardt and Philbin show this equality to be [26]

$$n^2 = n'^2\left(\left(\frac{\partial x'}{\partial x}\right)^2 + \left(\frac{\partial x'}{\partial y}\right)^2\right) = n'^2\left(\left(\frac{\partial y'}{\partial x}\right)^2 + \left(\frac{\partial y'}{\partial y}\right)^2\right). \tag{25}$$

Transformations developed using Cauchy-Riemann will be conformal; that is, they will preserve the angles formed by gridlines and therefore preserve the applicability of Fermat's principle in transformed space. However, conformal transformations place a limitation on the cross-applicability of Fermat's principle because they are only applicable "to materials with an isotropic refractive index profile," [26].

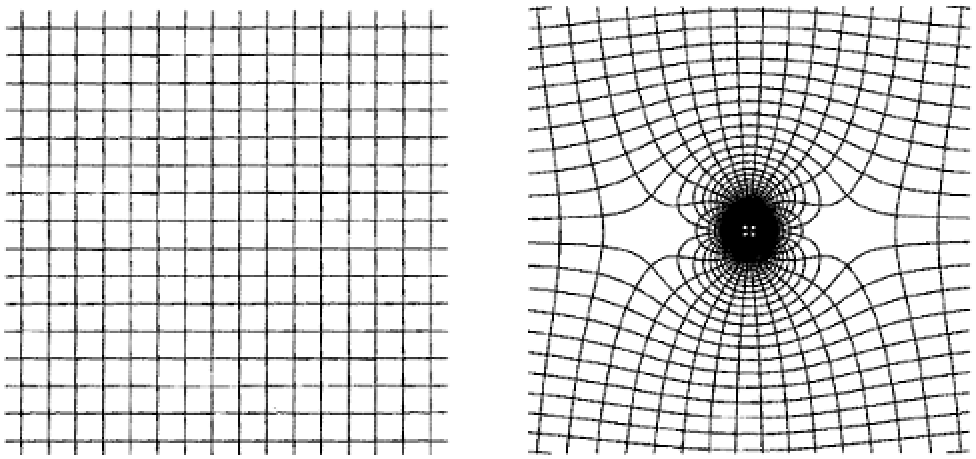

(a) (b)

Figure 14. Optical conformal mapping in [26]. (a) This is the orignial Cartesian coordinate system before transformation in physical space. (b) Straight Cartesian grid lines converted via optical conformal mapping. Note that the conformal nature of the transformation ensures the grid lines in the curved coordinate system are orthogonal, just as they were in the original Cartesian coordinate system.

Coordinate transformations preserve the bending of rays but these transformations must also hold for electromagnetic waves in TO applications. Proof of the applicability of Fermat's principle for waves can be developed by an evaluation of Helmholtz's wave equation with particular emphasis on rewriting the equation's Laplacian [26]. A generalized version of Helmholtz equation is [16]

$$\left(\nabla^2 + \frac{\omega^2}{c^2} n^2\right)\psi = 0 \tag{26}$$

where ψ is the amplitude of either optical polarization for the current example. The Laplacian can be written in terms of complex terms as

$$\nabla^2 = \frac{\partial^2}{\partial x^2} + \frac{\partial^2}{\partial y^2} = \left(\frac{\partial}{\partial x} + j\frac{\partial}{\partial y}\right)\left(\frac{\partial}{\partial x} - j\frac{\partial}{\partial y}\right). \tag{27}$$

Leonhardt and Philbin then use Equations (24) to show that the first and second terms on the right-hand side of Equation (27) can be written as

$$\left(\frac{\partial}{\partial x} + j\frac{\partial}{\partial y}\right) = \left(\frac{\partial y'}{\partial y} + j\frac{\partial x'}{\partial y}\right)\left(\frac{\partial}{\partial x'} + j\frac{\partial}{\partial y'}\right), \tag{28b}$$

$$\left(\frac{\partial}{\partial x} - j\frac{\partial}{\partial y}\right) = \left(\frac{\partial y'}{\partial y} - \frac{\partial x'}{\partial y}\right)\left(\frac{\partial}{\partial x'} - j\frac{\partial}{\partial y'}\right), \tag{28a}$$

Completing the product shown in Equation (27) leads to

$$\nabla^2 = \left(\left(\frac{\partial x'}{\partial x}\right)^2 + \left(\frac{\partial y'}{\partial x}\right)^2\right)\nabla'^2 = \left(\left(\frac{\partial x'}{\partial y}\right)^2 + \left(\frac{\partial y'}{\partial y}\right)^2\right)\nabla'^2 \tag{29}$$

This result shows that the mapping of a wave from one coordinate to another is both invariant and conformal. The index of refraction experienced by a wave in the transformed space can therefore be described by Equation (25).

2.3.2 Transformation Optics Approach with Constitutive Parameters.

The Helmholtz equation dictating wave optics should be invariant during a coordinate transformation. However, many transformations are not conformal. Exact treatment of wave propagation and interaction with transformed space therefore requires derivation from Maxwell's equations. The curl relationships between fields and sources were provided previously but for simplicity they are reproduced here as the full set of electric and magnetic source-free Maxwell's equations such that

$$\nabla \times \boldsymbol{E} = -j\omega \boldsymbol{B}, \tag{30a}$$

$$\nabla \times \boldsymbol{H} = j\omega \boldsymbol{D}, \tag{30b}$$

$$\nabla \bullet \boldsymbol{D} = 0, \tag{30c}$$

$$\nabla \bullet \boldsymbol{B} = 0. \tag{30d}$$

The application of Maxwell's equations to the four-vector manifold Minkowski space or spacetime and transformations therein are best related by the use of Einstein notation. Using this notation, a range of numbers can be denoted by

$$V^i \equiv \{V^i, i = 1,2,3\} \tag{31}$$

where the superscripted letter (i in this equation) represents an axis from Euclidean space. As an example l^3 would indicate a *z*-directed length component l, not the cube of the length. Distances and summations can be expressed with covariant and contravariant vectors. Covariant vectors transform with the basis vectors of space and are denoted by subscripted indices, such as V_i and have no real geometrical definition. Contravariant vectors transform against a basis and are the tangent to a manifold at a particular point. Contravariant vectors are distinguished by superscripted indices V^i [51, 75]. Vector summation is denoted by the presence of two of the same indices so that

$$V_{\mathrm{i}} W_{\mathrm{i}} = V^{\mathrm{i}} W^{i} \equiv \sum_{\mathrm{i}} V_{\mathrm{i}} W_{\mathrm{i}} \tag{32}$$

for all i and allows the consolidation of notation so that

$$V_{\mathrm{ijk}}^{\mathrm{i}} \equiv \left\{ \sum_{\mathrm{i}} V_{\mathrm{ijk}}^{\mathrm{i}}, \mathrm{j} \,\&\, \mathrm{k} = 1,2,3 \right\} \tag{33}$$

Now consider the form of a differential length as it is transformed from original space $\{dx^{i}\}$ to prime space $\{dx^{i'}\}$. The differential term of one coordinate can be written with respect to the other as [26]

$$dx^{i} = \frac{\partial x^{i'}}{\partial x^{i}} dx^{i}, \tag{34a}$$

$$dx^{i} = \frac{\partial x^{i}}{\partial x^{i'}} dx^{i'}. \tag{34b}$$

A comparison of the left- and right-hand sides of Equations (34) shows that the transformation matrices $\Lambda^{i}_{i'}$ and $\Lambda^{i'}_{i}$ are the leading differential terms of each right-hand side term and are thus labeled [26]

$$\Lambda^{i}_{i'} = \frac{\partial x^{i}}{\partial x^{i'}}, \tag{35a}$$

$$\Lambda^{i'}_{i} = \frac{\partial x^{i'}}{\partial x^{i}}. \tag{35b}$$

These transformation matrices are simply Jacobian matrices. For a Cartesian-to-Cartesian transformation, the matrices can be written as

$$\Lambda = \frac{\partial(x', y', z')}{\partial(x, y, z)} = \begin{pmatrix} \partial x'/\partial x & \partial x'/\partial y & \partial x'/\partial z \\ \partial y'/\partial x & \partial y'/\partial y & \partial y'/\partial z \\ \partial z'/\partial x & \partial z'/\partial y & \partial z'/\partial z \end{pmatrix}. \tag{36}$$

The differential terms of Equations (34) can be compared to Equations (35) to show that the product of the transformation matrices is the Kronecker delta

$$\delta^{i}_{j} = \Lambda^{i}_{i'}\Lambda^{i'}_{j}, \tag{37a}$$

$$\delta^{i'}_{j'} = \Lambda^{i'}_{i}\Lambda^{i}_{j'}. \tag{37b}$$

The transformation matrices are therefore inverses of each other. They can be used to derive the metric tensor in the original and transformed coordinates, denoted per the current convention as g_{ij} and $g_{i'j'}$. Distance is an invariant quantity therefore a differential element of area can be written as [75]

$$g_{\mathrm{ij}} dx^{\mathrm{i}} dx^{\mathrm{j}} = g_{\mathrm{i'j'}} dx^{\mathrm{i'}} dx^{\mathrm{j'}} \tag{38}$$

where it is clear the transformation matrices are inverses. Rewriting these equations yields

$$g_{\mathrm{i'j'}} = \Lambda^{\mathrm{i}}_{\mathrm{i'}} \Lambda^{\mathrm{j}}_{\mathrm{j'}} g_{\mathrm{ij}}, \tag{39a}$$

$$g_{\mathrm{ij}} = \Lambda^{\mathrm{i'}}_{\mathrm{i}} \Lambda^{\mathrm{j'}}_{\mathrm{j}} g_{\mathrm{i'j'}}, \tag{39b}$$

for the orthonormal transformation matrices where

$$\Lambda^{-1} = \Lambda^{T}. \tag{40}$$

In this case, Equation (40) can be generalized for a tensor F as

$$F' = \Lambda^{T} F \Lambda \tag{41}$$

with

$$\Lambda = \Lambda^{\mathrm{i}}_{\mathrm{i'}}, \tag{42a}$$

$$\Lambda^{T} = \Lambda^{\mathrm{i'}}_{\mathrm{i}}. \tag{42b}$$

The relationship of Equation (41) provides a nearly complete description of the invariant transformation of constitutive parameters. Following the excellent geometrical derivation of [76], the concept of differential area can be extended to derive the complete equations for the transformed constitutive parameters. This derivation yields a coordinate system in which corresponding components of the permittivity and permeability tensors are equal due to form invariance of Maxwell's equations. The familiar equations are

$$\varepsilon^{i'j'} = \frac{\Lambda_i^{i'}\Lambda_j^{j'}}{\det\left(\Lambda_i^{i'}\right)}\varepsilon^{ij}, \tag{43a}$$

$$\mu^{i'j'} = \frac{\Lambda_i^{i'}\Lambda_j^{j'}}{\det\left(\Lambda_i^{i'}\right)}\mu^{ij}, \tag{43b}$$

2.3.3 Transformation Optics Implementation.

Implementation of TO can range from very simple to various complex. The math involved could involve either a single- or multi-dimensional transformation. Further, a transformation might occur within the confines of a single coordinate system, e.g. a Cartesian-to-Cartesian transformation, or it could involve a set of intermediate coordinates employed to make analysis simpler. An example of intermediate coordinates would be the conversion from Cartesian to cylindrical coordinates to facilitate development of radial transformations for a cylindrical cloak or wave rotation.

Chief among priorities for TO implementation is the consideration of the boundary behavior for the transformation. Discontinuous transformations do not provide a smooth gradient transition as waves exit the transformed or prime space and are well-suited for structures whose design is purpose is a spatially isolated effect [24, 52, 74]. Thus the field modulation within the transformation device cannot be transferred to an outside medium. Embedded transformations purposely include a smooth transition from prime space to original space so as to effect some permanent change on the surrounding electromagnetic environment.

The term “embedded transformation” was coined to fully describe the treatment of electromagnetic wave transformation material interfaces [52]. The term was borrowed from research in the early 1980s conducted to more efficiently account for material inclusions in Schrödinger’s equation that provided localized potential and therefore field perturbations [19]. The author of that research claimed that it was “possible to deal with a small Hamiltonian confined to the perturbed region of the crystal, adding on an extra effective potential which automatically ensures that the wavefunctions match onto the substrate” [19]. This method of adjusting the Hamiltonian of the surrounding region to account for the boundary surface potential was termed “embedding” [19]. The process of embedding provides a continuous transition of electromagnetic effects.

The enforcement of a continuous transition has important applications in the study of transformation optics. To emphasize the potential applications, Rahm et al. derived the mathematical arguments differentiating discontinuous and embedded transformations and then demonstrated them as seen in Figure 15. The discontinuous method obviously requires the consideration of the boundary between Region I and free space during the development of the transformation. The embedded method specifically ignores the boundary. The arrows of Figure 15 indicate the direction of power flow and show that embedded transformations ensure continuous and natural power flow between the transformed and free space regions.

The discussion of smooth inter-boundary power flow implies the possibility of a reflectionless boundary to the inter-region boundary where the electromagnetic waves escape back into the surrounding medium is continuous [52], as is shown in Figure 16.

Note that while embedded transformations can result in suppressed reflections, diffraction is not suppressed and, in fact, is on obvious display in Figure 16.

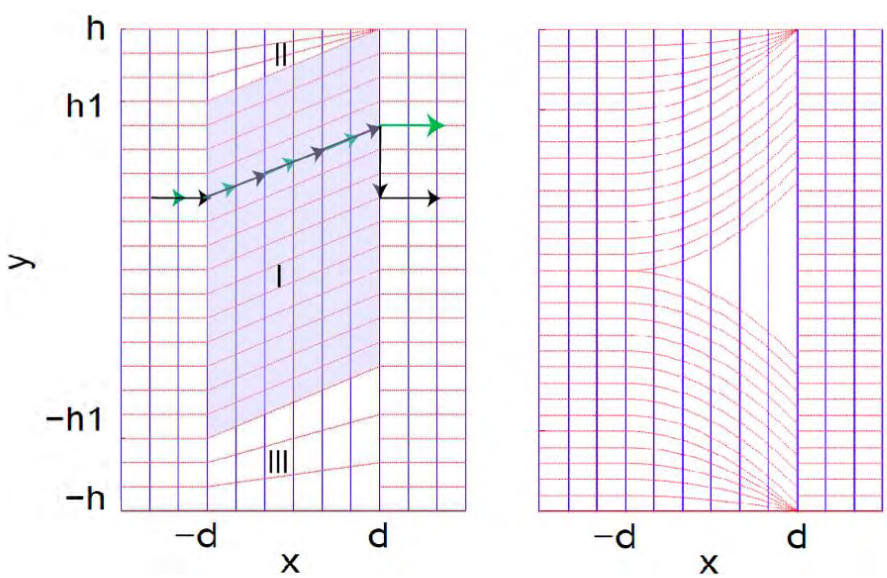

(a) (b)

Figure 15. Spatial coordinate transformations illustrating the embedded transformation method in [52]. (a) Ray path of parallel beam shifter created with a linear spatial coordinate transformation. The black arrows show the ray path for a discontinuous transformation while the green arrows represent an embedded transformation. (b) Design of a split beam shifter using the embedded transformation process to enact a nonlinear spatial coordinate transformation.

Smooth power flow and suppressed reflections open transformation optics to a number of additional applications beyond the limits of discontinuous transformations. Beam steering is one prime example of the use of embedded transformations. Another important application of embedded transformations is field concentration, which is the focus of this thesis.

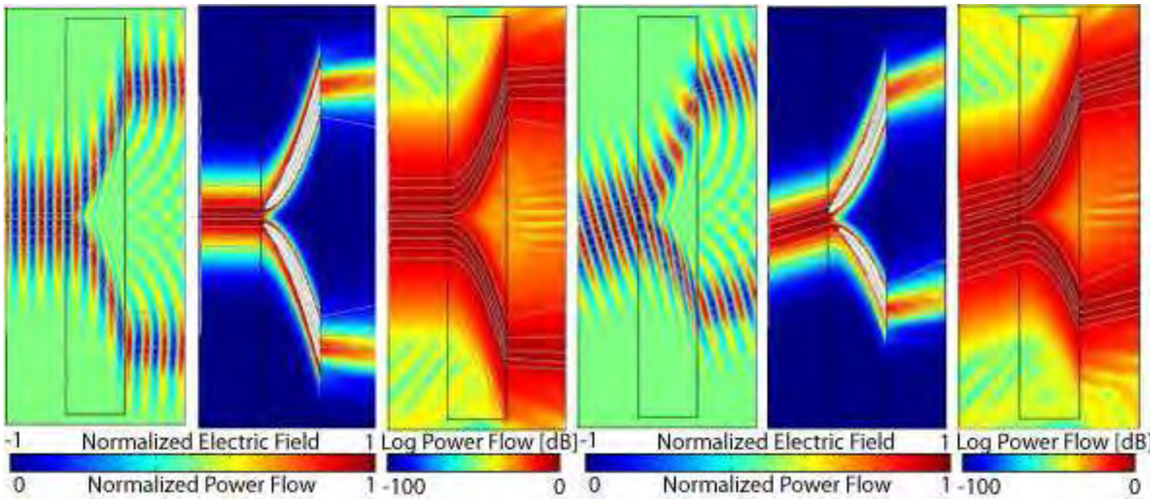

(a) (b) (c) (d) (e) (f)

Figure 16. Field and power measurements of a split beam shifter in [52]. Using plane wave illuminaton, the normalized electric field and power flow are plotted. Plots (a) – (c) use a beam shift parameter to designate perpendicular incidence. Plots (d) – (f) use a beam shift parameter to designate an oblique incidence plane wave. Note the presence of diffraction, particularly as the split beam exits the dielectric.

2.4 Rapid Design of Metamaterials

The plethora of research publications on TO has overwhelmingly relied on simulations to substantiate proposed metamaterials. There is a noticeable dearth in papers that connect the cognitive conception of a metamaterial design to its physical realization. In fact, the task of linking the geometry of a basic repeated metamaterial cell or metaparticle to the Bloch parameters of a device is a rather involved task. Certainly, metaparticles have been optimized before but until now a means of rapid metamaterial has not been well defined [55]. A method has been developed by AFIT that allows effective and fast recreation of the relative bulk media properties demanded by TO metamaterial devices [43].

2.4.1 Design Methodology.

The AFIT rapid design methodology is based in part on the work of [28]. The methodology can be described as matching the bulk material parameters of a metamaterial design to a library of metaparticles or cells. The application of this methodology requires several computationally intensive steps and necessitates upfront work to create a library of cells. The library is generated from one or more cells that have several geometrical features that can be parameterized. The rapid design code implemented by AFIT utilizes a library based on the variation of three geometrical features for a single cell, one employed in [43, 55]: a_θ (the spacing between parallel planar boards of cells), r (the curvature radius), and s (the arm height). This design is shown in Figure 17. More parameters could be chosen and a larger library could be created at the cost of greater computation time.

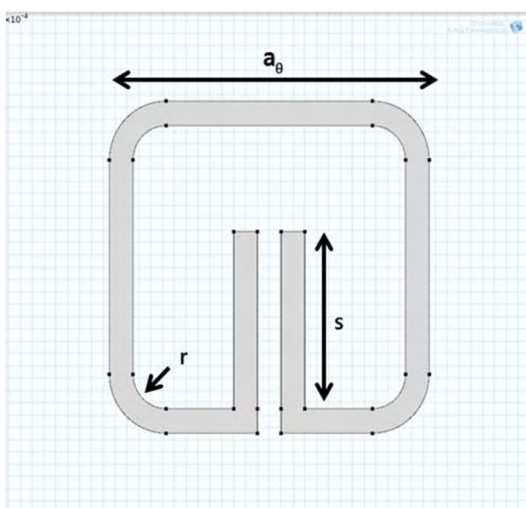

Figure 17. SRR unit cell with geometrical variables used for the rapid design process in [43].

In summary, the first step in the rapid design process is to create the library of reference cells. Paul explains that the next step is simulating each cell to gather the S-parameters [43]. These simulations utilize a unit cell with periodic boundary conditions so as to model an infinite metamaterial medium. The S-parameters extracted for a cell really represent the bulk electromagnetic response or the response of the entire infinite material. The effective bulk material parameters for each library entry can therefore be determined from the calculated impedance and index of refraction developed from the corresponding S-parameters extracted for that entry [43]. Either the effective/extracted constitutive parameters or modified parameters for each library entry are then curve fit to an appropriate mathematical model. The result of each curvefit is a set of parameters that, when expanded in a three-variable geometric series, display dependence on the parameterized cell variables $\{a_\theta, r, s\}$. The coefficients of the expansion provide the mathematical link between the parameterized cell values and bulk material parameters of the cell. These parameters can be used to design approximations to the anisotropic designs generated in metamaterial research efforts.

2.4.2 Bulk Media Property Extraction.

The explicit goal of extraction is the recovery of effective bulk material properties. The use of these effective values is central to the field of metamaterials which is why there has been significant research about the best extraction method and disagreements about the scientific rigor with which the subject of extraction has been approached [61].

At the core of the debate about extraction techniques is the implication that a collection of discrete particles can represent a material that displays the properties of a homogeneous material. A homogenous material is characterized by effective parameters that are "a result of a more or less precise averaging of the Maxwell equations for true (microscopic) fields and polarizations at which the polarization of particles is replaced by the polarization continuously distributed in the medium," [61].

Unfortunately, homogenization is not necessarily a straightforward task. Some published homogenization or extraction methods have been shown to suffer from violations of causality or passivity, which requires $\Re(\eta),\Im(n)>0$ [61]. Other methods are incorrectly assumed to apply to the entirety of a material's passband, where homogenization can be applied. In the passband however, certain frequencies can result in a resonance shortening of the wavelength, increasing the relative size of the lattice periodicity such that the quasi-static approximation (displacement current in Ampere's law goes to zero), used for the homogeneity assumption cannot be applied [61].

Extraction techniques are focused on both conceptual (infinite) and physical (finite) periodic lattices. These structures can be homogenized with proper care during the derivation of the homogenization procedure. Homogenization procedures can be grouped into two general approaches, one derived from evaluation of Maxwell's equations at the level of a unit cell and the other one derived from the bulk material's S-parameters.

The first homogenization approach describes efforts to use the local fields of a unit cell in a lattice [64]. Pendry et al. popularized a simplistic means of microscopic homogenization that describes the effective constitutive parameters for periodic lattice spacing much less than a wavelength in terms of the average local fields [47]. Extraction of these effective parameters from reflection and transmission coefficients is a well-established application of homogenization.

Time-domain techniques for retrieving the bulk parameters of linear media for microwave were introduced as early as 1970 [41]. Since then, several methods have been developed to apply a rigorous homogenization of metamaterial arrays. Most methods focus on the linear, passive responses to plane wave excitations of planar metamaterial arrays. These methods avoid complicated chiral and bianisotropic designs [10, 29, 63, 67]. Physically proper techniques address homogenization and particular issues such as dynamic intra-inclusion coupling or the definition of the free space-array interface through methods such as transition layers developed by Drude [29, 62].

Previous AFIT research used a technique tailored to address extraction issues such as first boundary determination (the plane beyond which a reflected plane wave regains its plane wave form), effective slab thickness determination, and more [10]. Unfortunately, this method violates the second law of thermodynamics by allowing negative energy in a portion of the resonance band [10, 61]. However, there are numerous other examples of S-parameter extraction techniques based on everything from line-reflect-line calibration techniques to Kramers-Kronig relationship that do not appear to have this limitation [34, 67].

AFIT's rapid design method utilizes several of these techniques but primarily relies on an extraction technique proposed by Smith et al. that is designed for passive materials and accounts for causality [65]. The transmission, reflection, impedance, and index of refraction terms are related in forms shown as [65]

$$\cos(nkd) = \frac{1}{2T}\left[1-\left(R^2-T^2\right)\right] = \mathrm{Re}\left(\frac{1}{T}\right)-\frac{1}{2|T|^2}\left(A_1R+A_2T\right) \tag{44}$$

and

$$\eta = \pm\sqrt{\frac{(1+R)^2-T^2}{(1-R)^2-T^2}} \tag{45}$$

where d is the length of the 1-D continuous material slab held in free space, R is the reflection parameter S_{11}, T is the transmission parameter S_{21}, and η is the impedance. The terms A_1 and A_2 are defined in [65] as functions of R and T that go to zero for a hypothetical lossless material. The retrieved or effective values of permittivity and permeability are

$$\varepsilon_r = \frac{n}{\eta}, \tag{46a}$$

$$\mu_r = n\eta, \tag{46b}$$

and can be related to free space by

$$\varepsilon_r = \frac{\varepsilon}{\varepsilon_o}, \tag{47a}$$

$$\mu_r = \frac{\mu}{\mu_o}. \tag{47b}$$

Equations (44) and (45) are multi-branched; they lead to multi-valued permittivity and permeability terms. Smith et al. address such ambiguity in Equation (45) by using the conditions of passivity. Only the positive root for η will be used given the condition on the real portion that $\Re(\eta)>0$. The passive condition on the index of refraction requires the electromagnetic absorption loss $\Im(\eta)>0$ and leads to

$$\Im(\eta) = \pm\Im\left(\frac{\cos^{-1}\left(\frac{1}{2T}\right)\left[1-\left(R^2-T^2\right)\right]}{kd}\right). \tag{48}$$

The arccosine term in Equation (48) introduces the issue of branch selection for $\Re(\eta)$ which is not addressed by the passive condition. Smith et al. suggest determining the proper branch by repeated measurements of a sample with minimized thickness [65]. The sign of the branch selected for $\Re(\eta)$ is driven by the passive condition on $\Im(\eta)$. Given an integer m, $\Re(\eta)$ can be written as

$$\Re(n) = \pm\Re\left(\frac{\cos^{-1}\left(\frac{1}{2T}\right)\left[1-\left(R^2-T^2\right)\right]}{kd}\right)+\frac{2\pi m}{kd}. \tag{49}$$

Clearly, Smith et al. have attempted to design an extraction technique that provides physically realizable results that account for the requirement of passivity in addition to causality. Discussions of homogenization also deal with one other big issue: the material-environment boundary [10, 61]. Boundary selection allows unambiguous determination of the phase of the reflected waves. This boundary can be difficult to discern in metamaterials but Smith et al. address this problem for SRR metamaterial arrays by stating that the selection of the reference plane selection doesn't critically affect extraction results.

2.4.3 Design-To Modified Parameter Generation.

The primary goal of the extraction process is to link the extracted values to particular cell geometries. An effective method to develop this link is to create an analytic equation for the effective constitutive parameters that is dependent on the cell geometries. These effective or relative parameters are poorly fit by curves generated with various mathematical models [43]. Better curve fits can be generated from modifying the effective constitutive parameters.

2.4.3.1 Bulk Media Property Modification.

The effective or relative constitutive parameters can be written in terms of the impedance and the index of refraction, as was previously shown. These terms can also be written in terms of average parameters that "represent the local field responses by structures with finite dimensions," [27]. Average parameters have previously been used to predict constitutive parameters [27] but Paul suggests such applications are limited to a single type of resonance [43].

The AFIT rapid design methodology improves approximations of constitutive parameters by replacing the use of average parameters with the use of modified parameters. SRRs display magnetic resonance [27] but metamaterials can display both electric and magnetic resonance. Modified parameters were introduced in [28] to improve constitutive parameter approximations and account for both types of resonance when using the Drude-Lorentz model for curve fitting. The modified parameters are independent of the average constitutive parameters and can be written as [43]

$$\varepsilon_m = \frac{2}{\eta k_o d} \tan\left(\frac{n k_o d}{2}\right), \tag{50a}$$

$$\mu_m = \frac{2\eta}{k_o d} \tan\left(\frac{n k_o d}{2}\right), \tag{50b}$$

where $k_o = \omega\sqrt{\mu_o \varepsilon_o}$. Equations (50) show that in the effort to improve curve fitting, the connection between the cell geometry and the effective parameters is lost. The use of the tangent term in Equations (50) means that retrieval of effective parameters from the modified parameters is impractical because the arctangent term is a multivalued function.

2.4.3.2 Curve Fitting Approaches.

Curve fitting links modified parameters with a metamaterial cell's geometric features. A geometry-dependent function is generated for the curve fit of each constitutive parameter but the accuracy of the curve fit depends on the model used to predict the modified constitutive parameters. Metamaterial cells can be electrically resonant, magnetically resonant or both so minimizing the error for a fit of the resonant or non-resonant constitutive parameter may necessitate the use of different curve models for permittivity and permeability.

The Lorentz model and variants thereof are one well-known means for curve fitting [27, 28, 42]. The Lorentz model is a popular causal model commonly used in asymptotic methods [42]. In the presence of resonance polarization, this model can accurately describe dielectric dispersion of metamaterials (where spatial dispersion is assumed to be minimized) [27]. Fitting the modified parameters to the Lorentz model leads to Equations (51) [43]

$$\varepsilon_m = \mu_b \left(1 - \frac{F_\mu f^2}{f^2 - f_{o\mu}^2 + j\gamma_\mu f}\right), \tag{51a}$$

$$\mu_m = \varepsilon_b \left(1 - \frac{F_\varepsilon f^2}{f^2 - f_{o\varepsilon}^2 + j\gamma_\varepsilon f}\right), \tag{51b}$$

where $\gamma_{\varepsilon,\mu}$ are the damping factors; μ_b, ε_b, and F_ε are constants; and the $f_{o\mu}$ and $f_{o\varepsilon}$ terms correspond to the frequencies at which the imaginary part of the curves are maximum.

All the right-hand side terms in Equations (51) are found through curve fitting, with the exception of the F_ε and F_μ terms which are found from geometric expansion. The task of altering cell geometries to generate bulk material properties implies the resonance frequency f used in Equations (51) will not be known. The rapid design method addresses this problem by iterative frequency sampling and curve fitting and selecting the design that maximizes curve fit accuracy [43].

Application of Equations (51) is a common method for curve fitting the resonant cell parameter. Approaches for curve fitting non-resonant parameter include a combination of frequencies and geometry expansions for dispersive parameters [28], a single-term approximation for non-dispersive parameters, and modifications of the Lorentz model such as the one proposed in [43]

$$\varepsilon_m = v + \mu_b \left(\left(\frac{f}{x_s}\right)^2 + \frac{F_\varepsilon f^2}{f^2 - f_{o\varepsilon}^2 + j\gamma_{cd} f} \right) \tag{52}$$

where the additional term v is a vertical curve shift, x_s is the local curve slope at frequency f, and γ_{cd} is the damping term for the curve.

Employing separate methods for calculating the resonant and non-resonant parameters is work- and time-intensive and does not necessarily result in accurate curve fitting for both parameters. Simovski and Treyakov proposed a method of local parameters that allows the accurate calculation of both the resonant and nonresonant terms [62]. The method of local parameters is based on an analysis of finite lattices [62]. Basing their analysis on the observations of Drude, Simovski and Tretyakov stated that finite lattices with periods comparable to a wavelength (including the $\lambda/10$ metamaterial standard periodicity), do not truly display homogeneous behavior due to non-negligible phase shifts on an incident field induced by the lattice [62]. That is, a lattice is not equivalent to bounded volume of constant permittivity. Further, there appear to be transition regions between unit cells that complicate discernment of the locations of the lattice interfaces.

The end result of the application of Drude's findings by Simovski and Tretyakov [62] was that extraction methods presented to date provide local parameters independent of both polarization and wave incident angle. These local parameters were found to be the result of Bloch impedance Z_B (not wave impedance), and represent the macro level or bulk material parameters [62]. Bloch impedance, the positive root of Equation (45), helps determine the input impedance for a unit cell evaluated as a transmission line component [62]. This scenario is shown in Figure 18. The input impedance Z_i in terms of the lattice period spacing d_l is

$$Z_i = \frac{Z_B - j\tan\left(\frac{k_o d_l}{2}\right)}{1 - jZ_B\tan\left(\frac{k_o d_l}{2}\right)}. \tag{53}$$

The local parameters can then be written as [62]

$$\varepsilon_L = \frac{q\left(q+k_o Z_i\right)}{k_o\left(k_o+qZ_i\right)}, \tag{54a}$$

$$\mu_L = \frac{q\left(k_o+qZ_i\right)}{k_o\left(q+k_o Z_i\right)}, \tag{54b}$$

where $q = k_o n$ and n is calculated from Equation (44).

The form of these local parameters and the similarity between the construction of the local permittivity and permeability provides the advantage of curve fitting with the Lorentz model [43]. Local parameters are thus an attractive alternative to other modified parameters for the purposes of curve fitting.

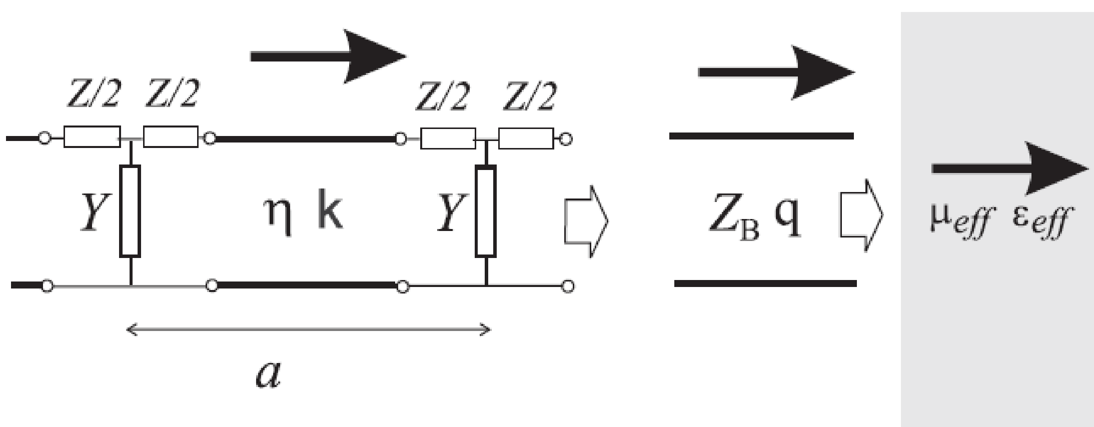

Figure 18. Relationship between a lattice unit cell and a transmission line representation in [62]. First observe a periodically loaded transmission line subjected to an incident wave with a given impedance and propagation constant. The characteristic impedance of the wave on the transmission line can be described as the Bloch impedance Z_B. Likewise, the loaded propagation constant can be written as the wave number, here written as q. These two terms form the new transmission line model and in turn describe the effective constitutive parameters. These effective parameters define the lattice unit cell.

2.4.3.3 Model Parameter Determination.

The Lorentz model equations used to curve fit the local or modified parameters are dependent on parameters such as F_ε or F_μ that can be both expanded into geometric series and expressed as functions of the unit cell's variable geometric features $\{a_\theta, r, s\}$ [43]. Each term of a geometric expansion is preceded by a Taylor coefficient. These coefficients may be solved for using, for example,

$$\begin{pmatrix} 1 & s_1 & r_1 & a_{\theta 1} \cdots s_1 r_1 a_{\theta 1}^2 \\ 1 & s_2 & r_2 & a_{\theta 2} \cdots s_2 r_2 a_{\theta 2}^2 \\ \vdots & \vdots & \vdots & \vdots \ddots \quad \vdots \\ 1 & s_n & r_n & a_{\theta n} \cdots s_n r_n a_{\theta n}^2 \end{pmatrix} \begin{pmatrix} a_o \\ a_1 \\ \vdots \\ a_n \end{pmatrix} = \begin{pmatrix} f_{p\mu}^{(1)} \\ f_{p\mu}^{(2)} \\ \vdots \\ f_{p\mu}^{(n)} \end{pmatrix}. \tag{55}$$

where the right-hand side of the equations is a vector of the $f_{p\mu}$ frequencies associated with the minimum real value of the modified constitutive parameter that is being curve fitted (permeability in this example) [43]. This minimum will occur at a frequency above resonance.

Each line of the matrix shown in Equation (55) is associated with an unique cell geometry. The form of the matrix shows that the row rank of the left-hand side matrix must match the column rank of the right hand side. There must be as many unique unit cells as expansion terms. If there are fewer cells than expansion terms a rank-deficient situation will result. Paul leverages the opposite condition of overdetermination, when there are more cells than expansion terms [43].

Overdetermination allows some optimization through selection of the Taylor coefficient that most closely solves the set of resulting linear equations. The solution of the Taylor coefficients then allows the determination of F_ε or F_μ for any $\{a_\theta, r, s\}$. The various combinations of $\{a_\theta, r, s\}$ can used with the new F_ε or F_μ equations to create a set of all attainable values of achievable design-to modified parameters.

2.4.3.4 Selection of Design-To Modified Parameters.

Ideally, the achievable design-to modified parameters would be matched exactly to the effective constitutive parameters collected from the S-parameter measurements. The design-to modified parameters can be directly tied to the modified parameters but due to the irreversible nature of the process to create them discussed previously, the modified parameters cannot be tied to the effective parameters from which they were generated. Therefore the achievable modified parameters can only be matched to the modified parameters.

The initial matching process used by the AFIT rapid design considers both real and imaginary error contributions. Paul found that by considering the modified parameters of a cell as a point with real and imaginary coordinates, the most effective means to match parameters was to measure distance between the ideal and achievable or possible parameters so that [43]

$$distance(\psi) = \sqrt{\left(\mathrm{Re}\left(\psi_{design}\right) - \mathrm{Re}\left(\psi_{possible}\right)\right)^2} + \sqrt{\left(\mathrm{Im}\left(\psi_{design}\right) - \mathrm{Im}\left(\psi_{possible}\right)\right)^2} \quad (56)$$

where ψ is either permeability or permittivity. This distance can be interpreted as error. If the intent is to match both the modified permeability and permittivity then the sum of their distances shown below must be minimized such that

$$Total\,distance = distance(\varepsilon) + distance(\mu). \tag{57}$$

2.4.4 Validation of Design Methodology.

The rapid design methodology was validated by comparing the effective parameters extracted from full wave simulations with the achievable modified parameters resulting from three separate curve-fitting approaches [43]. Paul found the best curve fitting method applied a Lorentz model to local parameters [43]. All models appeared to accurately fit permeability, the resonance parameter. The distinguishing factor between the studied curve fitting approaches was their accuracy in the non-resonant parameter, permittivity. The results of the validation showed that application of the Lorentz model for curve fitting will be best for this thesis.

2.5 Computational Methods

A computational approach is a smart and necessary means to designing and testing electromagnetic devices. Computational methods allow the application of Maxwell's equations to understand the electromagnetic response of everything from small and geometrically straightforward devices to electrically large, vastly complex collections of materials and geometrical features that would otherwise be impossible to accurately predict by hand. Computational tools can report the results of those simulations using visualization tools that display everything from field distribution, power flow, effective constitutive parameters, and surface currents to S-parameters and beyond.

A variety of computational methods can be selected, depending on the simulation feature required. TO designs produce spatially-variant, anisotropic constitutive parameter tensors that are easily simulated using COMSOL®. COMSOL® is a well-known commercial full-wave electromagnetic computational tool that simulates 2-D or 3-D designs using FEM. CST Microwave Studio® (CST MWS®) is another oft-used computational tool that can also simulate 2-D or 3-D designs but cannot simulate spatially-variant, anisotropic constitutive parameter tensors. CST MWS® is a particularly intuitive program and makes 3-D design simulations effortless.

Both COMSOL® and CST MWS® were utilized to visualize, optimize, and test the electromagnetic concentrator before it was manufactured. This section provides background to explain the mathematical architecture that COMSOL® and CST MWS® are based on. The boundary conditions used during the implementation of each method are also discussed. Finally, several computational studies will be provided to demonstrate how the methods have been used in research.

2.5.1 Finite Integration Technique.

CST MWS® uses the computational method FIT. For this thesis, FIT was used for simulating the 3-D array of circuit boards printed with optimized metamaterial cells. Weiland first introduced FIT in 1977 as an alternative to contemporary methods for solving Maxwell's equations through volume discretization [12, 32, 72]. The key to Weiland's reformulation was to apply discretization to the integral form of Maxwell's equations, shown as

$$\oint_{\partial A} \boldsymbol{E} \cdot d\boldsymbol{s} \;=\; -\frac{d}{dt}\int_{A} \boldsymbol{B} \cdot d\boldsymbol{A}, \tag{58a}$$

$$\oint_{\partial A} \boldsymbol{H} \cdot ds \;=\; \int_{A} \left(\frac{d}{dt}\boldsymbol{D} + \boldsymbol{J} \right) \cdot d\boldsymbol{A}, \tag{58b}$$

$$\oint_{\partial V} \boldsymbol{D} \cdot d\boldsymbol{A} \;=\; -\frac{d}{dt}\int_{V} q_{ev} dV, \tag{58c}$$

$$\oint_{\partial V} \boldsymbol{B} \cdot d\boldsymbol{A} \;=\; 0, \tag{58d}$$

where $\boldsymbol{J}$ is the electric current vector and is q_{ev} the electric charge density. FIT was originally designed work with Maxwell's equations in the frequency domain but it can be applied in the time domain as well [38, 72, 73]. In fact, FIT can be considered a generalization of the finite difference time domain approach [72].

FIT creates a one-to-one translation between a set of algebraic equations and the field relations summarized in Equations (58) therefore ensuring a unique solution in discrete space [32, 38]. Clemens et al. explain the multi-step process involved in this translation [12]. The first step, they explain, is defining a target for the spatial discretization. This generally involves creating bounded, simply connected computational domain in Euclidean space that contains the device or environment that will be simulated. The next stated step is the decomposition of the computational domain or creating the mesh. The repeated unit of this decomposition or discretization consists of a rectangular dual grid doublet [11, 72]. Figure 19 shows that the doublet consists of two cubes $\{G, \tilde{G}\}$, the primary and its dual, overlapped in such a way that when repeated, the centroid of each cubic cell serves as a corner for another cell.

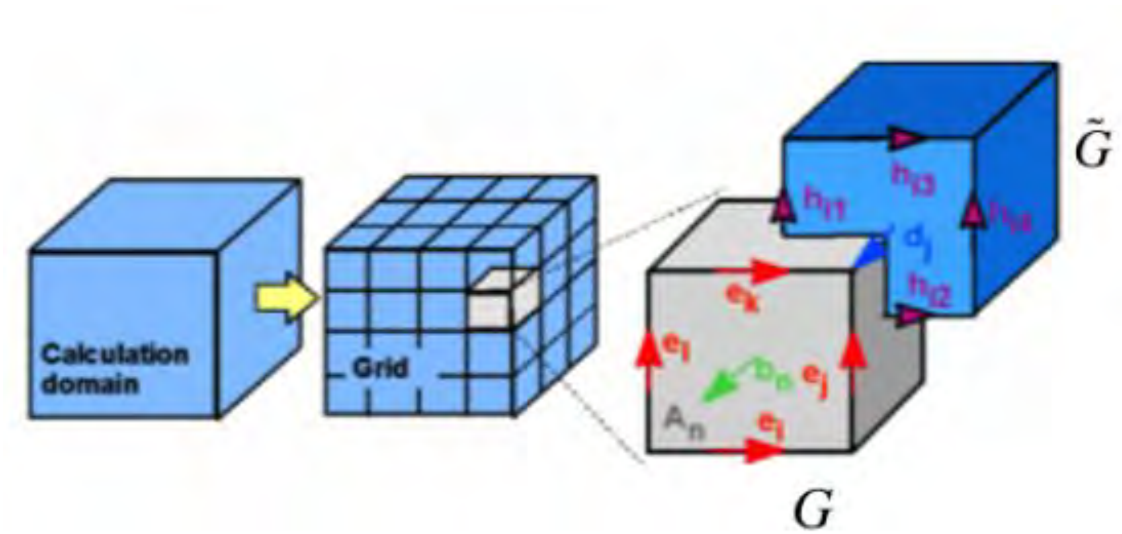

Figure 19. Formulation of calculation domain with doublets in [1].

The discretized cubic volumes and charge location result in different sets of electromagnetic quantities corresponding to the dual grid doublet. Figure 19 shows that the G vector quantites are $\boldsymbol{e}$ and $\boldsymbol{b}$. These terms correspond to the line integral of electric field or an electric voltage and the magnetic induction flux through each face respectively. The quantities on $\tilde{G}$ include $\boldsymbol{d}$, $\boldsymbol{h}$, and $\boldsymbol{j}$ which correspond to electric displacement flux, the integral of magnetic field or magnetic voltage, and charge current. Assuming the cell edges of the n^{th} G and $\tilde{G}$ cells are length L_i and $\tilde{L}_i$ respectively and the corresponding facet or face areas are A and $\tilde{A}$ then the two sets of terms can be written as [11]

$$e_i = \int_{L_i} \boldsymbol{E} \cdot ds, \tag{59a}$$

$$\boldsymbol{b}_i = \int_{A_i} \boldsymbol{B} \cdot d\boldsymbol{A}, \tag{59b}$$

$$\boldsymbol{d}_i = \int_{\tilde{A}_i} \boldsymbol{D} \cdot d\boldsymbol{A}, \tag{59c}$$

$$\boldsymbol{h}_i = \int_{\tilde{L}_i} \boldsymbol{H} \cdot d\boldsymbol{s}, \tag{59d}$$

$$\boldsymbol{j}_i = \int_{\tilde{A}_i} \boldsymbol{J} \cdot d\boldsymbol{A}. \tag{59e}$$

These terms can be transformed into the discrete analogues of Equations (58) through the use of the topological matrices $\boldsymbol{C}$, $\tilde{\boldsymbol{C}}$, $\boldsymbol{S}$, and $\tilde{\boldsymbol{S}}$ where the terms without the tilde correspond to G and the terms with a tilde correspond to $\tilde{G}$. Topological matrices describe the orientation of fields at a surface. The support matrix operators $\boldsymbol{C}$ and $\tilde{\boldsymbol{C}}$ represent the discrete equivalent of "curl" and $\boldsymbol{S}$ and $\tilde{\boldsymbol{S}}$ represent the discrete equivalent of "divergence" [11]. Further, because these terms are topological matrices and describe the orientation of the cell edges, their entries are limited to the set $\{-1, 0, 1\}$ [12, 72].

Using the topological matrices, Maxwell's equations convert to Maxwell's Grid Equations (MGE) [72, 73]

$$\boldsymbol{Ce} = -\frac{d}{dt}\boldsymbol{b}, \tag{60a}$$

$$\tilde{\boldsymbol{C}}h = \frac{d}{dt}\boldsymbol{d}, \tag{60b}$$

$$\tilde{\boldsymbol{S}}\boldsymbol{d} = q_{ev}, \tag{60c}$$

$$\tilde{\boldsymbol{S}}\boldsymbol{b} = 0. \tag{60d}$$

An example of this entire process was included in [72] and is reproduced in Figure 20.

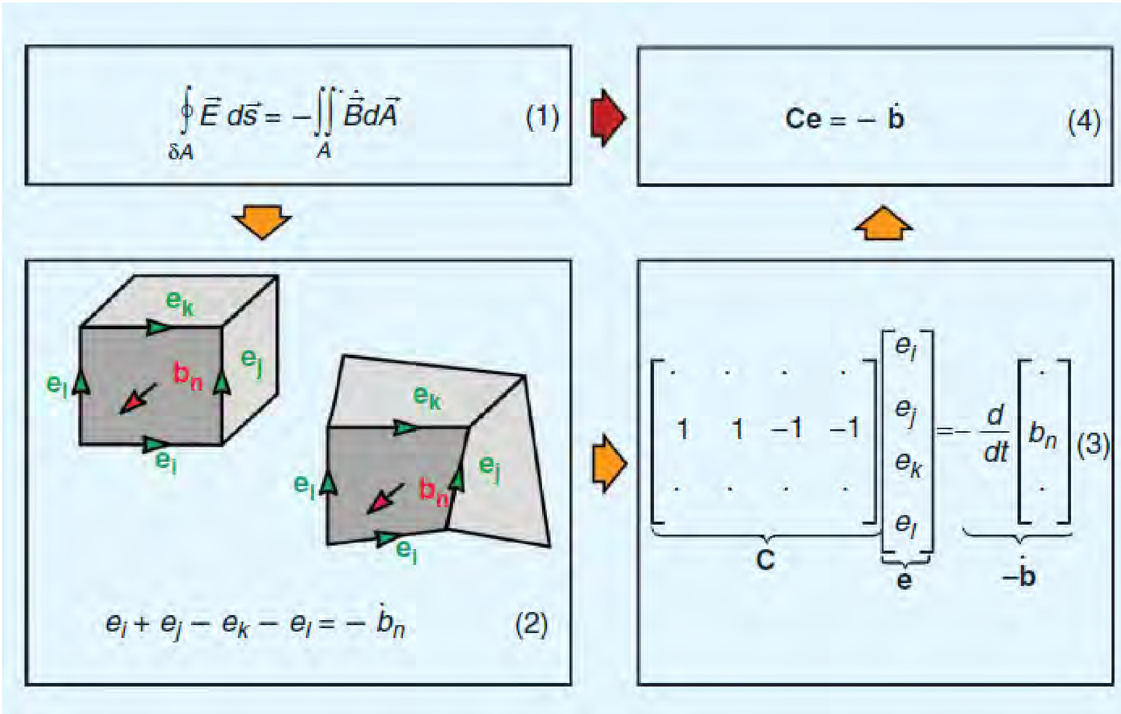

Figure 20. Example steps of discretization of Faraday's law in [72].

MGE are exact; they contain no approximations. However, the constitutive equations needed to close the MGE couple these exact equations use matrix material parameters describing the average material parameters: electric permittivity (M_ε), magnetic permeability (M_μ), and polarization (M_σ) [11, 38]. Averages are naturally approximate therefore the constitutive relations are inexact. The constitutive equations can be written as [11, 38]

$$\boldsymbol{d} = \boldsymbol{M}_\varepsilon \boldsymbol{e}, \tag{61a}$$

$$\boldsymbol{b} = \boldsymbol{M}_\mu \boldsymbol{h}, \tag{61b}$$

$$\boldsymbol{j} = \boldsymbol{M}_\sigma e + \boldsymbol{j}_s. \tag{61c}$$

Together, Equations (60) and (61) form a complete and closed set of time-domain equations that the computer will solve. The solution will depend in part on the frequency range over which the simulation will occur. Given a frequency range of interest, a frequency-dependent signal is created and transformed into a usable time-domain equivalent via an inverse Fourier transform. This time or excitation signal is then introduced to the simulated EM environment and a time-domain solution is found using Equations (60) and (61). A final Fourier transform moves the time-domain solution back into a frequency-domain solution.

The time-domain approach is a fast, convenient and popular way to implement FIT but FIT can also be implemented in the frequency domain that it was originally designed for. Operation in the frequency domain involves conversion of Equations (60) and (61) by substituting $\frac{d}{dt}$ for $j\omega$. Weiland explains that a solution to these equations is developed for a set of discrete frequency points because many behaviors are associated with a frequency band (72). This iterative approach of resolving the MGE and constitutive relation equations for a set of frequency points takes time. Interpolation methods can be employed to develop solution estimates in between frequency points and minimize the sum solution time (72). However the solution process is dependent on the accuracy of the solution desired with greater accuracy corresponding to longer solution times. The generally longer solution times of frequency domain approaches with respect to time domain approach solution times can become a constraint in finding the proper simulation method (72).

2.5.2 Finite Element Method.

Unlike CST MWS®, COMSOL® uses FEM. This method was introduced to the public in a two-page addendum to a speech written and given by the New York University mathematics professor Richard L. Courant [44]. Courant's 1942 address used the "piece-wise linear approximants on a set of triangles, which he called 'elements'" to apply variational methods to potential theory [44]. Application of FEM to electrical engineering designs first appeared by the end of the 1960s [44]. Since then, FEM has grown to become an important part of both time- and frequency-domain computational methods.

FEM is a numerical approach to solving Maxwell's equations and therefore seeks to minimize the degrees of freedom that must be solved for by dividing the computational space into finite number of subdomins. Like FIT, FEM is a volume discretization method [72]. Maxwell's equations are applied to each subdomain or cell and the results are summed over the entire mesh. The formed cells do not overlap and form a closed, simply connected surface. Each point where the vertices of various cells join is called a node. Applying Maxwell's equations at these finite locations leads to a set of simultaneous algebraic equations that must be solved. Solution development using FEM thus requires four basic steps [72]

1. subdivide the computational space,
2. choose an interpolation function,
3. create the system of equations, and
4. solve the system of equations.

2.5.2.1 Subdivision of Computational Space.

Discretization of the domain is the first step in FEM. The shape of the resulting subdomains or elements depends on the dimension of the original domain [21]. Figure 21 shows that the dimension of the element will reflect the dimension of the domain from which it was derived. Lines correspond to 1-D domains while triangles and rectangles correspond to 2-D domains. Shapes such as rectangular blocks, triangular blocks, or tetrahedrons represent 3-D domains. The element choice is dependent on the geometry of the discretized domain. For example, rectangular elements are best for rectangular domains and tetrahedral elements work best with triangular domains or complex shapes.

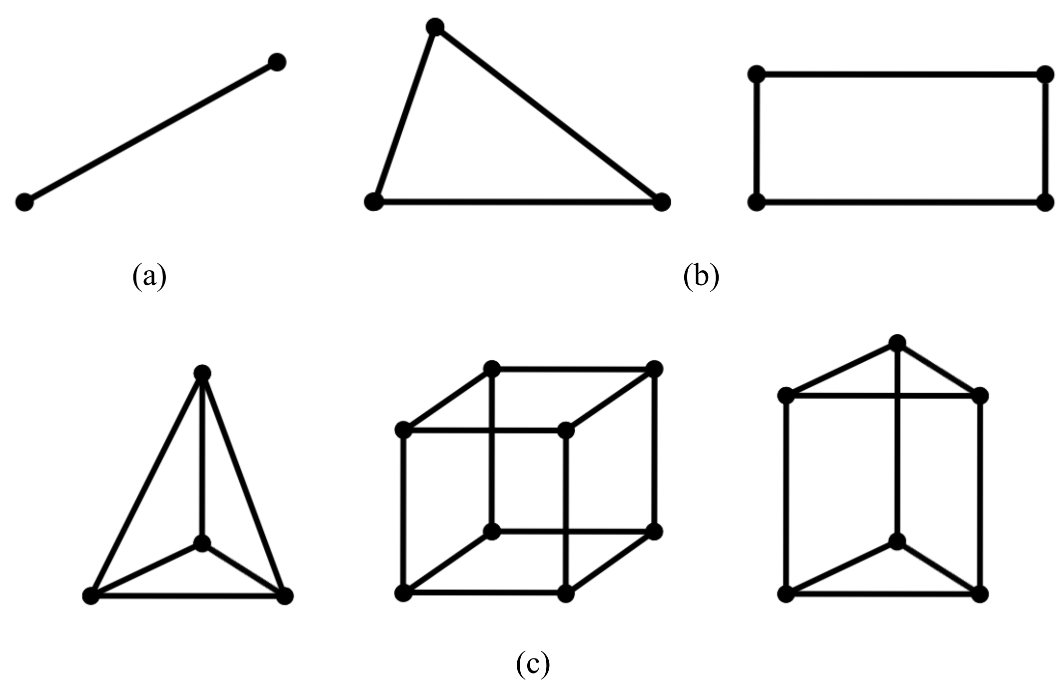

Figure 21. Basic element shapes used to create FEM meshes. (a) 1-D elements are either straight lines or curves. (b) 2-D elements are normally triangles and rectangles. (c) 3-D elements can be tetrahedral, rectangular blocks, or triangular prisms.

2.5.2.2 Interpolation Function Selection.

FEM is used to solve boundary value problems that can be written as [21]

$$\mathbb{F}\phi = f_e \tag{62}$$

where $\mathbb{F}$ is the property or differential operator, ϕ is the unknown behavior or quantity, and f_e is the action or forcing function. The differential equation shown in Equation (62) above can be rewritten so that the unknown behavior is

$$\phi = \mathbb{F}^{-1}f. \tag{63}$$

The unknown behavior is solved for with an interpolation function element-by-element to minimize interpolation error. Given an element e_m, Jin writes the element-specific behavior as a function of the sum of the interpolation function contributions to the element at each node [21]. He shows that the trial behavior $\tilde{\phi}^e$ associated with e_m is [21]

$$\tilde{\phi}^{e_m} = \sum_{\mathrm{j}_M = 1}^{M} N_{\mathrm{j}_M}^{e_m}\phi_{\mathrm{j}_M}^{e_m} = \left\{N^{e_m}\right\}^T\left\{\phi^{e_m}\right\} = \left\{N^{e_m}\right\}\left\{\phi^{e_m}\right\}^T \tag{64}$$

where M is the number of nodes or vertices of the element, $N_{\mathrm{j}_M}^{e_m}$ is the interpolation polynomial evaluated at node j_M, and $\phi_{\mathrm{j}_M}^{e_m}$ is the merely the quantity ϕ particular to node j_M. The order of the interpolation function is particular to the type of element being computed. For example, a line element shown in Figure 21 is interpolated with a linear function that is necessarily zero outside element, the region for which that particular function was developed.

2.5.2.3 Creation of System of Equations.

There are several mathematical methods used to solve for ϕ in Equation (63) and all are approximations due to the numerical approach of FEM. One of the more popular methods is the calculus of variations, which is a function-based approach to extrema calculations [18]. Whereas classical calculus involves the search for points that produce function minima or maxima, variational methods search for functions that provide these extrema. The key in the application of variational methods to FEM is the formulation of a function that both minimizes the behavior ϕ and satisfies the boundary conditions of the considered domain [18, 21].

A popular variational method employed in FEM is the Ritz method [21]. Jin provides a thorough development of this method, the result of which is a behavior defined as the summation of the product of constant coefficients and a set of expansion functions covering the entire domain. The summation is evaluated necessarily evaluated at all nodes. The second mathematical popular mathematical method, called the Galerkin method employs a different weighting scheme based on residuals. The weights are defined to enforce a zero sum residual requirement. The Galerkin method is similar to other available methods based on successive over-relaxation method that condition the sum of residuals to be 0 so as to ensure solution accuracy [18]. These methods include point collocation and subdomain collocation.

2.5.2.4 Determination of Solution.

The solution of the system of equations generated by the various methods employed will result in a system that is either inhomogeneous/forced (deterministic) or homogeneous/source-free (eigenanalysis). The deterministic form is represented as [21]

$$[K]\{\phi\} = \{\tilde{b}\} \tag{65}$$

with the known quantities being the system of equations matrix $[K]$ and the general solution vector $\{\tilde{b}\}$.

The inhomogeneous term $\{\tilde{b}\}$ is the result of either: the partial differential equations, the boundary conditions, or both [21]. The deterministic form involves a source excitation so in electromagnetics, the solution to radiation, scattering and other problems involving a source will be deterministic. In contrast, setting $\{\tilde{b}\}$ to 0 results in the eigenanalysis form. Eigenanalysis solutions are developed from problems without sources so in electromagnetics, this solution form may represent resonance activity or wave travel within a structure.

2.5.3 Boundary Conditions.

Boundary conditions are a necessary component of computation simulation. They allow for the exact formulation of and unique solution to the equations of the chosen computation method. Commercial modeling programs provide boundary conditions relevant for thermodynamics, mechanical modeling, and more. For electromagnetics applications, there are several important boundary conditions. Both CST MWS® and COMSOL® were used for simulations. These programs have common and unique boundary conditions that were applicable to simulations for this thesis.

2.5.3.1 Common Boundary Conditions.

Boundary conditions shared by both CST MWS® and COMSOL® included the perfect electric conductor (PEC), the perfect magnetic conductor (PMC), and the perfectly matched layer (PML). The PEC and PMC are the most basic boundary conditions in electromagnetics. The PEC condition means that the material electrical conductivity is treated as infinite. PMC materials are the magnetic dual of the PEC. They have an infinite magnetic conductivity.

The PEC and PMC boundary conditions are important because they can be used to simultaneously simplify computational models and speed up simulation times. PEC material approximations are perfect replacements for metals. A block of metal could be replaced with a PEC material. A metal structure, such as a waveguide, could be replaced simulated by PEC and PMC boundary conditions. These simulations provide such benefits as reducing mesh sizes, simplifying material interaction considerations, and speeding computation times.

In contrast with the PEC and PMC boundary conditions, the PML condition can be used to promote simulation realism but is primarily used to bound the simulated device and the environment. This boundary condition was first proposed in 1994 as a means to simplify analysis of unbounded problems solved with the finite difference time domain

[6]. The PML isolates the simulation by attempting to simultaneously absorb all radiation and reflect none back. Effective PML implementation is a complex problem; design of matched layers close to a scatterer requires the tailoring of several parameters including the theoretical normal reflection of the layer, the conductivity at PML-environment interface, and the rate of growth of conductivity within the PML [6].

This boundary condition is now employed in time- and frequency domain methods and by a variety of solvers. For example, CST MWS® uses the open boundary condition as its euphemism for a PML. However, unlike COMSOL®, the PML employed by CST MWS® is actually a convolution PML (CPML) [1]. This method boasts a number of benefits over traditional PML implementations. First, CPML is computationally efficient method and independent of its simulation environment so that it can be equally applied without modification to homogeneous/inhomogeneous, isotropic/anisotropic, lossless/lossy, and other such contrasting environments [53]. CPML also has shown superior absorption of evanescent waves [53].

2.5.3.2 Unique Boundary Conditions.

The PEC, PMC, and PML clearly do not cover all boundary conditions. Other implementable boundary conditions are program specific. For example, CST MWS® provides the user the choice of periodic and unit cell or Floquet boundary conditions not offered in COMSOL®. These boundary conditions are included for implementations of electromagnetic models in which there is a base repeated unit and group interaction considerations are important. The periodic condition repeats the base unit and its surrounding boundary space infinitely in the dimension in which the condition is applied. The unit cell merely implements the periodic boundary condition in 2-D. COMSOL® allows the use of layers which can provide up to 3-D periodicity.

2.5.4 Symmetry Planes.

Symmetry planes provide a convenient means to concurrently apply boundary conditions in CST MWS® and simplify the solution space. As the name implies, symmetry planes are used with EM devices or environments displaying symmetry across a plane defined by the major axes in the design environment. Solvers such as CST MWS® that employ symmetry planes only solve for the basic symmetry unit and project the simulation results to match the entire device. These symmetry planes are usually implanted by a PEC or PMC surface

2.5.5 Computational Studies.

Metamaterial devices and design methods are constantly being imagined, simulated, designed and tested. This section discusses some examples of the metamaterial development using FIT and FEM analysis.

2.5.5.1 Design of Arbitrarily Shaped Field Concentrators Using FEM.

A research effort led by Wei Jiang and including David Smith designed and verified a method for constructing arbitrarily shaped electromagnetic concentrators [20]. Their approach was based on developing a set of three concentric similar shapes created with piecewise rational Bézier curves, as shown in Figure 22. Jiang et al. utilized a design in which the field modulations were confined to within the concentrator. This approach, in combination with a central concentration region, necessitated a buffer region of expansion between free space and the concentration region.

The size of the concentric regions was arbitrarily set by adjusting a ratio of radii or widths (a so-called region ratio), between the three regions of each concentrator. The algorithm for mathematically defining the concentrator first involved parameterizing the Bézier curves, defining the transformation equations for each region, and determining the value of a constant associated with the parameterization of each curve from the curve's slope. Second, the Jacobian involving the parameterized curve coordinates was generated and implemented in the standard closed form, anisotropic constitutive parameter tensors for each region.

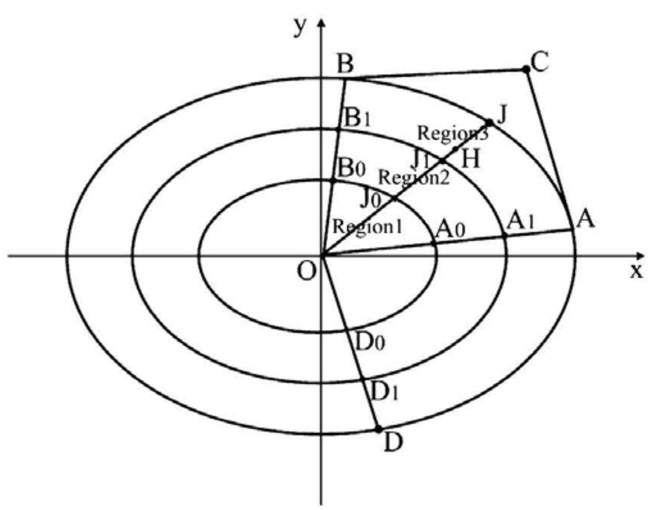

Figure 22. Cross-section of an arbitrarily shaped concentric curve concentrator in [20]. The concentric layers are designed with nonuniform rational B-splines divided into second-order Bezier curves. The point H is an arbitrarily located point in original coordinate system or original space.

The two types of curves were studied and simulated included a heart-shaped concentrator and a rectangular concentrator. The heart-shaped device employed second-order Bézier curves fully defined by three control points and three weights. Control points of (0, 0.1), (0, -0.1), and (-0.4, -0.2) and weights of 2, 1, and 2 were selected. The rectangular device employed first-order Bézier curves and quadrant-specific line parameterizations. The rectangular design was designed with a length-to-width ratio of 2:1 and both concentration devices used a seemingly arbitrarily selected region ratio of 1:6:10.

Both concentrators were created as 2-D structures in COMSOL simulations. A transverse electric (TE) polarized plane wave illuminated both structures. The results of the simulations are shown in Figure 23.

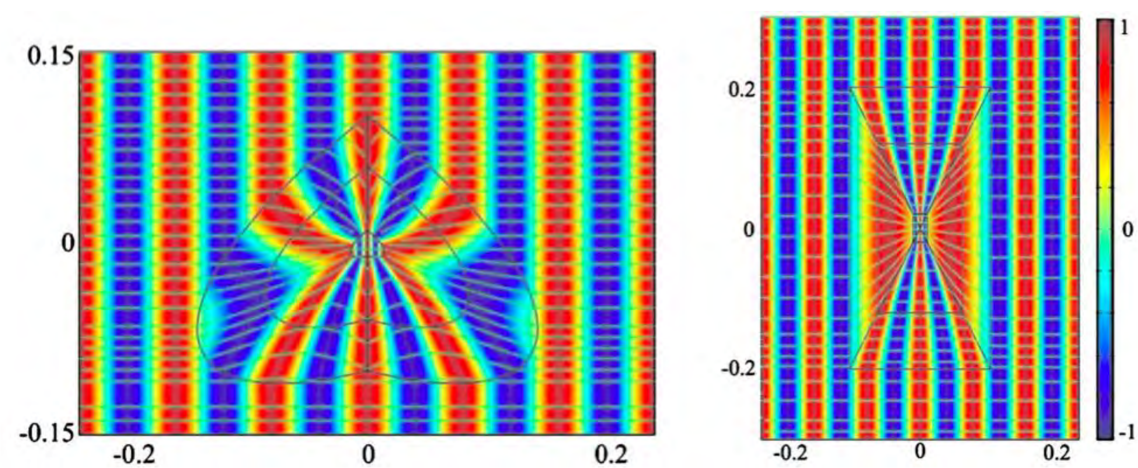

(a) (b)

Figure 23. Electric field distributions and power flow lines for two arbitrarily shaped concentrators in [20]. (a) Heart-shaped concentrator illuminated with plane waves traveling left to right. (b) Rectangular concentrator with plane waves also traveling left to right.

The concentrators simulated by Jiang et al. appear to operate as designed. This paper therefore demonstrates a successful algorithm for a flexible design. This paper also implies the importance to concentrator designs of an expansion section. The use of an expansion section with a concentric region concentrator might provide better concentration for narrow beams at obtuse incidence angles by expanding the beam into the region of concentration.

2.5.5.2 Model of Electromagnetic Beam Modulation Using FEM.

The research presented here by Xu et al. is a prime example of the implementation of TO with a finite-embedded coordinate transformation [74]. These scientists studied beam modulation in both Cartesian and cylindrical coordinates, using 1-D transformations to regulate permittivity and permeability.

Beam modulation in the one-to-one mapping of Cartesian coordinates was implemented by modifying the y coordinate in the transformed or prime space. The transformed term, y', was designed with a tunable modulation that could be set by a modulation coefficient ζ. Values of ζ greater than one would lead to beam expansion and values less than one would lead to beam width contraction. Using Equations (43) to define the constitutive parameters in the transformed or prime space relative to the original space, Xu et al. tested a dielectric slab utilizing these parameters in a FEM simulation. The simulation setup, shown in Figure 24, involved a Gaussian beam directed at a relatively tall test sample. The modulation coefficient ζ was tested at values of 0.5

and 1.5. The simulation results involving power flow and normalized transverse magnetic (TM) fields are reported below in Figure 25.

Slabs using the same two values of modulation coefficient were then tested at an oblique incidence to confirm whether or not the concentrator displayed the effectiveness. Figure 26 shows the results of the tests. Xu et al. claim that their results confirm angular-independent, reflectionless behavior for a TO-designed device. However, to confirm the reflectionless behavior, the authors next stacked and illuminated cascaded dielectric slabs, as displayed in Figure 27.

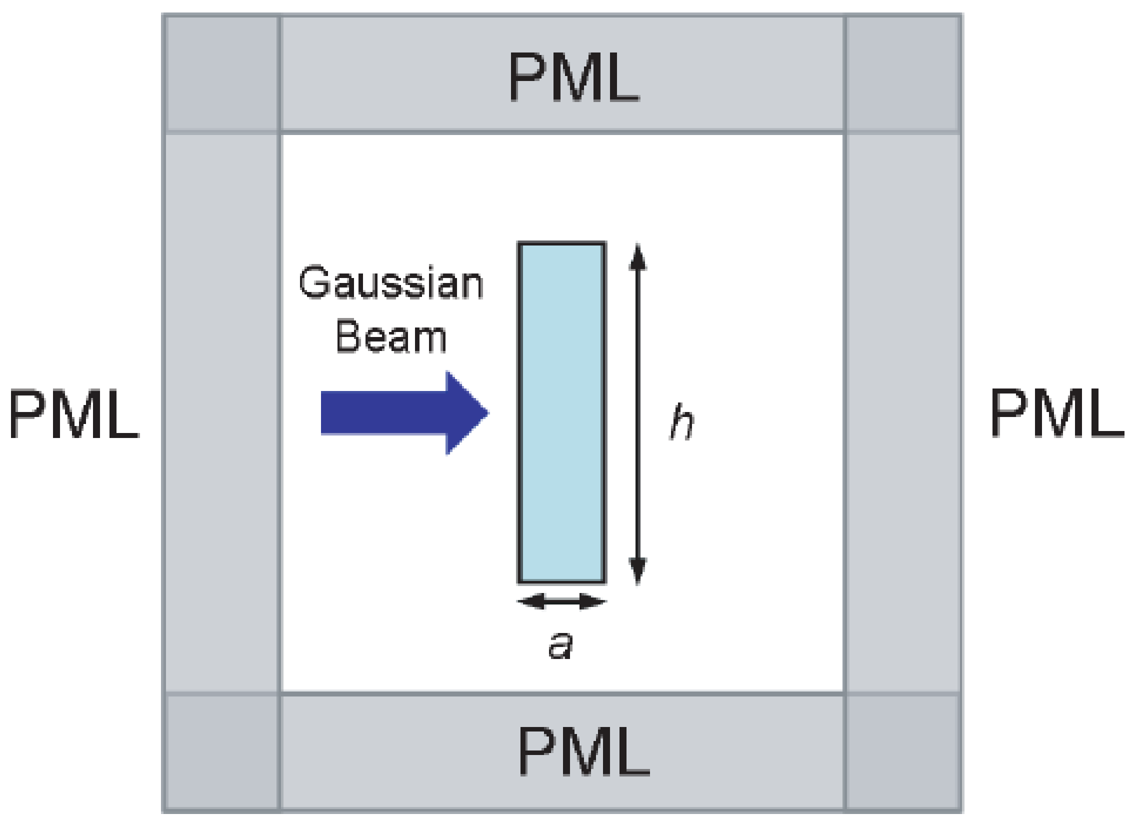

Figure 24. Simulation setup for measuring the amount of beam modulation for a single-layer device illuminated with Gaussian beam [74].

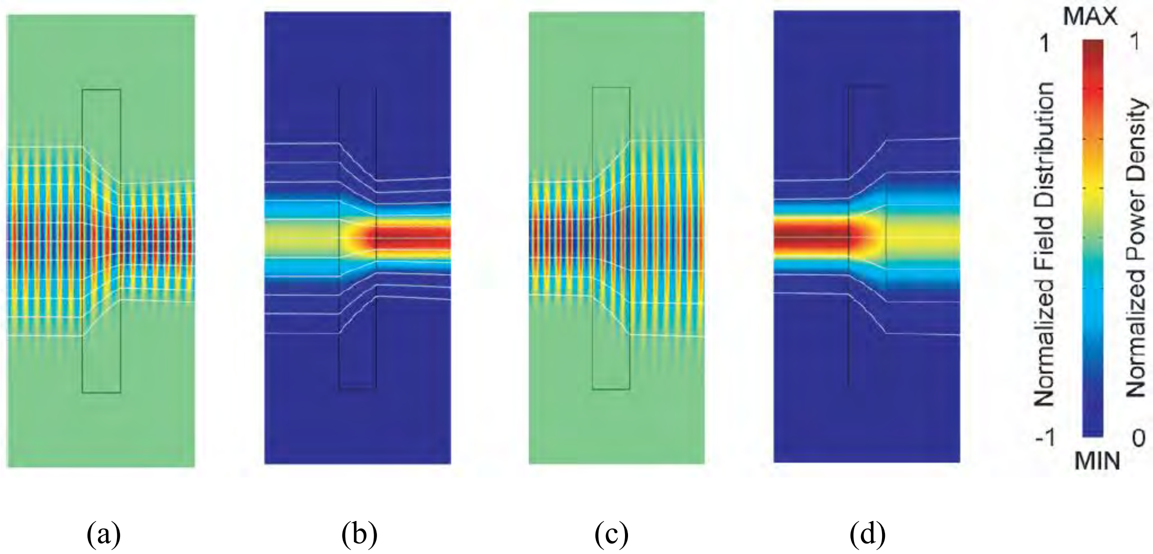

Figure 25. Normalized TM field and power density distributions with overlaid power flow lines for single slab beam modulation in [74]. (a) and (b) plot beam compression while (c) and (d) plot beam expansion. (a) and (c) show the normalized TM fields while (b) and (d) show the normalized power density.

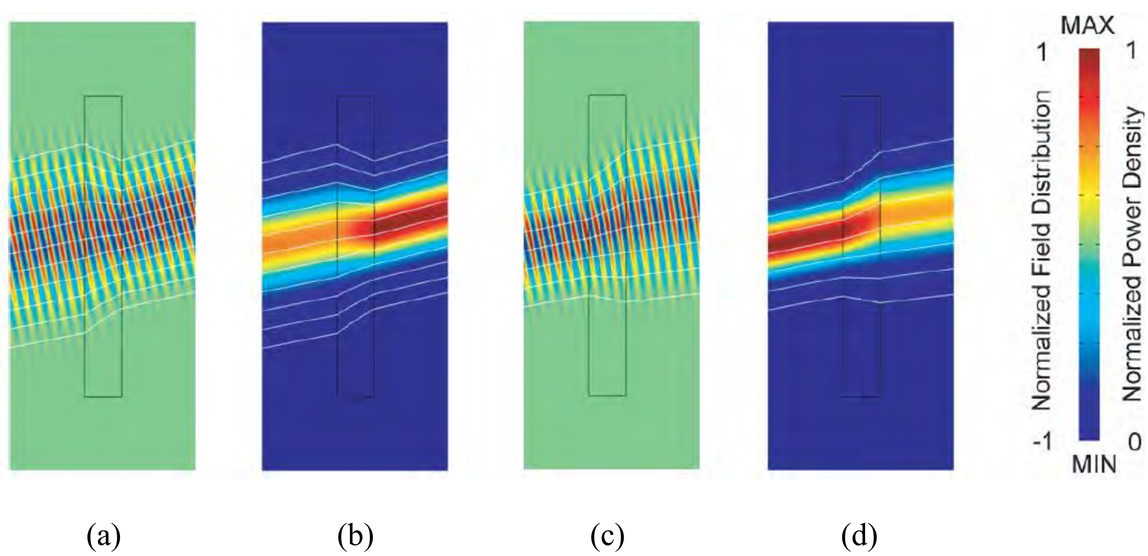

Figure 26. Normalized TM field and power density distributions with overlaid power flow lines for single slab beam modulation illuminated at an oblique incidence in [74]. (a) and (b) plot beam compression while (c) and (d) plot beam expansion. (a) and (c) show the normalized TM fields while (b) and (d) show the normalized power density.

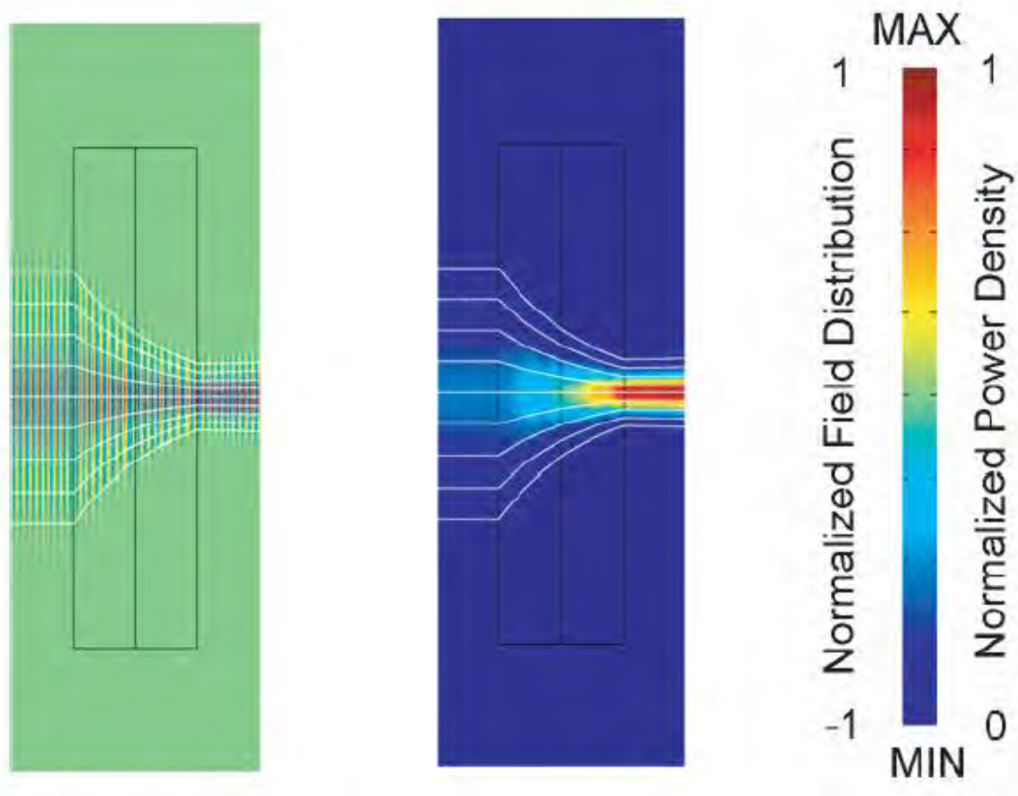

(a) (b)

Figure 27. Normalized TM field and power density distributions with overlaid power flow lines for cascaded slab beam compression in [74]. (a) Plot of normalized TM fields (b) Plot of normalized power density.

After completing the tests of modulation in Cartesian coordinates, beam modulation was tested in cylindrical coordinates, again using a 1-D transformation. The mapping to prime space in cylindrical coordinates, shown as Figure 28, involved the cylindrical coordinate θ which was altered by a factor of a_{shell}/ρ where a_{shell} is the inner shell radius and ρ is the shell radius variable. Xu et al. used the same invariant definitions of permittivity and permeability in transformed space to implement the rank 2 constitutive parameter tensors. The results of their simulations involving an isolated line source and a line source surrounded by the transformed cylindrical shell are shown in Figure 29 below.

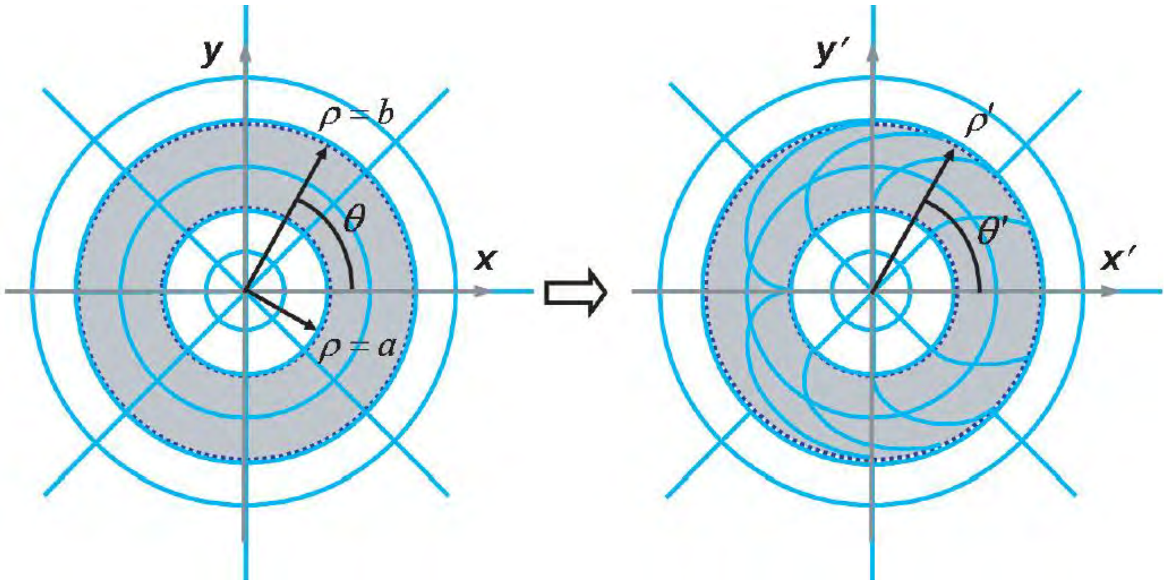

Figure 28. Coordinate transformation within a cylindrical region surrounding a point source in [74]. A coordinate mapping is conducted in the grey annular region from original space to prime space. The radial traces have been compressed from their original uniform distribution in the shell region to a limited area of the shell region in the prime space. The transformed radial traces only exist for $+x'$.

Xu et al. concluded that beam modulation at normal or oblique incidence is possible using embedded coordinate transformations. Simulations for this thesis showed that there is in fact a limitation to range of incidence angles for which no reflection of the incident Gaussian beam can occur. Nonetheless, this research proved invaluable in illustrating an ability to stack various transformed material together, underscored the importance of continuity equations and the applicability of embedded coordinate transformations, and demonstrated a simple formula for developing a 1-D transformation.

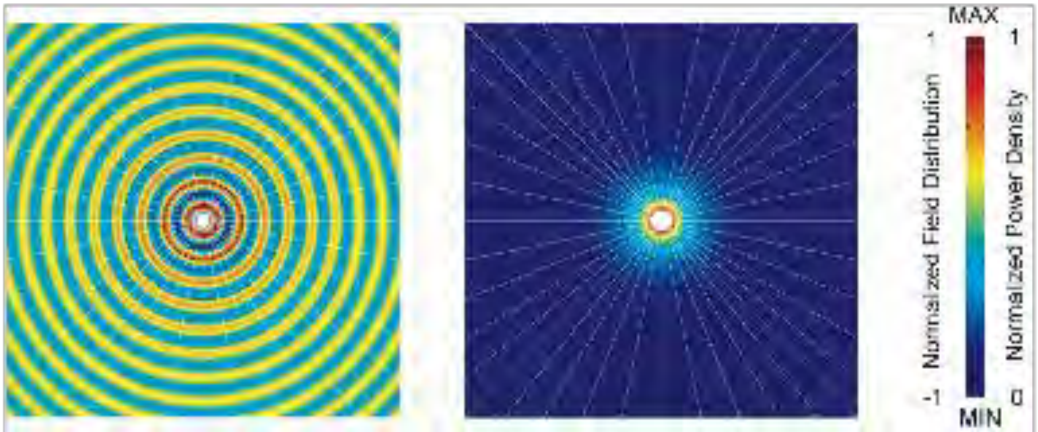

(a) (b)

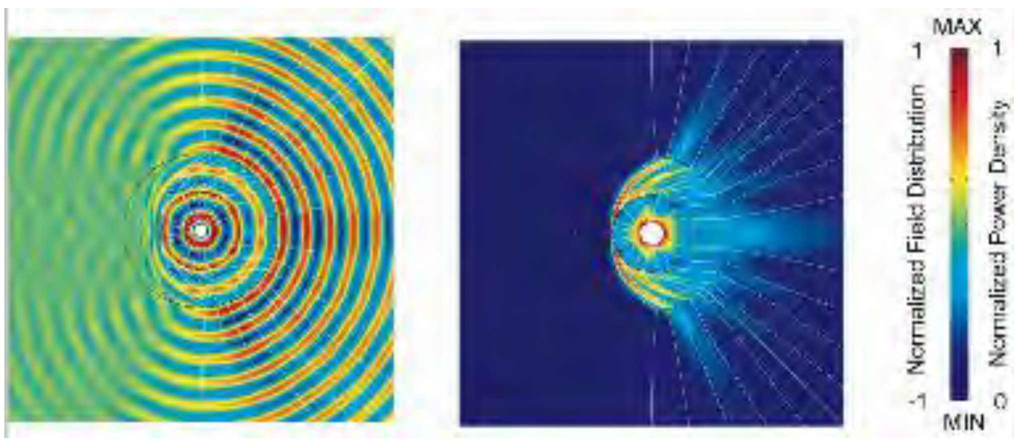

(c) (d)

Figure 29. Normalized TE field and power density distributions with overlaid power flow lines for a line source with and without transformed cylindrical shell in [74]. (a) and (b) plot the field and power distributions for an isolated line source while (c) and (d) plot the field and power distributions for a line source surrounded by a transformed cylindrical shell. (a) and (c) show the normalized TE fields while (b) and (d) show the normalized power density.

2.5.5.3 Verification of FIT with SRR Measurements.

Weiland et al. [73] used experimental measurements of SRR pass and stop bands published by Smith et al. [66] to validate FIT and the perfect boundary approximation. Among the series of simulations conducted to confirm the experimental data was the measurement of S-parameters. The simulation used in CST MWS® consisted of the base unit for the LHM developed by Smith et al. This LHM was a layered structure including a wire and two concentric split rings, arranged in a manner shown in Figure 30.

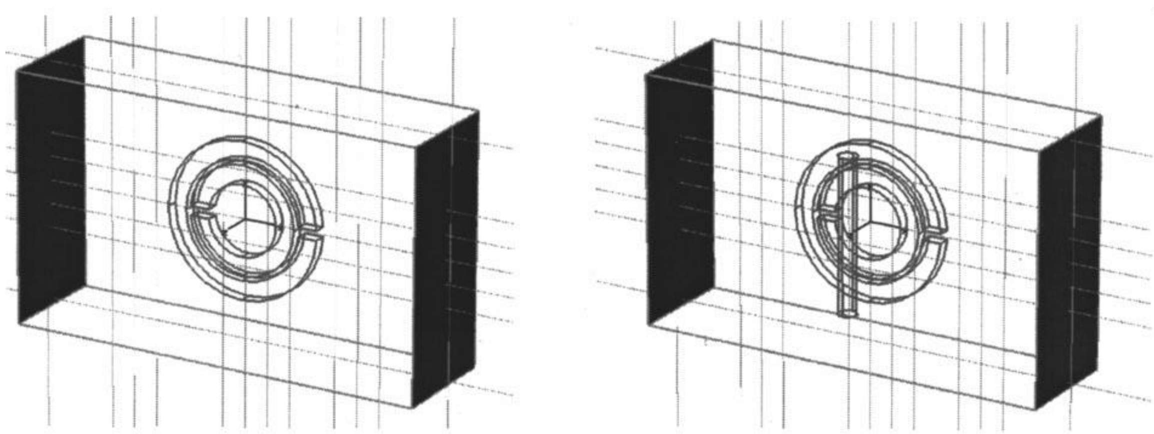

(a) (b)

Figure 30. Simulated models of a SRR used to compare the simulated S-parameters developed with FIT in [73] to previously published experimental measurements. (a) Simulation of the SRR without a wire. (b) Simulation of the SRR with a wire. The wire is centered on the SRR.

The device consisted of PEC wire and ring structures held in free space and enclosed using a perfect boundary approximation [73]. The device was bounded in a manner with the applied x-directed TE_y plane wave: electric boundary conditions for the $\pm y$ face planes and magnetic boundary conditions at the $\pm z$ face planes. The simulation operated in a frequency band of 4 – 6 GHz. Simulated and measurement results for both a single SRR/wire cell and an array of such cell is shown below in Figure 31.

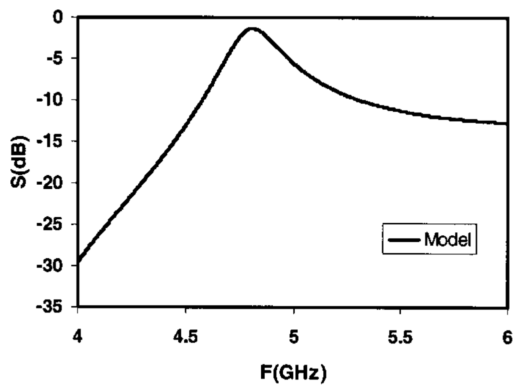

(a)

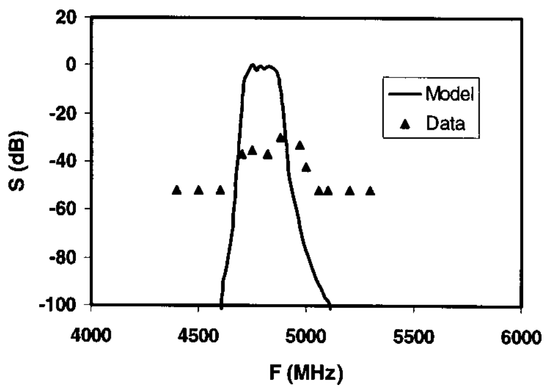

(b)

Figure 31. Simulated and measured results for a unit cell formed from a SRR and a wire in [73]. (a) Simulated results for a single unit cell. (b) Comparison of simulated data for a periodic array of unit cells to measured data for an identical periodic array.

Figure 31 appears to show that the FIT model misestimates the S-parameters for an array of devices. However, Weiland notes that the use of a PEC condition in the model for the wire and rings may have had an impact [73]. He further cites possible misalignment of the wires and rings in the experimental setup that may have result in erroneous experimental data [73]. These are possible sources of error that might arise during the simulation or testing of any device manufactured for this thesis and should be well-noted.

2.5.5.4 Scattering Measurements of SRRs Designed for Sensor Applications.

A study was conducted to explore the use of two different metamaterial topologies for use in an assortment of sensor applications. The two designs evaluated by Ekmecki et al. included a broadside-coupled SRR (BC-SRR) and a V-shaped resonator, shown in Figures 32 [13].

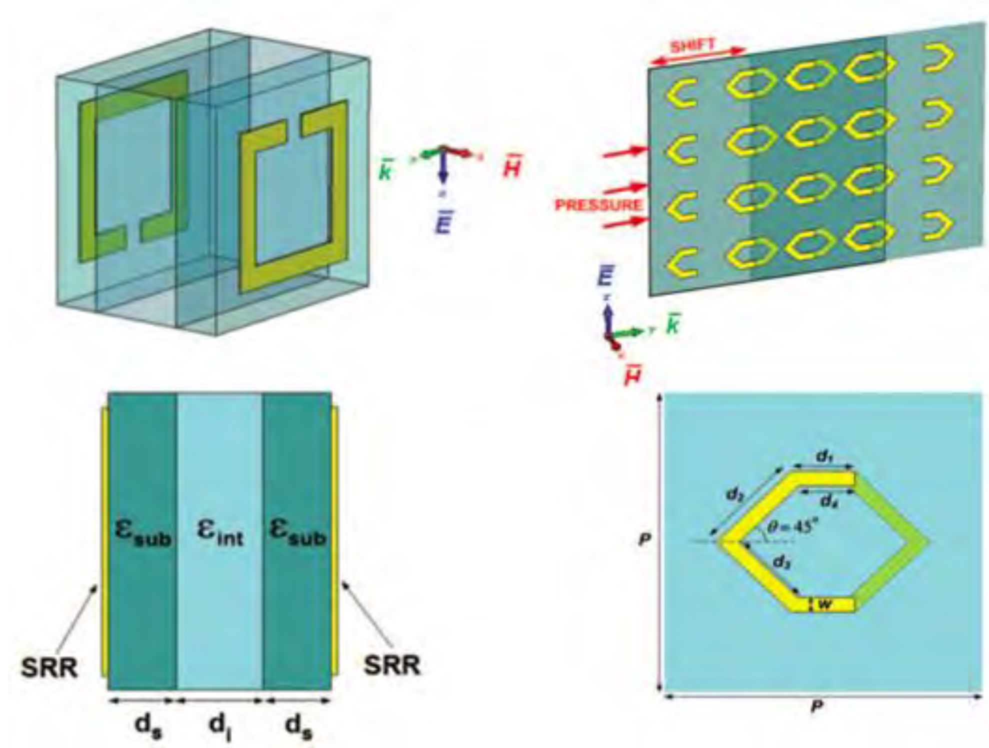

(a) (b)

Figure 32. Different metamaterial topologies considered for various sensor applications in [13]. (a) BC-SRR design. (b) V-shaped resonator.

Ekmecki et al. setup simulations using magnetic excitation, unit cell boundaries, and the frequency domain solver [13]. They showed that for the BC-SRR, resonance decreases with an increase in the interlayer permittivity and that dramatic resonant effects, due to inductive effects, occur at interlayer thicknesses under 0.2 mm [13]. These results are shown in Figure 33. Simulations showed a positive, linear relationship between the V-shaped resonator's shift and its resonance frequency, as seen in Figure 34 [13]. A shift in the baseline configuration of 1.4 mm raised the resonance frequency from 9.66 GHz to 15.39 GHz [13]. These results again emphasize the importance of cell alignment for any manufactured devices.

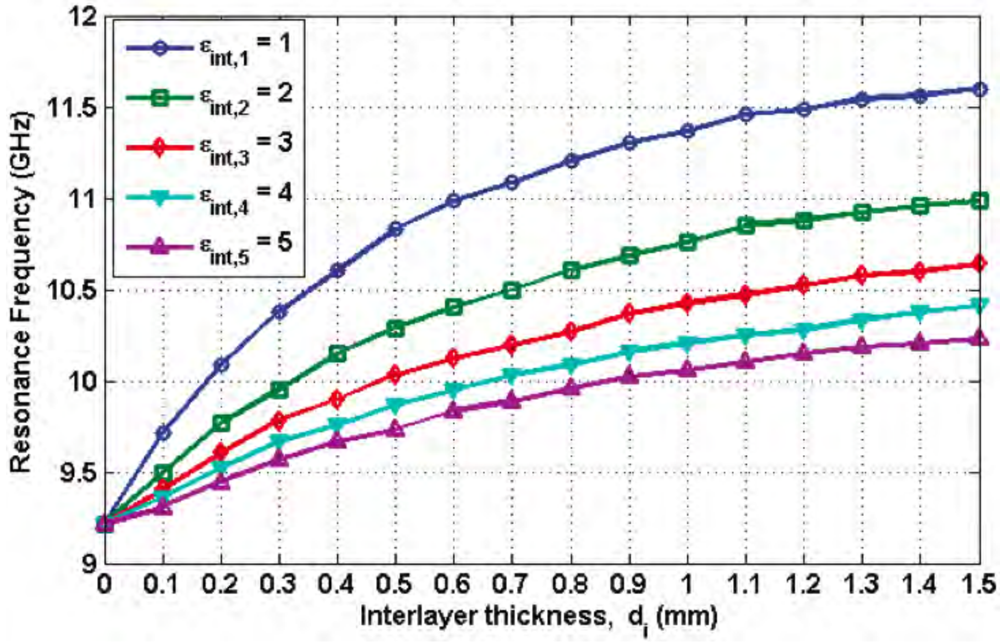

Figure 33. Simulated results showing the interconnected nature of resonance frequency, permittivity, and interlayer thickness for a BC-SRR in [13].

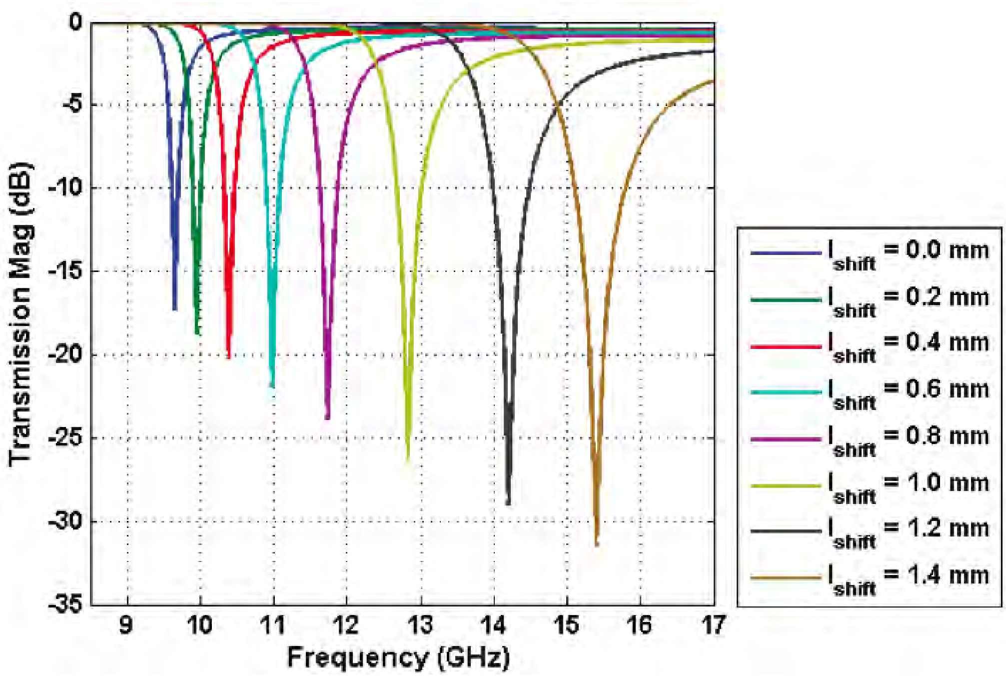

Figure 34. Transmission response of V-sensor for various shift distances in [13]. Larger shift distances indicate greater distance between the two halves of the V-sensor.

2.6 Experimental Studies Employing Transformation Optics

The limited number and application of experimental studies involving simulated or manufactured electromagnetic concentrators prohibit any discussion of such devices here. However, there have been numerous experimental studies conducted on metamaterials. A sampling of studies pertinent to the wedge of planar structures presented in this thesis is reported below in brief fashion.

2.6.1 Experimental Verification of a Left-Handed Material.

In 2001, on the heels of discoveries made by Pendry that allowed for the creation of negative permittivity and negative permeability materials, Shelby et al. created the first material with simultaneously negative constitutive parameters [57]. The base material of the manufactured LHM was 0.25-mm-thick G10 fiberglass circuit board material [57]. A shadow mask/etching method was used to create 2-D periodic arrays of wires and SRRs on the circuit boards that were then cut and assembled to create a 3-D interlocking design [57]. The design, displayed as Figure 35, centers vertically oriented wires behind each SRR. The unit cells used to create the metamaterial wedge were sized to be 0.5 cm each or one-sixth the center frequency of the tested frequency band of 8 – 12 GHz [57].

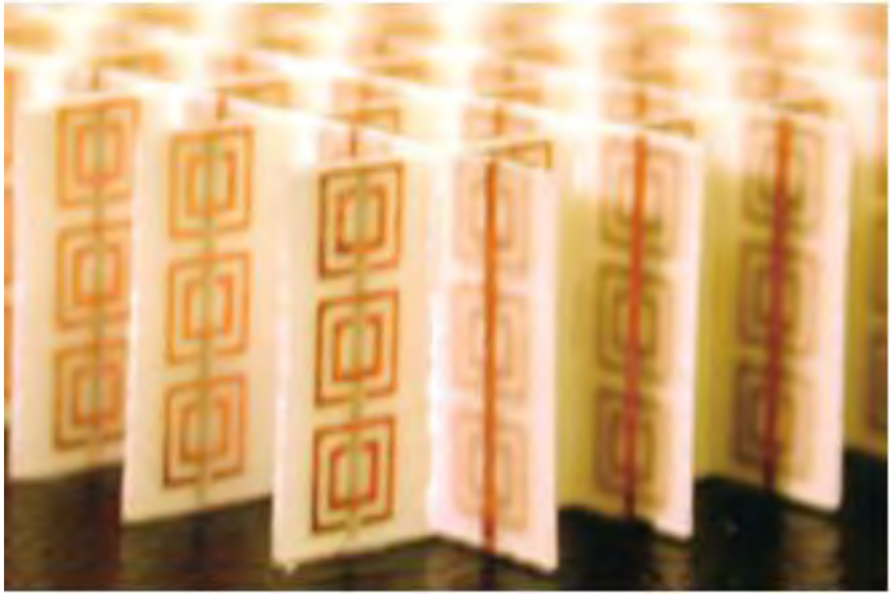

Figure 35. LHM sample built and tested in [57]. The sample was built as a periodic array of SRRs and wires and was designed to resonate at 10.5 GHz.

The instrumentation setup consisted of a detector, parallel plate waveguide, microwave absorber, two flat parallel sheets of aluminum, and a HP8756A scalar network analyzer (NWA) shown in Figure 36. The test procedure involved measuring the transmitted power spectrum for two test samples- the metamaterial wedge and an identically shaped metamaterial wedge.

Measurement results are shown in Figure 37. It is clear from the graphs that the normal to the Teflon wedge with respect to the incident surface was 18.43° or positive as expected. Data produced by Shelby et al. show the corresponding index of refraction was also positive, $n_{teflon} = 1.4 \pm 0.1$ [57]. However, the metamaterial wedge displayed markedly different results. The metamaterial normal was -61° with a correspondingly negative index of refraction of $n_{meta} = -2.7 \pm 0.1$.

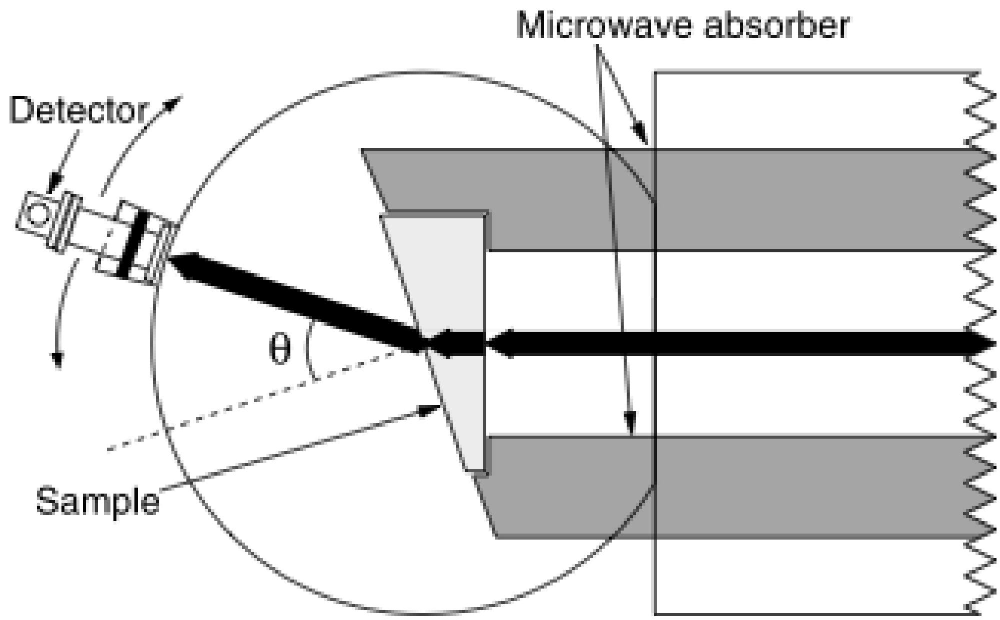

Figure 36. Experimental setup used to measure the transmission power spectrum of the Teflon and metamaterial samples in [57]. The electromagnetic field is incident on the right side of the wedge, not observable by the detector. The black arrows indicate the path positive refraction for 10.5 GHz. The detector was rotated in 1.5^{o} increments and power was measured as a function of angle from the normal of the sample's observed interface.

Figure 37 provides further evidence of differences between the test samples. The index of refraction is generally frequency-independent for the Teflon wedge whereas strong frequency dependence is noted in the measurement of the metamaterial wedge. This dependence indicates the presence of dispersion. It can also be noted that the predicted and measured indices of refraction for the LHM wedge are significantly off in the region surrounding the negative refraction region. Measured values of refraction do not exceed 3 or fall below -3. The authors attribute this finding to internal reflection induced by the manufacturing geometry.

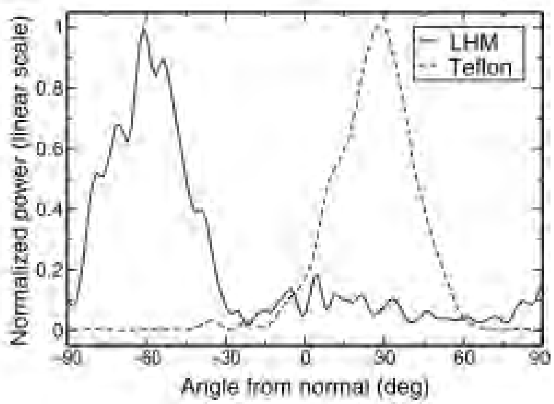

(a)

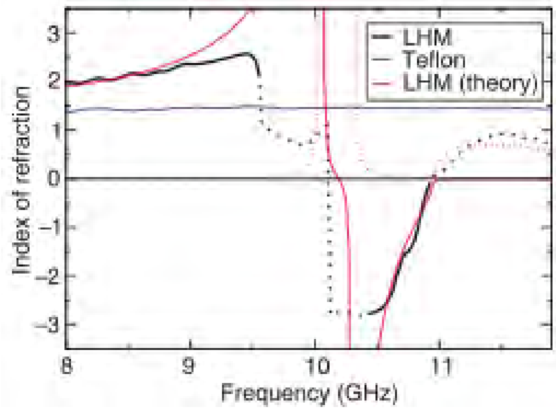

(b)

Figure 37. Experimental data for measurements of the Teflon and metamaterial samples in [57]. (a) Normalized power is plotted at 10.5 GHz. The angle from the normal is the refraction angle and is observed to be negative for the LHM and positive for Teflon. (b) The index of refraction is plotted around 10 GHz to observe any plot behavior for either test sample that may correspond to the normalized power plot at 10.5 GHz in (a). The plotted index values show that while the index remains unchanged for Teflon, the measured index for the LHM becomes negative at about 10.5 GHz. The dotted black line denotes regions where the expected index is outside the measurement capabilities of the researchers. The dotted red line is the plot of the imaginary component of the theoretical LHM index of refraction.

Since this experiment was conducted, there have been a number of arguments raised claiming that a LHM was not created. Some of these points are quite valid but this experiment remains important because it drove the research community to address the issue of LHM and sparked further interest. Some of the criticisms have also provided a means to improve the experimental rigor of future tests of metamaterials.

2.6.2 Cylindrical Electromagnetic Field Cloak.

In building an electronmagnetic concentrator, there are a number of lessons that may be drawn from studying other experimental TO devices. A well-known TO device is the metamaterial cloak built and tested by Schurig et al. [55]. The cloak described was the first physical implementation of the cloak. It was limited to 2-D cloaking effects but showed that some level of electromagnetic field manipulation was possible with even a relatively straight-forward design approach.

The cloak designed by Schurig et al. was cylindrical in shape. Cloaking involves bending waves around an object; the cloak described here was mathematically implemented by invoking a coordinate transformation that compressed the central region of the cylinder, $0 < r_{cyl} < b_{cyl}$ into an annular region $a_{cyl} < r'_{cyl} < b_{cyl}$ where a_{cyl} denotes the radius of the device, b_{cyl} is the inner radius of the annular region, r_{cyl} is the radius within the central region, and r'_{cyl} is radius within the annular region [55].

The resulting transformation equations relating the original and transformed cylindrical coordinates were converted to define the relative permittivity and relative permeability resulting from a TO approach. The cloak construction was further simplified by only considering a single illumination polarization E_z so that a reduced parameter set composed of ε_z, μ_θ, and μ_r could be implemented.

The concentric rings of the cloak were designed to provide the proper radial transition of constitutive parameters required to guide waves around the device. All unit cells placed at a particular radius were designed to share the same geometric features which were derived by parameterizing the corner radius and the height of the split arm, both of which are shown in Figure 38. The constitutive parameters for each combination of cell geometries were derived from simulations of the unit cells and an extraction procedure using S-parameters. The unit cells traces were etched onto Duroid 5870 and the rings were held and together with six radial spokes, as shown in Figure 39.

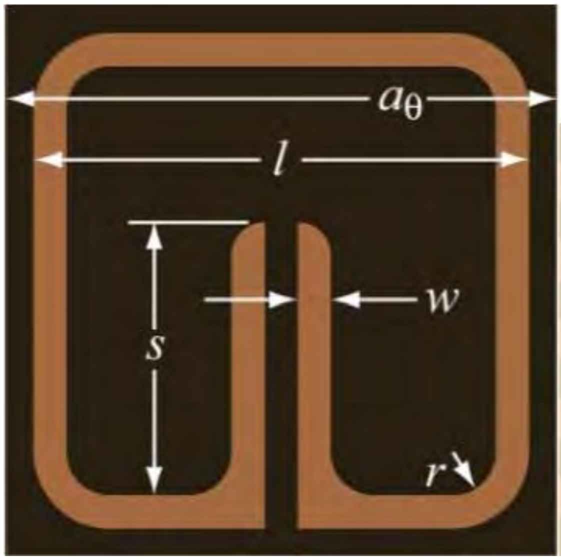

cyl.	r	s	μ_r
1	0.260	1.654	0.003
2	0.254	1.677	0.023
3	0.245	1.718	0.052
4	0.230	1.771	0.085
5	0.208	1.825	0.120
6	0.190	1.886	0.154
7	0.173	1.951	0.188
8	0.148	2.027	0.220
9	0.129	2.110	0.250
10	0.116	2.199	0.279

Figure 38. SRR design used to create the metamaterial cloak at microwave frequencies in [55]. The SRRs were printed on Duroid 5870 with copper 17 microns thick. Constitutive parameters can be designed by manipulating a set of geometric parameters of the SRR including the width of the cell a_θ, the trace width *w*, the arm height s and the corner radius *r*. The SRRs for the cylinders were created by altering s and *r*.

Schurig et al. first ran simulations before testing their physical construction. A model of the test setup is shown in Figure 40. Plane waves in the frequency band 8 – 12 GHz were introduced via a coaxial-to-waveguide transition [55]. The device was held in a parallel plate waveguide and surrounded by absorber to minimize field disturbances due to reflections from the waveguide [55]. An antenna in the top plate measured the fields that were mapped by moving the bottom plate and the test device [55].

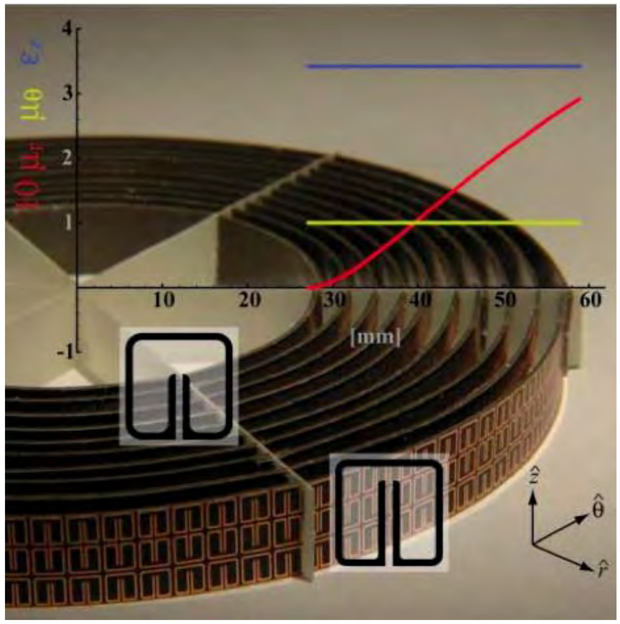

Figure 39. Constructed metamaterial structure providing 2-D microwave cloaking in [55]. Six radial spokes hold the concentric rings of SRRs together. The SRRs at any particular radius share the same geometry and produce constitutive parameters shown in the superimposed graph. Each cylinder is made of three rows of cells that have been flipped with respect to each other to minimize magnetoelectric coupling.

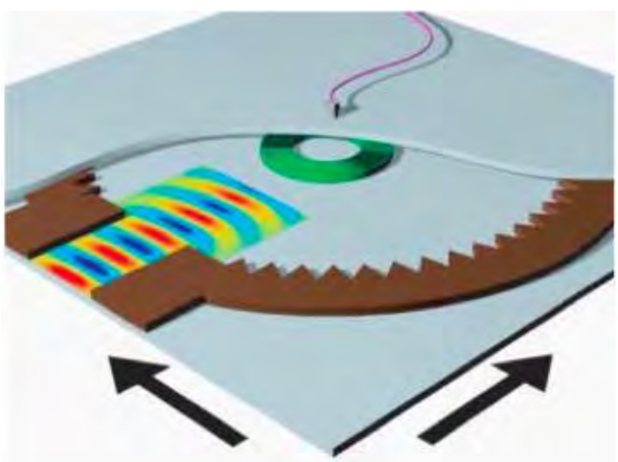

Figure 40. Model of parallel plate wave used to test metamaterial cloaking structure in [55]. Part of the top plate is cut away to show the inside. The cloaking structure is centered in the plates and is surrounded by sawtooth-shaped microwave absorber. A coaxial-to-waveguide transition generates the incident microwaves that are measured with antenna attached to the upper plate. Field mapping was conducted by translating the bottom plate.

The experimental results collected by Schurig et al. for the metamaterial cylinder displayed cloaking behavior as compared to a tested bare copper cylinder. The results, shown in Figure 41, have been claimed by Schurig et al. as proof that a cloak and therefore electromagnetic effects associated with LHM are achievable. More importantly, however, is the process of metamaterial device construction that Schurig and his colleagues helped to define. They showed that effective parameters could be linked to unit cell geometries to create constitutive parameter gradients.

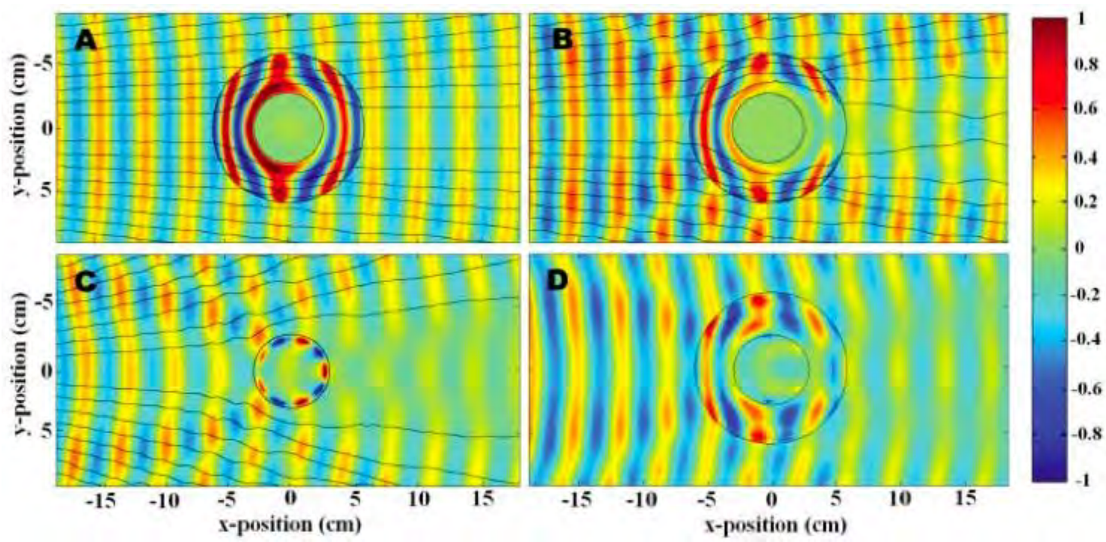

Figure 41. Simulated and measured steady-state electric field patterns at various instances in time in [55]. (a) Simulated field patterns for the exact metamaterial cloak. (b) Simulated field patterns for the cloak with reduced material properties. (c) Measured field patterns for the bare, conducting cylinder. (d) Measured field patterns for the cloaked conducting cylinder.

2.6.3 Metamaterial Planar Array Spacing and Arrangement.

Significant work is involved in translating a desired effective permittivity or permeability into a metamaterial cell. These cells are often arranged as periodic, planar arrays. The standard lattice periodicity between co-planar cells and between the planar arrays is $\lambda/10$ for metamaterial. Generally, little thought is given to the spacing and arrangement of the planar arrays aside from the frequency derived inter-array spacing requirement and the assumption the arrays should be row and column aligned. Unfortunately, such lack of forethought can lead to significant measurement error.

Errors introduced during the assembly of metamaterial planar arrays include inter-plane or intra-plane disorder. These errors and periodicity are investigated by Aydin et al. [3]. These authors describe inter-plane disorder as misalignment of the boards in directions both parallel and normal to the board; intra-plane disorder as the aperiodicity of the SRR cells in the plane of the array [3].

The portion of the experiment testing inter-plane disorder studied 24 stacked arrays of 10 x 15 periodically arrange circular SRRs [3]. Aydin et al. explain that measurements were made with an HP 8510C network analyzer for a frequency band from of no greater than 3 – 6 GHz. Three inter-plane disorder schemes were employed involving aperiodicity in the board spacing: transverse to the direction of propagation, parallel to the direction of propagation, and both parallel and transverse to the direction of propagation. Distance shifts for the three schemes were limited to $\lambda/4$, $\lambda/8$, and $\lambda/2$ respectively. The schemes and their results are shown in Figure 42.

The baseline arrangement for the SRR arrays is, of course, a periodic arrangement in all axes that maximizes both coupling and the associated width of the band gap in measured transmission. Disorder in both directions tested did not appear to affect the resonance frequency of the SRRs but did affect band width, which narrowed for aperiodic arrangements [3].

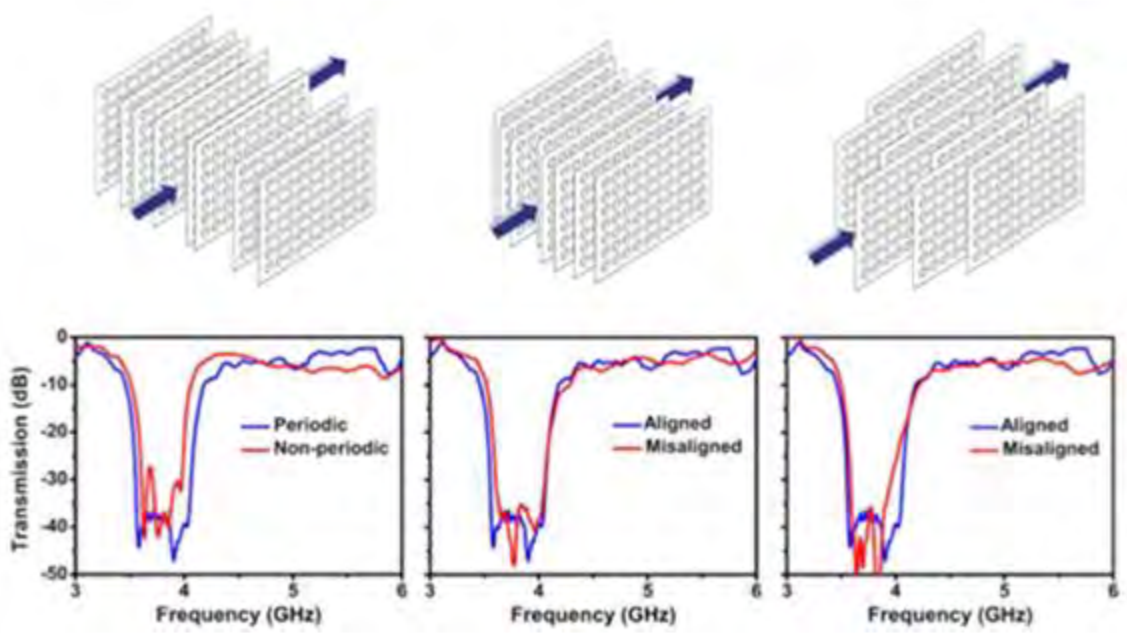

(a) (b) (c)

Figure 42. Depiction of three different types of disorder in [3]. (a) Disorder is applied in the *z*-direction only so that inter-plane spacing is disrupted. Distance shifts are limited to $\lambda/4$ or less. The result is narrowed bandwidth but an unaffected magnetic resonance gap. (b) Disorder is now applied in the *x*-direction only. Distance shifts are limited to $\lambda/8$ or less. (c) Disorder applied in (b) is now increased. Distance shifts are limited $\lambda/2$ or less. Measurements from (b) and (c) show that the disorder applied in the measured directions does not affect the magnetic resonance gap.

Intra-plane disorder was tested next. This disorder was characterized by a randomness parameter, $|\delta_r|$ [3]. Figure 43 shows the results of measurements for two different values of $|\delta_r|$ equal to $1/9$ and $1/5$ of the periodic lattice spacing. Intra-plane disorder appears to increase within the transmission band gap (3.55 – 4.10 GHz) [3]. It appears that disorder disrupts the magnetic resonance and consequently lower transmission that characterizes periodic arrangements.

The third graph, Figure 43, shows that a combination of inter- and intra-plane disorder or 3-D disorder leads to a superposition of effects. A simultaneous decrease in the band gap width and increase in transmission is identifiable in the data. The findings of this experiment may ultimately help explain differences simulated and experimental transmission data and provide a means to improve array construction techniques.

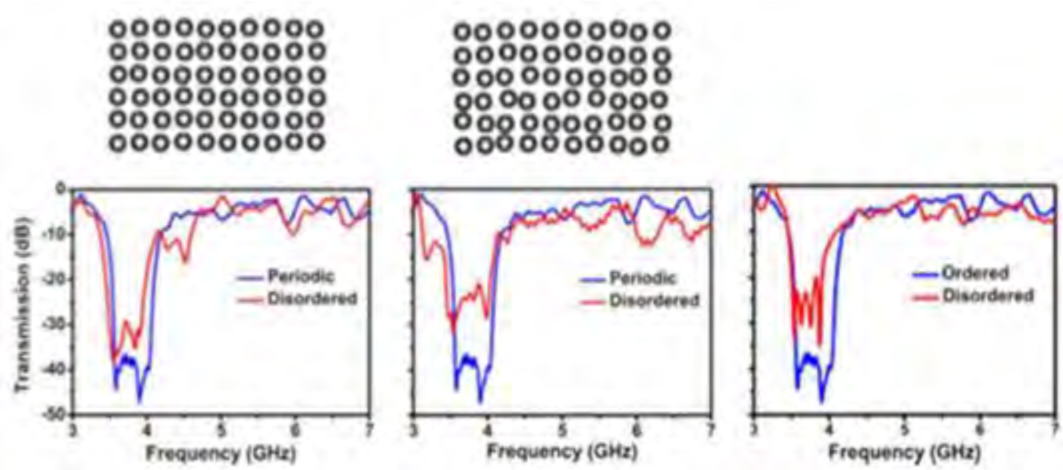

(a) (b) (c)

Figure 43. Depiction of the effects of intra-plane and total disorder in [3]. (a) Intra-plane disorder is implemented by setting $|\delta_r|$ equal to $1/9$ of the periodic lattice spacing. The result is increased transmission in the band increases. (b) Intra-plane disorder and transmission are greatly increased by increasing $|\delta_r|$ to $1/5$ of the periodic lattice spacing. (c) Inter-plane disorder is now added to the intra-plane disorder to show a superposition of effects.

III. Calculations and Models

3.1 Chapter Overview

This chapter describes the design and simulation of a metamaterial field concentrator. The first section of this chapter explains the design process and provides:

1. conceptual reasoning for the shape and size of the device,
2. mathematical descriptions of the relative constitutive parameters,
3. development of the periodic, planar array of MTM cells, and
4. constitutive parameter optimization.

The result of this section is a manufacturable design for a periodic, planar array structure composed of metamaterial cells. The geometry of each cell is optimized to produce constitutive parameters particular to the cell's coordinate location in an anisotropic, continuous design. This array serves as the basic, repeated unit for the field concentrator whose S-parameters will be measured with AFIT's focus beam measurement system.

The second section is devoted to presenting simulations of the field concentrator. The two simulation software packages described earlier, COMSOL® and CST MWS®, provide the simulation data for the ideal and achievable concentrator designs respectively. 2-D versions of the field concentrator and its components using the anisotropic constitutive parameter tensors are modeled with COMSOL®. 3-D constructions utilizing the metamaterial cells to homogenize the anisotropic design are modeled with CST MWS®.

Simulations from both software packages provide field, power, and S-parameter measurements needed to quantify the quality of the concentration achieved and to ensure that any constructed device will work. The conclusion after review of the simulation data is that field concentration is achievable with a stack of printed circuit boards (PCB) using copper etchings of metamaterial cells.

The third and final section briefly describes the construction of the physical model. Construction of the device was contracted out to a commercial manufacturer so this section highlights the standard manufacturing process. Various pictures are used to demonstrate the quality of the manufacturing.

3.2 Design and Optimization of Electromagnetic Field Concentration

This section describes the size, shape, and functionality of the various components comprising the field concentrator design. Derivations of mathematical equations necessary to implementing field concentration are included in this section, as is a discussion of the development of the metamaterial cells. This section then discusses the optimization effort that was appended to AFIT's rapid design method. This optimization process involves several steps including:

1. determine the design frequency, device scale, and metamaterial lattice spacing;
2. create a grid of cells covering the area defined by TO;
3. calculate the constitutive parameters for each cell;
4. use the rapid design process and a material selection process to find a cell/material combination providing the required constitutive parameters;
5. vary the size of the concentrator to optimize the match of constitutive parameters;
6. create the metamaterial cells in a design program such as CST MWS®; and
7. simulate and construct the homogenized approximation of the TO structure.

This section ends with a discussion of the optimization process invoked to tune the device and provide a best approximation to ideal concentration performance.

3.2.1 Initial Design Requirements.

The physical form of the concentrator was inspired, in part, by previous research [20, 51] that explored creating TO devices from designs involving concentric squares. These devices were created using transformations that are continuous at the device-free space boundaries but do not perturb the free space fields. The use of concentric shapes provides flexibility in designing the shape and efficiency of the concentrator.

Testing and manufacturing considerations also influenced the device design. The first consideration was that final product needed only to be a proof-of-concept instead of a refined, installation-ready product. Simplicity of the device was important. The second consideration was that the designed device must be testable with AFIT instrumentation.

AFIT's focus beam measurement system imposed a size limitation on the concentrator and its components because metamaterial cells should be size to be $\lambda/10$. The focus beam instrument is designed for operation from 2 – 18 GHz, works well at 10 GHz, and provides unreliable results for frequencies under 4 GHz due to the effects of spillover. The metamaterial cells should be designed to resonate within the frequency band of 4 – 18 GHz so a design-to frequency of 10 GHz was selected. A design or resonance frequency of 10 GHz sets the width of the repeated metamaterial cells and the lattice spacing (which will be the same distance), to be 3 mm.

The focus beam provides further restrictions on the size of the device under test (DUT) because it only produces plane waves over about a 5-inch-wide area for the 10

GHz illumination frequency. The field concentrator could be tested with non-planar waves but determination of the effectiveness of the device would be best accomplished by minimizing phase effects with predictable, easy to simulate, planar incident radiation. The limited area of plane waves produced by the focus beam system restricts the dimensions of the concentrator transverse to the path of propagation of the beam. The desire to exploit the plane waves developed by the focus beam further restricts the dimension of the device parallel to the path of propagation. The DUT should be long enough that its position can be easily adjusted longitudinal axis while simultaneously short enough that when the device is held in place for testing it is not cantilevered to the point of where it might dip down.

3.2.2 Application of Transformation Optics Mathematics.

If field concentration is designed within a restricted area of free space then there must simultaneously exist coordinate expansion and compression in that area. Cloak and concentrator designs such as those in [20, 51] use concentric shape devices to define these expansion and compression sections. The most common shapes used to implement coordinate transformations are squares and cylinders. A simple square shape was chosen for this thesis.

Design of the concentric square field concentrator used in this thesis is based on of embedded transformations because its designed operation imposes a field effect on the surrounding environment. The proposed device is developed through use of a process depicted in Figure 44. The use of one quadrant and not the full square design allows for embedded transformations. A rectangle-shaped device is cut from the single quadrant because it is easy to manufacture, hold, and shift in the focus beam test fixture.

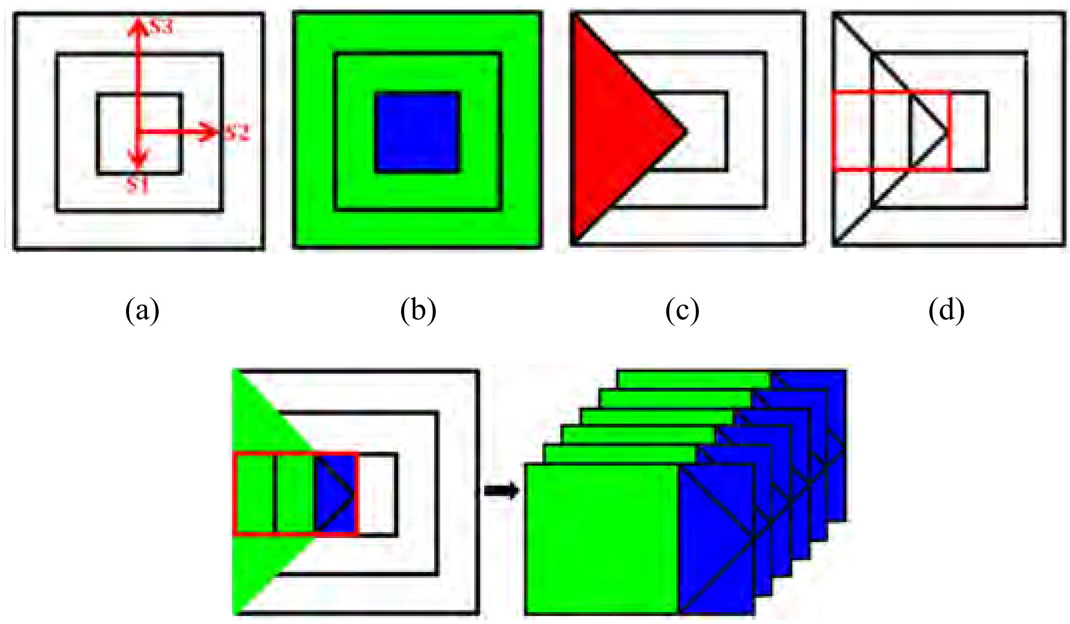

(e)

Figure 44. Basic design of the field concentrator. (a) Design was based on a design of three concentric squares of increasing half-width: *S1, S2,* and *S3.* (b) Innermost region, colored blue, is used to compress the fields while the outer two squares provide the expansion. (c) Only one quadrant of the square design is manufactured. (d) Simplest manufacturable geometry from one quadrant is the rectangular board drawn with a red line. (e) Superposition of (b) and (d) show which areas of the manufactured design will be compression and which will be expansion. (f) Manufactured device is an array of parallel, stacked rectangular boards.

The first section of the concentrator encountered by the incident electromagnetic field is the expansion section. The total expansion region was designed to include both regions 2 and 3 to minimize the compression area and therefore maximize the field concentration of the coordinate transformation. The second section represents region 1 and is composed of triangular sections, each belonging to different quadrants of the original concentric rectangle design.

The coordinate transformation equations for each section are based on the simplest of transformations: linear, Cartesian-to-Cartesian coordinate transformations such as those presented in [74]. These transformations are built on the assumption of linearly polarized, perpendicularly incident transverse electromagnetic (TEM) waves. Given this assumption, the complexity of the coordinate transformation was further simplified by assuming *z*-invariance and 1-D expansion and compression limited to the *y*-directed electric field.

The transformation equations are written to provide continuity of the incident field at the free space-expansion and expansion-compression boundaries. The amount of expansion or contraction are controlled by a ratio based on all three regions, written in its simplified form as

$$\left\lfloor \frac{S3-S1}{S3-S2}-1 \right\rfloor \; or \; \frac{S2-S1}{S3-S2} \tag{66}$$

where $S1$ is the half the width of the innermost rectangle, $S2$ is the half the width of the middle rectangle, and $S3$ is the half the width of the outermost rectangle. These geometrical terms can be written as $S1:S2:S3,$ the S-ratio, and define the quality of the field concentration that is engineered. The equations using the S-ratio are written to provide concentration of the incident fields immediately after the end of the compression section and not at the free space-compression boundary. The intent of this design decision is to realize field concentration in real space. An arbitrary spacing of 1.5% of $S1$ provides the separation.

Borrowing from [74], the transformation equations presented here provide the same general form with the exception of the use of Equation (66) for the modulation coefficient and the continuity and spacing considerations just previously defined. In terms of the generalized S-ratio, the set of equations describing coordinate expansion at a point (x, y, z) in regions 2 and 3 can be written with respect to both free space and the TO origin between the expansion and compression regions as

$$x'_{\exp} = x, \tag{67a}$$

$$y'_{\exp} = y + y\left(\frac{S2 - S1}{S3 - S2}\right)\left(\frac{x + S3 - S1}{S3 - S2}\right), \tag{67b}$$

$$z'_{\exp} = z. \tag{67c}$$

The generalized form of the equation for the any triangular compression region is first written with respect to the expansion region the local coordinate origin at the center of the interface for the expansion and middle compression regions. The equations for all three compression regions must be rewritten with respect to free-space to provide the same reference for determining the constitutive parameters used for the expansion section. The conversion of $y'_{\exp}$ in the compression equations leads to a set of three complicated equations. The equation for the central triangular compression region (middle compression) is

$$x'_{midcomp} = x, \tag{68a}$$

$$y'_{midcomp} = \left(\frac{S1 + 0.015S1 - x}{S1 + 0.015S1}\right)\left(y + y\left(\frac{S2 - S1}{S3 - S2}\right)\left(\frac{x + S3 - S1}{S3 - S2}\right)\right), \tag{68b}$$

$$z'_{midcomp} = z. \tag{68c}$$

The top and bottom compression areas belong to quadrants rotated $\pm 90^{\circ}$ from the middle compression region. The equations for each of these sections can be obtained by applying the appropriate Euclidean rotation to Equation (68). In the Cartesian coordinate system, the 2-D rotation matrix is

$$\boldsymbol{R} = \begin{pmatrix} \cos(\varphi) & -\sin(\varphi) \\ \sin(\varphi) & \cos(\varphi) \end{pmatrix} \tag{69}$$

where φ represents a clockwise rotation about the origin. A 90° rotation produces the compression equations for the top compression triangle written as

$$x'_{topcomp} = \left(\frac{S1+0.015S1+y}{S1+0.015S1}\right)\left(x+x\left(\frac{S2-S1}{S3-S2}\right)\left(\frac{-y+S3-S1}{S3-S2}\right)\right), \tag{70a}$$

$$y'_{topcomp} = y, \tag{70b}$$

$$z'_{topcomp} = z. \tag{70c}$$

Likewise, a -90° rotation produces the equations for the bottom compression triangle written as

$$x'_{botcomp} = \left(\frac{S1+0.015S1-y}{S1+0.015S1}\right)\left(x+x\left(\frac{S2-S1}{S3-S2}\right)\left(\frac{y+S3-S1}{S3-S2}\right)\right), \tag{71a}$$

$$y'_{botcomp} = y, \tag{71b}$$

$$z'_{botcomp} = z. \tag{71c}$$

The relative permittivity and permeability tensors can be determined from the sets of equations presented for the expansion and compression sections by first calculating their respective Jacobian matrices. Next, the rank 2 tensors representing the relative permittivity and permeability of the transformed space can be determined using

Equations (43). The non-conformal transformation results in a symmetric tensor with coupled (xy) terms. The form invariance of Maxwell's equations ensures corresponding entries of permittivity and permeability are the same

$$\varepsilon_r = \mu_r = \begin{pmatrix} \varepsilon_{xx} & \varepsilon_{xy} & 0 \\ \varepsilon_{xy} & \varepsilon_{yy} & 0 \\ 0 & 0 & \varepsilon_{zz} \end{pmatrix}. \tag{72}$$

The task of creating the relative constitutive parameters requires minimal work for the expansion section. Slightly more effort is required to write these terms for the three sections of the compression region. First, the coordinate transformations for these areas are written with respect to the expansion section to maintain continuity in the y component at the inter-region transition boundary. Second, the constitutive parameters for each compression section must be written with respect to free space. Substitution of Equations (67) into Equations (68), Equations (70), and Equations (71) produces equations that,in conjunction with Equations (43), yields sets of transformation equations that will provide constitutive parameters relative to free space for each region. The resulting sets of equations for the expansion and compression sections describe frequency-independent transformations.

3.2.3 Metamaterial Unit Cell Array Design.

The coordinate transformations described define an anisotropic material with smooth and spatially variant relative constitutive parameters. Currrently, there is no means to produce such an anisotropic material. The physical realization of such a material may only be accomplished by discretizing the material to create locally homogeneous areas of constant relative constitutive parameters achieved with tuned metamaterial cells.

The relative parameters are frequency independent but the metamaterial cells used to create these parameters are not. The lattice periodicity defined by the cell dimensions is determined by the concentrator's designed resonant frequency and is found using the metamaterial standard, $\lambda/10$. The circuit traces associated with each cell must be tuned within a frequency band about the device's resonant frequency to create relative parameters specific to the coordinate location of that particular metamaterial cell. These will be the constitutive parameters at same coordinate location in the anisotriopic material.

The concentrator built for this thesis was constructed for operation at 10 GHz so, as was previously mentioned, intra- and inter-board lattice periodicity was set at 3 mm. Operation at 10 GHz provides an optimal middle ground for creating a manufacturable, design that provides a good, discrete-gradient approximation to the smooth, continuous spatially variant anisotropic relative parameters resultant from the coordinate transformations. A higher frequency would require a smaller lattice period that would better approximate the continuous variation in parameters at the cost of both smaller traces that might be harder to manufacture and an increase in modeling and design time as the number of cells rises. A lower frequency would reduce modeling and design time due to the presence of fewer cells and potentially larger traces. Unfortunately the decrease in cell counts will result in a poor approximation to the continuous parameter variation and a degraded ability to concentrate incident electromagnetic fields.

The metamaterial cells used to create a homogenous approximation of the anisotropic concentrator material were designed with AFIT's rapid design method. This method relies on magnetically resonant cells wherein all current is produced by H_z and travels around the trace. These cells can be oriented in either of two possible directions. Vertically oriented traces with induced push-push currents allow the vertically directed E_y to couple cells in the *y*-direction and leads to extraction of ε_y and μ_z. A horizontally oriented trace would result in extraction of ε_x and μ_z and would have non-resonant type behavior. Due to the limitations of the rapid design code, only one value of permittivity can be extracted at a time so it is not possible to design a cell to match the tensor of Equation (72) required for an anisotropic material. The desire to induce a compression of E_y guided the choice to limit testing to vertically oriented traces.

Designing for a subset of parameters related to the incident radiation is common in TO applications [20, 55]. These research efforts have also taken these parameter subsets and further reduced their forms to produce simpler equations that still have the same dispersion and therefore the same wave-material interactions as the original subsets [55]. Even when the permittivity-permeability products of the reduced set, e.g. $\varepsilon_y\mu_z$ and $\varepsilon_y\mu_x$ for the reduced parameter set $\{\varepsilon_y, \mu_x, \mu_z\}$ equal the products from the original subset, scattering can result. Therefore parameter simplification was not be used in this research effort, lest increased scattering prevent any achievable concentration.

The rapid design process was used with a library of cells representing all geometric combinations of the terms $\{a_\theta, r, s\}$ where a_θ, the inter-array or board spacing (also the inter-cell spacing), was set to 3 mm to maintain the standard $\lambda/10$ spacing for 10 GHz. All cells shared a designed a trace width of 2 mm. The parameters ε_y and μ_z were then extracted from the S-parameters. The standard rapid design procedure next dictated that modified or local parameters first be created from the extracted data and second be used for curve-fitting and the determination of the expansion coefficients.

The driving goal of implementing the rapid design process was to find cell geometries that would create extracted or effective relative constitutive parameters equal to the relative parameters dictated by the coordinate transformations. Unfortunately, the coordinate transformations only provide real values of the constitutive parameters whereas the modified/local parameters normally used to indirectly link cell geometries to effective relative constitutive parameters are complex-valued. Given the impracticality of arbitrarily estimating the material loss (the imaginary component), loss was ignored and the modified parameters were written in terms of the relative parameters created by the transformations.

The form of the extracted permeability or resonant parameter curve was conducive to curve fitting with the Lorentz model so the modified permeability was set equal to the transformed permeability. Unfortunately, the form of the permittivity curve extracted from the library's cells was not Lorentzian. This was expected for the nonresonant parameter. The form of the modified permittivity was altered to match a shifting and reflection of the relative permittivity. The modified parameters of the extracted data were thus written as

$$\varepsilon_m = 5 - \varepsilon_r, \tag{73a}$$

$$\mu_m = \mu_r. \tag{73b}$$

After Lorentz curves were fitted, the necessary terms of each model were expanded into geometric series and the coefficients of those series were solved for. The benefit of using the transformed relative parameters and not Equations (50) to define the modified parameters is that the geometry of the cells can be directly tied to an achievable value of the relative constitutive parameters.

The opportunity to directly link the relative and modified constitutive parameters associated with each cell's geometry further motivated the goal of exactly matching the cells' relative parameters to the ideal parameters derived from the coordinate transformation. This goal involved minimizing scattering, electromagnetic coupling, and differences between the achievable constitutive parameters of the metamaterial cells and predicted parameters from the coordinate transformation. Optimizing both the constitutive parameter matching of the rapid design process and the physical construction of the concentrator pursued allowed the aforementioned minimization tasks.

Optimizing the matching of constitutive parameters was the first and most important task. Developing metamaterial cells that provided the relative parameters from the coordinate transformation involved balancing many considerations including selecting the proper set of geometric variables, selecting the proper circuit board material and thickness as well as selecting the best S-ratio for the compression and expansion sections. First, the greater the number of variables selected and the greater the number of possible values per variable, the greater the number of geometry combinations.

More geometry combinations may lead to a greater likelihood of matching the ideal constitutive parameters with the relative parameters of a cell. The cost of increasing the size of the cell library is an increase in the time it takes to optimize the cell geometry. Since the arms of the traces provide the major tuning of the parameters, a cell library could be limited by increasing the number of arm lengths tested in the geometry set, s. Simplicity would suggest creating a set, s, with as few entries as possible to provide good constitutive parameter matches. The total number of cells for this thesis was predicated on the selection of a single a_θ value and dictated by the combinations of the terms r and s which were set to {0.1 0.17 0.25 0.3} and {0.25 0.5 0.75 1.0} mm respectively. Therefore a total 16 cells were used.

Second, selection of the proper backing for the metamaterial cells was important because the dielectric constant and thickness of the material alter the resonance and achievable constitutive parameters of the cell/backing combination. There are a number of different material/thickness combinations available for PCB. The selection must take into account the manner in which the PCB will be used and the range of constitutive parameters it will allow. A large array of stacked, parallel PCB might be an application best-suited for a rigid material, especially since board bending and warping can adversely effect the electromagnetic characteristics of a trace.

Differences in dielectric constants between materials are not an overriding consideration of optimization because such differences can be compensated by a change in the width of the cell traces. For example, a material with large loss will reduce a cell resonance but reducing the cell width can compensate for this drop in resonance. Board material selection for this thesis was simplified by considering the popular, easily accessible board materials: 0.13 mm TLY-5 and 0.787 mm FR4. Figure 45 and 46 show plots of the ranges of achievable real and imaginary permittivity for TLY-5 and the set

$\{a_\theta, r, s\}$. There are more than 16 points plotted because for each geometric variable in the set there is a vector of possible values defined by the low and high values of the set and some interpolation step set by the rapid design code. All combinations of the numbers in these vectors are plotted. Table 1 shows that the achievable values of constitutive parameters for 0.13 mm TLY-5 are not low enough.

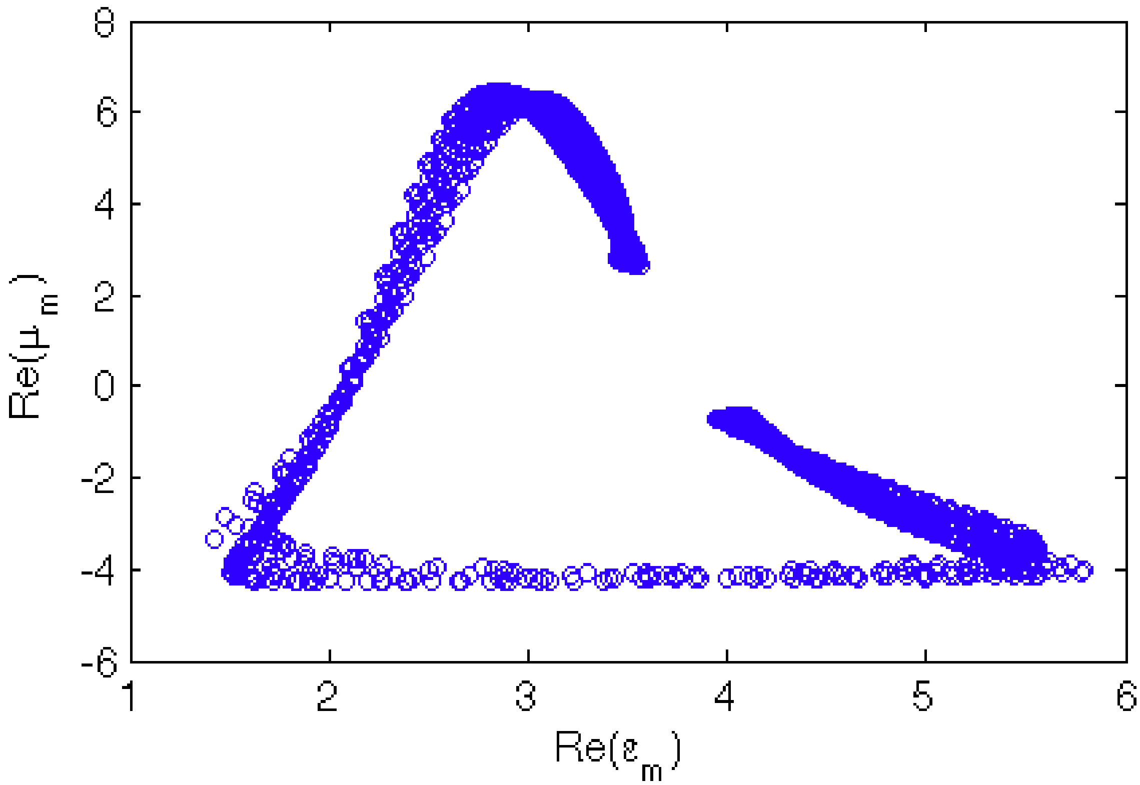

Figure 45. Plot of the real, achievable constitutive parameters for TLY-5.

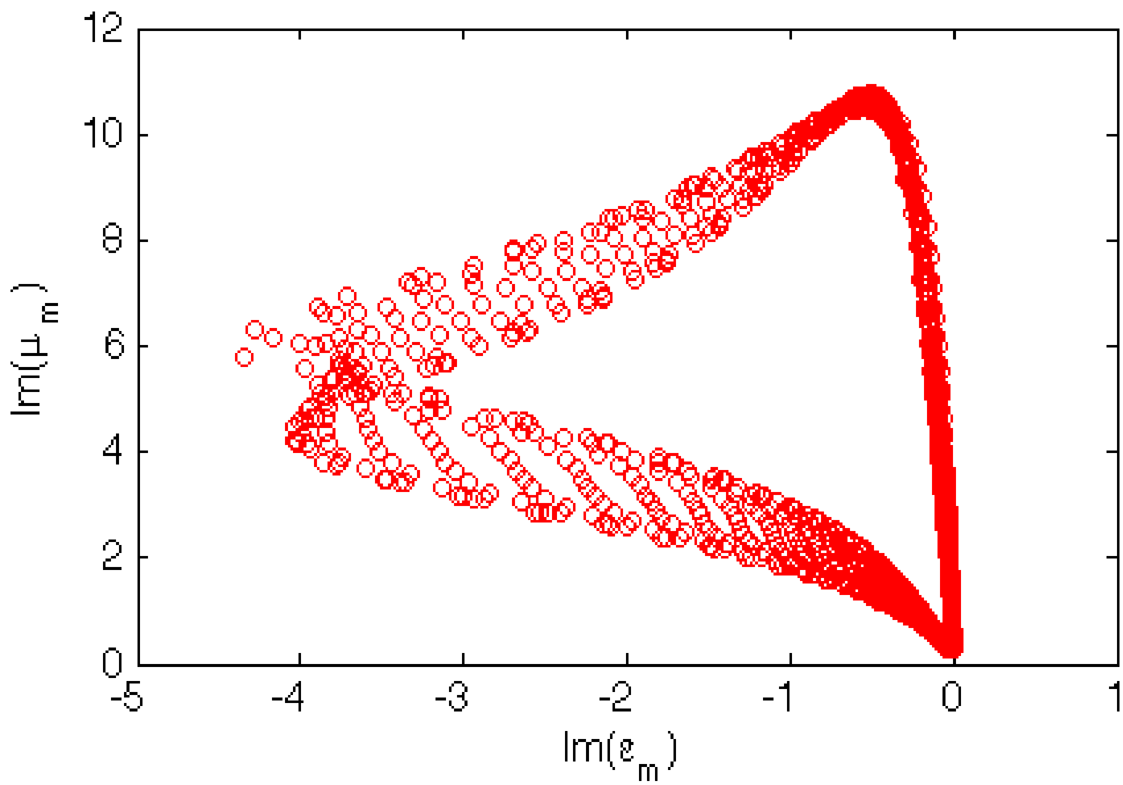

Figure 46. Plot of the imaginary, achievable constitutive parameters for TLY-5.

Table 1. Low and high values of constitutive parameters required by TO.

Section	Low Value	High Value
Expansion	1.0062	1.3784
Middle Compression	0.1860	2.1551
Top Compression	0.4250	0.6663
Bottom Compression	0.4250	0.6663

Another set of plots were made for 0.787 mm FR4. Figures 47 and 48 show that a 0.787 mm FR4 backing of the 16 cells clearly outperforms TLY-5 in constitutive parameter matching. The values of constitutive parameters are centered at or near 0. It is particularly noteworthy to see that the associated values of imaginary consistutive parameters are low because imaginary values of consistitutive parameters were not matched during S-ratio optimization and high values are associated with loss due to energy dissipation within a material.

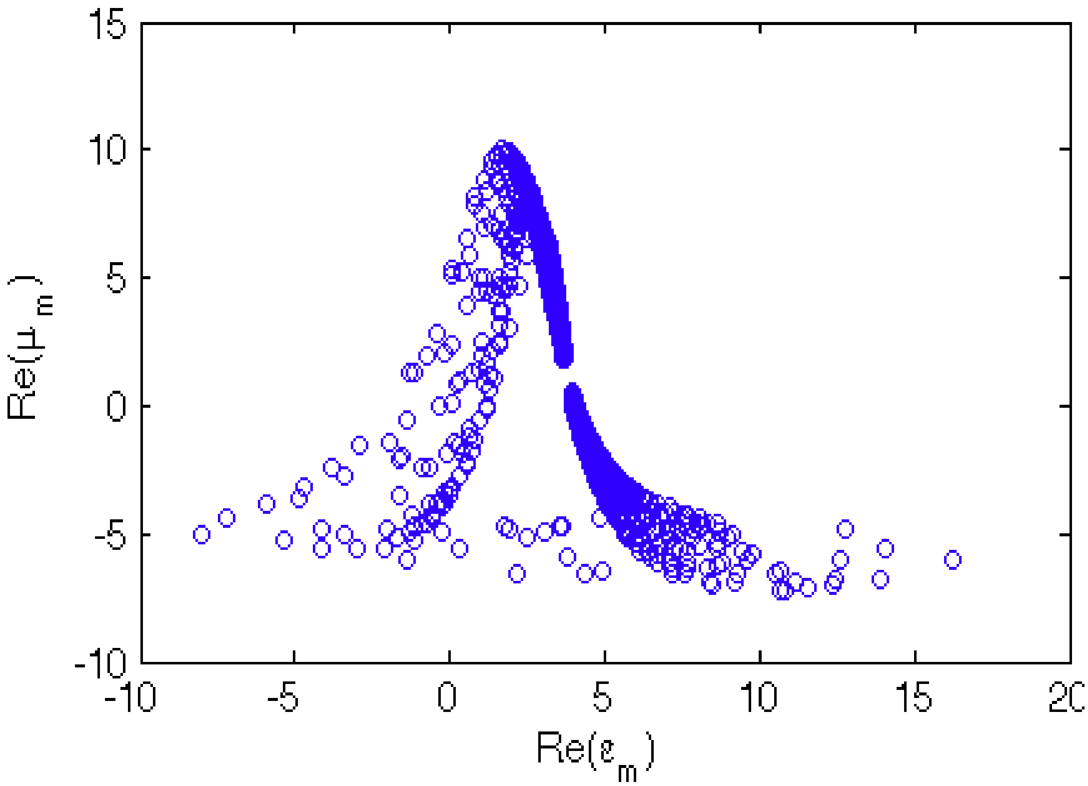

Figure 47. Plot of the real, achievable constitutive parameters for FR4.

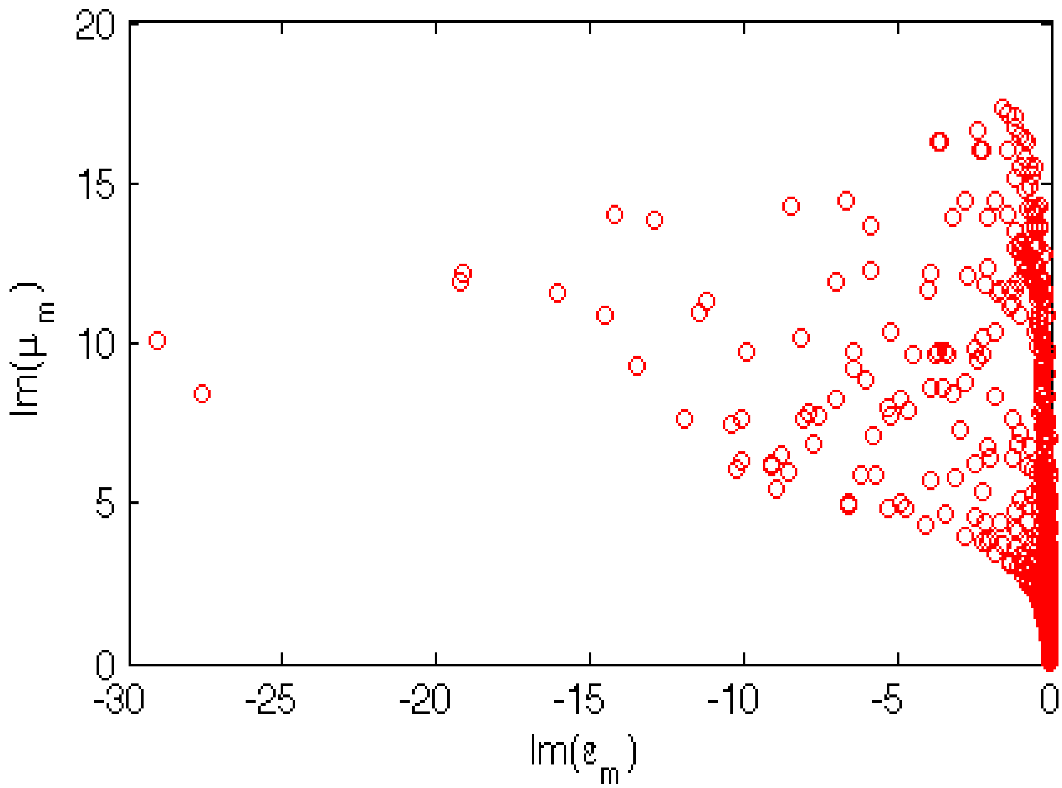

Figure 48. Plot of the imaginary, achievable constitutive parameters for FR4.

Third, selection of the best S-ratio was based on evaluating the distance between the transformation and real-valued extracted parameters for different circuit board materials and thicknesses. The minimum, maximum, and mean difference was calculated for each compression and expansion region. A total of 455 combinations were tested for possible S-ratio values ranging from 1 – 16. The results of the combinations were ordered with respect to the mean constitutive parameter value.

Table 2 – 5 show the top ratios selected for middle compression and expansion sections and provide a visual clue as to how optimization of a ratio for one region affects another region. The results observed in the tables highlight several observations made

during S-ratio optimization. Namely, expansion and compression in the central triangle (middle compression), are not optimized by the same S-ratio.

First, minimizing the difference in the middle compression region can improve or degrade the matching of parameters in the expansion region by by up to 3%. Minimizing the difference in the expansion region degrades the matching of parameters in the middle compression region by up to 15%. Second, middle compression can be optimized at the cost of slight degradation in the performance of the top and bottom triangles (top and bottom compression, respectively). Third, the expansion section can only be optimized at the cost of large degradation in the matching for the top and bottom compression regions. Note, however, that selection of the best ratio is further complicated by the fact that these relationships mentioned here are themselves inexact. Selection of the second best match in region 'A' should lead to a better match in region 'B' although this is not always true.

Table 2. Ratios optimized for the middle compression region and their associated constitutive parameters. The ratios shown below are the 10 best ratios for the middle compression region. Note that variation in the mean difference among all the ratios is only 0.0542 or 5.42% error.

Ratio	Mean	Low Value	High Value
1:3:12	0.8201	0.5573	0.9446
1:3:11	0.8257	0.4978	0.9445
1:2:6	0.8285	0.5019	0.9445
1:4:15	0.8516	0.6486	0.9445
1:2:15	0.8618	0.6589	0.9658
2:3:9	0.8640	0.3329	1.2949
2:4:15	0.8686	0.3153	1.4768
2:3:13	0.8738	0.4059	1.4581
1:3:10	0.8738	0.7386	0.9445
2:3:12	0.8742	0.4042	1.3269

Table 3. Ratios optimized for the middle compression region paired with the constitutive parameters of the expansion section. Note that the mean values obtained for the expansion region for the ratios developed from the middle compression region are similar. This matching would not exist if the middle compression ratios were used for the top and bottom compression regions.

Ratio	Mean	Low Value	High Value
1:3:12	0.8402	0.6534	0.9877
1:3:11	0.8040	0.4413	1.0034
1:2:6	0.7949	0.3797	0.9960
1:4:15	0.7724	0.4236	0.9909
1:2:15	0.7832	0.4738	1.0689
2:3:9	0.8661	0.6258	0.9967
2:4:15	0.8524	0.6199	1.0071
2:3:13	0.8799	0.6764	0.9442
1:3:10	0.7563	0.4177	0.9937
2:3:12	0.8789	0.6946	0.9442

Table 4. Ratios optimized for the expansion compression region and their associated constitutive parameters. The ratios shown below are the 10 best ratios for the expansion compression region. Note that variation in the mean difference among all the rations is only 0.0104 or 1.04% error.

Ratio	Mean	Low Value	High Value
7:8:12	0.7456	0.3775	1.0557
8:9:13	0.7475	0.3699	1.2968
6:8:15	0.7477	0.3679	1.0065
5:7:14	0.7505	0.3731	1.0065
6:7:11	0.7510	0.3775	1.0071
4:6:13	0.7528	0.3731	1.0065
2:5:15	0.7541	0.3741	0.9923
1:4:14	0.7544	0.3916	0.9844
3:5:12	0.7547	0.3790	1.0065
2:4:11	0.7560	0.3790	0.9937

Table 5. Ratios optimized for the expansion compression region paired with the constitutive parameters of the middle compression region. Note that the mean values obtained for the middle compression region from the ratios developed from the expansion region are off by around 0.15 but are still relatively close. This matching would be far worse if the ratios developed for the expansion region were used for the top and bottom compression regions.

Ratio	Mean	Low Value	High Value
7:8:12	0.9122	0.1150	1.7056
8:9:13	0.9045	0.1089	1.7055
6:8:15	0.9447	0.0952	1.9635
5:7:14	0.9378	0.1924	1.7328
6:7:11	0.9191	0.1235	1.7044
4:6:13	0.9441	0.2897	1.9267
2:5:15	0.9350	0.5372	1.6202
1:4:14	0.8934	0.7476	0.9592
3:5:12	0.9572	0.4258	2.0581
2:4:11	0.9293	0.4245	1.6760

It is apparent that the complex relationship between the various regions of the field concentrator with respect to variation in the S-ratio necessitates a complex algorithm. However, this complexity would defeat the simplicity in the selection of the minimum, maximum, and mean criteria without necessarily providing significantly better optimized relative constitutive parameters.

In sum, there is no perfect ratio that may be picked. The top expansion and middle compression ratios have similar mean deviations from the ideal constitutive parameter values and each ratio selected requires a performance tradeoff in other regions. Other ratios cause constitutive parameter mismatches of 10,000% or more that would cause even even worse performance in the other regions. The top and bottom compression regions are best suited for compressing and directing fields normally incident to each respective surface. Since the incident plane waves should be normally incident or incident at acute angles, the expansion and middle compression blocks will provide the primary source of concentration. The decision was made to optimize the S-ratio for the expansion section. Based on a qualtitative analysis of mean error in other regions based on an optimized expansion ratio, the S-ratio selected was 4:6:13.

Addressing the physical construction of the concentrator was the second major method for obtaining an optimized electromagnetic field concentration. Aside from the sizing of the concentrator and its placement in the focus beam system, as was previously discussed, there should be a concerted effort to minimize construction error and enhancement efforts to produce concentration.

Construction error can take the form of traces not manufactured according to the designed arm length and radius, rough or jagged trace etching, cell placement on the PCB, and the position of the PCB with respect to each other. Traces not manufactured to specification can result in interrupted current flow or altered capacitance and inductance values, all of which can alter the resonance of the affected cells. Since each cell is designed to produce particular constitutive parameters at 10 GHz, resonance at a different frequency will not provide the designed constitutive parameters and will adversely alter the field propagation.

Alignment of the cells and hence the traces both on a circuit board and between the PCB can affect cell-to-cell coupling which will also affect resonant behavior. Operation at a particular magnetic resonance can be enforced by minimizing magnetoelectric coupling which can shift the resonance of the cells and hence the permittivity or permeability that that they produce [33]. This coupling can be minimized by rotating the orientation of all cells in a row 180° with respect to the adjoining upper and lower rows, as seen in later figures generated with CST MWS®. Clearly, there will still be coupling between rows, particularly because two vertically adjacent cells may have different geometries and hence equivalent inductance and capacitance values. However, this method has been used in previous research [55] and is incorporated as standard practice for this thesis.

Adhering to other design requirements can also control coupling and hence magnetic resonance. The set of planar arrays forming the device should have their edges aligned so that the cells in each row are perfectly aligned and spaced $\lambda/10$ apart in all dimensions. The alignment of cells on each board and between boards will minimize inter- and intra-plane disorder, thus maximizing magnetic resonance at 10 GHz [3].

In addition to ensuring the proper resonant response, cell placement strategies can also contribute to concentration by providing a finer constitutive parameter gradient for directing incident fields. Cells should be designed for a metamaterial size of $\lambda/10$ but can be made smaller, leading to a larger cell count as was previously discussed. Cells can also be arranged to better use the space on each circuit board. The coordinate transformation equations were designed to center the concentration spot behind the TO device therefore cells were laid down on the centerline of the device and laid out towards the edges, as shown in Figure 49. The result was more cells in the middle compression region within a set distance from the concentration point.

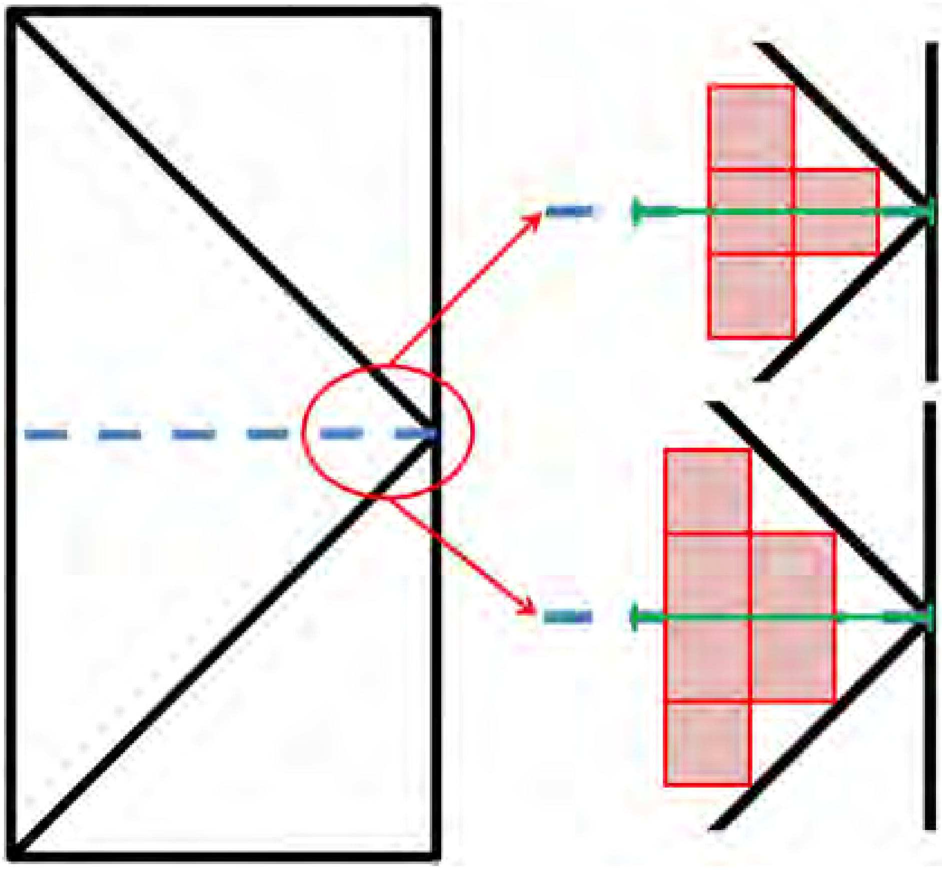

Figure 49. Depiction of various methods of cell stacking. Note that using a pattern that stacks the cells on the centerline places more cells in a set distance marked by the horizontal green line. More cells withing a given area means a better approximation of an anisotropic material.

3.3 Modeling and Simulation of Electromagnetic Field Concentration

Modeling and simulation of the metamaterial was conducted for the ideal, anisotropic dielectric material and for the homogenized approximation using an array of periodically arranged metamaterial cells. All simulations were conducted on AFIT's low observable radar and electromagnetic network. The network computers are Hewlett Packard® Z800 workstations with two Intel Xeon® quad-core 3 GHz CPUs with 48 GB RAM running Microsoft Windows® 7 64bit operating system.

3.3.1 Anisotropic Compression and Expansion Components.

Modeling and simulation of the anisotropic dielectric material resulting from the coordinate transformations was completed with COMSOL®. Simulations conducted for this thesis with COMSOL® share several characteristics including:

1. frequency domain analysis,
2. a 2-D simulation environment,
3. single layer modeling,
4. an expansion/compression component modeled in free space,
5. x-directed TE fields described by E_y,
6. a bounding box of PML one λ thick.

The primary goal of the simulations was to prove the compression or expansion equations were developed correctly and that the electromagnetic fields correspondingly compress or expand. Initial simulations were conducted with simple setups designed to produce easily identifiable concentration. As such, these initial simulations standards are the simplest whole-number S-ratio (1:2:3) using a meter scale and 4 GHz incident plane waves. A frequency of 4 GHz was selected because it represents the largest reliably measurable incident wavelength produced by the focus beam measurement system. Simulation of the compression stages was conducted first to ensure the primary function of the field concentrator would be achievable.

3.3.1.1 Compression Models.

Compression is achieved by using regions from three separate quadrants of a concentric rectangle design. Each region was tested separately and then together.

3.3.1.1.1 Middle Compression.

The simulation setup for middle compression region and a plot of the normalized *y*-directed electric field or E_y for the initial simulation conditions is shown in Figure 50. Per the design of the coordinate transformations, E_y is consolidated to a small region just past the back of the compression material. The transformations are designed to focus the incident fields to a point but as with glass lenses, diffraction-limited focusing is noted.

The completed simulation shows three paths of compression that can be seen within the material before one primary concentration region develops outside the material. These points are due to the three primary trajectories of fields in a material. One set of fields close to the horizontal, bisecting centerline of the block pass through with no or little perturbation. These fields account for the central point of field compression. Another set of fields is incident on the block at a large, positive vertical displacement with respect to the centerline and is bent towards the center. These fields create the upper point of field compression. By symmetry, the bottom point is formed from fields incident on the block at a large, vertical, negative displacement with respect to the centerline.

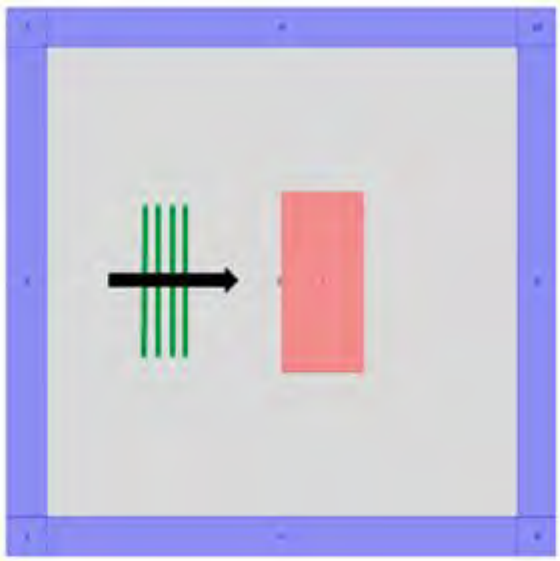

(a)

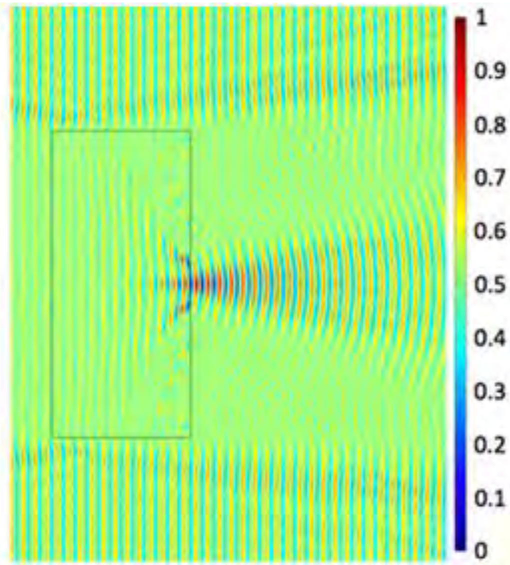

(b)

Figure 50. Middle compression simulation setup and its associated normalized *y*-directed electric field concentration for the initial simulation standards. (a) Test setup. (b) Normalized *y*-directed electric field distribution.

Figure 51 shows that concentration effect applies to the entire incident plane wave because the *z*-directed magnetic field or H_z is also compressed along the *y* coordinate. Diffraction at the dielectric-free space interface where the concentration is located explains the field and power spreading that occurs with both the electric and magnetic field components. Reflections off the top and bottom edges in both plots are expected for a compression block of finite size with top and bottom faces that are not mathematically continuous with free space and thus not impedance matched.

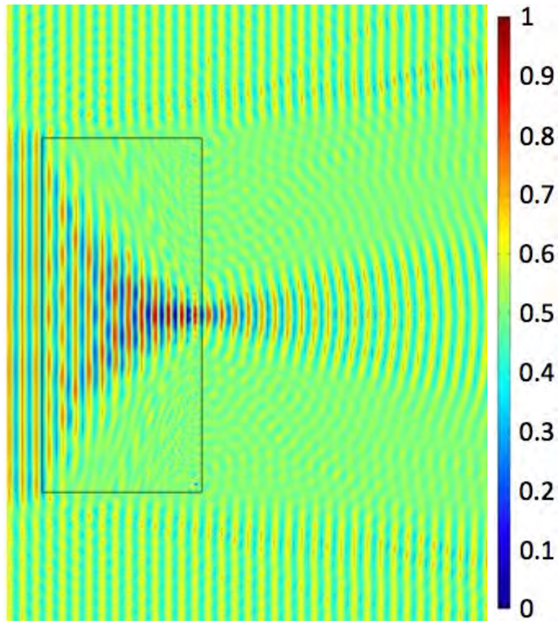

Figure 51. Normalized *z*-directed magnetic field distribution associated with the middle compression region for the initial simulation standards.

A plot of the uniform density time-average power flow shown in Figure 52 below confirms the concentration of electric and magnetic fields. Power appears to flow through the center of the block. The power flow shows that not all power is confined to the path of concentration though. Fields appear to meander out of the material and diffract away without contributing to the concentration. The power flow demonstrates the limitations of applying the transformation with a finite-sized compression region whose top and bottom boundaries are not impedance matched with the surrounding environment. The transformation is designed to take fields entering through the front of the compression region and compress them. However, incident and diffracted fields entering the compression region through the sides create interference patterns. The result of this interference in regions outside the main path of compression is the appearance of meandering power flow.

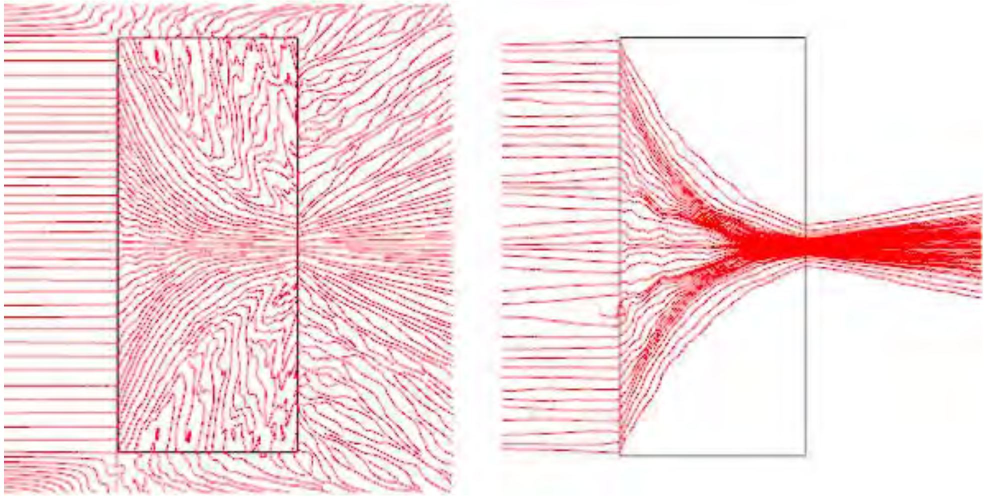

(a) (b)

Figure 52. Depiction of the time-average power flow associated with the middle compression region for the initial simulation standards. (a) Uniform density power flow. Power flowing in through the sides causes interference. (b) Path of power flowing through the left face. The lines outside the region are not entirely straight and even due to constructive and destructive wave interactions with the finite-sized region.

After proving concentration with the anisotropic, spatially-variant middle compression region, a triangular wedge was simulated as seen in Figure 53. Simulation of the triangular middle compression region confirms that the top and bottom portions of the middle compression block have little influence on the concentration for *x*-directed plane waves, per the design of the TO equations. Figure 53 shows the triangular wedge of middle compression material produces a similar concentration of E_y as the middle compression block, shown above in Figure 50. There appears to be a greater geometrical compression of the waves with respect to the entire middle block although the region of higher normalized fields seems to have reduced. Figure 54 below reveals the uniform density time-average power flow that confirms the concentration displayed in Figure 53.

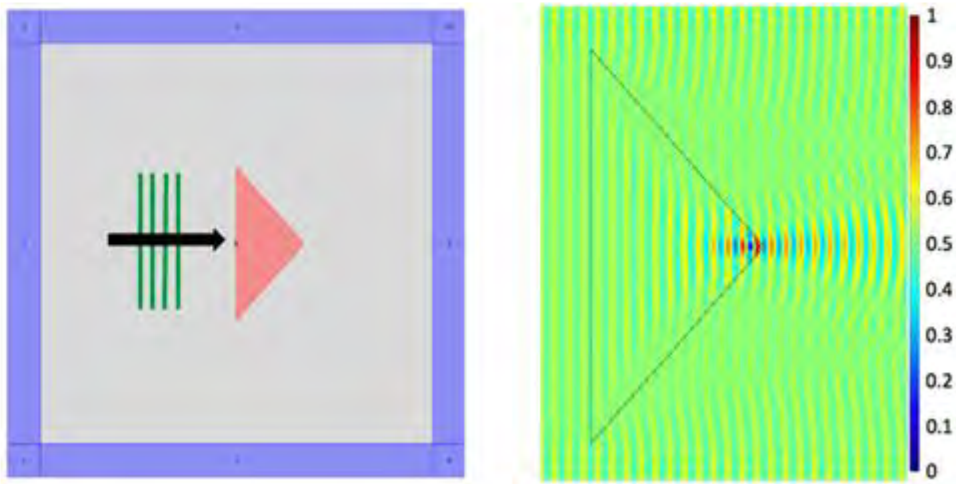

(a) (b)

Figure 53. Middle compression triangle simulation setup and its associated normalized *y*-directed electric field concentration for the initial simulation standards. (a) Test setup. (b) Normalized *y*-directed electric field distribution.

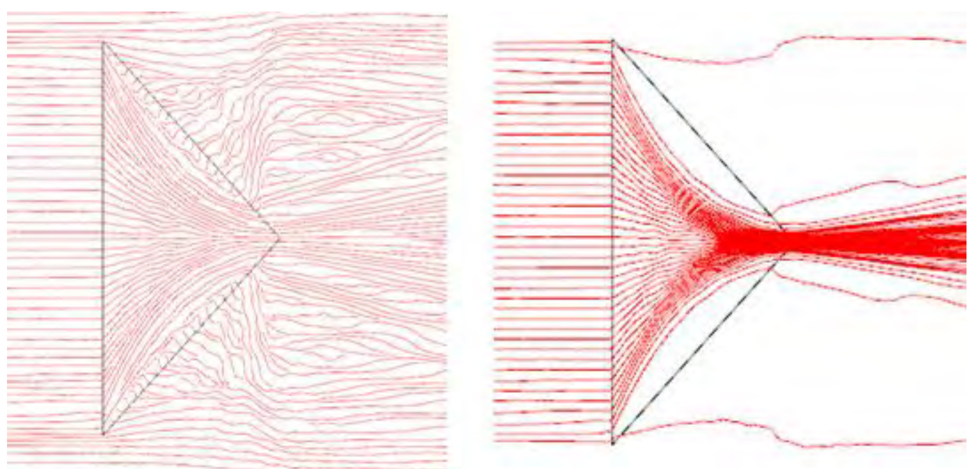

(a) (b)

Figure 54. Depiction of the time-average power flow associated with the middle compression triangle for the initial simulation standards. (a) Uniform power flow. (b) Power flow over the left boundary.

3.3.1.1.2 Top and Bottom Compression.

The compression region is composed of three quadrants, each with a different set of equations. The middle quadrant was shown to concentrate x-directed incident plane waves. The two other quadrants formed from the top and bottom compression regions work best for $+z$- and $-z$-directed incident plane waves respectively. In order to understand their contribution to the operation of the field concentrator, these quadrants are simulated. First, the compression blocks from which these quadrants are formed were simulated. The test setups for these simulations are displayed in Figure 55.

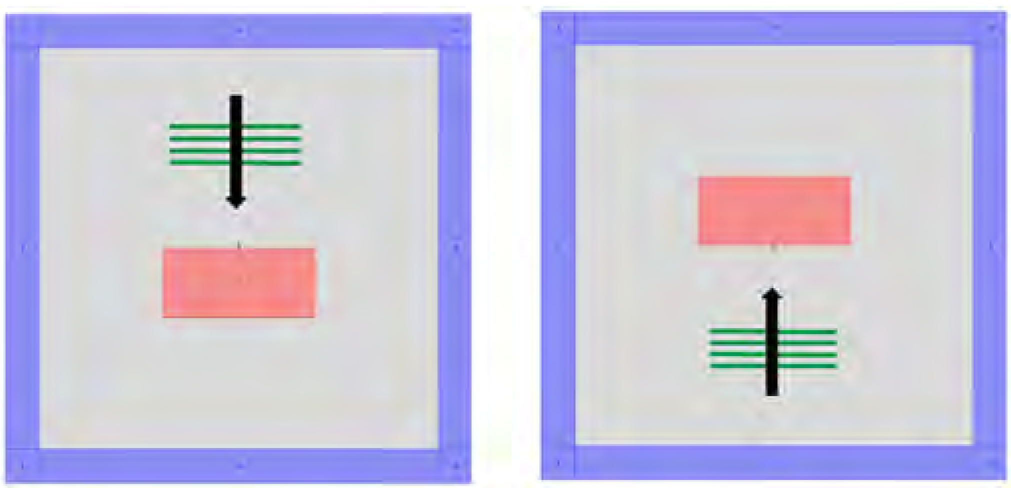

(a) (b)

Figure 55. Top and bottom compression block simulation setups. (a) Top compression setup. (b) Bottom compression setup.

Again using the initial simulation standards, Figure 56 shows that, as expected, the concentration of the middle block is not altered when it is rotated $\pm 90^{\circ}$ and illuminated with normally incident plane waves. The same concentration of electric field leads to the same magnetic field and time-average power concentration plots, merely rotated. Therefore no power flow plot for the top and bottom compression regions is shown.

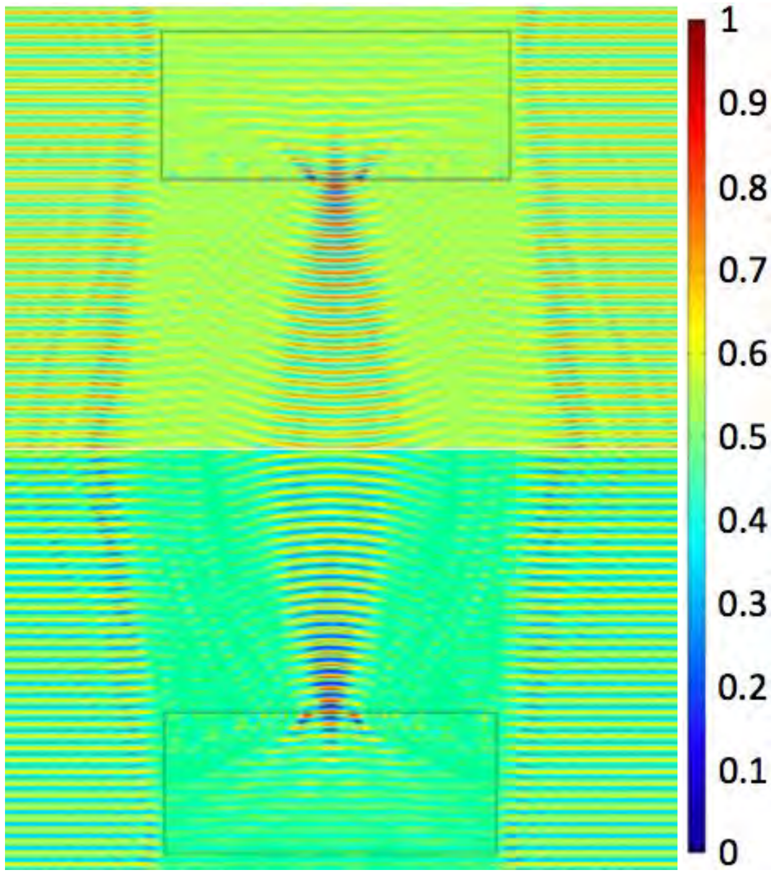

Figure 56. Normalized *x*-directed electric field distribution for top and bottom compression regions generated with the initial simulation standards. The top picture shows top compression and the bottom picture shows bottom compression.

The top and bottom compression blocks were then reduced to their triangular quadrant equivalents. The superimposed plots of E_x and time-average power flow for these regions are shown in Figure 57 for the initial simulation standards. Note that because these blocks are designed to concentrate perpendicularly incident fields, they respond uniquely to the tangentially incident *x*-directed waves. Both reflection and transmission are observed. Reflections occur off the front face while the transmitted fields appear to be the result of surface traveling waves per the discussion of Chapter II. These fields propagate along a vector defined by a component of travel in the original direction of propagation and a component in the direction of concentration for the block of interest. The effect is that both top and bottom compression blocks direct x-propagating fields approximately towards the middle compression concentration point.

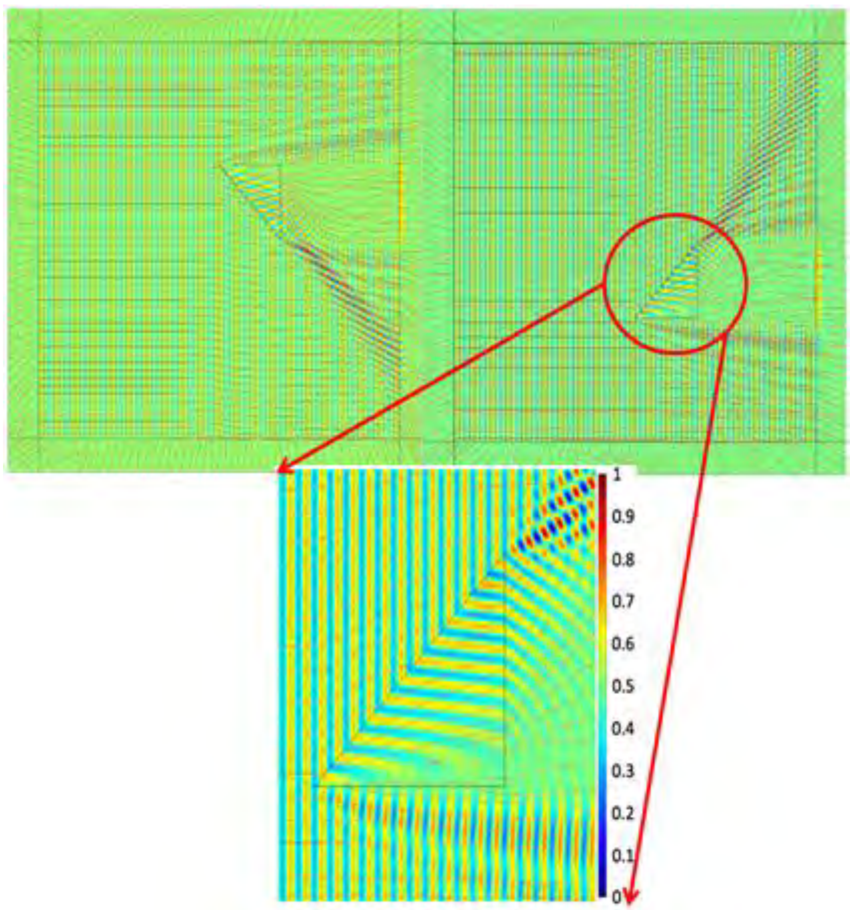

Figure 57. Normalized y-directed electric field distribution with superimposed time-average power flow lines for the top and bottom compression quadrants using the initial simulation standards. The simulations show the same response to incident fields for each quadrant. An enlarged view of the lower quadrant provides a detailed view of the field interactions.

3.3.1.1.3 Consolidated Compression Model.

After simulating each of the compression quadrants separately, all three were joined to form the consolidated compression model. Figure 58 shows the resulting compression of the incident plane waves for the initial simulation standards. As the waves travel forward or to the right in the figure, the waves compress.

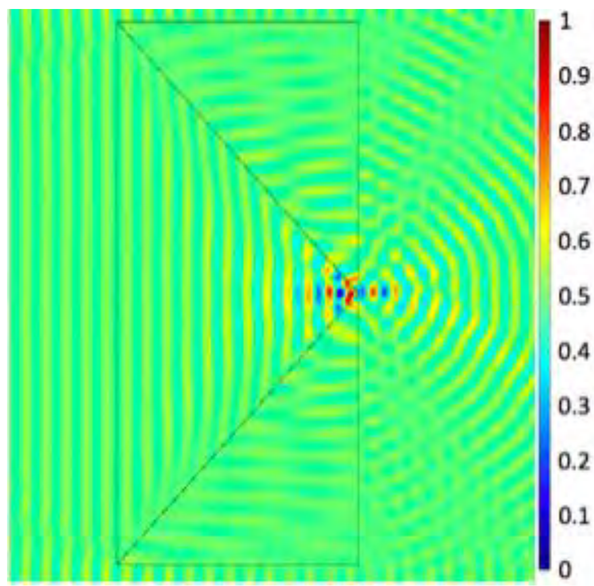

Figure 58. Normalized *y*-directed electric field distribution for the consolidated compression region using the initial simulation standards. The results displayed appear to merely be a superposition of the field responses of the individual quadrants.

Figure 58 shows reflections in the corner of the middle compression region that emanate spherically in all directions. These reflections produce constructive and deconstructive field effects both within all three quadrants and outside the consolidated compression device. The wave behavior in the top and bottom quadrants matches the simulations of those quadants isolated from the other compression sections. That is, the there appear to be surface traveling waves. The result of the deflected waves from the top and bottom quadrants is constructive and deconstructive interference that leads to the bifurcation in the concentration response away from the centerline of the device. Two sidelobes of elevated field concentration exist, one approximately 45° above and one approximately 45° below the centerline.

Figure 58 shows that concentration of E_y by the consolidated compression region appears to be a superposition of the field responses of each individual compression quadrant. The plot of H_z also appears to be a superposition of the individual responses to the magnetic field. The resulting response is shown below as Figure 59.

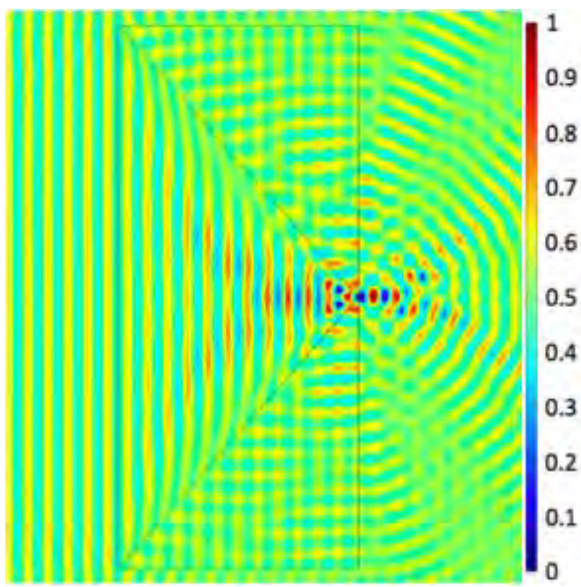

Figure 59. Normalized *z*-directed magnetic field distribution for the consolidated compression region using the initial simulation standards. Note the interference centered at the middle compression tip. Also note the central point of compression.

3.3.1.2 Expansion Models.

Priority was placed on confirming the functionality of the compression regions first since a goal of this thesis was to produce a device that concentrates fields. The compression simulations presented here ignore the fact that the left-hand side of the concentration device was not designed to interact with incident waves from free space resulting in some front face reflections. The compression region is designed accept incident waves from an expansion region.

The expansion region was built using the same initial simulation standards. Figure 60 shows the expansion of E_y. Note that the field strength is strongly attenuated after passing through the expansion region. The field expansion observed is confirmed with a plot of the time-average power flow in Figure 61.

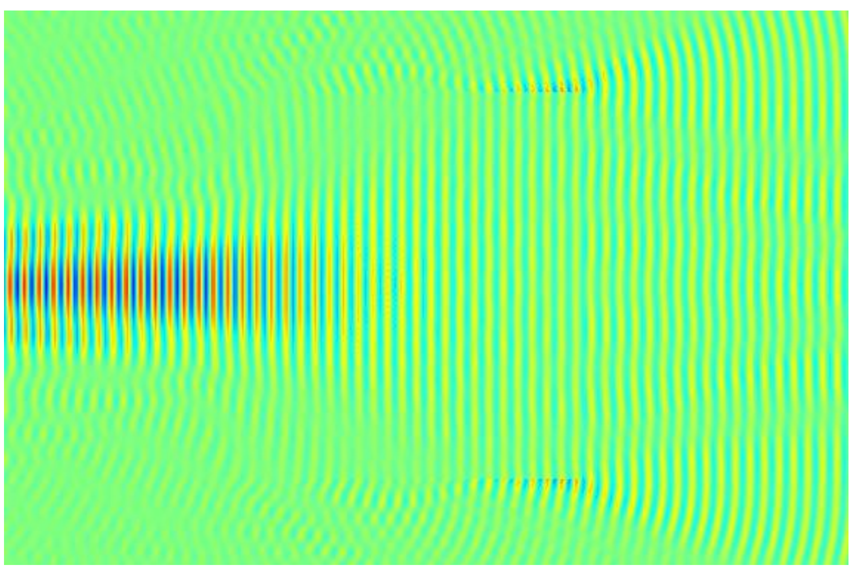

Figure 60. Normalized *y*-directed electric field distribution for the expansion region using the initial simulation standards. Port illumination is used. Expansion coincides with field strength attenunation.

It was previously shown that for a solid region of compression (the middle compression region), that concentration of the distribution of E_y coincides with concentration of the distribution of H_z. The reverse should also be true; expansion in one distribution will lead to the expansion of the other distribution. Therefore the more important graph of fields to evaluate is the time-average power flow observed in Figure 61.

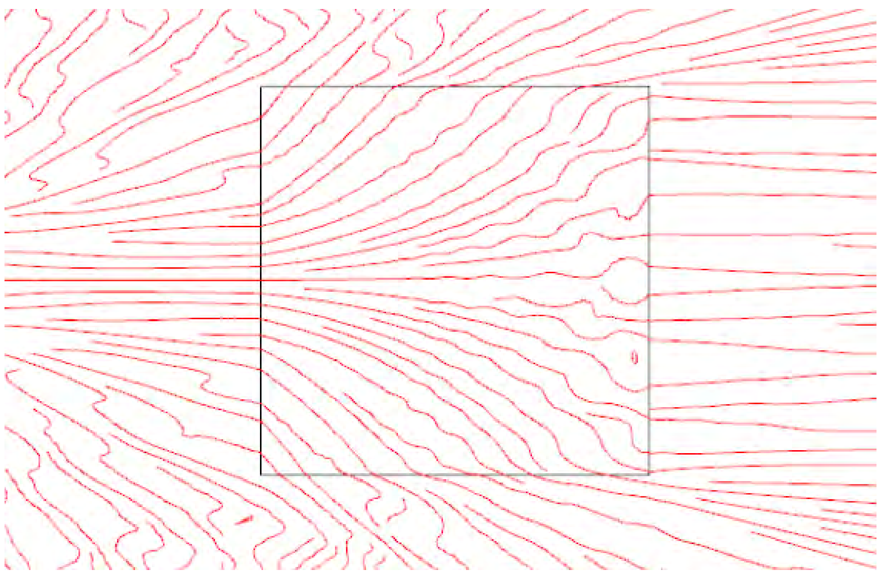

Figure 61. Depiction of the time-average power flow associated with the expansion region for the initial simulation standards. Diffraction appears to bend the exit rays back towards the center line of the expansion region some distance behind the device.

The time-average power flow observed in Figure 61 shows that there is not only attenuation of the post-expansion field strength but there is attenuation due to the dispersion effects of the expansion. The act of expansion turns away some of the incident waves entirely so that some power is bled out the sides of the expansion block. The rest of the power is directed towards the compression section. The curvature in the power flow lines observed in Figure 61 obscures the fact that the power is still spread out. This curvature and the field interference implied by the wavering of the diverted power flow lines are artifacts of the frequency and scale of the device.

3.3.1.3 Complete Concentrator Models.

All components of the complete concentrator wew tested separately and worked. First, the various compression quadrants were combined and found to concentrate fields. Second, the consolidated compression region was combined with the expansion region to form a complete concentrator model that was tested using the initial simulation standards. Field concentration coincides with concentration of the time-average power flow so it is most important now to plot the normalized E_y field distribution.

Simulation of the consolidated compression section showed that superposition of field effects occurred when different regions are brought together so in simulating the complete field concentrator, superposition of previous field distributions was expected. Figure 62 shows that this superposition does in fact occur. For example, the pattern of concentration points on the centerline behind the apex of the middle compression occurs in both the consolidated compression and complete field concentration designs.

The results of previous simulations allowed the prediction of not only the time-average power flow and superposition of field distributions, but also the distribution of H_z. This field component need not then be plotted but has been here because it provides an illustration of the interaction of the expansion and compression regions not seen in

Figure 62. Figure 63 shows the completed concentrator and illustrates that expansion creates patterns of high and low field concentration that are created due to interference patterns from reflections off the extenal and internal expansion-compression boundaries.

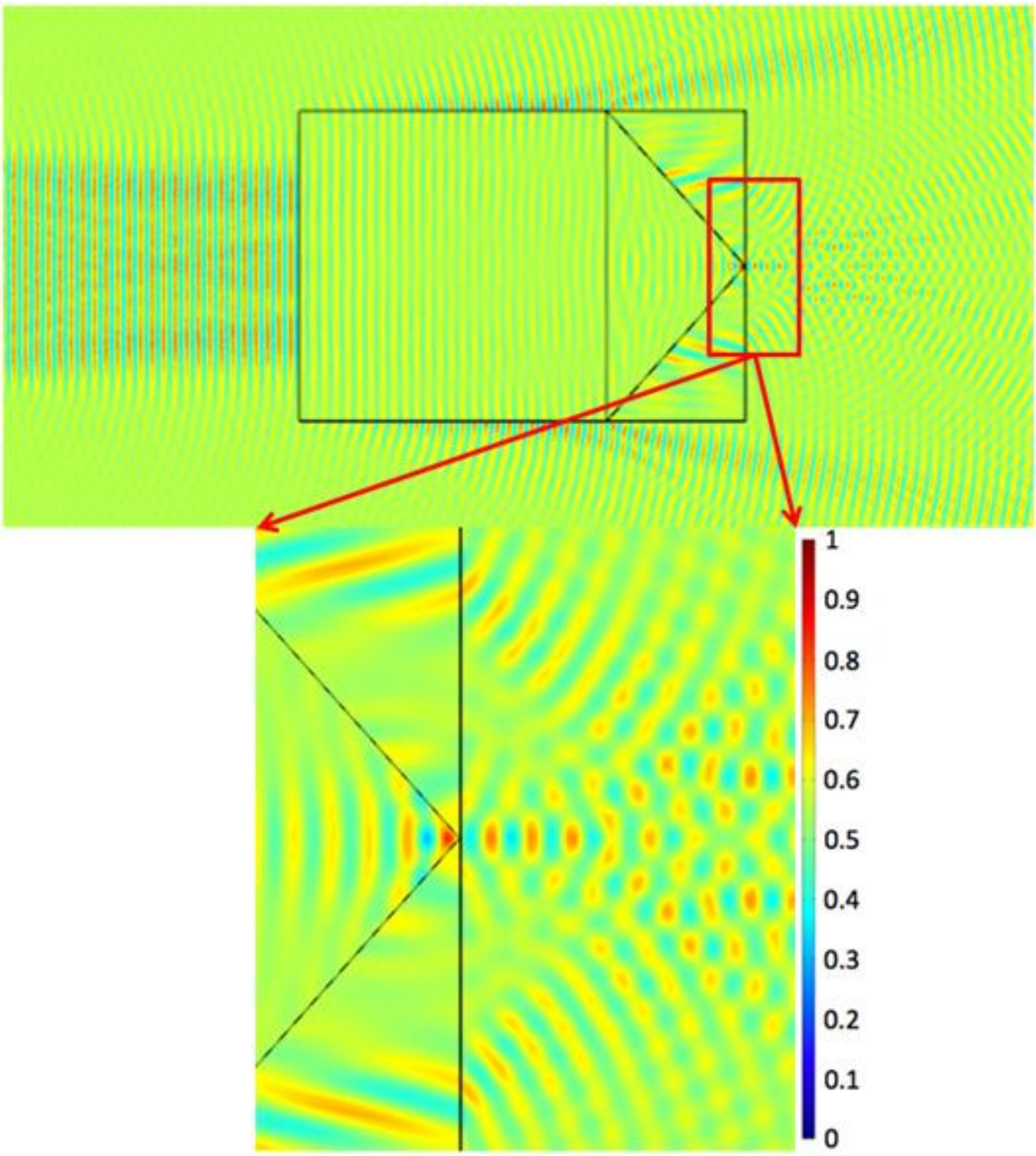

Figure 62. Normalized *y*-directed electric field distribution for the complete concentrator using the initial simulation standards. Note the pattern of concentration points along the centerline as well as the pattern of points created by diffraction and refraction of fields from the top and bottom compression regions.

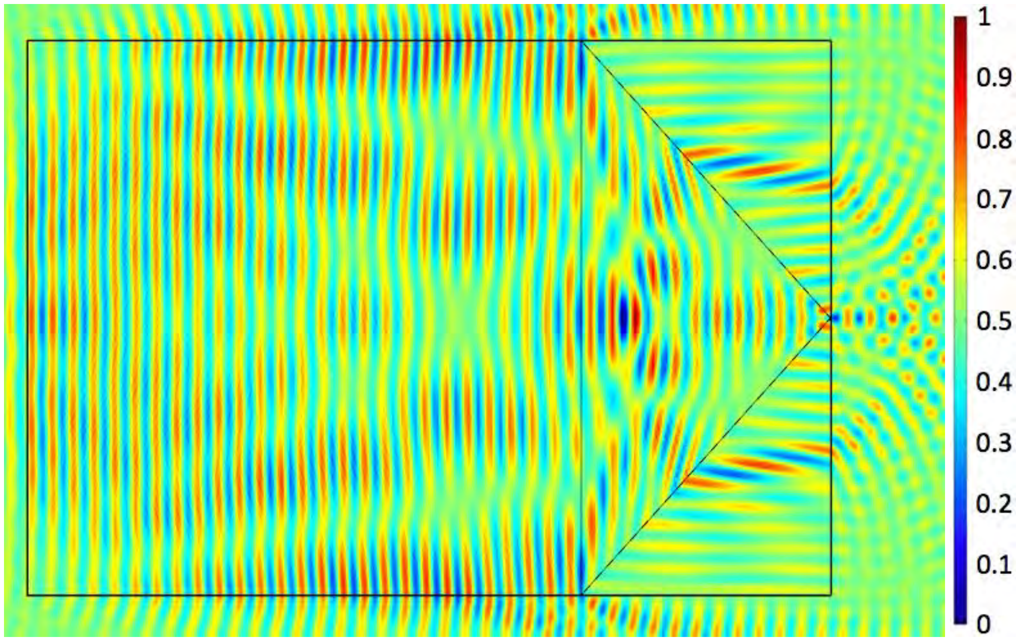

Figure 63. Normalized *z*-directed magnetic field distribution for the complete concentrator using the initial simulation standards. Note the interference patterns created by reflections off the internal and external boundaries that are present but not readily apparent in the plot of the normalized *y*-directed electric field distribution.

3.3.1.4 Scaling and Frequency Considerations.

The initial simulation standards involved meter-scale devices tested at a lower frequency than the resonance frequency the constructed device will be tuned for. While a complete field concentration device has been created, questions about scaling and frequency must be addressed.

The issue of scaling brought up during discussion of the expansion section. Figure 64 shows that if the simulation producing Figure 60 is rerun with a centimeter-scale device, such as the one that will be constructed, time-average power flow (and therefore the associated field distributions), looks much smoother. The incident wave frequency and the scale of the device explain such improvement. For a set frequency, a progressively smaller device will not perturb the incident field as much. The relative incident wavelength rises to be to be far greater in magnitude than the width and height of the device so that the device and its geometrical features become indistinguishable. Diffraction and reflections will be reduced.

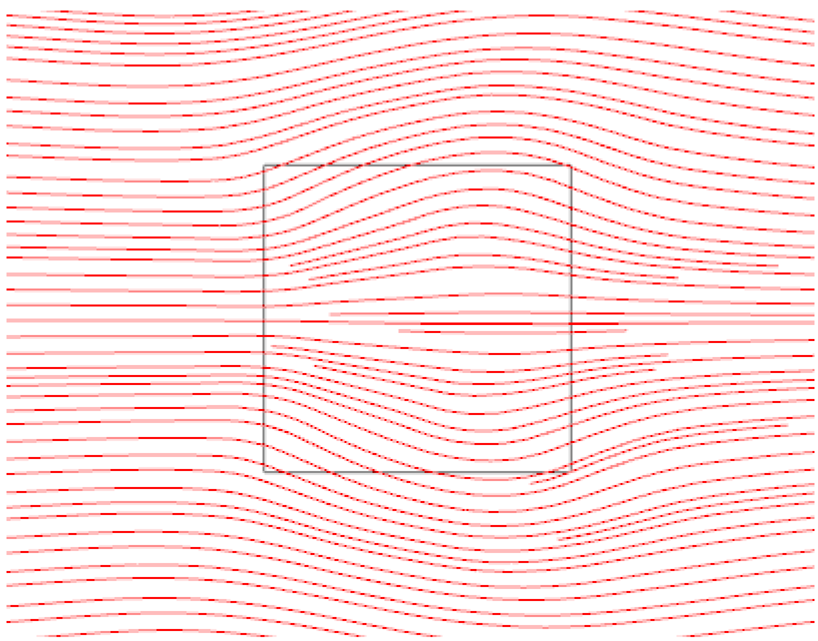

Figure 64. Depiction of the time-average power flow associated with the left-hand side of the same expansion region depicted in Figure 61 but with dimensions on the centimeter scale. The lines outside the block are not entirely straight and even due to constructive and destructive wave interactions with the finite-sized block.

Another issue involving the initial simulation standards that should be addressed is the frequency used. The initial simulations used 4 GHz but the centimeter-scale device to be constructed will be designed for resonance at 10 GHz. Figure 65 shows the normalized $\boldsymbol{E}_y$ field distribution and overlaid time-average power flow lines for the middle compression region simulatd with the initial standards but with frequency changed to either 2 GHz, 10 GHz, or 18 GHz.

The figure shows that the higher the frequency, the more the device interacts with the external field via reflections and diffraction. This observation makes sense because a change in frequency is a relative change in dimensions of the device. The higher the frequency, the larger the relative size of the device will be. Using this knowledge, it appears that a relatively large device leads to more direct compression of power flow lines. From this observation, it should be deduced that then for a given frequency, a device with a larger height and width may provide more direct compression.

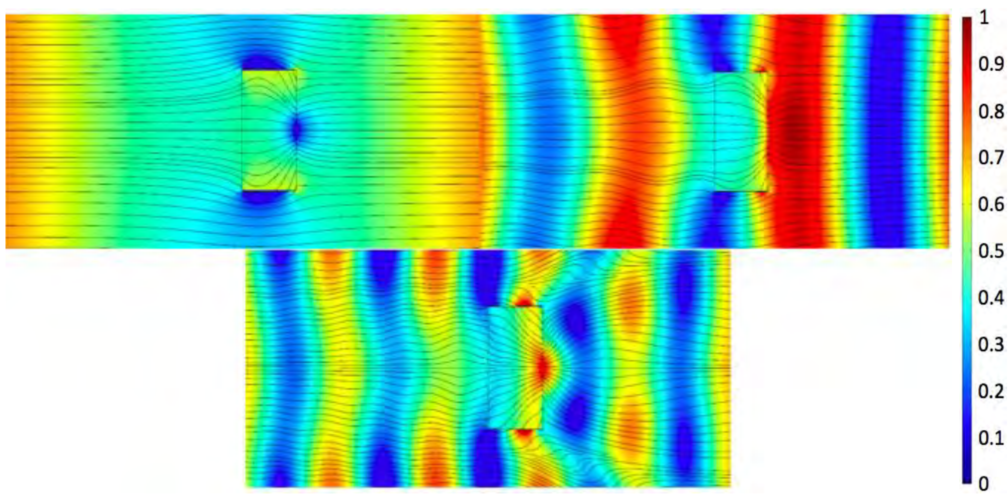

Figure 65. Plot of the normalized *y*-directed electric field distribution and overlaid uniform density time-average power flow lines for the middle compression region using the initial simulation standards but with the frequency varied. The upper left plot was generated for 2 GHz. The upper right plot was generated for 10 GHz, and the bottom plot was generated at 18 GHz.

Figures 64 and 65 work well together to emphasize the fact that while TO equations are frequency and geometry-scale independent, the application of the math is not. The primary conclusion from both these and other simulations is that a relatively large device with respect to the wavelength of the illumination beam will provide better field-device interactions and better concentration. Figure 65 shows the height and width directions relate directly to *S1* so a larger *S1* value will improve performance. This conclusion played into the selection of the optimized S-ratios.

3.3.2 Homogenized Electromagnetic Field Concentrator Model.

The anisotropic, continuous (ideal) expansion and compression regions are now shown to work separately and together. In order to construct the field concentrator or the combination of these two regions, the ideal material must be discretized based on the optimized S-ratio of 4:6:13.

In addition to outputting an optimal S-ratio for matching the constitutive parameters of the ideal material, the optimization code produces a distribution of unit cells sized for the design frequency of 10 GHz. The code specifies the location and dimension for each cell. A homogenized field concentrator model is built in CST MWS® using the code. Figure 66 shows that when like geometries are grouped by color, the pattern formed is similar to the plot of *y*-directed permittivity for the ideal material. This matching is encouraging because the permittivity at a corresponding coordinate in both the ideal and homogenized field concentration models should be the same. The cells appear to be placed along spherical wavefronts emanating from the front of the expansion region and the tip of the middle compression region. Colors emanating out from the tip of the middle compression region should emanate out from the front of the expansion region; Figure 66 shows this behavior.

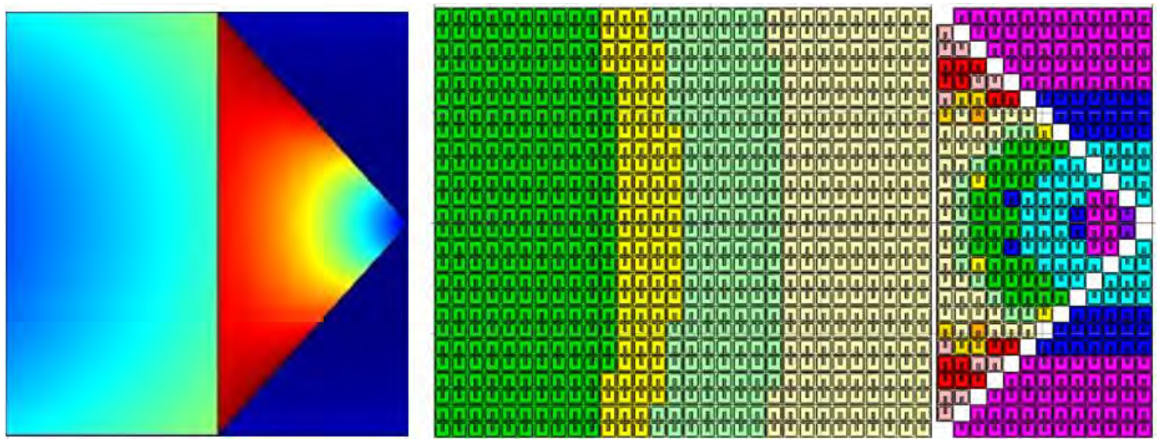

(a) (b)

Figure 66. Pictoral comparison of the relationship between *y*-directed permittivity and the similar cell geometries. (a) Anisotropic distribution of the *y*-directed permittivity. (b) Color-coded cell placement. Note during homogenization the optimization code arranges like-geometry cells in a fashion similar to the anisotropic distribution.

The goal of simulating the homogenized field concentrator is to predict the experimental data that will be collected. Based on the optimized S-ratio of 4:6:13, a 3-D concentrator will be based on a cube and will have dimension of $S1 \times S1 \times S3$. The circuit boards of the constructed device must be separated by 3 mm thick spacers. The ideal spacer material would have little influence on an incident plane wave. A readily available spacer material is Eccostock PP2, a closed cell polyethylene foam that boasts low density and low loss (given a dielectric constant of about 1.04). This material is 3.175 mm thick and was the thinnest low density, low loss spacer material available for construction of the field concentrator at AFIT. Thus, provided a combined board and copper foil thickness of 0.822 mm, an inter-board spacing of 3.175 mm, a block of 20 simulated circuit boards must be simulated.

There are a number of different ways to use the foam to space the circuit boards. The simplest method would have been to cut a full foam slab to separate the boards. While it is low loss, a large amount of low loss material could have a significant effect on the operation of the field concentrator. The ideal arrangement of the circuit boards is with the 3 mm periodic spacing and no spacers (open transmission), but since spacers must be used, another method of spacing must be used. The alternate method for spacing the boards was to put a small piece of foam in each corner of the board and then one piece in the middle, centered vertically and just behind the compression section. A small, low loss corner spacer of 1 cm square should not affect the compression region. This arrangement of spacers was selected for eventual construction because it ensured that neither the center nor corners of the circuit boards would bow and would most approximate opn transmission.

Several simulations were conducted to confirm the spacer selection chosen. Simulations were run for all three spacer configurtions: open transmission (no spacers), full foam corner slabs, and corner foam spacers. A transient analysis using – 40 dB accuracy and $\lambda/8$ boundary spacing was run on all configurations using identical port and boundary conditions. Figure 67 shows the port and boundary conditons set for the corner foam spacer model.

Port 1 was placed in a plane parallel to the front face of the expansion region and port 2 was set in a plane parallel to and behind back face of the compression region. The limited symmetry of the device allowed application of a symmetry plane to be placed along the center plane dividing the top and bottom half of the concentrator. Due to the magnetic resonance of the rings and the propagation direction of the incident plane waves, the two components composing the plane wave were a *y*-directed electric field and a *x*-directed magnetic field, shown in Figure 68 and Figure 69 respectively. It was this orientation of the incident electric field drove the choice of symmetry plane to be PEC.

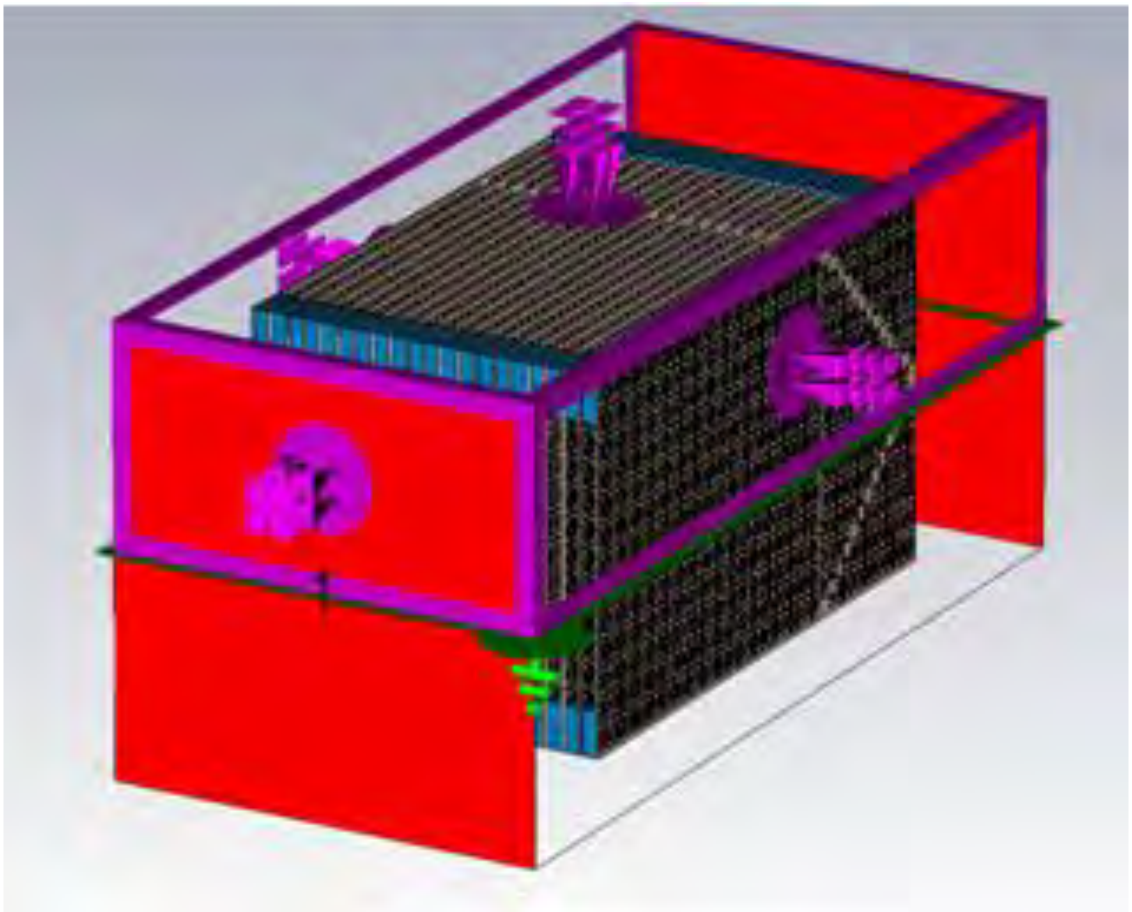

Figure 67. Depiction of the 20-board corner foam concentrator built in CST MWS® with boundary conditions and ports applied. The concentrator design utlilizes applied open (add air) boundary conditions with the PEC symmetry plane bisecting the device. Ports 1 and 2 are set at the front of the expansion region and behind the compression region respectively.

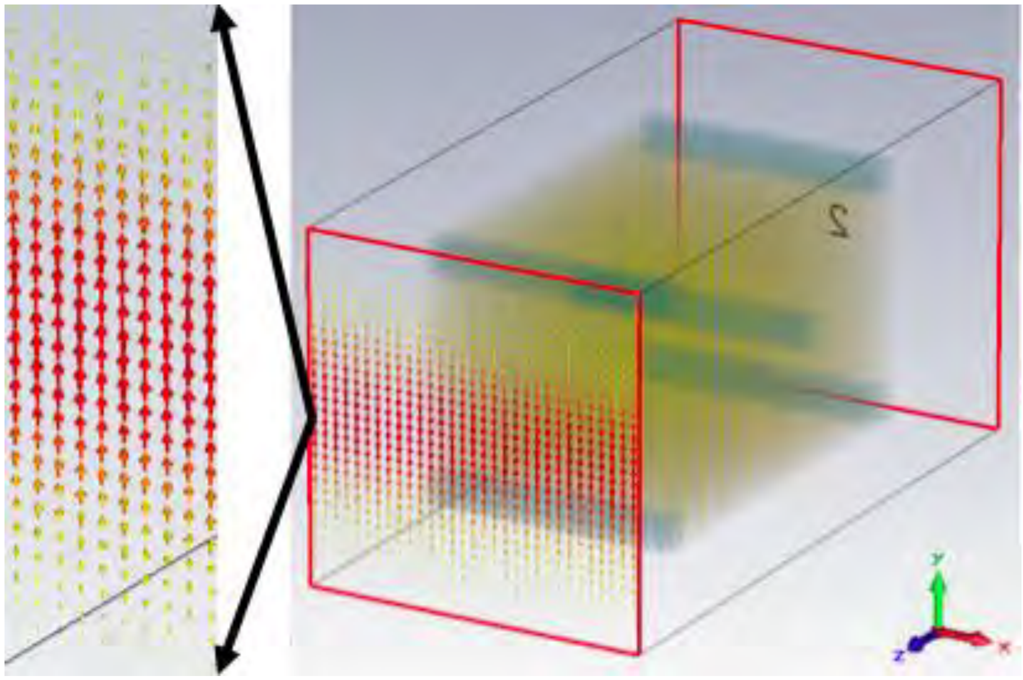

Figure 68. Depiction of orientation of the *y*-directed electric field component of the incident plane wave generated for the homogeneous field concentrator structure.

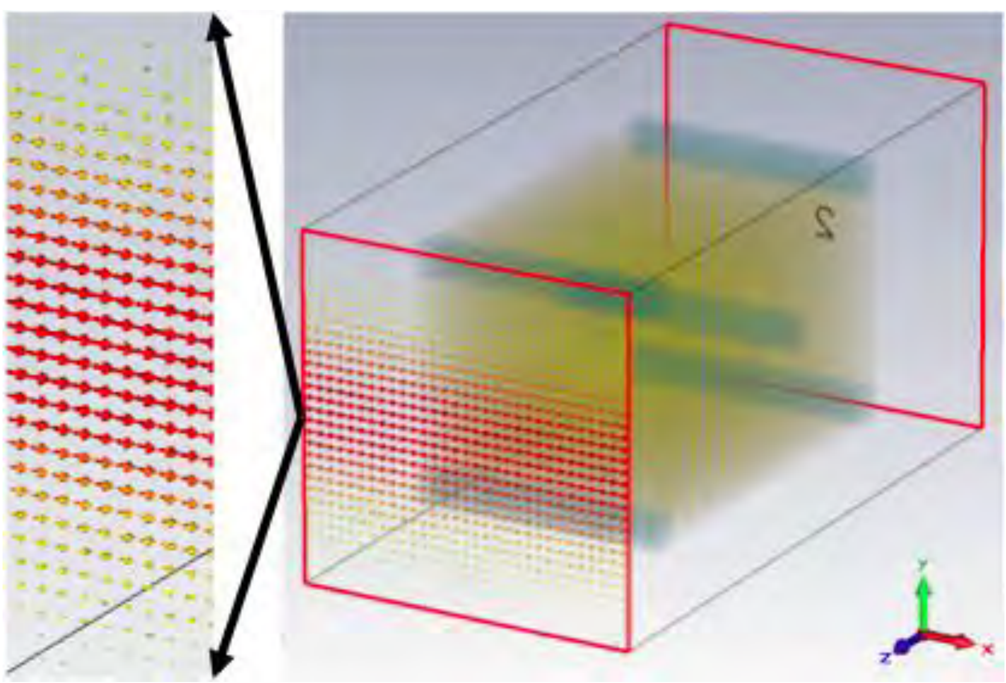

Figure 69. Depiction of orientation of the *x*-directed magnetic field component of the incident plane wave generated for the homogeneous field concentrator structure.

A PEC condition was also used for the material substituting the annealed copper that was the original material chosen to construct the traces. PEC was chosen as a trace material to speed the simulations. This trace material was laid on circuit boards made of lossy FR4 ($\varepsilon_r = 0.43$). Results of the S_{21} or transmission simulations of a 20-board design for the open, full foam, and corner foam simulations are depicted in Figure 70 – 72. The results show that there are no striking differences in performance between the spacer configurations. Given the lingering concerns that inconsistency of the material parameters of the manufactured spacer foam that could alter the collection of experiment, the corner foam spacer configuration is the first choice for manufacturing the field concentrator.

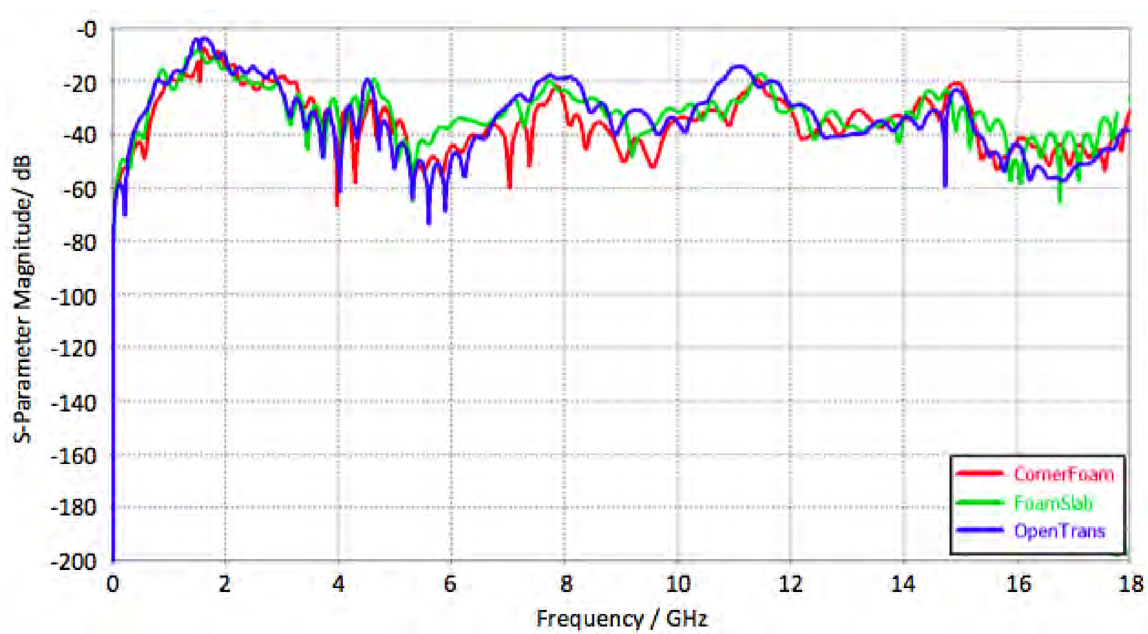

Figure 70. Plot of transmission magnitude in dB for all three spacing configurations for a field concentrator composed of 20 boards.

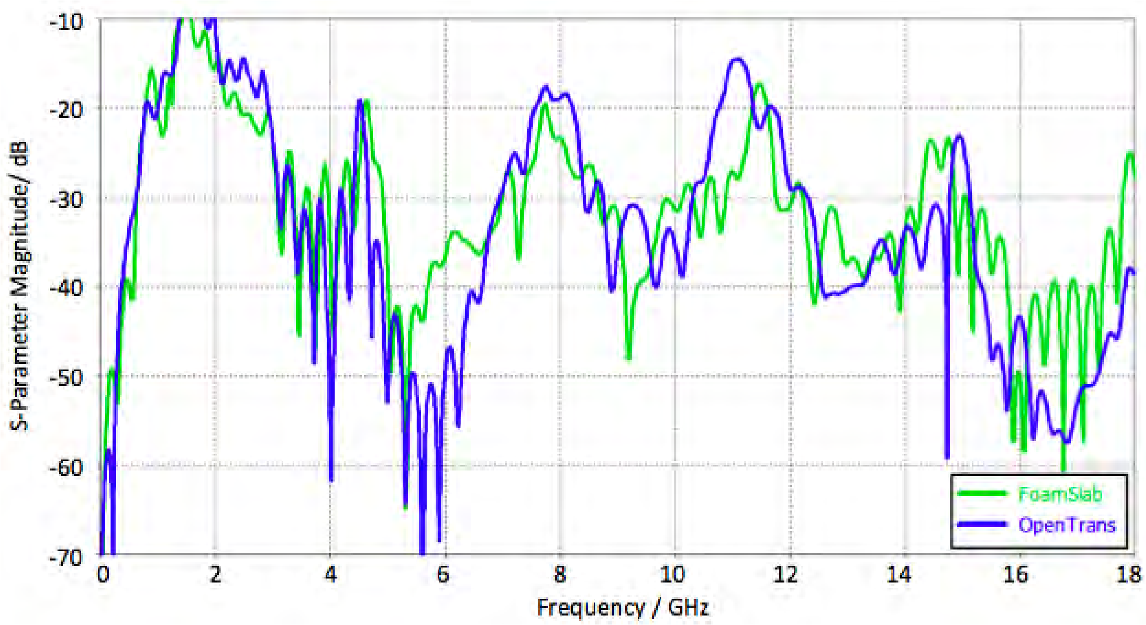

Figure 71. Plot of transmission magnitude in dB for the open and full foam slab spacer configurations for a field concentrator composed of 20 boards.

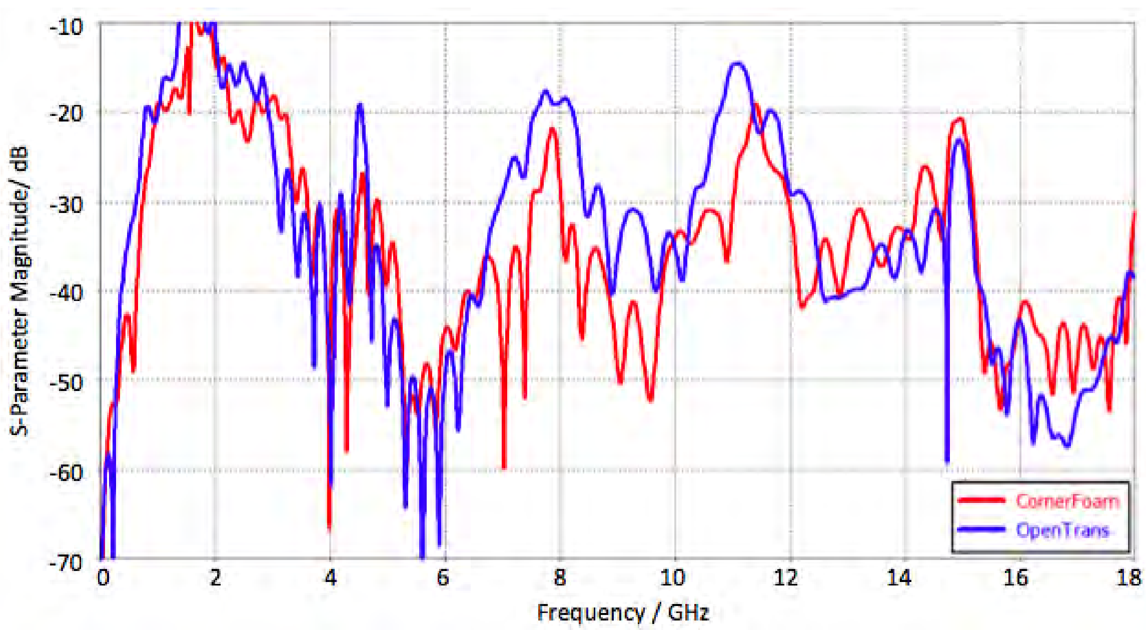

Figure 72. Plot of transmission magnitude in dB for the open and corner foam spacer configurations for a field concentrator composed of 20 boards.

Each of the boards used to produce the simulated data in Figures 71 – 73 above uses over 1000 cells so each transient analysis of a 20-board device is computationally intensive. If fewer boards can be used and still obtain identical results, then more simulations can be conducted. Figure 73 shows a review of the transmission data for 5-, 10-, 15- and 20-board configurations for full-foam spacers. The results are important for two reasons. First, the results show that the number of boards does matter, but does not cause drastic changes over the whole frequency band. Using fewer boards can be used to approximate transmission responses, Secondly and more importantly, increasing the number of boards appears to have several effects including lower resonance frequencies and strongly increased magnitude of the resonance response. This finding is indicative of the increased capacitance, loss, and field coupling introduced by the additional boards.

The same resonance peaks affected by using different numbers of boards will be used to fingerprint the experimental data and match it to the simulations. Therefore, despite the ease of running faster simulations, 500 MHz shifts in predicted resonance values make comparison of simulated and experimental data difficult. Only 20-board simulations are used for comparison with the experimental results.

Other simulation results that will be compared with experimental data include plots of field concentration. Figure 74 shows a cut of the time-average magnitude of the *y*-directed electric field in a plane parallel to the boards and at the center of the device. Figure 74 shows severe attenuation of the incident plane waves that might be expected given the low transmission of the device as a whole seen in Figure 73. Figure 74 is noteworthy because it shows the field response of the device involves the entire device. Individual cells can be seen resonating to the illumination in every region. Field interaction within the board may create interference patterns as in Figure 63 that helps or hinders resonance and explains the selective response of the cells to the incident field seen in Figure 74. Figure 75 shows a more even but still not equal resonance response at 10 GHz.

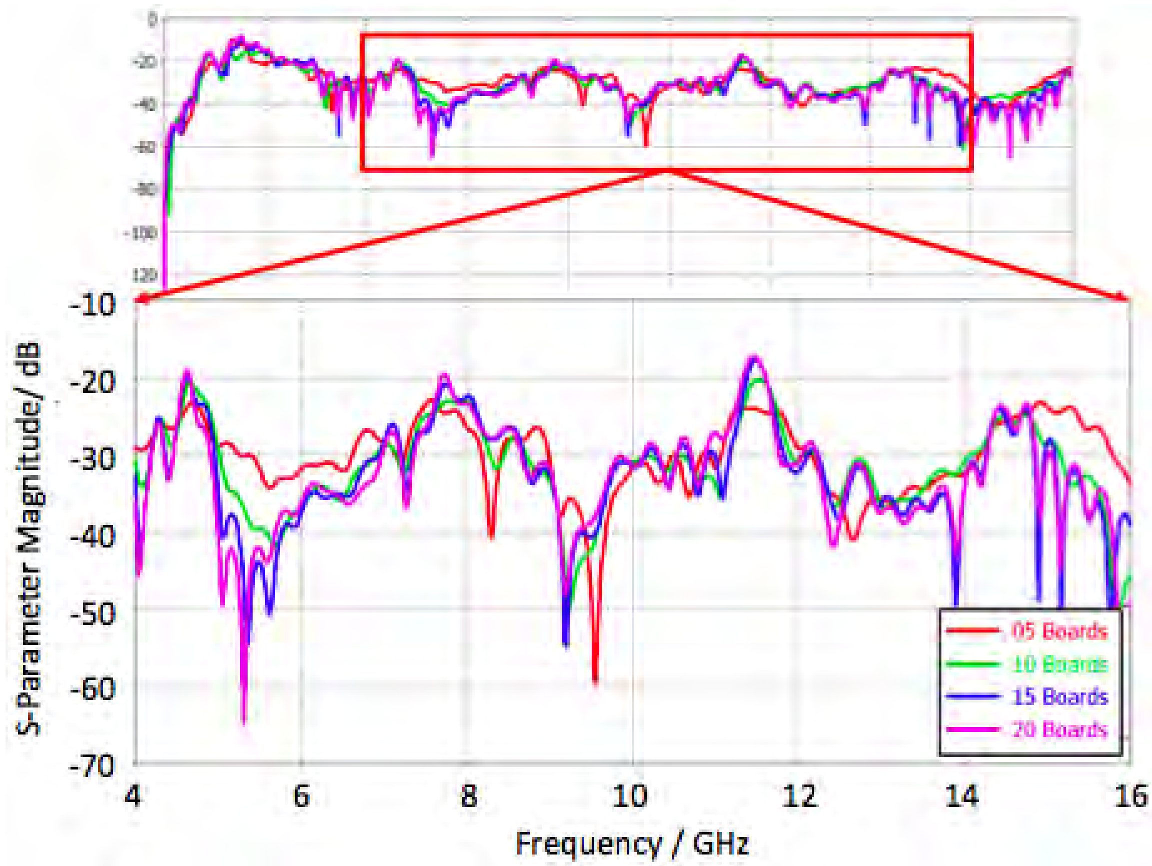

Figure 73. Plot of transmission magnitude in dB over 4 – 16 GHz for a field concentrator composed of foam slab spacers and a varying number of circuit boards ranging from 5 – 20.

Figure 75 uses a log scale to show the same behavior that could have been observed in Figure 74. The incident waves create a broad path of magnetic resonance and resulting electric response. The constitutive parameters of the top and bottom compression regions prevent significant wave travel and therefore help duct the propagating waves down the gaps in between the compression regions to form a region of concentration that broadens away from the back face of the compression region as the exiting waves are diffracted away.

The time-average transmission magnitude plotted in Figures 74 and 75 have a phase counter-part that is shown in Figure 76. The concentration generated by the stack of boards creates a small region of in-phase plane waves, just as any lens focusing on a particular point might do. Figure 77 is another plot of phase but at a distance past the outermost set of traces, at maximum distance from the center of the field concentrator. This figure shows that, as expected, the concentration and hence the in-phase waves are contant across the face of the board.

Simulations were then run to see the development of the confirmed concentration. Figure 78 examines the field concentration as it occurs in the compression section. The plots show that the primary source of concentration are the two “air ducts” above and below the middle compression region and visible in the color-coded cell map, Figure 66.

The gaps forming these “air ducts” were a consquence of approximating diagonal lines with square cells. As was aluuded to previously, the large discontinuity in constitutive parameters in going from low to high values from the middle to the top or bottom compression regions redirects the forward propagation of the waves towards the concentration point. The gap provides a simple waveguide for travel. Figure 78 shows this convergence of waves via two bars of field magnitude closing in on the center and then forming a bar of concentration at the back face of the compression region that is further focused into a point by interference with the diffracted edge waves that are clearly visible.

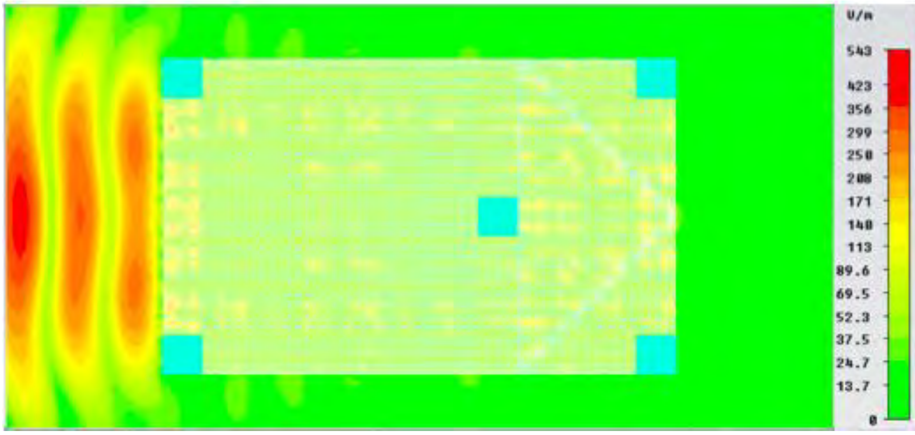

Figure 74. Side view plot of magnitude of the *y*-directed time-average electric field in a plane parallel to the boards and at the center of the optimized field concentrator using corner foam spacers. Note the strong fields surrounding individual cells that resonant at 10 GHz. The field response is weak or nonexistent for many cells but does occur in the expansion region and each of the three quadrants of the compression region. At this scale, it is difficult to discern any concentraton.

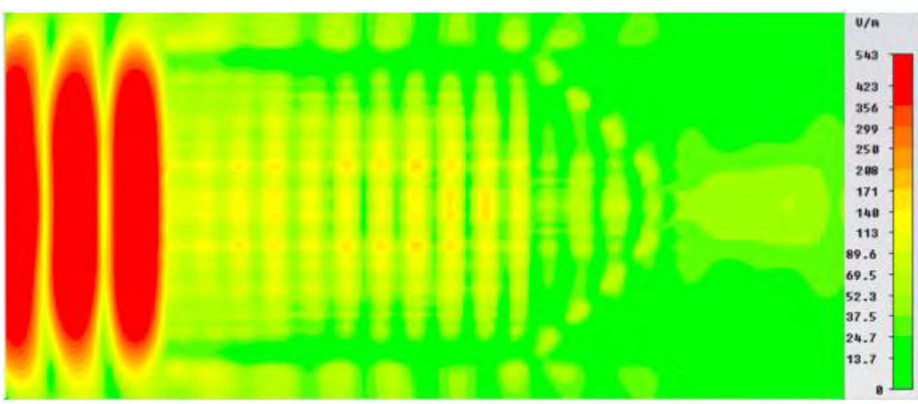

Figure 75. Side view plot of magnitude of the *y*-directed time-average electric field in a plane parallel to the boards and at the center of the optimized field concentrator using for open transmission or no spacers. A log scale is used to see the field response. At this scale it is easier to see a broader resonance response of the device at 10 GHz and the resulting field concentration.

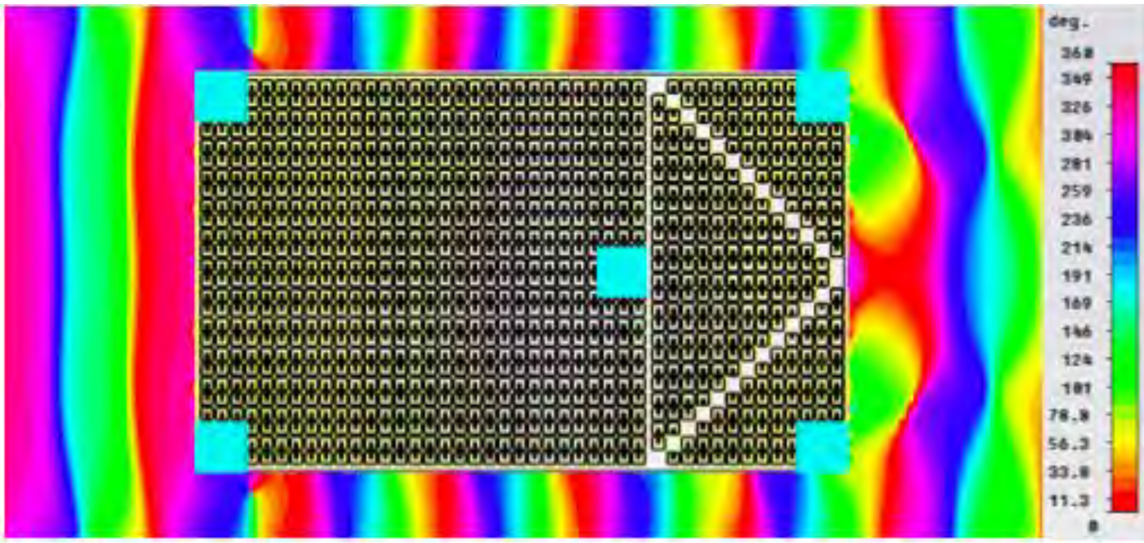

Figure 76. Side view phase plot in a plane parallel to the boards and at the center of the optimized field concentrator using corner foam spacers. Note the small in-phase area behind the compression section where concentration occurs and how the phase at the face of the back of the compression region ties into the phase at various diplacements beyond the face.

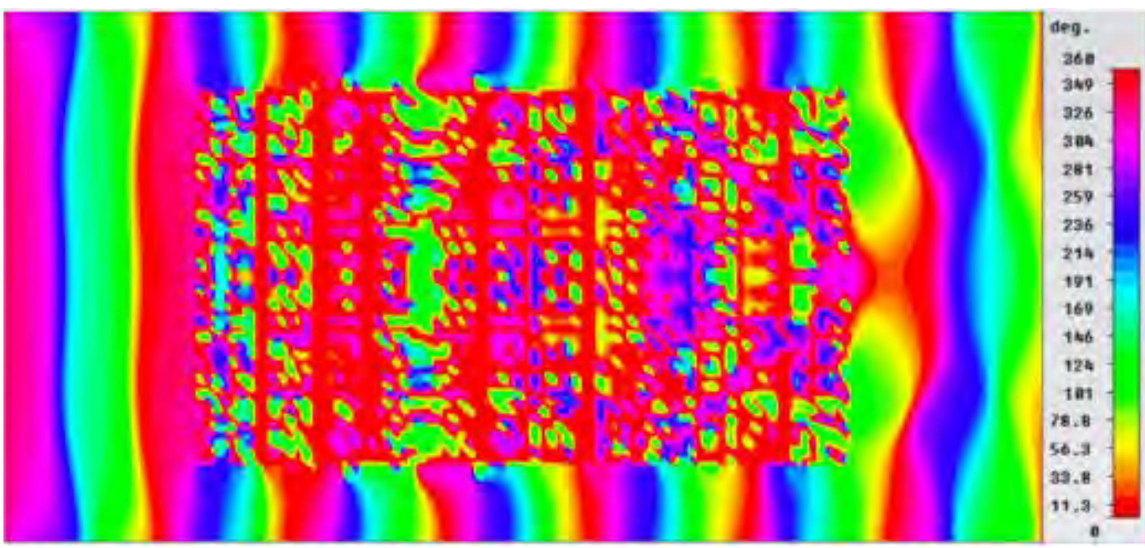

Figure 77. Side view phase plot in a plane parallel to the boards and at the outermost board of the optimized field concentrator using corner foam spacers. For this top board, it is easy to see the phase response at the various cells along the path of propagation.

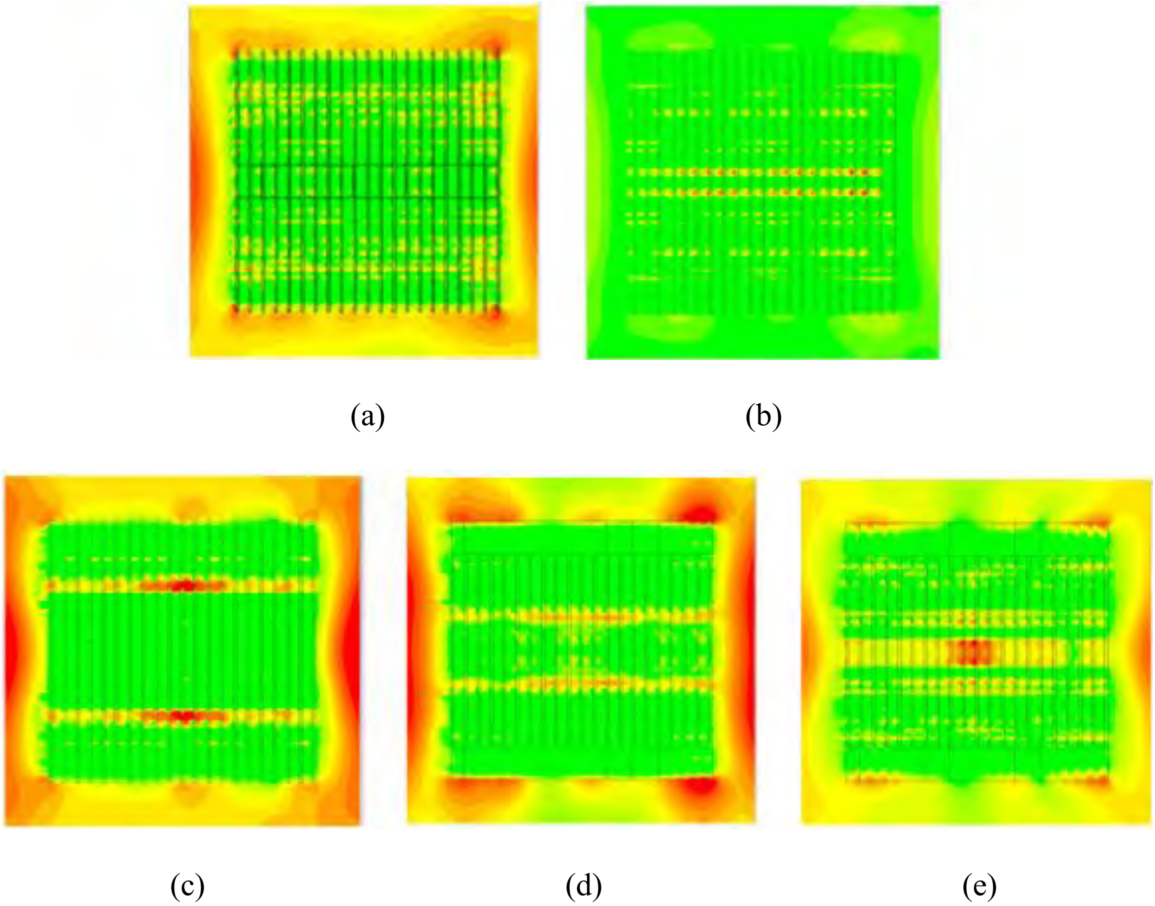

Figure 78. End view cross-section slices displaying the magnitude of the *y*-directed time-average electric field in the compression section of the optimized field concentrator with a compression width of 40 mm. Distances provided are displacements from the expansion-compression interface towards the back face or the interface of the compression region with free space. (a) 0 mm. (b) 10 mm. (c) 20 mm. (d) 30 mm. (e) 40 mm. Note the two lines in (b) are not concentration but merely two lines of cells resonating.

The gaps forming these "air ducts" were a consequence of approximating diagonal lines with square cells. As was aluuded to previously, the large discontinuity in constitutive parameters in going from low to high values from the middle to the top or bottom compression regions redirects the forward propagation of the waves towards the concentration point. The gap provides a simple waveguide for travel. Figure 78 shows this convergence of waves via two bars of field magnitude closing in on the center and then forming a bar of concentration at the back face of the compression region that is further focused into a point by interference with the diffracted edge waves that are clearly visible.

The field concentration seen in the last plot of Figure 78 continues briefly into free space before the waves ducted to create the concentration diffract away and are replaced by E_y concentration patterns that appear to be formed from mode behavior within the field concentration device. Figure 79 shows the set of end view cross-sections of the time-average electric field at various displacements from the back face of the field concentrator. As expected, Figure 79 shows that concentration due to the ducted fields reveals itself as a centered, horizontal bar of elevated magnitude across the face compression region. The device was only built to compress in one direction so the appearance of a concentration spot at the center of the back face is surprising but was previously explained as a result of interference due to the clearly visible vertical soft edge (left and right edge) diffraction.

Finally, the focus beam system cannot generate integrated pictures of field strength as are shown in Figures 78 and 79 so the *y*-directed time average electric field was evaluated along lines to provide a means for comparison with the discrete measurement of field strength made by a dipole probe stepping along a single dimension. The primary concentration of interest is that which occurs in the *y* direction. Evaluation of the field concentration at displacements of 1 mm, 2 mm, and 3 mm are shown in Figure 79.

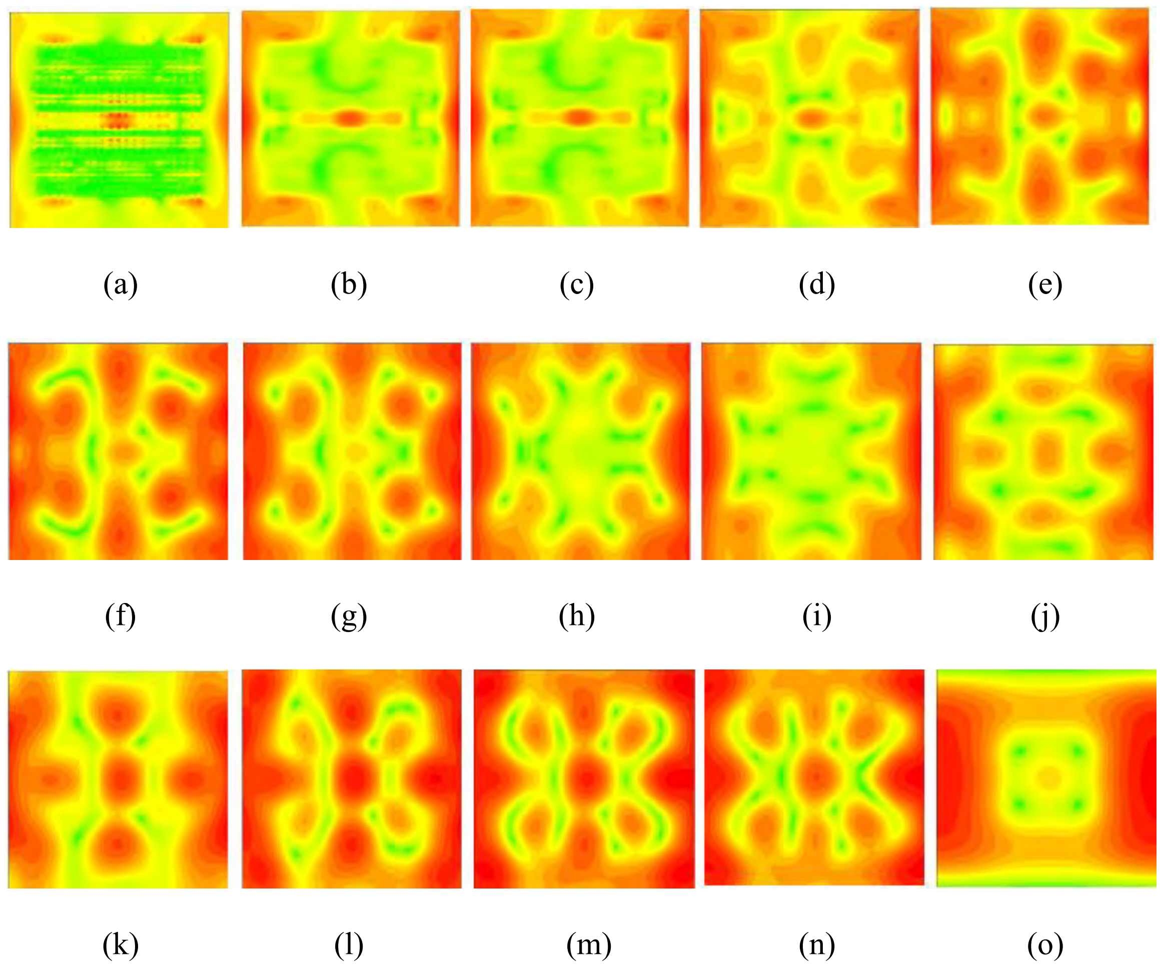

Figure 79. End view cross-section slices displaying the field strength of *y*-directed time-average electric field in free space, behind the compression section of the optimized field concentrator. Distances provided are displacements from the expansion-compression interface towards the back face or the interface of the compression region with free space. The field pattern at a displacement not displayed here is the same as that of the nearest, smaller displacement displayed here. (a) 1 mm. (b) 2 mm. (c) 3 mm. (d) 4 mm. (e) 7 mm. (f) 9 mm. (g) 13 mm. (h) 15 mm. (i) 17 mm. (j) 20 mm. (k) 23 mm. (l) 26 mm. (m) 28 mm. (n) 31 mm. (o) 38 mm.

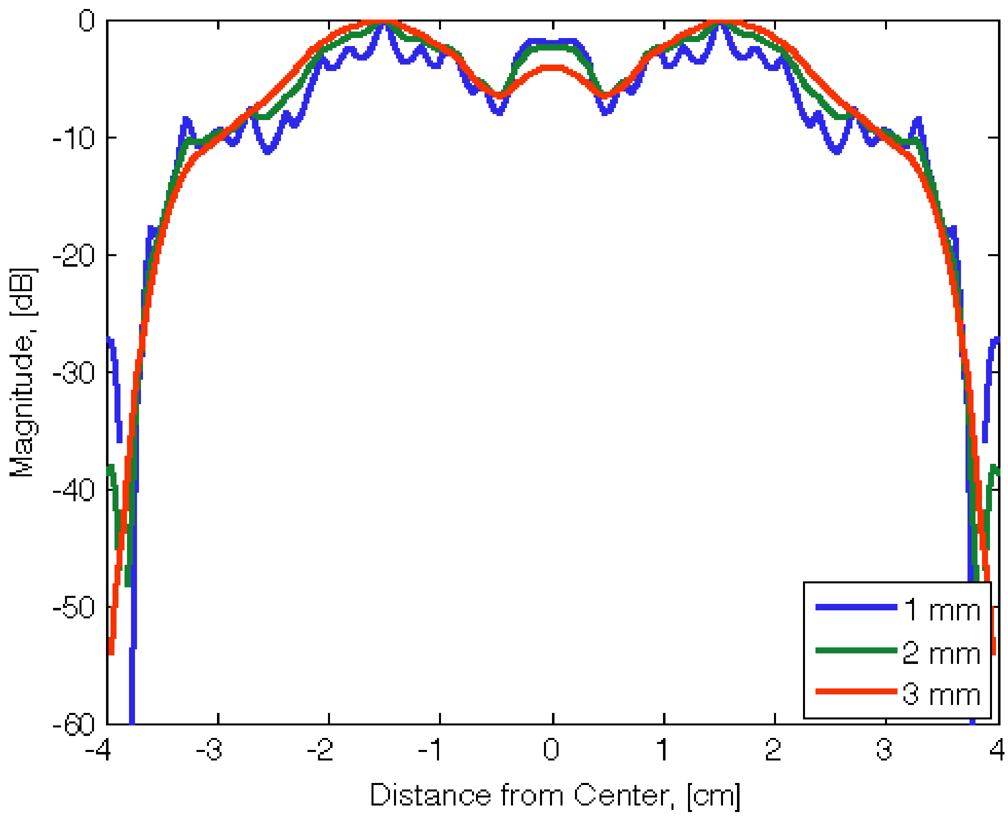

Figure 80. Plot of the magnitude of the *y*-directed time-average electric field in free space, behind the compression section of the optimized field concentrator at vertically oriented evaluation lines centered in the cross section. The magnitude of the fields are evaluated at various displacements from the back face of the. (a) 1 m. (b) 2 mm. (c) 3 mm.

The magnitude of E_y concentration in the vertical direction, at the center of the compression face, and at 1 mm, 2mm and 3 mm displacements shown in Figure 80 above has been normalized. The results show that the magnitude of E_y is maximum towards the center of the face of the field concentrator. There is a broad region of large magnitude for each displacement at the center of the face of the concentrator due to the ducting that is displayed by two peaks. Interference resulting from the concentration of the waves leads to the center undulation in magnitude. Smaller displacements show the higher the concentration as designed.

3.4 Manufacture of the Electromagnetic Field Concentrator

The thin traces, close spacing, and the requirement for trace radius differences as small as 0.01 mm makes in-house manufacturing of the PCB with a simple 1:3 mixture of muriatic acid and hydrogen peroxide impractical. The fine details necessitate commercial manufacturing of the etched printed circuit boards. Commercial manufacturing was based on a single-layer Gerber format file created from the simulations using CST MWS®, an example of which is shown in Figure 81 below.

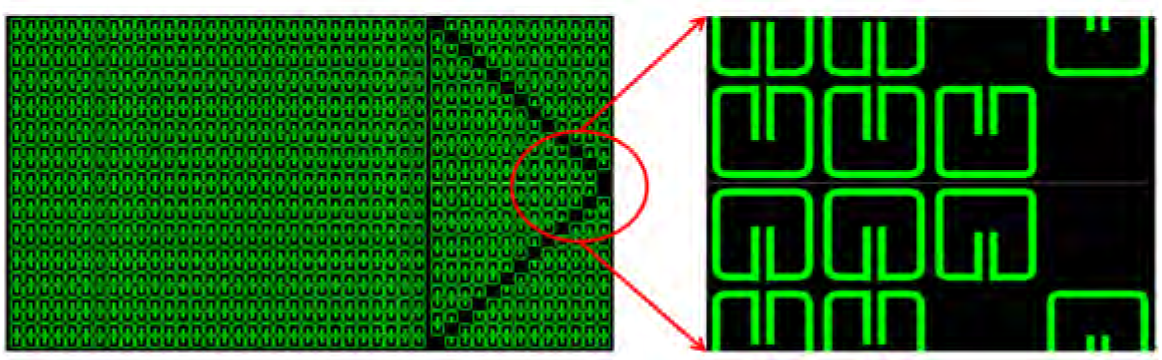

Figure 81. Image exported and used for manufacture of the field concentrator circuit boards.

Referencing the results of the optimization process, the boards are manufactured with 0.787 mm thick FR-4. The boards are clad on one-side with 1-ounce copper, producing a thickness of about 0.035 mm. The boards were certified to the best commercial practice, IPC-A-600, a common fabrication standard for rigid or flexible PCB that has been used since the 1960s.

Figure 82 shows the end result of the manufacturing process. Each PCB is first laminated with a photoresist and then exposed to an ultraviolet light with a silver halide film containing the Gerber file image. The exposed resist film is developed and the FR-4 panels are then run through a conveyer line that uses ammonia to spray etch the desired traces. Control of the temperature and chemistry of the etching liquid as well as the speed of the conveyer line are all key to good trace development. Also key to proper manufacturing is the alignment of each production panel. The drill holes and copper pattern around each of the PCB in Figure 82 are used for alignment.

The end product of the etching process is a production panel of PCB with copper traces. Figure 83 shows that the resulting quality of the copper traces is fairly good. The quality is certainly better than what could be achieved by in-house manufacturing. However, Figure 83 shows that consistent radius specification reproduction for each cell can be challenging, particularly for small radius corners.

Unfortunately, other problems can arise during the manufacturing process. The copper traces are normally finished in order to protect them from oxidation and abrasion. Several kinds of finish can be used, including the common solder mask. This was the finish used for the concentrator PCB. Use of the solder mask can create a professional-looking final product, as is shown in Figure 84, but the simplicity of the solder finish comes at the price of several possible manufacturing defects. After the copper traces on the production panels are dipped in liquid solder, uneven layers of solder and little puddles of solder can result. Trace widths and radii can also change with the application of the solder mask. Figure 85 shows some manufacturing errors uncovered in concentrator PCB.

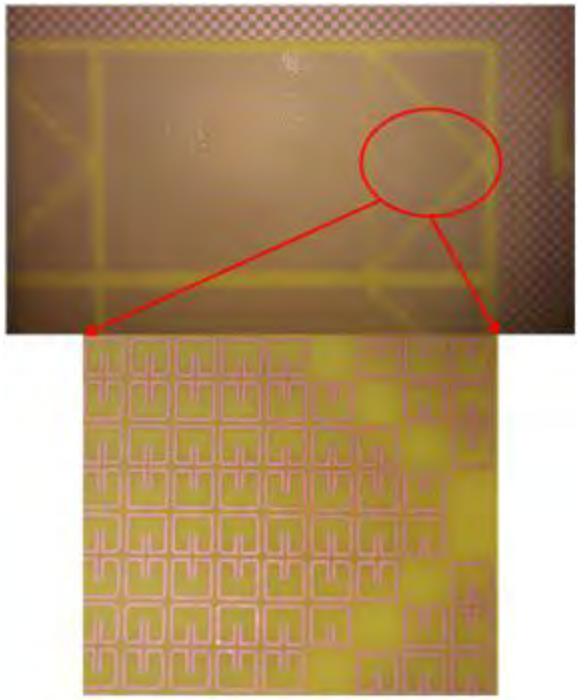

Figure 82. Picture of production panel and the acid-etched copper traces.

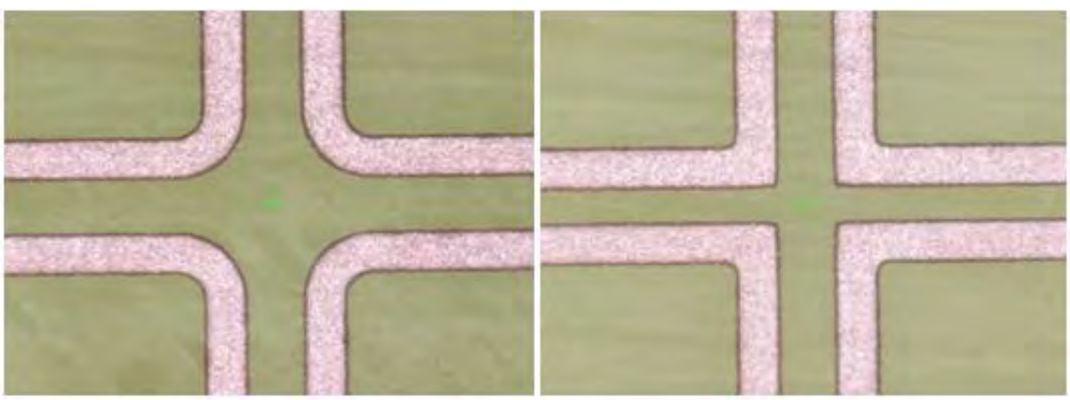

Figure 83. Close-in view of some of the radii formed by the acid etch. Note the discrepancies between the inner and outer radii. The picture on the right shows outer radii that are sharper than any trace was designed to have. These pictures show that there is a limit to the ability of commercial manufacturing to quickly and cheaply meet the design specifications required.

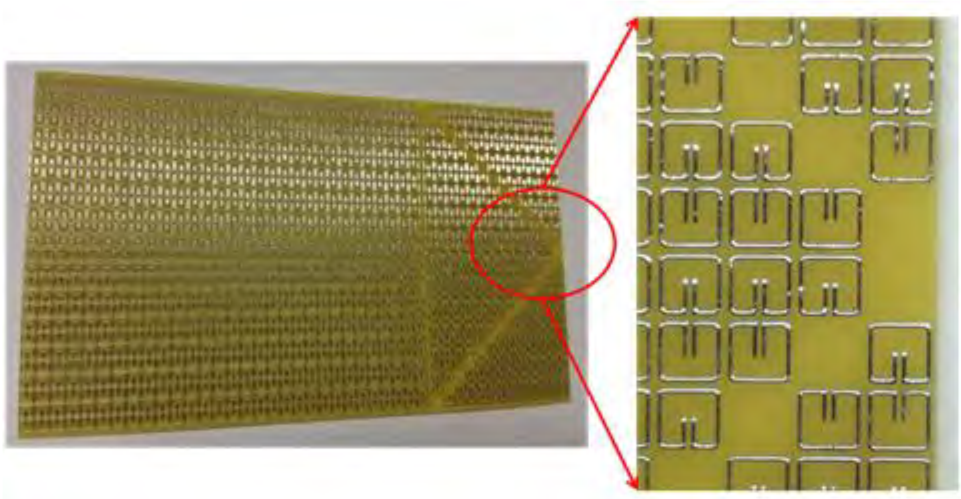

Figure 84. View of a completed circuit board with the solder mask applied.

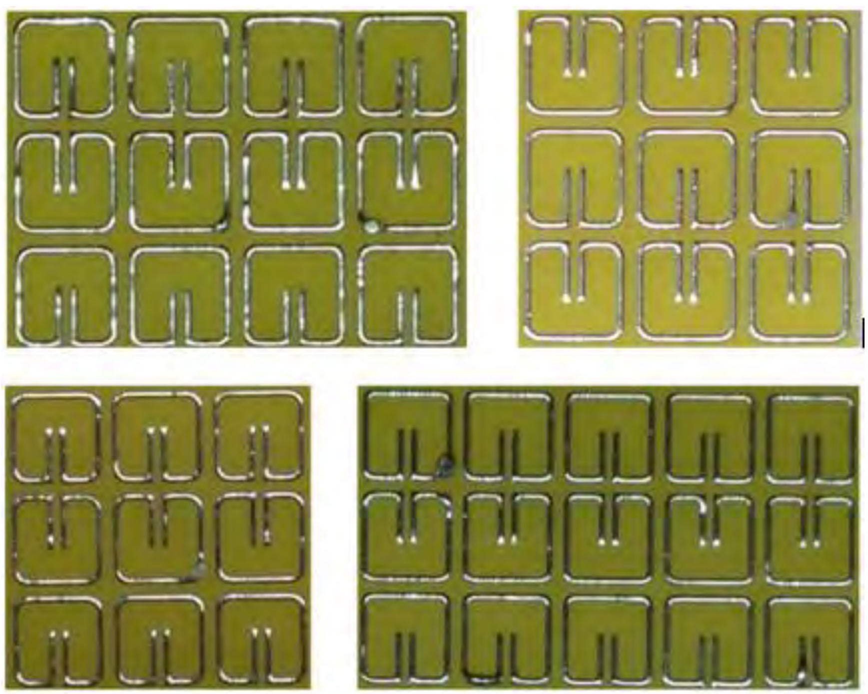

Figure 85. Pictures show manufacturing defects due to the solder mask. The solder mask has altered the shape of the corners of a number of cells and reduced their ability to produce the required constitutive parameters. No unit cells observed were shorted out by the solder.

IV. Experimental Results

4.1 Chapter Overview

The previous chapter devoted a large section to the explanation of the simulations developed to predict the electromagnetic response of the field concentrator to incident linearly polarized plane waves. Simulation data collected for the field concentrator design included S-parameters and predictions of the time-average field concentration developed by the DUT. This chapter describes the experimental methods used to test the field concentrator and then discusses the experimental data collected. Similarities and deviations between the simulated and experimental data are discussed as appropriate.

4.2 Measurement System Design and Procedures

The focus beam measurement system pictured in Figure 86 is a tool designed by the Georgia Tech Research Institute for collecting S-parameter measurements. The system consists of network cables, two large compound lenses, two horn antennas, and a mechanical structure that provides the means to hold test samples and rotate one or both measurement arms, each consisting of one lens and horn antenna. The system can be operated over a large frequency bandwidth but is mostly used produce a signal frequency in the range 2 – 18 GHz. However, due to over-illumination and the resulting spillover of waves that interfere with plane wave formation and S-parameter measurements, operation of the focus beam at less than 4 GHz does not provide reliable scattering results.

(a)

(b)

(c)

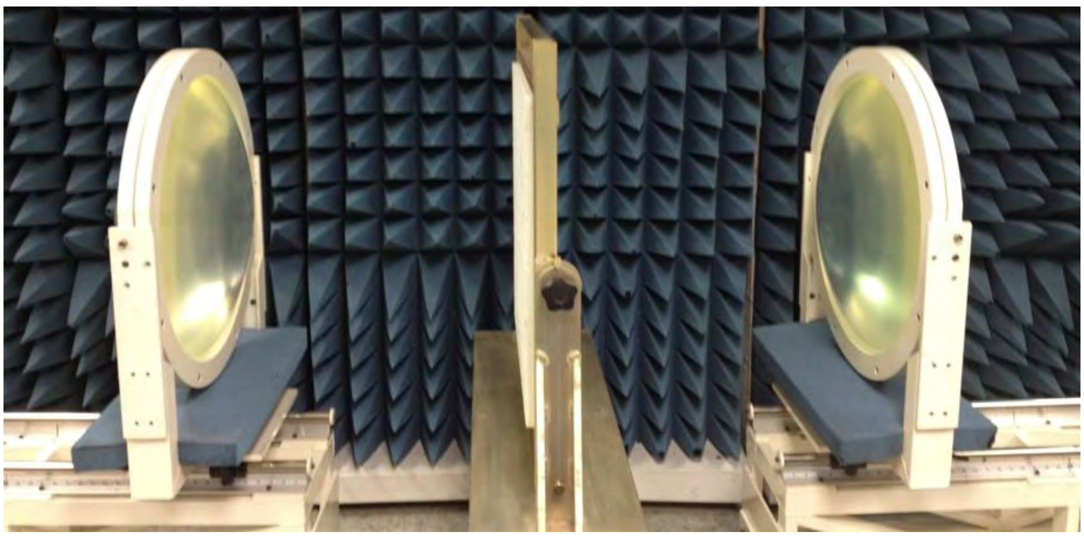

(d)

Figure 86. Pictures of the focus beam system setup for S-parameter measurements. (a) Picture of horn antenna. This can produce horizontal or vertical polarizations. (b) View from port 1. The horn antenna illuminates the back of the lens. (c) Picture of the port 1 compound lens. (d) Picture of center mount between the port 1 (left) and port 2 (right) lenses. Note the symmetrical spacing of the system.

Measurements of the complete field concentrator or total device S-parameters utilize the test setup shown in Figure 86 above. The first component of each compound lens encountered by the generated signal creates a Gaussian beam profile while the second component of each compound lens provides beam collimation. The width of the area of collimated plane waves at the center mount is frequency dependent. Operation at 10 GHz will produce a spot size of around 5 inches. S-parameters for the illuminated field test samples are directly provided by an attached. AFIT uses the E8362B Agilent PNA Series NWA.

The field concentration measurements utilize the same NWA and a test setup similar to that for the total device S-parameters. Figure 87 shows that for measurement of the field concentration, the port 1 lens and horn antenna are moved out of the way. A translation table is moved into place that provides 2-D coordinate control of an attached Hertzian dipole probe. Absorber is positioned behind the translation table to minize scattering returns. The probe is formed from stripped hardline, a 180° hybrid, a piece of pyramidal absorber meant to reduce scattering from the probe, a foam spacer, a mount for the hybrid, and a stand for the translation table.

(a) (b)

Figure 87. Pictures of the focus beam setup for the field concentration measurements. (a) View of the absorber setup in line with center mount, compound lens, and horn antenna. (b) View of the concentrator held in place with the probe conducting a measurement. Note the top of the port 1 lens has been swung out of the way.

4.2.1 Basic S-Parameter Data Collection.

S-parameters represent the ratio of the measured to incident wave voltages between the ports of a network under matched conditions. These frequency-domain values can either describe reflection from or transmission through the network. Reflection is described by S_{11} and S_{22} while transmission is described by S_{21} and S_{12}. The first subscript represents the port at which the wave is measured and the second subscript represents the port at which the wave is launched. Due to network reciprocity, the symmetrical nature of the forward and backward scattering, $S_{11} = S_{22}$ and $S_{12} = S_{21}$ so to avoid unnecessary redundancy this thesis will only reference S_{11} and S_{21}. Provided the assumption of a perfectly matched termination load for the second port, S_{11} can be described as the reflection coefficient and S_{21} can be described as the transmission coefficient. These terms can be written as [50]

$$S_{11} = \left.\frac{V_1^-(f)}{V_1^+(f)}\right|_{V_2^+=0} \tag{74a}$$

$$S_{21} = \left.\frac{V_2^-(f)}{V_1^+(f)}\right|_{V_2^+=0} \tag{74b}$$

where the ‘ $-$ ’ superscript denotes a measured wave voltage, the superscript ‘ $+$ ’ denotes an incident wave voltage, and $V_2^+ = 0$ implies impedance matching.

4.2.2 S-Parameter Enhancement and Correction Procedures.

The finite dimensions of the lenses, the sample holder, the intervening structure of the focus beam system, and even structures surrounding the focus beam system introduce scattering that alters the measured S-parameters and field concentration of a DUT. Likewise, the mechanical components of the probe can introduce scattering that interferes with field concentration measurements. Use of pyramidal foam absorber, as seen in Figures 86 or 87 can minimize scattering from structures immediately surrounding the focus beam system. However, there are still a number of scattering sources that confound the experimental data. The influence of these sources can be reduced in a number of ways. First, one can institute time gating to reduce outside scattering. Second, smoothing can be used to make the gated data more readable. Third, application of a full two-port calibration or 12-term error correction can provide further correction to the scattering data collected.

4.2.2.1 Time Gating.

Gating is a means of supplementing the system calibration to improve the accuracy and readability of measured data. Time and distance are referenced to the cable hookup at the back of each horn antenna. The measured data can be converted to the time domain and gating can be applied by evaluating the S-parameters measured with and without a metal plate setup as a target in the center mount as seen in Figure 88. The metal plate can be found by looking for a jump in reflection, S_{11}. Gates times can be selected to put a window around the DUT to create a window of evaluation. Signals received before or after this window are filtered out.

An appropriate selection of gate times involves setting the observation distances close to the front and back of the DUT to eliminate observed reflections from intermediary focus beam and exterior structures. The roundtrip for the signal through the horn to a metal test plate or through a dipole probe and back is about 13 ns. The similarity in times for the horn and dipole probe gating is due to the positioning of the ends of the cables at which calibration is made.

The evaluated signal is fast; it travels about 1 ft every 1 ns. Given the small size of the field concentrator, a 1 ns gate was placed on either side of the zero phase plane where the DUT is located for measurements with both the horn antenna and the dipole probe. Application of this gating therefore minimized the scattering and associated plot ripple or magnitude oscillations due to sources more than 1 ft away from the zero phase plane that otherwise cause constructive and destructive interference, as can be seen in Figure 88.

Figure 88. Metal plate held in the center mount. The metal plate was used to find the location of the zero phase plane in the time domain so that the NWA gating window could be set to include the target.

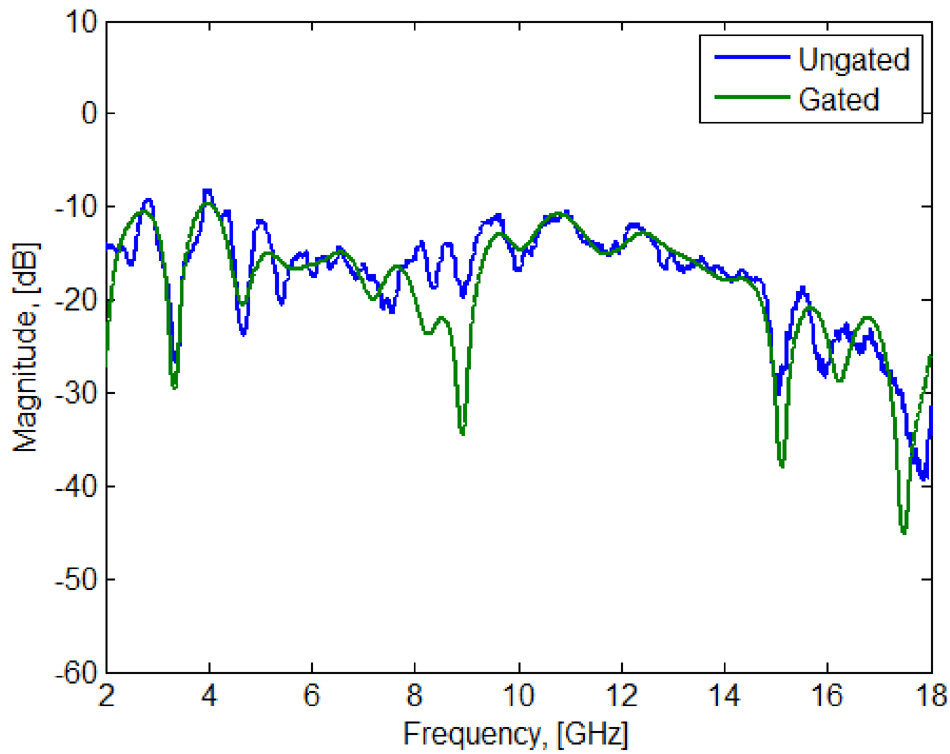

Figure 89. Plot of measured reflection data before and after application of gating applied to the time domain. The effects of gating are significant, particularly at the mid- and upper-band frequencies. Gating removes some of the scattering influence of the focus beam and the surrounding environment that causes constructive and deconstructive interference with the scattering from the DUT.

4.2.2.2 Plot Smoothing.

All measured S-parameter data include noise from the measurement device and scattering from external sources within the time window containing the DUT. The varying frequency response at adjacent frequency measurement points can be reduced so as to approximate the average scattering response by using smoothing. Smoothing is the process of developing a scattering response at a particular frequency sample by averaging several adjacent measurement points. It is a moving average filter. Application of smoothing must be limited so as not to over-average and minimize the test sample resonant responses. Increasing the number of sample points for a given percentage of sampling can reduce potential concerns about over-averaging. Measurements of the total device S-parameters for this thesis used 1.1% smoothing for 1601 points within the test band of 2 – 18 GHz resulting in the averaging of 17 adjacent sample points. Figure 104 shows an example of the effects smoothing when the number of averaged points rises from 10 to 17.

4.2.2.3 Sources of Measurement Error.

The simplest and most convenient method of obtaining scattering data from a DUT is to conduct an uncorrected measurement. This measurement method simply involves placing the DUT in the measurement system and recording the S-parameters. The downside of this convenience is that the scattering response of the DUT is confounded by large measurement error.

Measurement error is composed of random, drift, and systematic errors [9]. As the name implies, random errors cannot be removed via calibration due to their unpredictability. Random errors are functions of time and are introduced via such sources as instrument noise. Multiple measurement-averaging can isolate and eliminate the various noise and other measurement-to-measurement variations. Reducing the intermediate frequency (IF) or the bandwidth seen by the receiver can also cut the instrument noise levels associated with network analyzer operation [1].

Drift errors are similar to random errors in that they are also functions of time. This category of errors refers to changes in the performance of the test system with respect to its initial calibration. A change in the test environment can introduce changes in the operation of the test system or the collection of data. A primary source of drift error is therefore temperature variation, particularly during a test of long duration. Multiple calibrations can be used to remove drift error, such as an initial and final calibration.

Systematic errors are prevalent in scattering measurements due to the variety of source types that can produce them. The six types include [1]

1. source mismatches,
2. load impedance mismatches,
3. crosstalk,
4. directivity,
5. transmission tracking, and
6. reflection tracking.

These errors mostly relate to signal reflections and leakage [1]. For example, directivity describes signals from the surrounding environment, not the DUT, that are incident upon the reflected wave detector. Crosstalk can also exist whether or not a DUT is present because it describes leaked signals from one port that are received at the other port. Errors that are related to neither signal reflections nor leakage are the result of frequency response, such as transmission tracking and reflection tracking. Specifically, frequency response can be related to the detector response, phase delay and path loss [9]. Those errors that are invariant with time can be eliminated by calibration.

4.2.2.5 Two-Port Calibration.

Calibration can help eliminate many of the errors confounding DUT S-parameter measurements, which is why calibrated measurements are more accurate than than uncorrected measurements. The three types of calibrated measurements include the response, one-port, and two-part calibrations. The most accurate calibration is the two-port correction.

Two-port correction is generally implemented by either the use of through-reflect-line or full two-port calibration, also known as short-open-load-through (SOLT) calibration [9]. SOLT calibration is by far the more popular method. This method removes all systematic error from the measurements. Development of the equations for the corrected S-parameters is included in [9]; this reference illustrates how the total removal of systematic error is conducted by considering both the forward and reverse directions. Systematic error is the sum of the six types of error listed previously so consideration of the forward and reverse paths requires accounting for 12 different error terms. Hence, the full two-port or SOLT calibration is also known as 12-term error correction. The procedure for implementing SOLT calibration or the 12-term error correction is summarized below in Figure 90 along with pictures of the calibration. The test signals are calibrated to the ends of the cables at the back of the horn antennas or the dipole probe.

Calibration Step	Port 1	Port 2
1	Open	-
2	Short	-
3	Load	-
4	Through	Through
5	-	Open
6	-	Short
7	-	Load

(a)

(b)

Figure 90. Summary of SOLT calibration method for AFIT's focus beam measurement system. (a) SOLT calibration steps provided in chronological order as directed by the NWA. (b) Picture of calibration components. Pictured first is the "open" attachment, followed by the "short," "load," and "through" attachments.

4.3 Metamaterial Field Concentrator Measurements

The focus beam system was calibrated each day before use. After each calibration as finished, measurements were conducted. The field concentrator was characterized by measuring both its S-parameters and the time-average field concentration it produced. The first measurements made were the total device S-parameters.

4.3.1 Total Device S-Parameter Data Collection and Analysis.

The test setup for measuring the total device S-parameters first involved placing the lenses and antennas comprising ports 1 and 2 opposite one another. The transmission and reflection parameters were then measured for an empty center mount, that is, a center mount with no target or foam holder. The results of this measurement, displayed in Figure 91 below, show transmission near 0 dB (complete transmission) and reflection several orders of dB below that. Deviations from complete transmission are expected due to effects such as scattering from the center mount.

Next, the foam holder was centered in the mount between each lens, as shown in Figure 92. Another measurement was made to quantify the effect of the foam holder and the center mount on the transmission and reflection parameters. The results of the this measurement are included in Figure 93 and show the scattering effects of the foam are negligible. The transmission and reflection responses closely match that of an empty center mount.

After the empty foam holder was tested, the boards composing the field concentrator were loaded into the foam holder. The field concentrator was placed evenly in the foam holder so that the device was approximately evenly spaced between the lenses. The boards were oriented vertically and placed so that concentration would occur on the port 2 side. This configuration is shown in Figure 94 along with close-ups of the DUT in Figure 95 and 96.

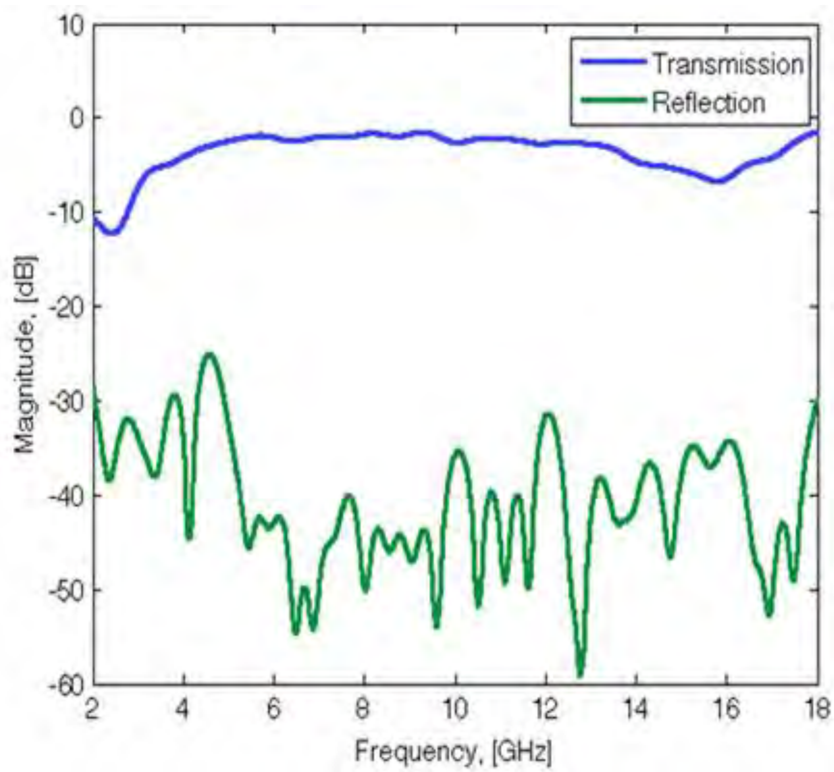

Figure 91. Measurement of the transmission and reflection in the absence of both the field concentrator and its foam holder. Note that transmission is near 0 dB for transmission, and is very low or around -45 dB for the reflection.

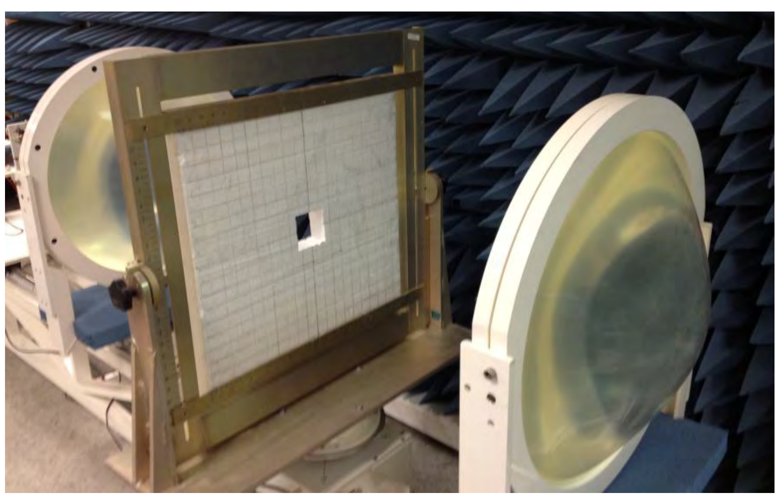

Figure 92. Angled view of AFIT's focus beam measurement system with the foam holder in the center mount. This picture more clearly shows the positioning of the foam holder in the center mount. Port 1 is shown on the left and port 2 is on the right.

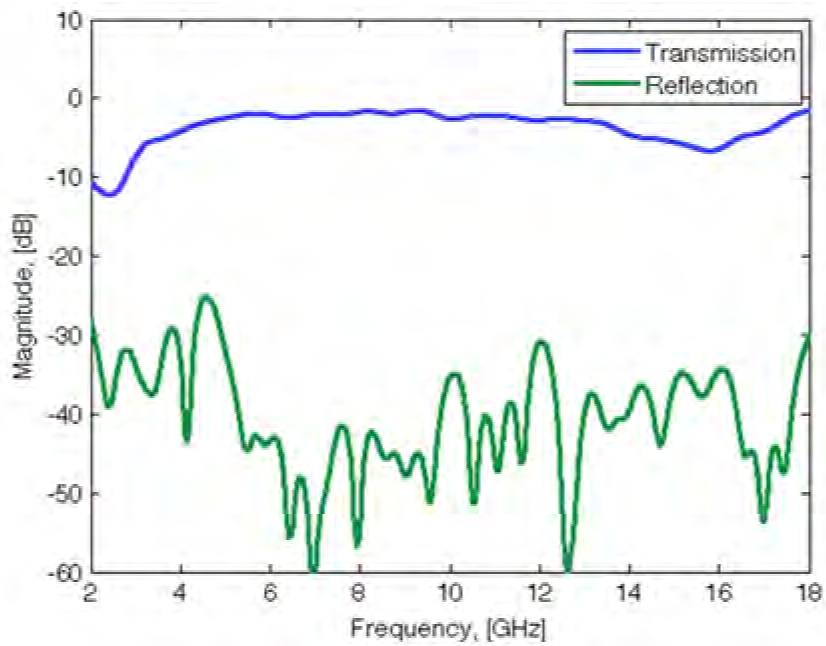

Figure 93. Measurement of the transmission and reflection of the foam holder without the field concentrator target. Note that transmission is near 0 dB for transmission, and is very low or around -45 dB for the reflection. These results make sense given the extremely low dielectric constant of the foam holder. The lack of perfect transmission or reflection seen in the data can be attributed to several reasons, chiefly reflections off the center mount and various components of the focus beam system.

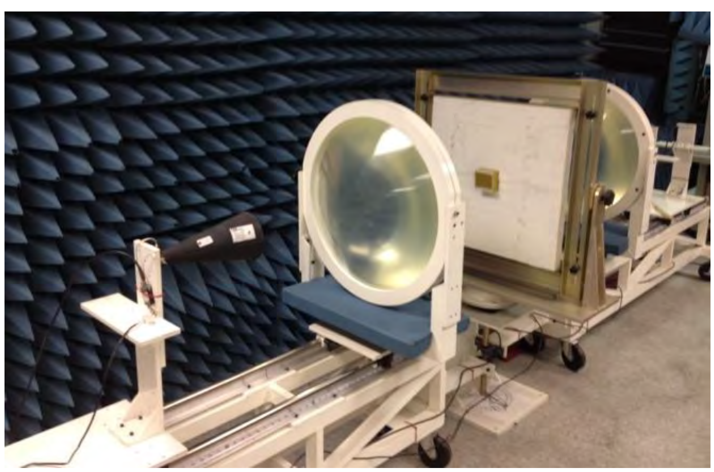

Figure 94. Full test setup as viewed from port 1 in the foreground. The horn antenna illuminates the expansion section.

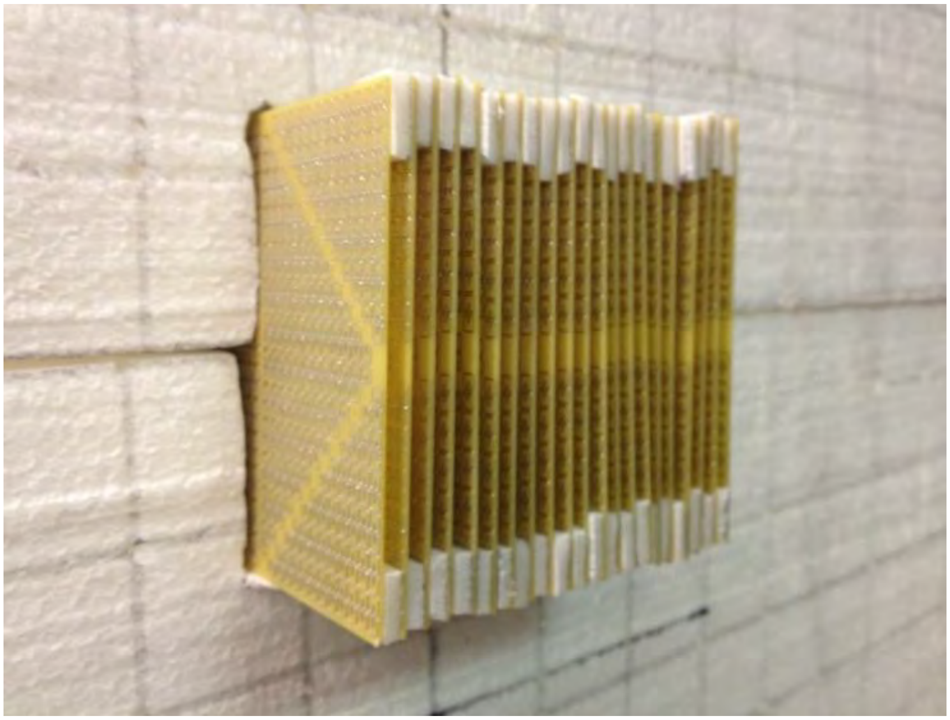

Figure 95. Angled view of the back, compression section of the field concentrator placed in the foam holder. A ruler was used to initially ensure that the back edges of the boards were flush with each other although the edges still appear to be uneven due in part to the uneven styrofoam on which the boards are sitting.

Figure 96. End view of the back, compression section of the field concentrator placed in the foam holder. As with the angled side view of the loaded target, some uneven back edges exist. This view also allows one to see uneven spacing in the board separation. The uneven spacing is due to the uneven Styrofoam on which the boards are sitting.

After the boards were mounted, an initial set of scattering measurements was made for 2 – 18 GHz. When the first measurement was completed, the boards were removed then restacked, placed back in the foam holder, realigned so that the boards were even with each other and centered in the foam holder, and then retested. This entire process was completed one more time for a total of three separate measurements using the same initial calibration. The transmission of each measurement is included in Figure 97 below. Figure 97 shows that all three measurements are very similar to measurements 1 and 2 almost identical with only very minor variation low frequencies in the pass band.

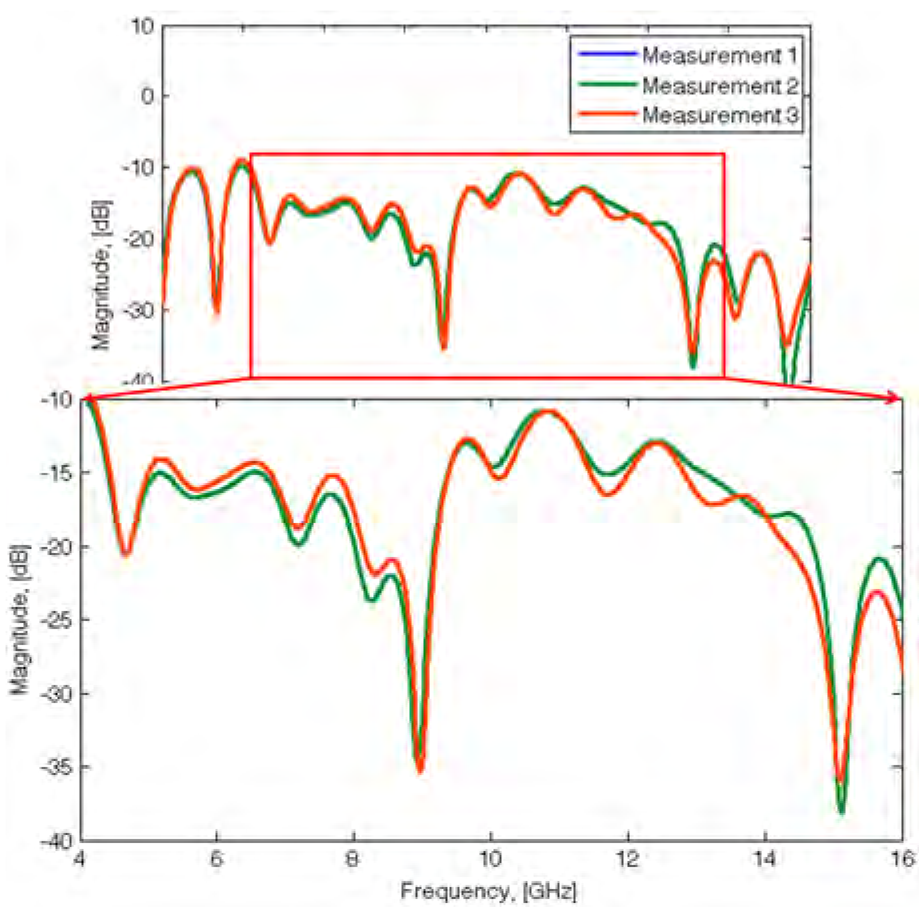

Figure 97. Plot of all three transmission magnitude measurements for the DUT evenly positioned in the foam holder. Plot data are smoothed and gated.

The three measurements form a mean transmission response that is plotted in Figure 98. Note the resonance null present at 8.94 GHz and prominent nulls at 15.11 and 17.48 GHz that appear to represent electric resonance. An immediately striking feature seen in Figure 98 is the appearance of magnetic resonance near the designed resonance frequency of 10 GHz. It might be noted that the designed device is a concentrator so this fact warrants evaluating the presence of resonance. It might be supposed that at the frequency for which a concentrator is designed, the concentrator will have a jump in transmission. However, the concentrator operates by creating a structure with an approximate smooth gradient in constitutive parameters. Each cell of the concentrator produces its particular design permittivity and permeability at its resonance so observed effective resonance of the constructed device makes sense.

A more legitimate concern then may not be the presence of the resonance but the location of the resonance since the device was originally designed for resonance at 10 GHz. However, the cells were inadvertently created with a wider cell trace than was originally designed for resonance at 10 GHz. All other things equal, increasing the width of a cell trace will lower the resonance of the cell. The field concentrator is formed from a variety of over-sized cell traces with a corresponding range of resonance values under 10 GHz. The shift in resonance from 10 GHz can therefore be largely explained by the use of wider cell traces than was originally designed.

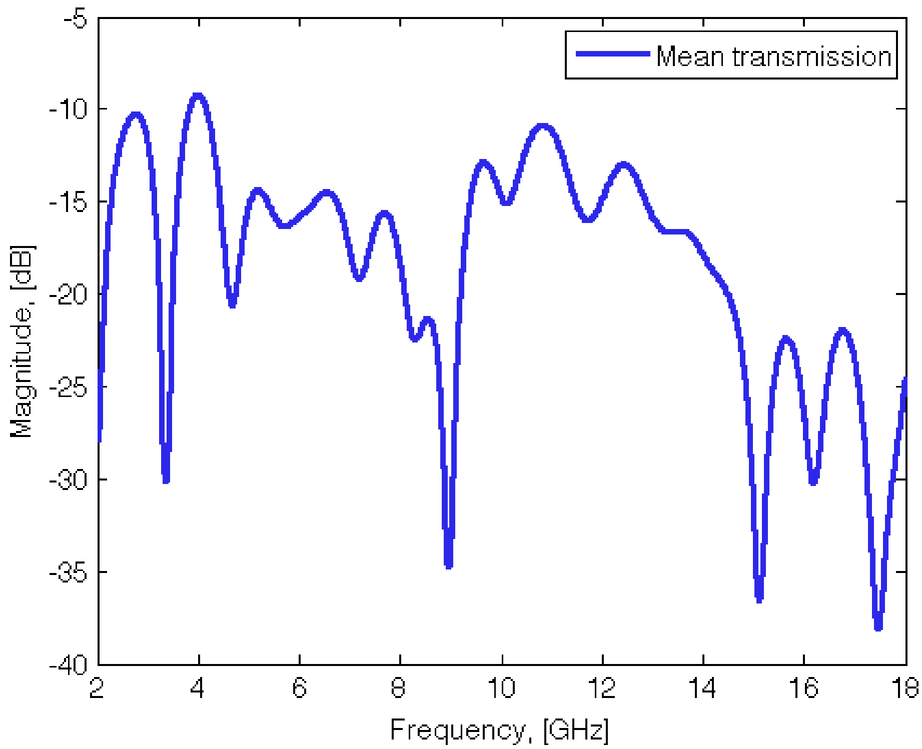

Figure 98. Plot of the smoothed, gated mean transmission magnitude for all three measurements of the DUT evenly or symmetrically positioned in the foam holder.

The mean transmission plotted in Figure 98 is derived from three separate measurements of the constructed field concentrator that were placed centered (evenly) in the foam holder. A measure of the uncertainty in the magnitude of the transmission data is captured in Figure 99. The greatest uncertainty is at 8.94 GHz where the range is 3.6 dB, linking a maximum transmission magnitude of -26.99 dB to a minimum of -30.73 dB. Table 6 shows what appears to be obvious from Figure 99 that there is very good correlation between the measurement samples.

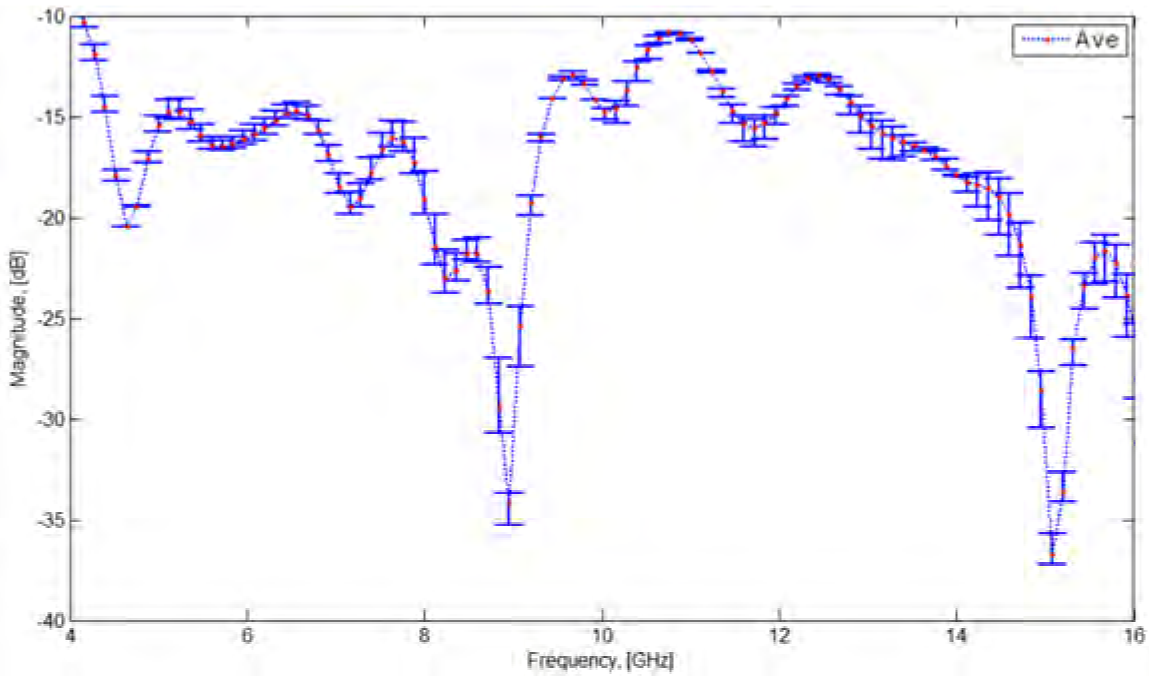

Figure 99. Error bar plot displaying uncertainty in transmission magnitude measurements. Low and high magnitude deviations from the mean measured data are displayed for every 8th frequency point. The plot covers a 12 GHz wide passband about the frequency of interest, 10 GHz. The range of 4 – 16 GHz is plotted instead of the measured range of 2 – 18 GHz to provide a clearer visual depiction of the error bars.

Table 6. Correlation matrix for the DUT evenly positioned in the foam holder.

	Measurement 1	**Measurement 2**	**Measurement 3**
Measurement 1	1.0000	0.9996	0.9610
Measurement 2	0.9996	1.0000	0.9610
Measurement 3	0.9610	0.9610	1.0000

On the related subject of characterizing the maximum possible shifts in frequency response due to placement error in the foam holder, measurements were made for the DUT placed in two different positions. First, the DUT was positioned so that the front of the expansion region was flush with the Styrofoam face on the port 1 side (front flush). This configuration is shown in Figure 100 below. Next, the boards were shifted so that the DUT was positioned with the back of the compression region flush on the port 2 side (back flush).

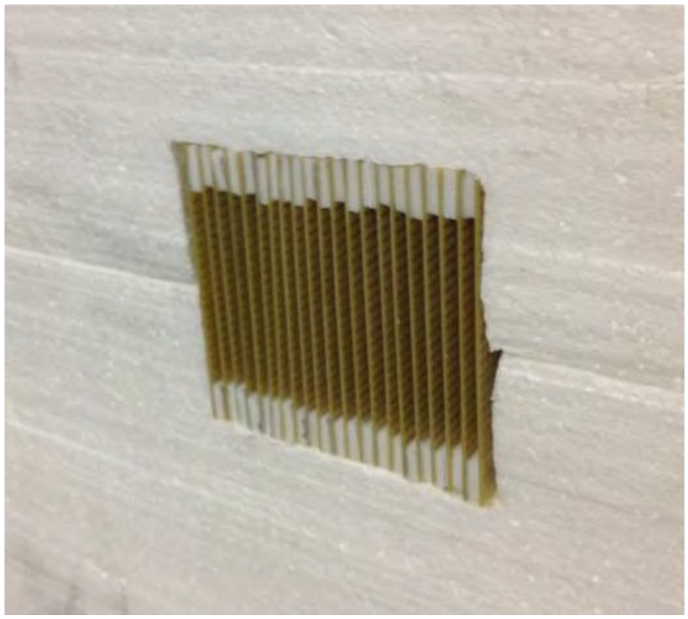

Figure 100. Picture of target mounted so that the expansion section illuminated by port 1 is flush with the Styrofoam holder. This configuration is called front flush.

The mean transmission for evenly placed boards is plotted against transmission for front and back flush positions in Figure 101 below. The results show that below 14 GHz positional variance does not significantly affect transmission. Above that frequency threshold, positional variance appears to change the magnitude of transmission but not the frequency at which that transmission occurs. These magnitude changes are likely due to differences in the shape of the incident waves. The focus beam is designed to produce plane waves equidistant between the lenses so shifting the DUT may expose it to non-planar waves that produce different resonant responses than the incident plane waves for which the DUT was designed.

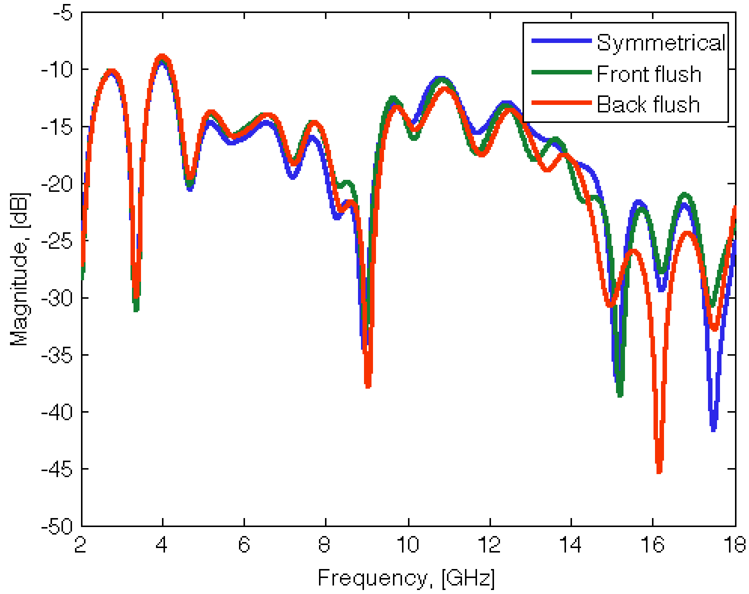

Figure 101. Graphical depiction of the positional dependence of measured transmission data. The mean measurements for the DUT centered in the foam holder are compared to alternate positions of the DUT in the foam holder. Measurements were taken with the boards flush with the foam holder on the port 1 side (front flush) and with the boards flush with the port 2 side (back flush). The results in part provide an idea of the maximum uncertainty in the frequency of certain resonant behaviors.

The transmission measured is S_{21} so it stands to reason that a front flush measurement might provide a more accurate depiction of the response of the concentrator to incident plane waves. If this is true then the major electric resonance response (which generally occurs at a frequency above that of the magnetic resonance) is at 15.11 GHz. The mean transmission of the evenly placed boards displays this resonance along with a resonance at 17.48 GHz.

These resonance values are a valid point of comparison between the measured and simulation data. Unfortunately, not many other comparisons can be made between the simulation and measured data. The simulated S-parameters are collected in an ideal environment with ports placed immediately in front of and behind the concentrator, as was previously shown in Figure 67. This data is, in effect, narrowband. The measured data, while gated, is the superposition of scattering from the concentrator, the test system, and the surrounding environment. The measured data is also subject to random measurement error that does not exist in the simulation. This data is wideband. Indeed, Figure 102 confirms wide differences between the smoothed measured and unsmoothed simulation data for a field concentrator of 20 boards using corner foam spacers.

Even similar resonance behavior between unsmoothed simulation and smoothed measured data is difficult to discern from Figure 102. In order to isolate the existence of effects not modeled in the simulation with corner foam spacers, Figure 102 is replotted to graph unsmoothed simulation data generated from a field concentrator with full foam spacers plotted against the smoothed measured data.

Both Figures 102 and 103 show simulated devices that are more reflective than the device measured and both have noisy patterns. However, a plot of the measured data and simulation data collected for a field concentrator operated with full foam spacers hints at some agreement in resonance frequencies. Figure 103 does display the magnetic resonance at 8.94 GHz that is obtained in the measurements. A possible explanation for the differences between the full foam and corner foam spacer simulations may be that the foam acts as a dampener and cuts some of the resonant noise generated by incident fields.

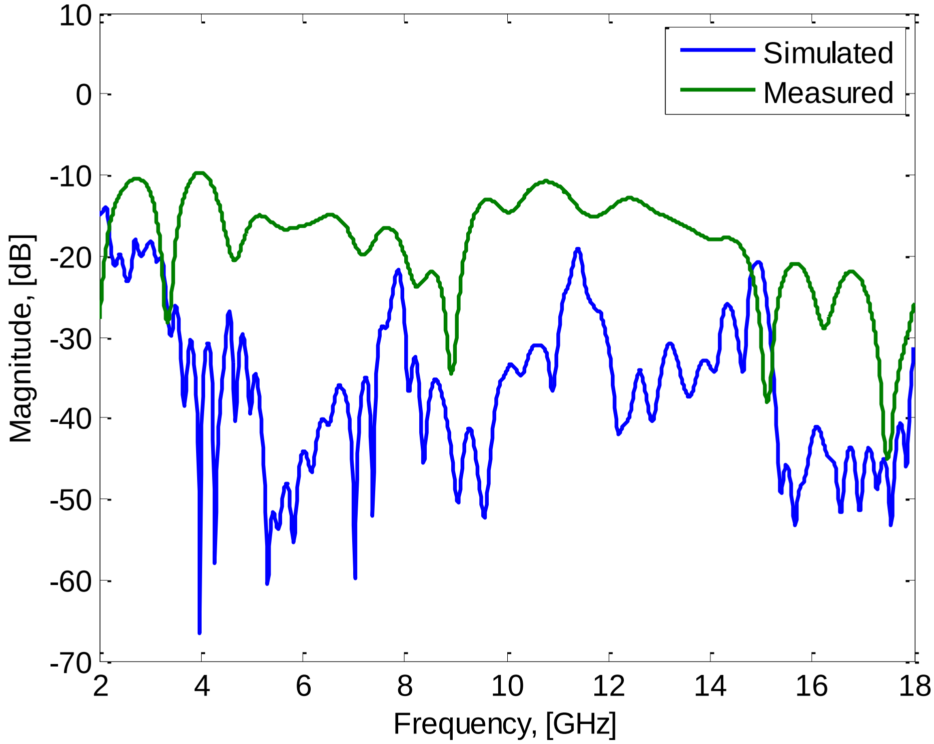

Figure 102. Plot of the smoothed average measured data and the unsmoothed simulation scattering data for 20 circuit boards separated by corner foam spacers (the simulation of the design tested). The measured data demonstrates that the physical construction allows more transmission than simulated. Resonance at 9 GHz in the simulation data is hard to discern.

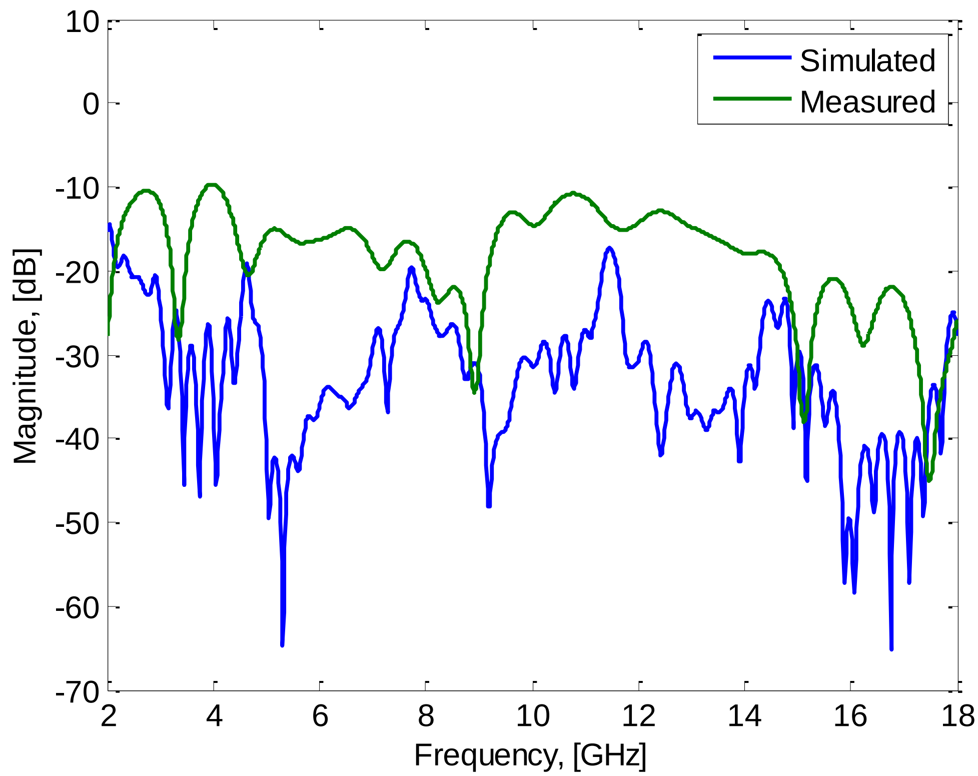

Figure 103. Plot of the smoothed average measured data and the unsmoothed simulation scattering data for 20 circuit boards separated by full foam board spacers. The measured data demonstrates that the physical construction allows more transmission than simulated. There appears to be a good agreement of resonance at or about 9 GHz.

The presence of this resonant noise is hinted at by the vertical displacement in the either plot of measured and simulation data. Figure 102 and 103 appear to show a general increase in transmission for the entire pass band when moving from simulation to measurement that may be fixed in part by altering the dielectric constant and other material characteristics as necessary of the simulated material. Lossy FR4 was used, for example, in simulations but a lossless FR4 circuit appears to have been a better potential simulation material.

Another difference between the simulation and measured data in Figures 102 and 103 is the smooth measured data and the noisy nature of the simulation data which is due to the 1.1% smoothing applied. Figure 104 shows the measured data replotted with smoothed simulation data. 10- and 17-point smoothing is applied to for each spacer configuration.

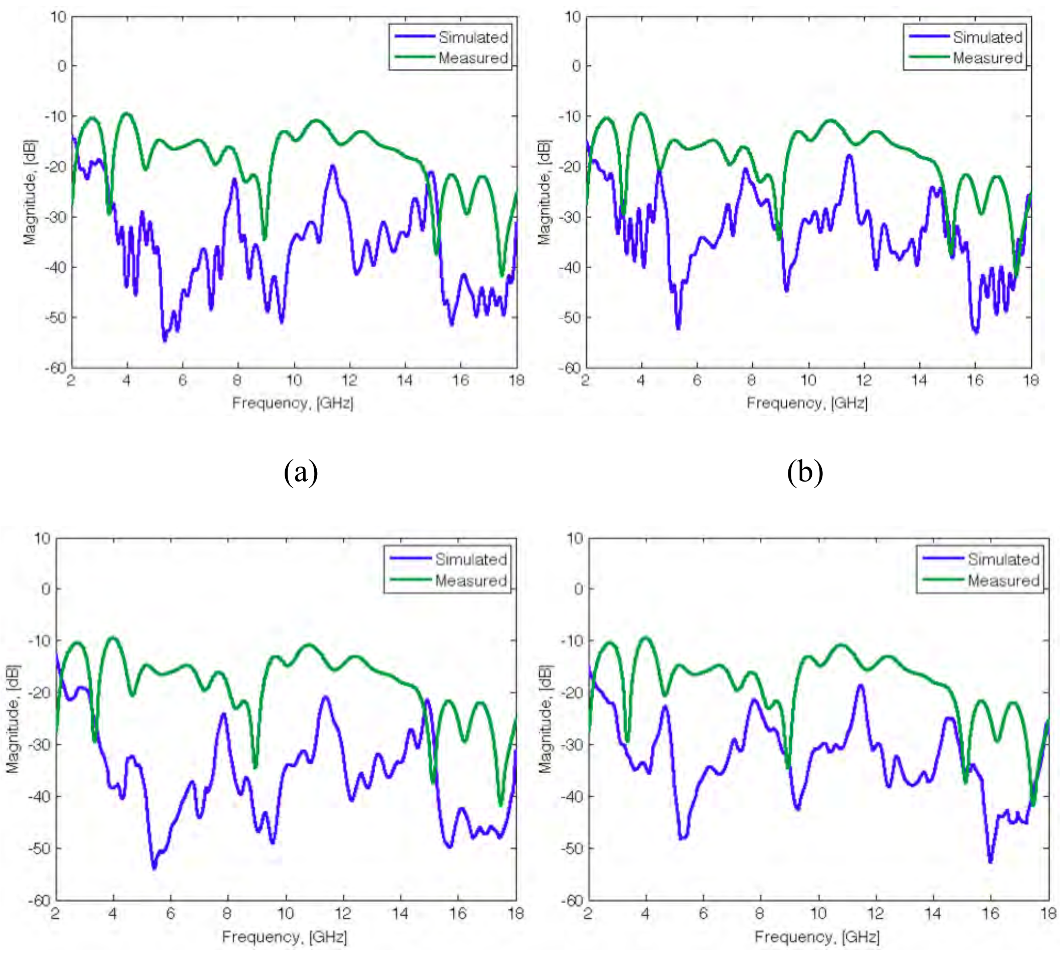

Figure 104. Plots generated to compare average measured and smoothed simulation data. Plots (a) and (b) show simulations data smoothed with a 10-point moving average window while plots (c) and (d) use a 17-point moving average window. Simulation data in (a) and (c) was generated for a 20-board device with corner foam spacers. Simulation data in (b) and (e) was generated for a 20-board device with full foam spacers. Increased smoothing makes the presence and location of resonant peaks far more obvious.

The 17-point smoothing seems to provide the best resolution of the resonance peaks for both spacer configurations although both sets of smoothed simulation data show the resonance frequency around 9 GHz that was measured. The simulation with the full foam spacers further shows a more prominent electric resonance around 16 GHz. Finally, it might be noted, for example, that were it valid to strongly correlate the variations in transmission plotted over 2 – 18 GHz between the measured and simulation data, the additional capacitance of the circuit boards created by such sources as the solder mask appears to have shifted resonance values lower, as is typically the case for raising the capacitance of SRRs.

4.3.2 Field Concentration S-Parameter Data Collection and Analysis.

Testing the field concentration generated by the constructed device required a test setup similar to that shown in Figure 94 earlier. As part of the setup for taking the field concentration measurements, the focus beam system was calibrated again with the SOLT method, gated in a manner described previously, and data was collected at an IF of 50 Hz first and then at the faster rate of 300 Hz when no difference was observed in the scattering curves. The dipole probe used for measuring the fields was characterized first before measuring any data.

Dipole probes are designed to have a small antenna length with respect to the incident wavelength. The tip-to-tip antenna length was measured to be 27 mm long or 13.5 mm per tip on average. Given the size of the antenna tip, resonant behavior was expected for higher frequencies. Determination of the region of measurable transmission was the first measurement made after the probe was calibrated. The motivation to know the measurable transmission region was based purely on a desire to have a probe that can measure the scattering at the frequencies most of interest, that is, 9 – 10 GHz. In order to obtain this information, the probe was connected at its difference port to the port 1 cable and probe transmission measurements or S_{12} data were collected. Figure 105 shows the transmission data of the resulting measurement taken in the middle of the center mount. Field concentration measurements should be taken in a region without discontinuous magnitude changes so Figure 105 shows that the probe will work from 6 – 11 GHz and has resonance behavior at 14.38 GHz.

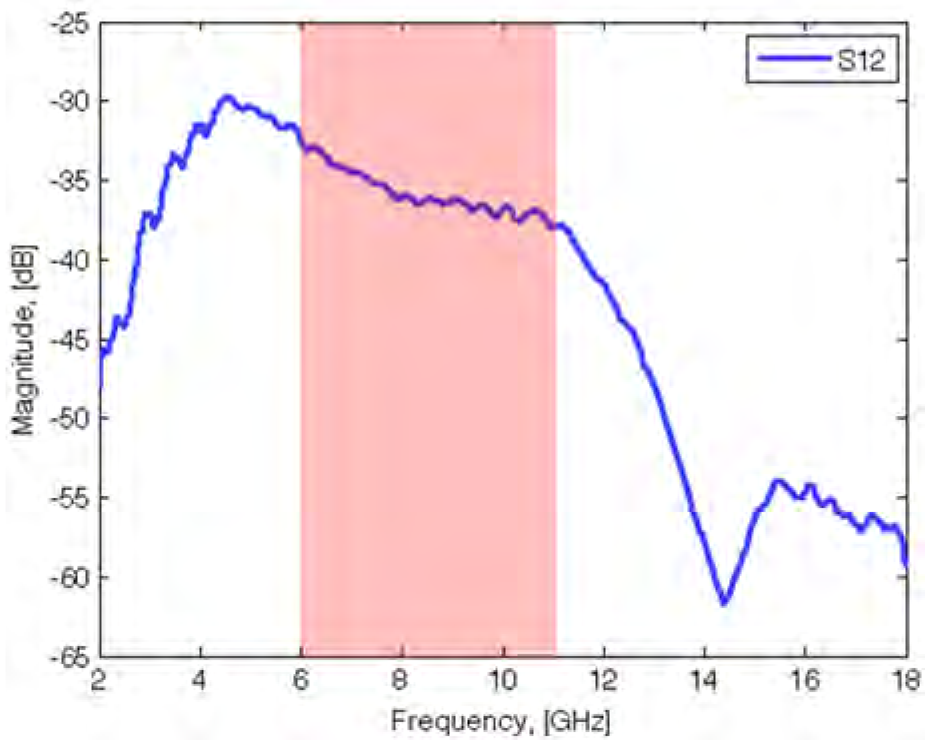

Figure 105. Plot of the frequency-dependent transmission behavior for the dipole probe. Highlighted in red is the region from 6 – 11 GHz of relatively stable magnitude response.

This probe was then used to find the fields in the middle of the center mount with no foam holder to confirm the plane wave illumination that was expected. Figure 106 displays the measured magnitude, whose plot would, if measured over a wide enough distance, look Gaussian. Note that for this and other figures, the abcissa is shown as if looking at the back face of the compression region so negative distances from the center track the left side of the field concentrator and positive distances from the center track to the right side.

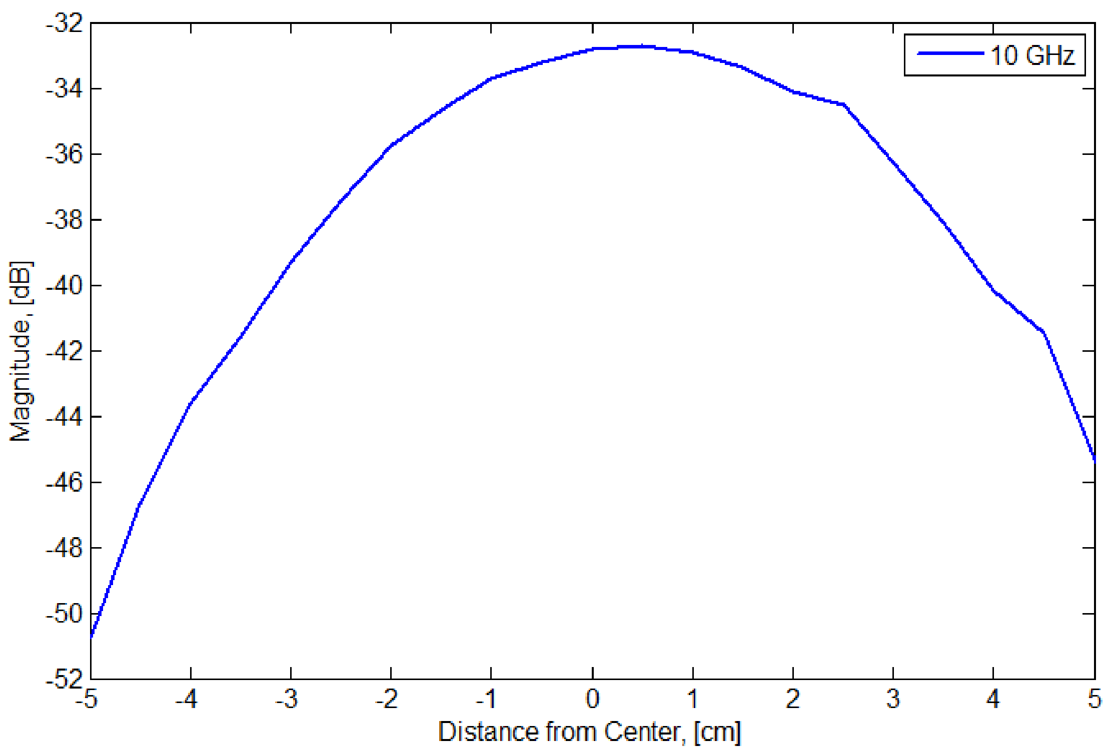

Figure 106. Plot of the transmission magnitude for a Gaussian, collimated 10 GHz signal in the middle of the center mount.

Figure 106 above shows a good distribution of magnitude values while Figure 107 plots the associated phase. A constant phase front is ideal but was not achieved across the width of the center mount tested. However, given that $\pi/8$ rad or 0.397 rad is the standard applied to phase taper for plane waves and the deviations in phase at 10 GHz noted in Figure 107 are limited to 0.25 rad for -4 – 4 cm then at 10 GHz, the waves are planar with phase variation about 0 rad of 0.397 rad or less. Both sets of measurements were made across the width of the center mount or along a line orthogonal to the path of signal propagation.

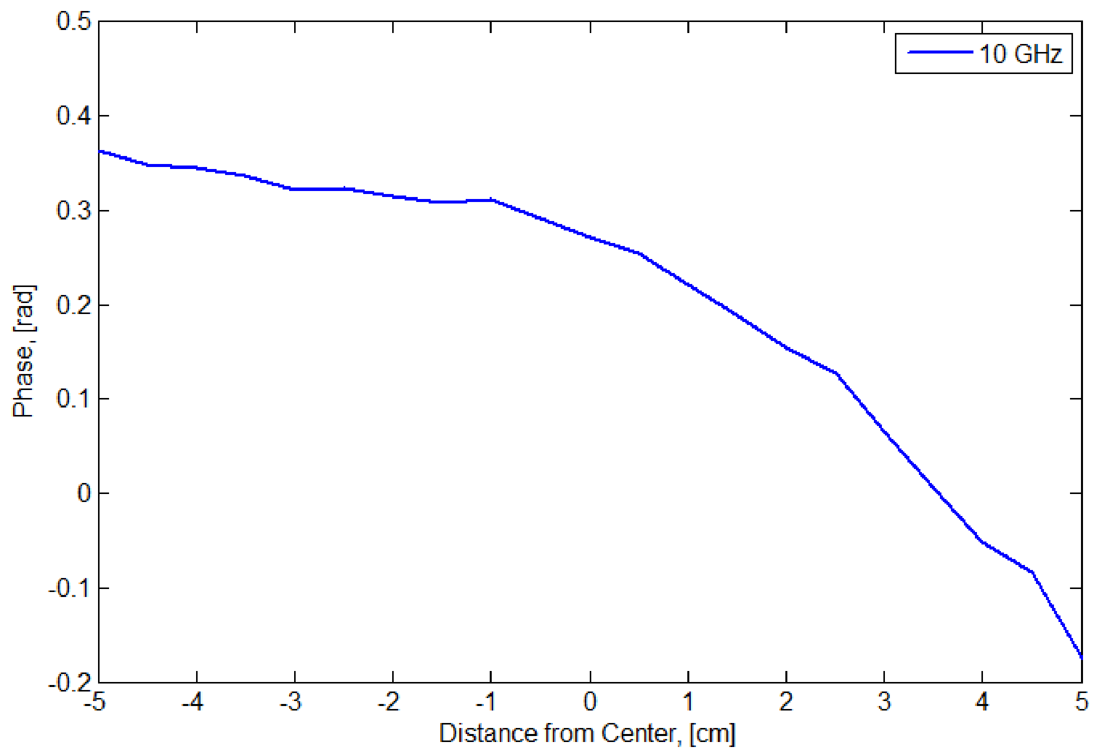

Figure 107. Plot of the transmission phase, in radians, for a Gaussian, collimated 10 GHz signal in the middle of the center mount.

After the measurements of the empty center mount were taken, an initial measurement was made of the free space behind the end of the boards of the field concentrator where the device would be installed. This measurement was made with the foam holder in place and was conducted to reveal any strong diffraction off the edges of the foam holder that might perturb the measurement results. The measurement location was found to be 11.1 cm behind the back of foam and thus over 12 cm from the vertical, bisecting plane of the center mount. Figure 108 shows the magnitude plotted for the scenario described. The plot shows apparent lobing in the magnitude response that indicates the edges of the foam holder do provide constructive and deconstructive interference.

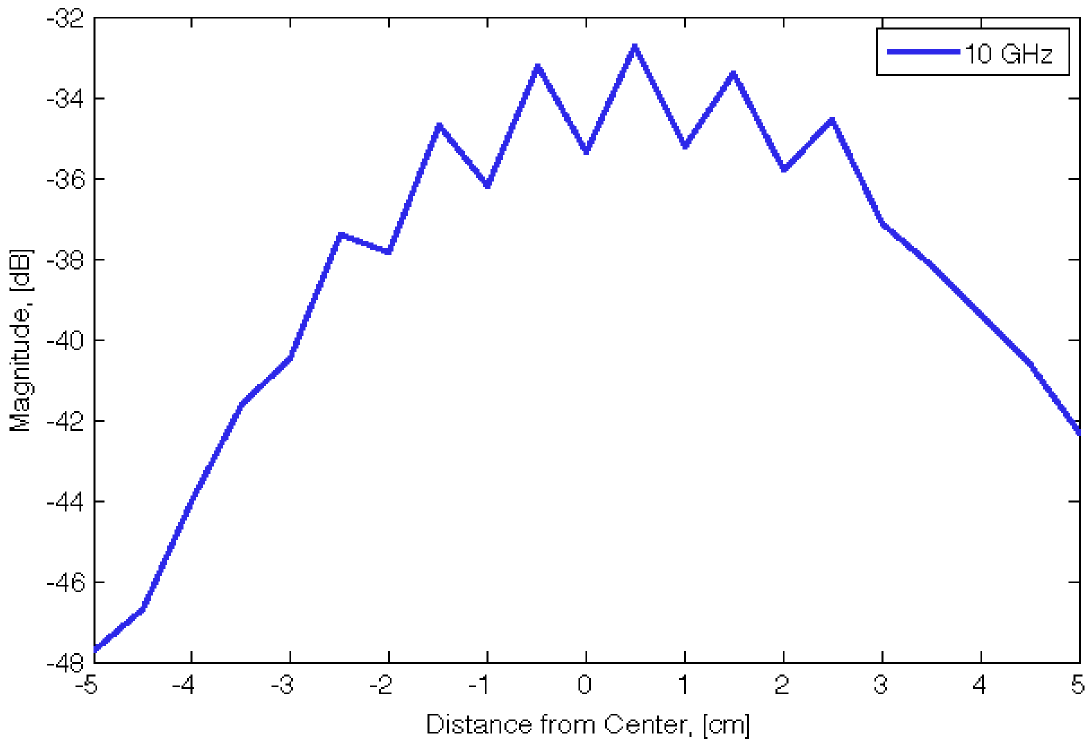

Figure 108. Plot of the transmission magnitude for a Gaussian, collimated 10 GHz signal in the middle of the center mount with the foam holder in place. The saw-tooth peak centered at the origin is indicative of constructive and deconstructive interference due to diffraction from the edges of the foam holder. The asymmetrical nature of the lobing with respect to the center of the foam holder indicates misalignment of likely both my probe and the foam holder with respect to the path of incident plane waves.

Figure 109, plots the phase of the scattering presented in Figure 108. This plot shows that there appears to greater phase variation at this measurement location with respect to the measurement at the center mount shown in Figure 107. This variation makes sense provided the diffraction off the edges of the foam holder as indicated by the magnitude plot, Figure 108. In essence, over the full width of the field concentrator, the field at the back of the concentrator is no longer in phase.

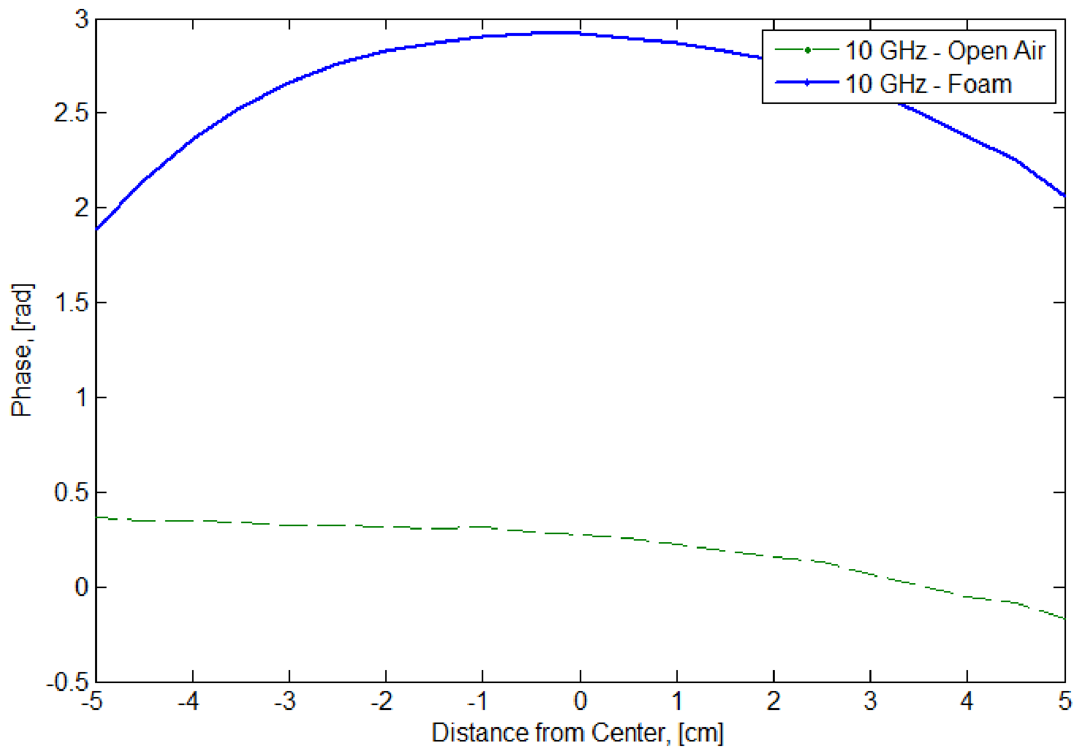

Figure 109. Plot of the transmission phase, in radians, for a Gaussian, collimated 10 GHz signal for an empty foam holder approximately 1 cm behind where the compression section would end or 11.1 cm from the back of the foam holder. The waves here appear less in phase than in the center mount. Here, phase variation is under 0.8 rad whereas for the center mount it was under 0.6 rad.

After these initial measurements, the boards were placed vertically oriented in the foam holder for the initial concentration measurement. The first measurement made was designed to characterize the concentration along the axis orthogonal to the designed compression action (termed secondary concentration in this discussion). In order to collect the necessary data, the probe tip was placed close to the ends as is shown in Figure 110. The scan direction was orthogonal to the propagation of waves and along the air gap seen at the center of the end of each board. A scan was made from 1 cm before the board shown in the foreground of Figure 110 and was terminated 1 cm beyond the last board. On the plots this is travel from positive to negative distances from the center. In Figure 110, the probe tip is closest to the last board. The scan was made 1 mm away from the edge of the boards. Measurements for this and the other board configuration were made at a sampling spacing of 0.5 cm.

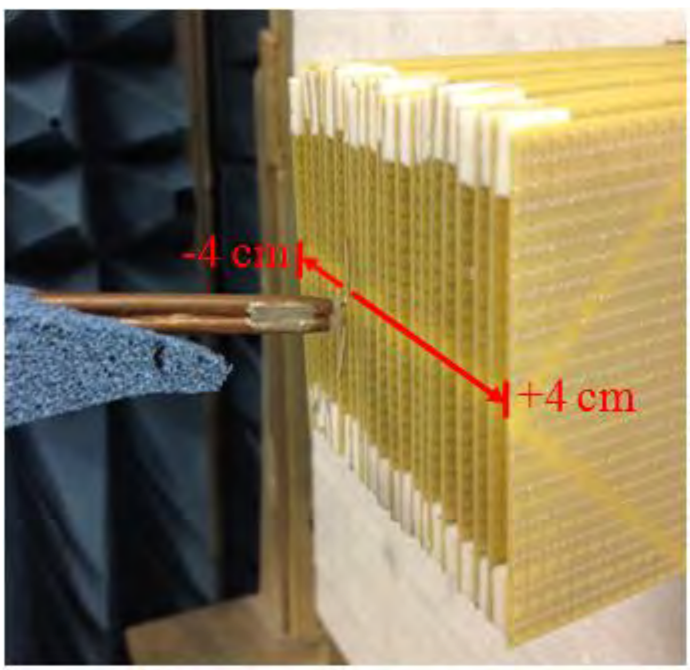

Figure 110. Dipole probe tip in place behind the stack of vertically oriented circuit boards of the field concentrator. Note that the boards are slightly uneven, and tip of the absorber cannot and does not cover the full length of the exposed probe. These observations may play into error observed in the measured results.

Due to the rather low sampling spacing, the transmission magnitude and phase results collected appeared to be rather rough. Therefore these and all other field concentrator measurements results presented have been interpolated at 4 times the normal sampling frequency. Due to the resonance of the dipole probe and the limited accuracy of focus beam measurements below 4 GHz, no results outside of the narrow 6 – 11 GHz evaluation band were included in analysis.

The first plot made for the scan of the vertically oriented circuit boards is shown in Figure 111. A second plot, Figure 112, was made to evaluate concentration at 9 GHz and 10 GHz where the concentrator was found to be magnetically resonant and where the concentrator was designed to operate. Figure 111 is extremely interesting in that it shows that the greatest concentration or magnitude occurs around the designed operating frequency of 10 GHz. Once the dipole probe is behind the concentrator, the concentration jumps dramatically for ranging from 9 – 11 GHz. This jump in concentration happens quickly after the outer edge of the concentrator has been crossed and remains fairly constant at around -42 dB (a 15 dB jump) from about 2 cm into the stack of boards until the probe passes by the last board 6 cm later.

The delay in the magnitude increase may in part be edge effects leading to asymmetric variation in magnitude across the face of the field concentrator or may be due to asymmetry in the placement of the boards. Figure 111 also shows that there is no increased concentration (beyond the broad magnitude increase), near the center of the concentrator except for the measurement at 8 GHz, which does not even have that general rise in magnitude.

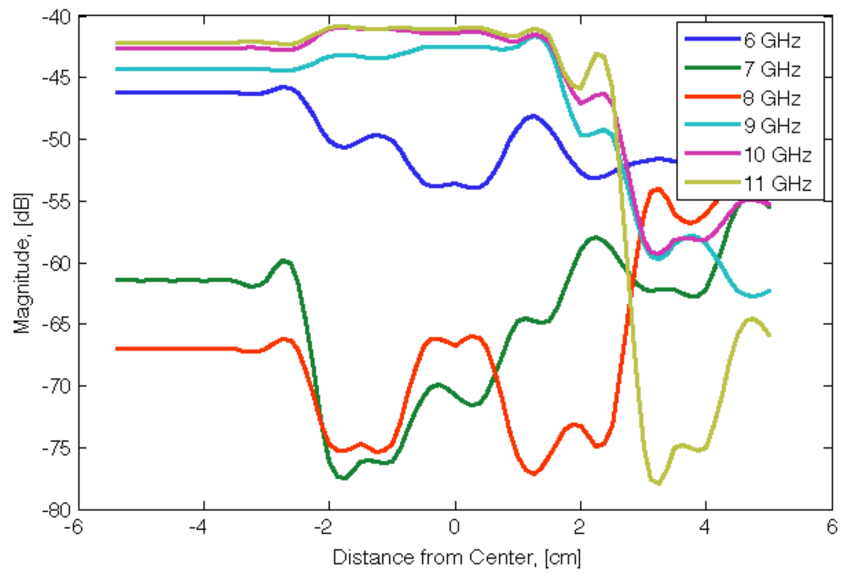

Figure 111. Measured magnitude of transmission at the back of a concentrator with vertically oriented boards for 6 – 11 GHz.

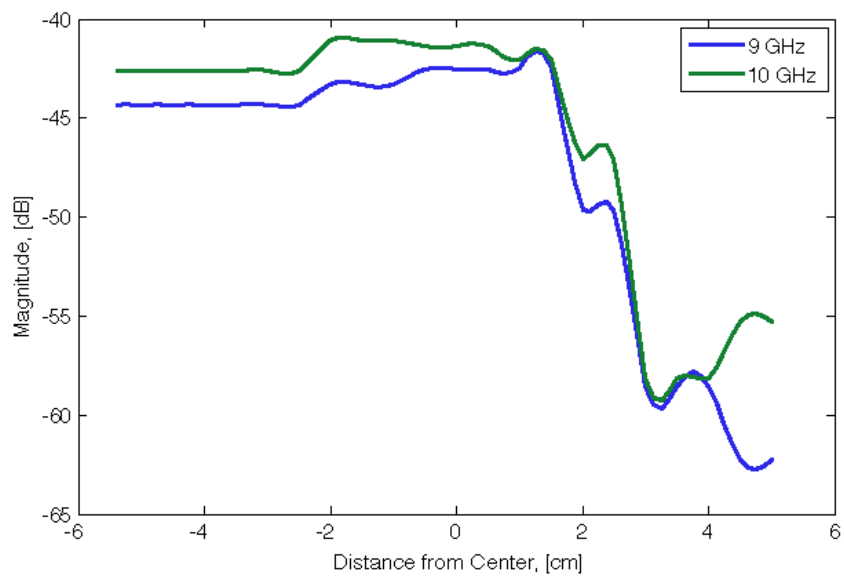

Figure 112. Measured magnitude of transmission at the back of the concentrator with vertically oriented boards for 9 GHz and 10 GHz. Note the broad increase in magnitude but no drop off as the probe moves past the last board at -4 cm.

Figure 113 confirms that the magnitude jump behind the concentrator with 9 GHz and 10 GHz incident waves coincides with a fairly level phase profile. This figure confirms that the span of the field jump is the result of in-phase waves, which is what should be expected. Pendry's perfect lens would not work if waves arrived at the same point but out of phase as has been discussed in Chapter II.

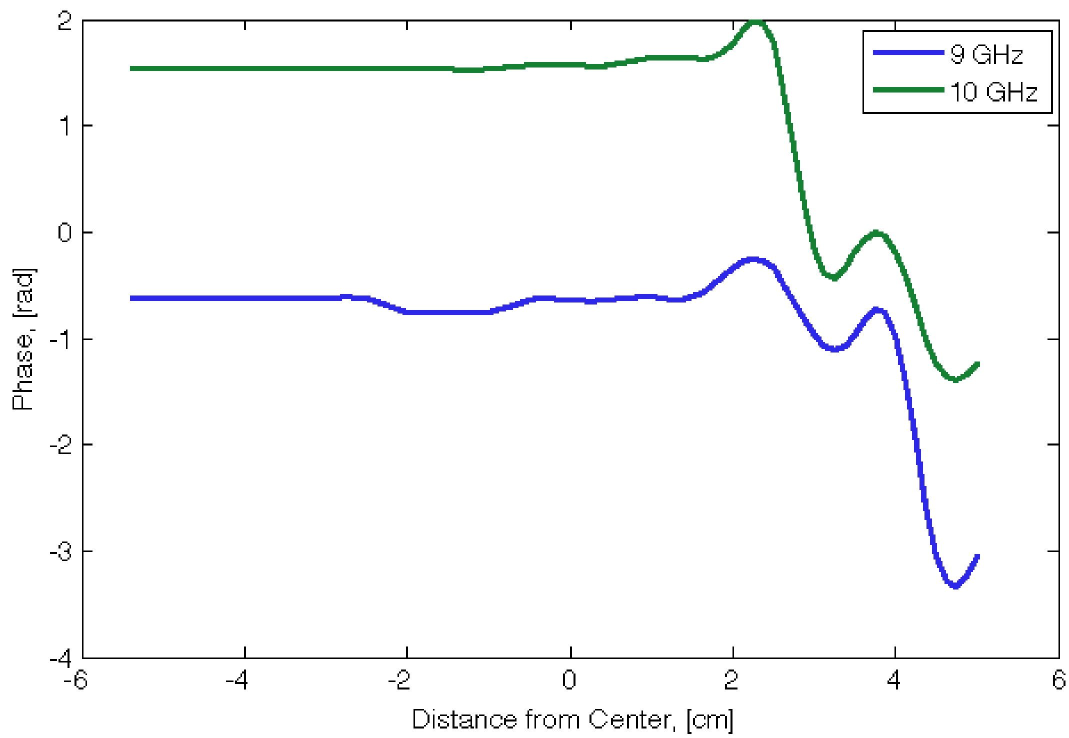

Figure 113. Plot of the transmission phase, in radians, for vertically oriented boards illuminated at 9 GHz and 10 GHz. Note that the exiting waves are planar at both frequencies and for most of the width of the concentrator.

Unfortunately, while the data of Figure 113 seems to confirm the magnitude result of Figure 111, these magnitude results do not match extremely well to the simulation results obtained from CST MWS®. Figure 114 shows the plot of the simulation and measured data for the vertically oriented boards and secondary compression orientation. The simulation data have been normalized and vertically shifted downwards so that they share the same magnitude as the measured data at a distance of -4 cm. This shift is made to make a qualitative comparison of the shape of the magnitude pattern and the relative rises and drops between various parts of the plots. Figure 114 shows some general agreement in the field patterns. The measured data indicate strong fields off the sides of the field concentrator but both the simulation and measured data show a delayed onset in concentration that occurs about 1 cm in from the right edge of the back of the field concentrator. Both simulation and measured data track a rapid rise in magnitude followed by fairly consistent increased field strength or concentration all the way off the left side of the back of the field concentrator. Simulation data predict a peak in concentration at about the center of the face of the compression region that does not appear in the measured data. The absence of this peak may indicate intereference generated in the constructed device that was not predicted or may involve a superposition of the field response of the field concentrator and some diffraction due to the foam holder. Finally, also not apparent in the measured data is the dip in concentration at -2 cm. Different interference patterns in the constructed device due to its assembly may be filling in that null.

The measurement steps taken for the vertically oriented boards were next repeated but for a concentrator that was horizontally oriented with the circuit boards parallel to the ground. The dipole probe was rotated 90° from the orientation shown in Figure 110 so that the arms were parallel to the ground. The travel in displacement direction from the center was the same but with a switch to horizontal polarization the probe was now measuring, from the bottom to the top of the concentrator, the fields along what is the y direction in the simulations, the dimension of compression. This is the primary concentration orientation.

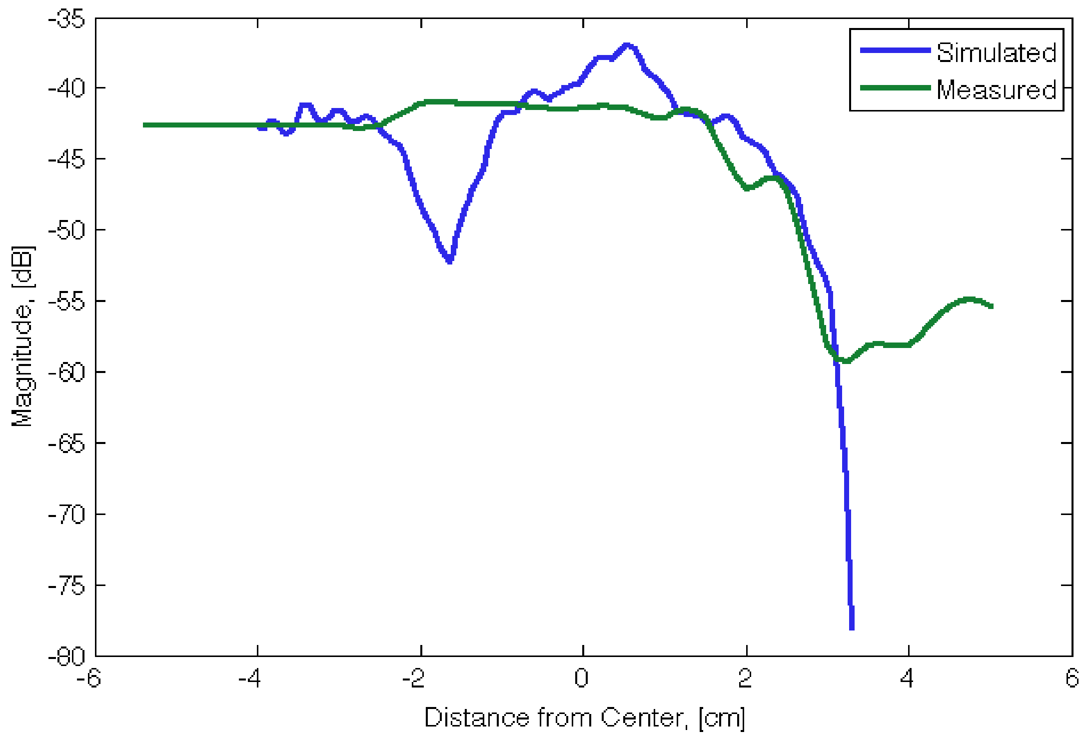

Figure 114. Comparison of simulation and measured transmission magnitude data for vertically oriented boards illuminated at 10 GHz.

Data were again collected for the frequency range 6 – 11 GHz and are presented in Figure 115 below. Several things are immediately noticeable about the form of the data plotted upon reference to Figure 115 showing data for secondary concentration. First, peak concentration is again achieved with frequencies ranging from 9 – 11 GHz about or at the designed resonance. Second, concentration is again not symmetric when it should be however there are key differences from Figure 111 including the fact that compression begins close to the center and dies off at the far side or top of the concentrator. The rise and fall of the concentration is quite apparent because it occurs quite suddenly with respect to position shifts. Not only does the concencentration end sooner but within the concentration regions there appears a slight peak near the center of the concentrator at 1 cm. This peak exists at all measured frequencies. Third, there appears to be a striking and more visible difference in the performance of the concentrator at low or high frequencies. Both the high or 9 – 11 GHz and low or 6 – 8 GHz are grouped within 5 dB of each other and the groups are separated by about 20 dB each.

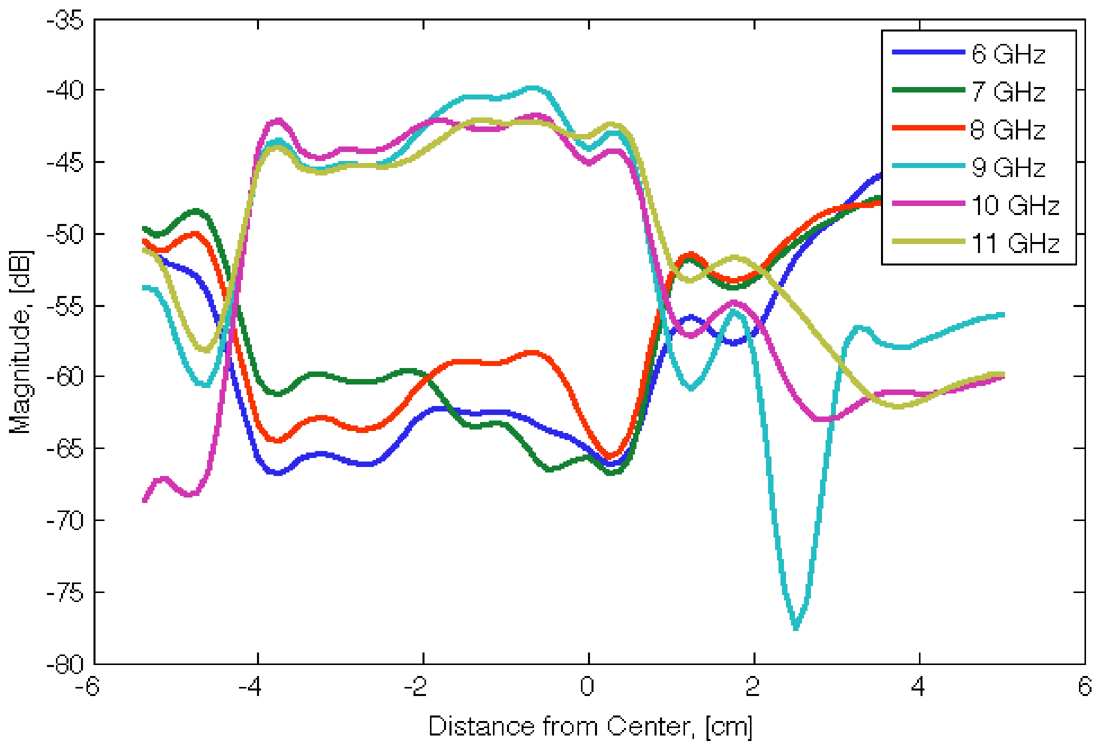

Figure 115. Measured magnitude of transmission at the back of a concentrator with horizontally oriented boards for 6 – 11 GHz.

Figure 116 breaks out the plots for 9 GHz and 10 GHz for further evaluation. Concentration at these two frequencies is fairly similar for a majority of the back of the field concentrator, from -4 – 1 cm. Even towards the edges of the concentrator the performance is fairly similar between the two frequencies. Both plots display a field concentration and rough symmetry about a point to the left of the center of the back of the compression region. The boards were evenly spaced and appeared aligned in the two other dimensions so the concentration patterns about the shifted origin may suggest a skewed placement of the entire field concentrator.

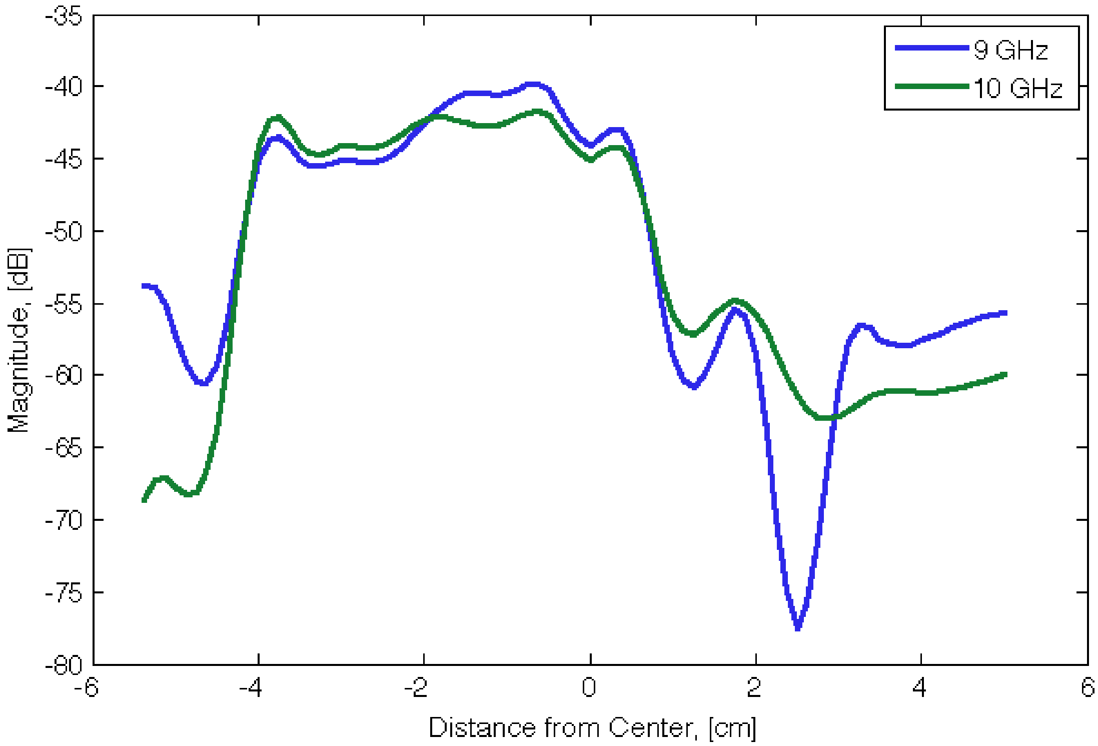

Figure 116. Measured magnitude of transmission at the back of the concentrator with horizontally oriented boards for 9 GHz and 10 GHz.

The phase plot corresponding to the magnitudes plotted in Figure 116 is shown as Figure 117 below. The most prominent feature of this graph is the -4 – 2 cm region in which the phase is comparatively stable compared to the stable at the edges of the concentrator. Indeed, deviations in phase at 10 GHz are limited to 0.25 rad for -4 – 2 cm at the designed resonance so the waves are planar. The waves are planar for a small geometric span at 9 GHz and are nearly planar given deviations in phase of about 0.5 rad for the entire geometric span.

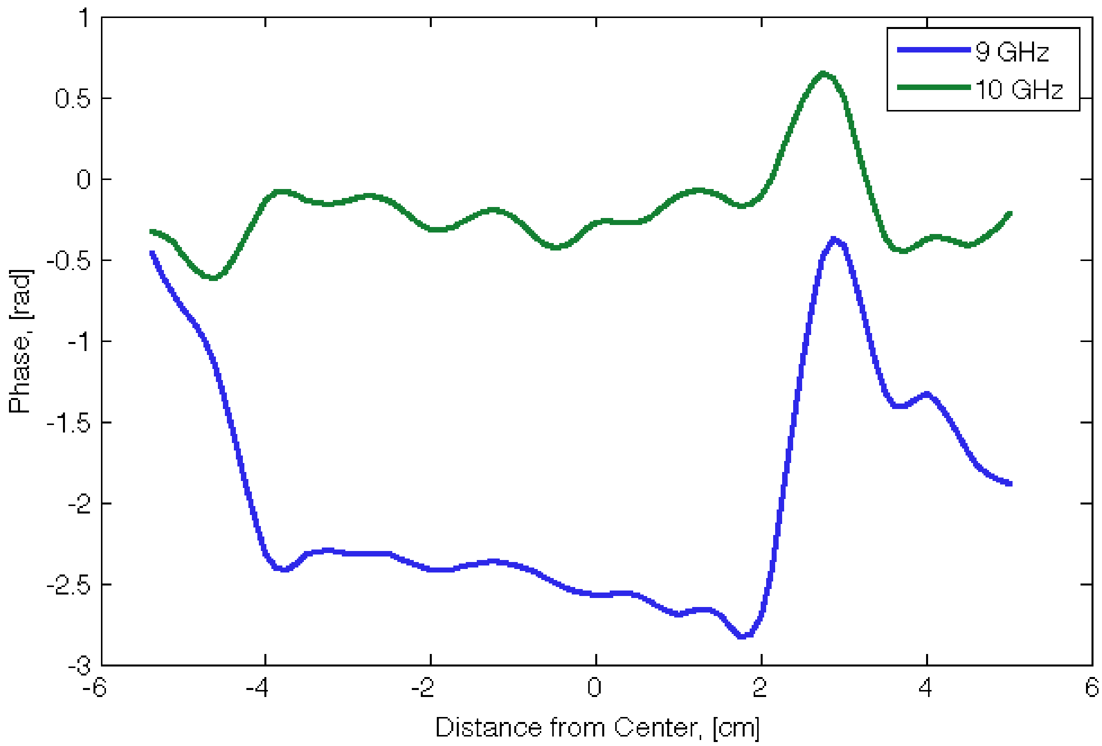

Figure 117. Phase plot for S_{12} and horizontally oriented boards illuminated at 9 GHz and 10 GHz.

After showing related behavior in the magnitude and phase plots for the horizontally oriented boards, a plot was made to compare the simulated and measured magnitudes so as to cement a relationship between the measured and simulation data. The simulation data have again been normalized and vertically shifted downwards so that the main comparison that can be made between the plots is limited to the shape of the pattern.

Figure 118 shows the plot of both sets of data and immediately illustrates that there is not a lot of similarity between the plots. Simulation data show that aside from a local magnituden maximum at the center of the back of the compression region, the magnitude initially increases away from the face and then drops off quickly at the edges. The measured data shows a rapid drop off in magnitude past the left edge of the concentrator and at the center of the back face of the field concentrator. Again, it appears as if the measured data have been shifted. However, even with this shift the concentration behavior noted in the simulation data does not appear in the measured data which show constant concentration.

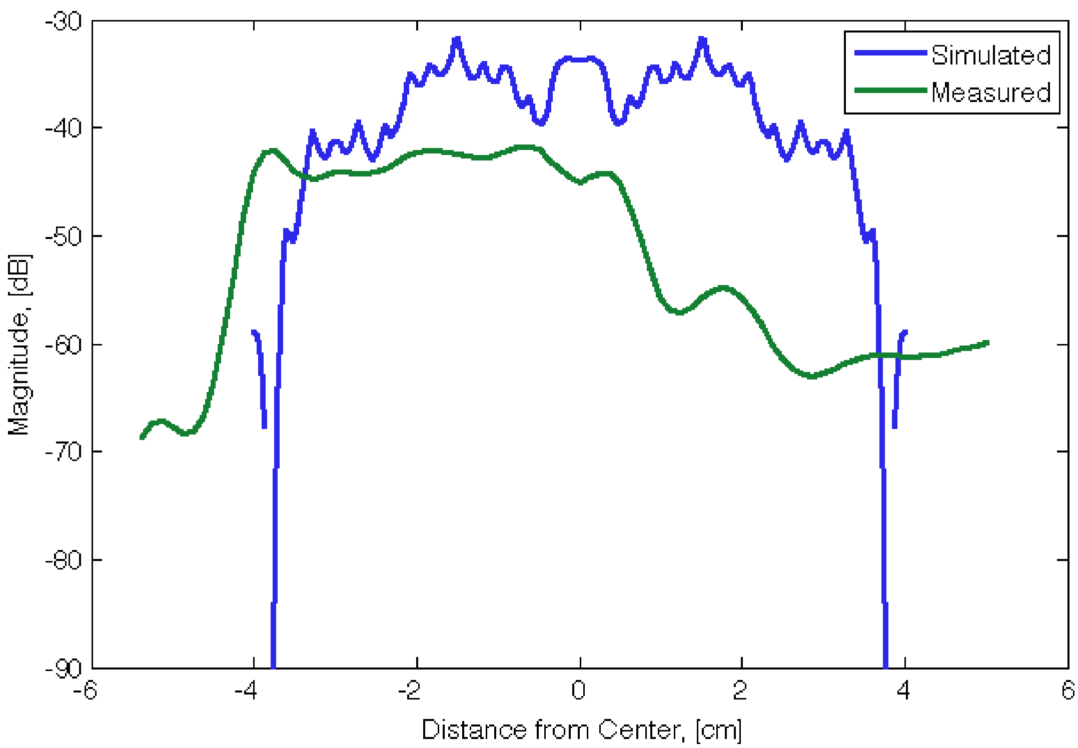

Figure 118. Comparison of simulation and measured transmission data for horizontally oriented boards illuminated at 10 GHz.

At this point, the measured data for each board orientation has been evaluated and compared to the respective simulation data. It is important to close this presentation of measured data with a comparison of measured data for both orientations. A comparison of the magnitude for orientations is shown below in Figure 119. The plot shows some behavior that we might expect along the two orthogonal axes of the back, exit face of the compression region. First, Figure 119 shows that the magnitude of concentration is about the same for both orientations but slightly higher for the primary concentration which is what should be expected. The plot also shows that the concentration point has been shifted left with respect to the origin in the middle of the back face of the compression region. This was not an expected finding. Another and more important observation is that in agreement with simulations, the primary concentration with the horizontally oriented boards is more focused than the secondary concentration in the x direction or orthogonal to the edge of the boards. Observation of the width of the geometric span of increased concentration for each type of concentration supports this conclusion.

Finally, a comparison of phase for the two board orientations in Figure 119 shows matched behavior over the face of the concentrator. Both orientations provide almost an equal percentage of the face of the concentrator over which the fields are in phase. In both cases the region of planar waves corresponds with the observed concentration.

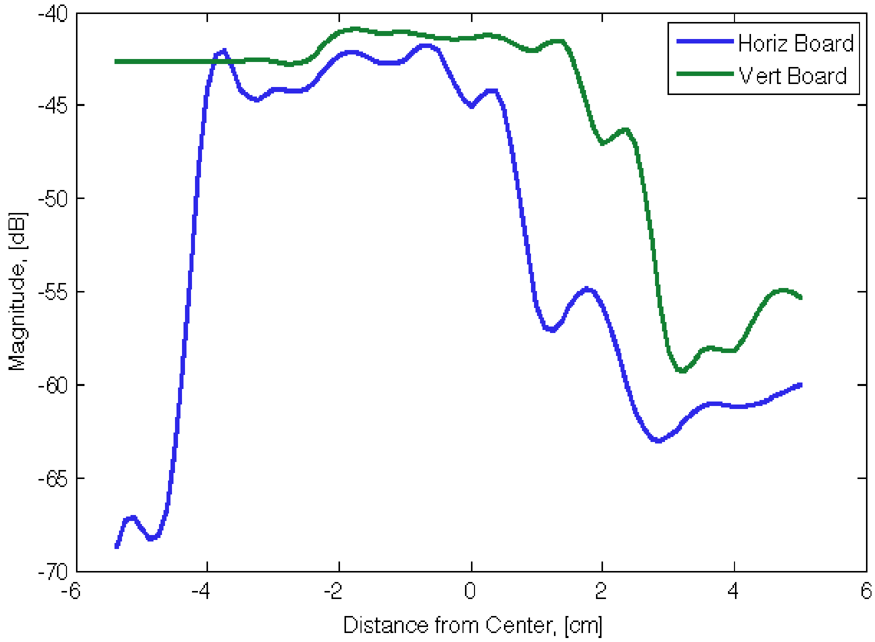

Figure 119. Comparison of measured transmission magnitude for horizontally and vertically oriented boards illuminated at 10 GHz.

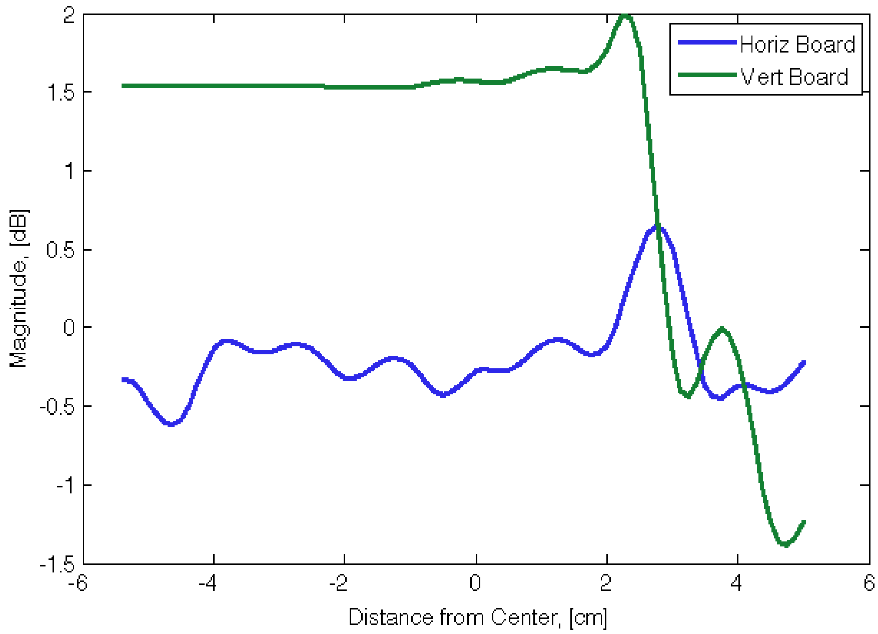

Figure 120. Comparison of measured transmission phase for horizontally and vertically oriented boards illuminated at 10 GHz.

V. Conclusions and Recommendations

5.1 Metamaterial Field Concentrator Summary

In summary, this thesis serves to validate an AFIT-developed metamaterial rapid design process by using the process to go from paper design to physical construction of a metamaterial device. This thesis contributes to AFIT's rapid design process by improving it and making it capable of producing optimized metamaterials to use as homogeneous approximations to theoretical and unachievable abstractions such as continuous, anisotropic materials.

This thesis leveraged TO to construct a novel device that responds to linearly polarized fields and concentrates these fields in a single dimension. The device was designed for optimizing 10 GHz using metamaterial cells similar to those found in [55] but with three geometric characteristics varied $\{a_\theta, s, r\}$. In combination with these metamaterial cells, basic circuit board materials were evaluated on the industry standard 0.787 mm FR-4 using 1-ounce copper foil.

Full wave electromagnetic simulations were conducted of 2-D continuous, anisotropic materials as well as 3-D homogenized versions of the field concentrator to obtain the S-parameters of the device and the total field concentration at various postion planes behind the compression section. Simulations of the device display field concentration. In particular, simulations showed that compression is better in the *y* direction (parallel to the height of the concentrator), as should be expected. A band of concentration is seen across the front of face of the compression section in the *x* direction (parallel to the width of the concentrator). The simulations showed that this band does not stretch the entire width of the concentrator due to the interaction of edge scattering with the central compression region along the *x* direction (parallel to the length of the concentrator). The concentration point is best located within 3 mm of the back face of the compression region before the fields diverge. Simulated S-parameter measurements showed a magnetic resonance at about 9 GHz that coincides with strong field concentration.

The physical DUT was measured with a focus beam system that collects the S-parameters of the entire concentrator. Field concentration was measured using the dipole probe to collect the magnitude of transmission, $|S_{12}|$. The results suggest that there appears to be concentration in both directions, per the simulation results. The edge effects appear to be stronger for vertically oriented bars but nonetheless concentration appears to exist. Further, field concentration appears to be best suited at frequencies near the magnetic resonance of about simulated resonance frequency of 9 GHz that was also confirmed experimentally. However, these observations must be caveated. The measurements reported herein are very preliminary and need to be more fully validated. Validation could be against published computational or measured data or canonical problems with analytic solutions. Once validated, far more might be concluded about what concentration field concentration was achieved.

5.2 Recommendations for Future Research

There are a number of suggested avenues that could be taken separately or together to improve and build upon the research presented in this thesis. These recommendations relate to the basic design of the field concentrator, the rapid design process, and the measurement system utilized to characterize the scattering and field concentration of the device.

5.2.1 Metamaterial Field Concentrator Recommendations.

The design of the concentrator developed for this thesis is by no means settled and the approach used to design it and physically construct it could be changed. The first possible change suggested is to create a cylindrically shaped concentrator. Cylindrical cloaks have been extensively tested so there are plenty of designs out there that could serve as blueprints for a new cylindrical concentrator. This cylindrical design would still be easy to test with the focus beam system and would have a decided advantage in the new compact measurement system developed to fit in the BANTAM.

The current design could only fit in the two inch gap provided for the test samples if it was cut to size or if the boards were laid flat. The first approach would alter the concentration effects and these changes would be compounded by the PEC conditions encountered in the compact measurement system that would in effect create a vertical structure of infinite extent. Further, because only vertical polarizations are generated in the compact measurement system, boards laid flat would produce entirely different constitutive parameters that they were not designed for.

The field concentrator could be designed to provide a different amount or type of concentration. That is, concentration need not theoretically be designed to direct all incident fields to one particular point. The location of the concentration with respect to the back of the compression section could be altered, and an attempt to build a concentrator that responds to different polarizations could also be explored to make a more useful device. Finally, greater concentration might be achieved by employing concentrator design employing two-axis compression instead of the design employed in this thesis that only concentrates along a single dimension.

5.2.2 Rapid Design Approach Recommendations.

There are numerous methods in which the rapid design approach could and should be improved. For example, the approach employed for this thesis used small metamaterial cells found in [55]. There is no overwhelming reason why other metamaterial cells could not be used. Otherwise, if the currently implemented cell is used again, a larger vector of geometric characteristics could be employed to more finely tune the constitutive parameters.

Another seemingly obvious potential for improvement is the optimization of the S-ratio. Assuming a concentric design is employed in future testing, improvement of this portion of the optimization process would be an avenue worth exploring. Only combinations with *S3* sizes up to and including 16 were tested so a larger number of combinations of ratios could be tested by increasing the maximum size of *S3*. Further, only the metric of mean, low, and high values were developed to select an S-ratio with which to build the concentrator. The complicated nature of the relationships between the expansion and each of the three compression regions may prevent development of a more extensive algorithm for distinguishing one ratio to the next. Optimizing for one area (expansion or one of the three compression regions), will degrade the performance of the constitutive parameter matching in another section so at some level, the designer will have to make a somewhat arbitrary decision on which ratio to pick. This decision will be based on both manufacturing considerations and on considerations of what section performance is most important for optimization considering the proposed application of the designed device.

Another area for optimization is the material on which the designs are printed. A cylindrical design would require a flexible material like TLY-5. A rigid device such as the rectangular concentrator built for this thesis would have access to a wider array of PCB. In any event, given the basic selection of metamaterial trace and circuit board material sets has a large impact on the range of achievable constitutive parameters.

5.2.3 Field Concentration Measurement Recommendations.

S-parameters for the constructed device as well as field concentration measurements were made with AFIT's focus beam measurement system. The focus beam system is a proven design that has been extensively used for research both here at AFIT and at the Georgia Tech Research Institute. Unfortunately, the method of using the focus beam system in conjunction with a translation table a dipole probe is new and requires improvement.

The first improvement would involve finding a replacement for the translation table or finding a better way to use the translation table with existing software. Translation of the dipole probe along two axes is necessary to align the probe and concentrator and obtain the necessary measurements. The translation table currently can move in two axes but does not respond well to button pushes commanding a desired position. More frequently than desired, the table will experience position drift of several millimeters during a test because its response time to a previous requested position change is sometimes neither immediate nor existent.

There is sufficient time spent adjusting the position to the desired value or simply walking over to the table to set a new position that future work might benefit from tying position commands to software on a computer in the microwave laboratory. This connection could be made via the voltage control connections on the translation table's position control panel. The benefit of the use of software is both the exact position setting but also the time saved of having to go physically operate the table. This software would be even more useful if it was able to tie together the NWA and data collection. That is, using software to control the position of the probe on the translation table and automate position shifts, single trigger operation of the NWA, and data collection would be ideal.

The second improvement would be building a dipole probe with improved performance over the frequency band 2 – 18 GHz. The performance of the current probe degrades after 11 GHz due to the resonance of the probe. The arms of the dipole probe should also be reduced in length so that when buried in pyramidal absorber, the cantilever effect of the absorber on the arms can be minimized.

The third improvement would be an improved design for the brace holding the hybrid and the stand that provides vertical height adjustment. The current brace for the hybrid was made from some aluminum scrap and meant as nothing more than a quick, passable means to hold the dipole probe. The current brace can hold the hybrid vertically or horizontally but neither position is well balanced. The stand holding the brace has legs that are too low for the hybrid and make measuring the center of the DUT difficult, particularly in horizontal positions of the hybrid. These legs should be raised. Ideally, there could be a way to provide fine, repeatable vertical displacements of the probe. Automated up and down features and commands to a desired vertical position would be preferred.

Bibliography

[1] "Applying Error Correction to Network Analyzer Measurements". Agilent Technologies, Inc.© application note, 2002.

[2] "The Simulation Method". CST Microwave Studio® help file, 2010.

[3] Aydin, Koray, Kaan Guven, Nikos Katsarakis, Costas Soukoulis, and Ekmel Ozbay. "Effect of disorder on magnetic resonance band gap of split-ring resonator structures," *Opt. Express*, 12(24):5896–5901, 2004.

[4] Balanis, Constantine A. *Advanced Engineering Electromagnetics.* John Wiley & Sons, Inc., Hoboken, New Jersey, 1989.

[5] Bérenger, Jean-Pierre. "A Perfectly Matched Layer for the Absorption of Electromagnetic Waves," *J. Comput. Phys.*, 114:185–200, 1994.

[6] Bérenger, Jean-Pierre. "Perfectly matched layer for the FDTD solution of wave-structure interaction problems," *IEEE Trans. Antennas Propag.*, 44(1):110–117, 1996.

[7] Brown, J. "Artificial Dielectrics Having Refractive Indices Less Than Unity," *IEEE Monograph No. 62R*, 100(5):51–62, 1953.

[8] Cai, Wenshan, Uday K. Chettiar, Alexander V. Kilishev, and Vladimir M. Shalaev. "Optical cloaking with metamaterials," *Nature Photon* **1**, 224–227, 2007.

[9] Chen, L. F. *Microwave Electronics: Measurement and Materials Characterization*. John Wiley & Sons, Inc., 2004. ISBN 040844922.

[10] Chen, Xudong, Tomasz M. Grzegorczyk, Bae-Ian Wu, Joe Pacheco, and Jin Au Kong. "Robust method to retrieve the constitutive effective parameters of meta-materials," *Phys. Rev. E: Stat. Phys., Plasmas, Fluids*, 70(1), 2004.

[11] Clemens, M., E. Gjonaj, P. Pinder, T. Weiland. "Numerical simulation of coupled transient thermal and electromagnetic fields with the finite integration method," *IEEE Trans. Magn.*, 36(4): 1448–1452, 2000.

[12] Clemens, M. and T. Weiland. "Discrete Electromagnetism with the Finite Integration Technique," *Progress Electromagn. Res. (PIER)*, vol. 32, pp. 65–87, 2001.

[13] Ekmecki, Evren and Gonul Turhan-Sayan. “Metamaterial Sensor Applications Based on Broadside-Coupled SRR and V-Shaped Resonator Structures,” *Antennas and Propagation (APSURSI), 2011 IEEE International Symposium*, 1170–1172, 2011.

[14] Engheta, Nader. “Is Foster’s Reactance Theorem Satisfied in Double-Negative and Single-Negative Media?” *Microw. Opt Tech. Lett.*, 39(1):11–14, 2003.

[15] Engheta, Nader and Richard Ziolkowski (editors). *Metamaterials: Physics and Engineering Explorations*. John Wiley and Sons, Inc., Hoboken, New Jersey, 2006.

[16] Hecht, Eugene. *Optics*. Pearson Education, Inc., San Francisco, California, 2002.

[17] Hohlfield, R. and N. Cohen. “Self-Similarity and the Geometric Requirements for Frequency Independence in Antennae,” *Fractals*, 7(1):79–84, 1999.

[18] Humphries, S., Jr. “Finite-element Methods for Electromagnetics,” 2010.

[19] Inglesfield, J. E. “A method of embedding,” *J. Phys. C: Solid State Phys.* 14, 3795–3806, 1981.

[20] Jiang, Wei Xiang, Tie Jun Cui, Qiang Cheng, Jessie Yao Chin, Xin Mi Yang, Ruopeng Liu, and David R. Smith. “Design of arbitrarily shaped concentrators based on conformally optical transformation of nonuniform rational B-spline surfaces,”*Appl. Phys. Lett.*, 92(26), 264101, 2008.

[21] Jin, Jianming. *The Finite Element Method in Electromagnetics*. John Wiley & Sons, Inc., New York, 2002.

[22] Khaleel, H., H. Al-Rizzo, Y. Rahmatallah, D. Rucker, and S. Mohan. “An investigation on the effect of bending of split ring resonators,” *Antennas and Propagation Society International Symposium*, 1490, 2011.

[23] Kock, Winston E. “Metal-Lens Antennas,” *Proceedings of the IRE*, 34(11):828–836, 1946.

[24] Kundtz, N. B., D. R. Smith, and J. B. Pendry. “Electromagnetic Design with Transformation Optics,” *Proc. IEEE.*, 99(10): 1622–1633, 2010.

[25] Langford-Smith, F. (editor). *Radiotron Designer’s Handbook*. RCA Victor Division, Harrison, New Jersey, fourth edition, 1954.

[26] Leonhardt, Ulf. “Optical Conformal Mapping,” *Science*, 312(5781):1777–1780, 2006.

[27] Liu, Ruopeng, Tie Jun Cui, Da Huang, Bo Zhao, and David Smith. "Description and explanation of electromagnetic behaviors in artificial metmaterials based on effective medium theory," *Phys. Rev. E.* 76, 026606, 2007.

[28] Liu, T., D. Smith, and R. Liu., Eds.,. *Metamaterials: Theory, Design, and Applications*. Springer, New York, 2010.

[29] Liu, Xing-Xang. and Andrea. Alu. "First-principle homogenization of magnetodielectric metamaterial arrays," *Antennas and Propagation (APSURSI), 2011 IEEE International Symposium*, 1522–1525, 2011.

[30] Lundell, Christopher. *Characterization and Measurement of Passive and Active Metamaterial Devices*. MS thesis, AFIT/GE/ENG/10-15. School of Electrical and Computer Engineering, Air Force Institute of Technology (AU), Wright-Patterson AFB OH, 2010.

[31] Luo, Yu, Hongsheng Chen, Jiangjing Zhang, Lixin Ran, and Jin Au Kong. "Design and analytical full-wave validation of the invisibility cloaks, concentrators, and field rotators created with a general class of transformations," *Phys. Rev. B.*, 77(12), 2008.

[32] Marklein, R. "The finite integration technique as a general tool to compute acoustic, electromagnetic, elastodynamic, and coupled wave fields," in *Review of Radio Science: 1999–2002*, 201–244, 2002.

[33] Marqués, Ricardo, Francisco Medina, and Rachid Rafii-El-Idrissi. "Role of bianisotropy in negative permeability and left-handed metamaterials," *Phys. Rev. B.*, 65(14), 2002.

[34] Martini, E., G. M. Sardi, F. Caminita, and S. Maci. "Retrieval of metamaterial constitutive parameters through a generalization of the Bloch theory," *ICECom, 2010 Conference Proceedings*, 1–4, 2010.

[35] Munk, Ben A. *Frequency Selective Surfaces: Theory and Design*. John Wiley & Sons, Inc., New York, 2000.

[36] Munk, Ben A. *Metamaterials: Critique and Alternatives*. John Wiley & Sons, Inc., Hoboken, New Jersey, 2009.

[37] Munk, Ben A., Dan S. Janning, Jonothan B. Pryor, and Ronald J. Marhefka. "Scattering from surface waves on finite FSS," *IEEE Trans. Antennas Propag.*, 49(12):1782–1793, 2001.

[38] Munteanu, I. and T. Weiland. “RF & Microwave Simulation with the Finite Integration Technique – From Component to System Design,” *Scienctific Computing in Electrical Engineering*, 11(3):247–260, 2007.

[39] Newton, Isaac. *Opticks: Or, A treatise of the Reflections, Refractions, Inflexions and Colours of Light.* London, 1704.

[40] Nicolson, A. M. “Broad-band microwave transmission characteristics from a single measurement of the transient response,” *IEEE Trans. Instrum. Meas.*, 17(4):395–402, 1968.

[41] Nicolson, A. M. and G. F. Ross. “Measurement of the intrinsic properties of materials by time-domain techniques,” *IEEE Trans. Instrum. Meas.*, 19(4):377–382, 1970.

[42] Oughstun, Kurt and Natalie Cartwright. “On the Lorentz-Lorenz formula and the Lorentz model of dielectric dispersion,” *Opt. Express*, 11(13):1541–1546, 2003.

[43] Paul, J. “Rapid Design of Metamaterials,” unpublished.

[44] Pelosi, G. “The finite-element method, Part I: R. L. Courant [Historical Corner],” *IEEE Trans. Antennas Propag.*, 49(2):180–182, 2007.

[45] Pendry, J. B. “Negative Refraction Makes a Perfect Lens,” *Phys. Rev. Lett.*, 85(18):3966–3969, 2000.

[46] Pendry, J. B., A. J. Holden, D. J. Robbins, and W. J. Stewart. “Low frequency plasmons in thin-wire structures,” *J. Phys.: Condens. Matter*, 10(22):4785–4809, 1998.

[47] Pendry, J. B., A. J. Holden, D. J. Robbins, and W. J. Stewart. “Magnetism from conductors and enhanced nonlinear phenomena,” *IEEE Trans. Microwave Theory Tech.*, 47(11):2075–2084, 1999.

[48] Pendry, J. B., A. J. Holden, W. J. Stewart, and I. Youngs. “Extremely Low Frequency Plasmons in Metallic Mesostructures,” *Phys. Rev. Lett.*, 76(25)4773–4776, 1996.

[49] Pendry, J. B., D. Schurig, and D. R. Smith. “Controlling electromagnetic fields,” *Science*, 312(5781):1780–1782, 2006.

[50] Pozar, David M. *Microwave Engineering Electromagnetics.* John Wiley & Sons, Inc., Hoboken, New Jersey, third edition, 2005.

[51] Rahm, Marco, David Schurig, Daniel A. Roberts, Steven A. Cummer, David R. Smith, and John B. Pendry. "Design of electromagnetic cloaks and concentrators using form-invariant coordinate transformations of Maxwell's equations," *Photon. Nanostruct.: Fundam. Appl.*, 6:87, 2008.

[52] Rahm, Marco, Steven A. Cummer, David Schurig, John B. Pendry, and David R. Smith. "Optical design of reflectionless complex media by finite embedded coordinate transformations," *Phys. Rev. Lett.* 100, 063903, 2008.

[53] Roden J. A., and S. D. Gedney. "Convolution PML (CPML): An Efficient FDTD Implementation of the CFS-PML for Arbitrary Media," *Microw. Opt. Tech. Lett.*, 27(5):334–339, 2000.

[54] Rowling, J. K. *Harry Potter and the Chamber of Secrets*. Scholastic, New York, 1999.

[55] Schurig, D., J. J. Mock, B. J. Justice, S. A. Cummer, J. B. Pendry, A. F. Starr, and D. R. Smith. "Metamaterial Electromagnetic Cloak at Microwave Frequencies," *Science*, 314(5801):977–980, 2006.

[56] Shalaev, Vladamir M. and John Pendry. "Transformation Optics," *J. Opt.*, 13(2), 2011.

[57] Shelby, R. A. D. R. Smith, and S. Schultz. "Experimental Verification of a Negative Index of Refraction," *Science*, 292(5514):77–78, 2001.

[58] Sihvola A. "Electromagnetic emergence in metamaterials," in *Advances in Electromagnetics of Complex Media and Metamaterials*, S. Zouhdi, A. Sihvola, and M. Arsalane, Eds., vol. 89 of NATO Science Series II: Mathematics, Physics, and Chemistry (Kluwer Academic, 2003), pp 3–17.

[59] Silver, Joel (producer). *Matrix Revolutions*. [Videorecording]. Burbank, California: Warner Bros. Pictures, 2003.

[60] Simovski, Constantin R. "On electromagnetic characterization and homogenization of nanostructured metamaterials," *J. Opt.*, 13(1):, 2010.

[61] Simovski, C. R. "Material parameters of metamaterials (a Review)," *Opt Spectrosc.*, 107(5):726–753, 2009.

[62] Simovski, Constantin R. and Sergei A. Tretyakov. "Local constitutive parameters of metamaterials from an effective-medium perspective," *Phys. Rev. B: Condens. Matter*, 75(19), 2007.

[63] Smith, D. R., D. C. Vier, Th. Koschny, and C. M. Soukoulis. "Electromagnetic parameter retrieval from inhomogeneous metamaterials," *Phys. Rev. E.: Stat. Nonlinear Soft Matter Phys.*, 71(3):1–11, 2005.

[64] Smith, David R. and John B. Pendry. "Homogenization of metamaterials by field averaging (invited paper)," *J. Opt. Soc. Am. B*, 23(3):391–403, 2006.

[65] Smith, D. R., S. Schultz, P. Markoš, and C. M. Soukoulis. "Determination of effective permittivity and permeability of metamaterials from reflection and transmission coefficients," *Phys Rev. B.*, 65(19), 2002.

[66] Smith, D. R., W. J. Padilla, D. C. Vier, S. Nemat-Nasser, and S. Schultz. "Composite medium with simultaneously negative permeability and permittivity," *Phys. Rev. Lett.*, 84(18):4184–4187, 2000.

[67] Szabó, Z., Gi-Ho Park, R. Hedge, Er-Ping Li. "A unique extraction of metamaterial parameters based on Kramers-Kronig relationship," *IEEE Theory Tech. Soc.*, 58(10):2646–2653, 2010.

[68] Teixeira, F. L. and W. C. Chew. "Perfectly Matched Layers and Transformation Optics," *Antennas and Propagation (APSURSI), 2009 IEEE International Symposium*, 1–4, 2009.

[69] Ulaby, Fawwaz T. *Fundamentals of Applied Electromagnetics*. Pearson Education Inc., Upper Saddle River, New Jersey, fifth edition, 2007.

[70] Veselago, V. G. "The electrodynamics of substances with simultaneously negative values of ε and μ," *Phys. Usp.*, 10(4):509–514, Jan. 1968.

[71] Ward, A. J. and J. B. Pendry. "Refraction and geometry in Maxwell's Equations," *J. Mod. Opt.*, 43(4):773–793, 1996.

[72] Weiland, T., M. Timm, and I. Munteanu. "A practical guide to 3-D simulation," *IEEE Microwave Mag.*, 9(6):62–75, 2008.

[73] Weiland, T., R. Schumann, R. B. Greegor, C. G. Parazzoli, A. M. Vetter, D. R. Sith, D. C. Vier, and S. Schultz. "Ab initio numerical simulation of left-handed metamaterials: comparison of calculations and experiments," *J. Appl. Phys.*, 90(10):5419–5419, 2001.

[74] Xu, Xiaofei, Yijun Feng, and Tian Jiang. "Electromagnetic beam modulation through transformation optical structures," *New J. Phys.* 10, 115027, 2008.

[75] Yan, Wei. *Manipulation of Light with Transformation Optics*. Ph.D. dissertation, KTH Royal Institute of Technology, Stockholm, Sweden, 2011.

[76] Zhang, Pu. *Theory of Transformation Optics and Invisibility Cloak Design*. Ph.D. dissertation, KTH Royal Institute of Technology, Stockholm, Sweden, 2011.

Vita

Capt Noel Humber was born in Ithaca, New York and graduated with honors from Ithaca High School. He entered undergraduate studies at Cornell University on a four-year Air Force ROTC scholarship. He graduated with a Bachelor of Science degree in Mechanical Engineering in May 2005. He was commissioned through Detachment 520 at Cornell University in May 2005.

His first assignment was to the Joint Strike Fighter Integrated Test Force at Edwards AFB, California. There, he helped stand up the 461st Flight Test Squadron (FLTS) and worked as an operations engineer on various programs supporting the development of the F-35. In February 2008 he was moved to the 412th Operations Group where he served as an executive officer for the Group Commander. After eleven months at that assignment he was temporarily reassigned as an operations engineer at the 445th FLTS. In May of 2009 he was assigned to Wright-Patterson AFB where he served as a project engineer for classified programs in Sensors Directorate for the Air Force Research Labs. In April 2010 he entered graduate school at the Air Force Institute of Technology. Upon graduation he will be assigned to Detachment 2 of the 46th Test Group at Holloman Air Force Base, New Mexico. His assignment involves operations at the National Radar Test Facility.

REPORT DOCUMENTATION PAGE	Form Approved OMB No. 074-0188

The public reporting burden for this collection of information is estimated to average 1 hour per response, including the time for reviewing instructions, searching existing data sources, gathering and maintaining the data needed, and completing and reviewing the collection of information. Send comments regarding this burden estimate or any other aspect of the collection of information, including suggestions for reducing this burden to Department of Defense, Washington Headquarters Services, Directorate for Information Operations and Reports (0704-0188), 1215 Jefferson Davis Highway, Suite 1204, Arlington, VA 22202-4302. Respondents should be aware that notwithstanding any other provision of law, no person shall be subject to an penalty for failing to comply with a collection of information if it does not display a currently valid OMB control number.
PLEASE DO NOT RETURN YOUR FORM TO THE ABOVE ADDRESS.

1. REPORT DATE *(DD-MM-YYYY)*	**2. REPORT TYPE**	**3. DATES COVERED** *(From – To)*
22-03-2012	Master's Thesis	Sep 2010 – Mar 2012

TITLE AND SUBTITLE	
Design, Modeling, and Measurement of a Metamaterial Electromagnetic Field Concentrator	**5a. CONTRACT NUMBER**
	5b. GRANT NUMBER
	5c. PROGRAM ELEMENT NUMBER
6. AUTHOR(S)	**5d. PROJECT NUMBER** ENG 11G562
Humber, Noel A., Captain, USAF	**5e. TASK NUMBER**
	5f. WORK UNIT NUMBER

7. PERFORMING ORGANIZATION NAMES(S) AND ADDRESS(S)	**8. PERFORMING ORGANIZATION REPORT NUMBER**
Air Force Institute of Technology Graduate School of Engineering and Management (AFIT/ENY) 2950 Hobson Way, Building 640 WPAFB OH 45433-8865	AFIT/GE/ENG/12-22
9. SPONSORING/MONITORING AGENCY NAME(S) AND ADDRESS(ES)	**10. SPONSOR/MONITOR'S ACRONYM(S)** AFRL/RX
Air Force Research Lab, Materials and Manufacturing Directorate Attn: Katie Thorp 2941 Hobson Way WPAFB OH 45433-7750 (937) 255-9145, katie.thorp@wpafb.af.mil	**11. SPONSOR/MONITOR'S REPORT NUMBER(S)**

12. DISTRIBUTION/AVAILABILITY STATEMENT
APPROVED FOR PUBLIC RELEASE; DISTRIBUTION UNLIMITED.

13. SUPPLEMENTARY NOTES

14. ABSTRACT
This document addresses the need to improve the design process for creating an optimized metamaterial. In particular, two challenges are addressed: creating an electromagnetic concentrator and optimizing the design of metamaterial used to create the electromagnetic concentrator. The first challenge is addressed by developing an electromagnetic field concentrator from a design of concentric geometric shapes. The material forming the concentrator is derived from the application of transformation optics. The resulting anisotropic, spatially variant constitutive parameter tensors are then approximated with metamatieral inclusions using the combination of an AFIT rapid metamaterial design process and a design process created for rapid metamaterial production. The second challenge of optimizing the design of the metamaterial is addressed by considering factors such as circuit board selection, various sets of metamaterial cell geometry combinations, and optimization of the ratio of the widths for the concentric geometric shapes. The resulting optimized design is simulated and shown to compress and concentrate the vertical electric field component of incident plane waves. A physical device is constructed based on the simulations and tested to confirm the entire design process. Experimental data do not definitely show concentration however an optimized design process has been proven.

15. SUBJECT TERMS
Metamaterials, Computational Electromagnetics, Electromagnetic Field Concentration, Focus Beam Measurements, Transformation Optics

16. SECURITY CLASSIFICATION OF:			**17. LIMITATION OF ABSTRACT**	**18. NUMBER OF PAGES**	**19a. NAME OF RESPONSIBLE PERSON** Dr. Peter J. Collins, ENG
a. REPORT	**b. ABSTRACT**	**c. THIS PAGE**			**19b. TELEPHONE NUMBER** *(Include area code)*
U	U	U	UU	242	(937) 255-3636, x7256; peter.collins@afit.edu

Standard Form 298 (Rev. 8-98)
Prescribed by ANSI Std. Z39-18